UNIVERSITY OF CALIFORNIA SAN DIEGO

Effects of kilotesla-level applied magnetic fields on relativistic laser-plasma interactions

A dissertation submitted in partial satisfaction of the
requirements for the degree
Doctor of Philosophy

in

Engineering Sciences (Engineering Physics)

by

Kathleen Joy Weichman

Committee in charge:

Professor Alexey Arefiev, Chair
Professor Farhat Beg
Professor Michael Norman
Professor Kevin Quest
Professor George Tynan

2020

The dissertation of Kathleen Joy Weichman is approved, and it is acceptable in quality and form for publication on microfilm and electronically:

_____

_____

_____

_____

_____

Chair

University of California San Diego

2020

DEDICATION

To my friends and mentors

TABLE OF CONTENTS

LIST OF FIGURES

LIST OF TABLES

ACKNOWLEDGEMENTS

I would like to thank Alexey Arefiev for being an inspiration in addition to a fine graduate advisor. I would also like to thank Gian Luca Delzanno for his infectious enthusiasm and support.

Chapter 2, in full, is a reprint of the material as it appears in A. P. L. Robinson, K. Tangtartharakul, K. Weichman, and A. V. Arefiev, "Extreme nonlinear dynamics in vacuum laser acceleration with a crossed beam configuration", *Physics of Plasmas* **26**, 093110 (2019), with the permission of AIP Publishing. The dissertation author contributed methodology, supervised visualization, and assisted in writing the paper.

Chapter 3, in full, is a reprint of the material as it appears in K. Weichman, A. P. L. Robinson, F. N. Beg, and A. V. Arefiev, "Laser reflection as a catalyst for direct laser acceleration in multipicosecond laser-plasma interaction", *Physics of Plasmas* **27**, 013106 (2020), with the permission of AIP Publishing. The dissertation author was the primary investigator and author of the paper.

Chapter 4, in part, is currently being prepared for submission for publication of the material. K. Weichman and A. V. Arefiev. The dissertation author was the primary investigator and author of this material.

Chapter 5, in full, is a reprint of the material as it appears in K. Weichman, J. J. Santos, S. Fujioka, T. Toncian, and A. V. Arefiev, "Generation of focusing ion beams by magnetized electron sheath acceleration", *Scientific Reports*, **10**, 18966 (2020). The dissertation author was the primary investigator and author of the paper.

Chapter 6, in full, is a reprint of the material as it appears in K. Weichman, A. P. L. Robinson, M. Murakami, and A. V. Arefiev, "Strong surface magnetic field generation in relativistic short pulse laser-plasma interaction with an applied seed magnetic field", *New Journal of Physics*, **22**, 113009 (2020). The dissertation author was the primary investigator and author of the paper.

Chapter 7, in full, is a reprint of the material as it appears in M. Murakami, J. J. Honrubia, K. Weichman, A. V. Arefiev, and S. V. Bulanov, "Generation of megatesla magnetic fields by intense-laser−driven microtube implosions", *Scientific Reports* **10**, 16653 (2020). The dissertation author contributed simulations, figures, and writing to the paper.

Chapter 8, in full, is a reprint of the material as it appears in K. Weichman, M. Murakami, A. P. L. Robinson, and A. V. Arefiev, "Sign reversal in magnetic field amplification by relativistic laser-driven microtube implosions", *Applied Physics Letters* (2020, accepted), with the permission of AIP Publishing. The dissertation author was the primary investigator and author of the paper.

Chapter 9, in full, is a reprint of the material as it appears in Y. Shi, K. Weichman, R. J. Kingham, and A. V. Arefiev, "Magnetic field amplification in a laser-irradiated thin collisionless plasma target by return current electrons carrying orbital angular momentum", *New Journal of Physics*, **22**, 073067 (2020). The dissertation author contributed conceptualization, methodology, and writing to the paper.

VITA

2013	Bachelor of Science in Nuclear, Plasma, and Radiological Engineering, University of Illinois at Urbana-Champaign
2013-2014	Teaching Assistant, University of Texas at Austin
2014-2017	Department of Energy Computational Science Graduate Fellow, University of Texas at Austin
2018	Department of Energy Computational Science Graduate Fellow, University of California San Diego
2018-2020	Graduate Student Researcher, University of California San Diego
2020	Doctor of Philosophy in Engineering Sciences (Engineering Physics), University of California San Diego

PUBLICATIONS

K. Weichman, A. P. L. Robinson, M. Murakami, and A. V. Arefiev, "Strong surface magnetic field generation in relativistic short pulse laser-plasma interaction with an applied seed magnetic field", *New Journal of Physics*, **22**, 113009 (2020).

K. Weichman, J. J. Santos, S. Fujioka, T. Toncian, and A. V. Arefiev, "Generation of focusing ion beams by magnetized electron sheath acceleration", *Scientific Reports*, **10**, 18966 (2020).

K. Weichman, M. Murakami, A. P. L. Robinson, and A. V. Arefiev, "Sign reversal in magnetic field amplification by relativistic laser-driven microtube implosions", *Applied Physics Letters* (2020, accepted).

H. Mao, **K. Weichman**, Z. Gong, T. Ditmire, H. Quevedo, and A. V. Arefiev, "Dynamics of a relativistic velocity collisionless ionization wave in an applied magnetic field," arXiv:2008.02920 (2020, under review).

M. Murakami, J. J. Honrubia, **K. Weichman**, A. V. Arefiev, and S. V. Bulanov, "Generation of megatesla magnetic fields by intense-laser-driven microtube implosions", *Scientific Reports* **10**, 16653 (2020).

Y. Shi, **K. Weichman**, R. J. Kingham, and A. V. Arefiev, "Magnetic field amplification in a laser-irradiated thin collisionless plasma target by return current electrons carrying orbital angular momentum", *New Journal of Physics* **22**, 073067 (2020).

K. Weichman, A. P. L. Robinson, F. N. Beg, and A. V. Arefiev, "Laser reflection as a catalyst for direct laser acceleration in multipicosecond laser-plasma interaction", *Physics of Plasmas* **27**, 013106 (2020).

A. P. L. Robinson, K. Tangtartharakul, **K. Weichman**, and A. V. Arefiev, "Extreme nonlinear dynamics in vacuum laser acceleration with a crossed beam configuration", *Physics of Plasmas* **26**, 093110 (2019).

ABSTRACT OF THE DISSERTATION

Effects of kilotesla-level applied magnetic fields on relativistic laser-plasma interactions

by

Kathleen Joy Weichman

Doctor of Philosophy in Engineering Sciences (Engineering Physics)

University of California San Diego, 2020

Professor Alexey Arefiev, Chair

Recent advances in magnetic field generation have made experimentally accessible new regimes in magnetized high energy density physics. However, relatively little is currently known about the effects of kilotesla-level magnetic fields in relativistic laser-produced plasma. In this dissertation, I discuss a number of common plasma configurations, including solid targets and laser propagation in underdense plasma, in which applied magnetic fields can fundamentally alter plasma dynamics and impact important observables, such as ion and electron energy. In this regime, the changes induced by the magnetic field proceed mostly from the magnetization of hot electrons. Crucially, clear effects can be produced even

when the magnetic field is not initially strong enough to magnetize electrons, suggesting that experimentally available applied magnetic fields may now be capable of delivering improvements for applications of relativistic short pulse laser-plasma interaction.

Chapter 1

Introduction

Understanding the potential of magnetic fields to shape plasma behavior is a crucial aspect of plasma physics research. Much of the recent study of magnetized plasma has been motivated by fusion energy applications, where particles are non-relativistic and extreme electric and magnetic fields are not present. Often, these applications are concerned with collective or fluid-like behavior, including, for example, heat conduction and the overall plasma confinement. In contrast, the plasma produced by intense short pulse lasers can be relativistic and inherently feature strong electric and magnetic fields. Furthermore, many of the applications of laser-plasma interactions feature distinctly kinetic dynamics and depend on a relatively small population of energetic particles rather than the bulk behavior. It is therefore critical to re-examine the potential effects of magnetic fields in the relativistic laser-plasma context. In this dissertation, I will present a variety of plasma configurations where important changes in plasma behavior and application-relevant observables can be produced by the application of a uniform, quasi-static kilotesla-level magnetic field. These scenarios have been selected to illustrate a number of interesting and potentially impactful effects of adding a strong magnetic field, and represent a promising new direction for relativistic laser-plasma research.

The development of high power laser technology [1] enables the investigation of plasma under high energy density (HED) conditions in facilities around the world [2–5]. Laser-produced HED plasma provides a convenient platform for investigations in laboratory astrophysics [6–9], imaging [10, 11], accelerator science [12, 13], and inertial confinement fusion [14–16]. The ability of the laser to deliver substantial energy to the plasma in the form of energetic electrons is a key feature of high intensity laser-plasma interaction. The production of charged particles [17, 18], neutrons [19], or high energy X-rays [20, 21] which make laser-plasma interaction attractive for applications is often driven indirectly by this hot electron population. As a consequence, understanding, and potentially controlling the dynamics of relativistic electrons is highly desirable. As I will demonstrate, the addition of an applied magnetic field can fundamentally change the electron dynamics. Changes to the electron dynamics can subsequently impart significant changes to the ion dynamics and are both of fundamental physics interest and beneficial for applications.

Magnetic fields are also an inherent component of relativistic laser-produced plasma and have a significant impact on plasma dynamics. For example, when the amplitude of the laser pulse is sufficiently high for electron motion in the laser pulse to be relativistic ("relativistic intensity"), the magnetic force exerted on electrons by the laser pulse enables electrons to move substantially in the laser propagation direction, and plays a key role in the net transfer of laser energy to electrons. The laser interaction with the plasma is also capable of self-generating strong quasi-static magnetic fields. For example, strong magnetic fields can arise at the surfaces of laser-irradiated solid targets, impacting the plasma dynamics (e.g. Ref 22). The presence of self-generated fields provides additional motivation for studies to understand the fundamentals of how magnetic fields affect the evolution and potential deliverables of laser-produced plasma.

In contrast with self-generated fields, applied magnetic fields offer external control over the magnetic field profile and can provide magnetic fields in configurations which

are not easily achievable using self-generated fields. In this dissertation, I will consider applied magnetic fields which are spatially uniform and static on the length and time scales relevant to laser-plasma interactions. For my purposes, this requires the magnetic field to be spatially uniform over a 100 μm to 1 mm scale and slowly evolving compared to a laser pulse which is tens of femtoseconds to tens of picoseconds long. Such magnetic fields are currently under experimental development using a variety of approaches including laser-driven coil [23–26] and pulsed power [27–29] sources. These magnetic field generation techniques have recently been demonstrated to produce near-kilotesla fields over hundreds of microns (e.g. Ref. 30) or greater than 100 T fields over millimeter distances (e.g. Ref. 29) at facilities where high power lasers are also available. It is therefore timely to consider the potential impact of kilotesla-level magnetic fields on relativistic laser-produced plasma.

1.1 Electron acceleration by picosecond laser pulses

As previously mentioned, the energization of electrons by the laser pulse underlies most of the interesting and desirable phenomena associated with laser-plasma interactions. Understanding the mechanisms responsible for this energy gain is therefore key to optimizing the laser and plasma conditions for applications. In Chapters 2-4, I will discuss electron acceleration by picosecond laser pulses, both with and without an applied magnetic field.

The dominant route to electron energy gain in laser-produced plasma depends on a number of factors, including the laser intensity, the plasma density profile, the pulse duration, and the presence of an applied magnetic field. The laser pulses I consider in this dissertation are relativistically intense. The threshold for relativistic intensity is the condition for an electron interacting with a laser in vacuum to obtain relativistic momentum ($|p| \sim m_e c$) within a single laser cycle, which corresponds to a peak intensity of $I_0 \gtrsim 10^{18}$ W/cm^2 for a 1 μm wavelength laser. Such a laser pulse is reflected by a plasma

if the plasma density exceeds the relativistically adjusted critical density γn_{cr}, where γ is the characteristic Lorentz factor of electrons undergoing motion in the laser pulse and $n_{cr} \sim 10^{21}$ cm^{-3} is the critical density in a cold plasma for a 1 μm laser [31].

It has been observed that relativistic multipicosecond laser pulses incident on solid targets can produce copious energetic electrons with higher density than can be obtained by individual electrons interacting with a single laser pulse in vacuum [32–35]. For modestly relativistic lasers with a 1 μm wavelength, solid targets are overdense ($n > \gamma n_{cr}$) and can produce strong laser reflection. Laser reflection can fundamentally change the dynamics of electrons and may introduce stochastic routes to energy gain. Chapter 2 demonstrates that the stochastic electron motion which is expected to occur in vacuum with crossed or counter-propagating laser pulses may not be accurately reproduced by standard simulation techniques, indicating a need for the development of new computational schemes. In Chapter 3, I demonstrate that laser reflection can also act as a catalyst for enhanced non-stochastic electron acceleration by multipicosecond pulses incident on solid targets, which suggests a different approach to optimizing hot electron production than stochastic heating.

The application of a kilotesla-level magnetic field can also enhance energetic electron production by enabling fundamental changes to the dynamics of electrons interacting with a laser pulse in underdense ($n < \gamma n_{cr}$) plasma. This magnetically assisted direct laser acceleration can substantially increase the electron energy relative to the non-magnetized case and promotes energy retention by the plasma after the laser has passed. In Chapter 4, I demonstrate that magnetically assisted direct laser acceleration is experimentally accessible with sub-kilotesla applied magnetic fields for moderately relativistic picosecond laser pulses. While magnetically assisted direct laser acceleration ordinarily requires a preheated plasma, I formulate a setup employing initially cold plasma in which a second, femtosecond duration pulse enables substantial energetic electron production by a modestly relativistic picosecond

pulse.

1.2 Ion acceleration with an applied magnetic field

While changes to energetic electron production by the laser pulse are one clear way in which a sufficiently strong applied magnetic field can benefit laser-produced plasma, important effects of the magnetic field can also be seen in regimes where electron acceleration by the laser is not significantly affected. The magnetic field can also impact the dynamics of hot electrons over distance and time scales which exceed those of the laser pulse and in regions where the laser is not present. In Chapter 5, I consider how a kilotesla-level applied magnetic field can impact sheath-based ion acceleration.

The expansion of a laser-heated electron sheath into vacuum [36, 37] is an experimentally robust and extensively studied platform for the generation of energetic ions [18]. In sheath-based ion acceleration (for instance, in target normal sheath acceleration [38–40]), an intense laser pulse heats electrons on one side of an overdense target. The hot electron population then streams through the target and out into the rear-side vacuum, establishing a sheath electric field which accelerates ions from the rear surface. The addition of a strong magnetic field along the target normal direction has the potential to prevent the transverse escape of hot electrons which ordinarily degrades the ion acceleration process and produces a diverging ion beam. In Chapter 5, I demonstrate that a kilotesla-level applied magnetic field results in an ion source with substantially enhanced energy and number, and which is focusing about the magnetic field direction. Such improvements are highly desirable for applications including isochoric heating (e.g. Ref 41) and ion fast ignition (e.g. Ref 42).

1.3 Magnetic field production by solid targets

In addition to directly impacting application-relevant electron and ion dynamics, applied magnetic fields can also trigger strong magnetic field generation. This is a somewhat surprising result because plasma is often considered to behave diamagnetically. Chapters 6-9 demonstrate that embedding magnetic fields in solid density targets can trigger the production of orders-of-magnitude stronger magnetic fields. These enhanced magnetic fields may then be sufficiently strong to directly impact the plasma dynamics.

The addition of an embedded target-transverse magnetic field to a laser-irradiated solid target leads to the gyrorotation of laser-heated electrons within the solid. At the same time, cold electrons within the target produce a compensating return current, which can prevent the magnetic field within the overdense plasma from significantly changing. However, as I demonstrate in Chapter 6, this configuration results in strong magnetic field production at the target surface. Although magnetic field production at solid surfaces is a normal feature of laser-plasma [43, 44], the structure, polarity, and overall magnitude of the surface field can be dramatically affected by the addition of the embedded magnetic field. The magnetic field can also be strong enough to alter ion acceleration from the target.

Applied magnetic fields can also affect magnetic field production away from solid surfaces, for example in imploding structured targets. Structured targets including nanowires [45], nanospheres [46, 47], and microchannels [21, 48, 49] have been shown to deliver improvements in particle [45–47, 49], radiation [48, 50, 51], and magnetic field generation [52, 53] sources. Such targets can also produce interesting effects in the context of applied magnetic fields. While it has long been known that implosions are capable of amplifying applied magnetic fields in the magnetohydrodynamic regime (mm-scale, non-relativistic implosions with sub-100 T applied fields) via flux compression [54, 55], the inherently kinetic dynamics of micron-scale relativistic laser-driven implosions require re-evaluating the potential mechanisms for magnetic field amplification. Chapter 7 demon-

strates strong magnetic field amplification in relativistic laser-driven microtube implosions in excess of what can be achieved via flux compression. In Chapter 8, I demonstrate that the magnetic field which is amplified in microtube implosions is not necessarily the applied field, but can also be the field generated at the solid surface, which has opposite sign. Microtube implosions are thereby able to deliver magnetic fields two orders of magnitude stronger than the applied seed, with a controllable sign.

Implosions are not the only context in which applied magnetic fields can be amplified by relativistic laser-plasma. As mentioned above, the populations of hot and cold electrons in a solid target generally carry current in opposite directions. While in the context of surface magnetic field generation, the hot electrons are responsible for driving the magnetic field production, Chapter 9 demonstrates magnetic field amplification by the cold return current in the case of a thin solid target with a target normal embedded magnetic field. In this scenario, the charge separation created by the expulsion of hot electrons by the laser pulse drives return current with orbital angular momentum favorable for magnetic field amplification.

1.4 Summary

In summary, I have examined a number of the possible effects of a kilotesla-level applied magnetic field on relativistic laser-plasma. These effects highlight new and potentially important physics in the magnetized high energy density context and indicate that applied magnetic fields can be desirable for applications. The physics I examine in this dissertation may additionally be applicable across a wide range of relativistic laser-plasma configurations with applied magnetic fields. The field of magnetized high energy density physics is rapidly growing and it is my hope that the work presented in this dissertation will provide a source of inspiration for its continued evolution and expansion.

Chapter 2

Extreme nonlinear dynamics in vacuum laser acceleration with a crossed beam configuration

2.1 Abstract

A relatively simple model problem where a single electron moves in two relativistically-strong obliquely intersecting plane wave-packets is studied using a number of different numerical solvers. It is shown that, in general, even the most advanced solvers are unable to obtain converged solutions for more than about 100 fs in contrast to the single plane-wave problem, and that some basic metrics of the orbit show enormous sensitivity to the initial conditions. At a bare minimum this indicates an unusual degree of non-linearity, and may well indicate that the dynamics of this system are chaotic.

2.2 Introduction

Since the development of Chirped Pulse Amplification lasers [56–59], the field of ultra-intense laser-matter interactions has grown considerably. Initially this technology allowed the development of TW-scale lasers that breached the $10^{18}\mathrm{Wcm}^{-2}\mu\mathrm{m}^2$, but subsequent progress has lead to the construction of 10PW scale systems [57], with 100PW systems under development. The field now spans a large number of sub-topics including laser wakefield acceleration of electrons [60], laser-driven ion acceleration [61], laser- driven x-ray [62] and neutron sources, advanced inertial fusion concepts such as Fast Ignition [63], studies of both Warm Dense Matter and Hot Dense Matter [64], radiation reaction studies, and even probing QED physics [65, 66]. It is likely that the latter topics in that list will become more dominant as multi-PW facilities become fully operational in the following years. Numerical simulation codes, particularly Particle-in-Cell (PIC) codes [67, 68], have been instrumental in driving the field forward, both in terms of interpreting experiments and in making predictions that have motivated crucial experimental work. Perhaps the best known example of PIC's predictive capabilities is that of Pukhov and Meyer-ter-Vehn's prediction [69] of the 'bubble regime' of laser wakefield acceleration, which was later validated by three different research groups [60].

The PIC algorithm is itself dependent on a number of algorithms, some of which were developed separately, such as the Yee FDTD method [70] for numerical electromagnetics. Importantly this includes a 'particle-pusher' algorithm which advances the macroparticles position and momentum. The quality and capability of any individual PIC code will depend on the set of algorithms chosen for these different components. A common choice for the particle-pusher is the Boris method [67]. The Boris method is a second order accurate leapfrog-type method that is centred in time. It is a method that has enjoyed considerable success, and which has been employed in a number of different PIC codes including EPOCH [71]. Developing higher order versions of the Boris method is a non-trivial

proposition, and it is has been questioned whether or this endeavour would actually yield any serious benefits to laser-plasma or accelerator science [72, 73].

In the past few years however it has been recognized that the Boris method has at least one serious defect, namely that constant motion is not maintained in the case of uniform crossed $\mathbf{E} \neq 0$ and $\mathbf{B} \neq 0$ fields (for the choice of particle velocity for which a force-free scenario is obtained). This was first identified by Vay [74], who proposed a variation on the Boris pusher that resolved this issue. Later Higuera and Cary [72] proposed an algorithm that both solved the issue of the $\mathbf{E} \times \mathbf{B}$ velocity and which also preserved phase-space volume (unlike Vay's method). Alongside these developments, Arefiev also showed that considerable care needs to be taken in setting the time step when integrating the orbits of an electron in a relativistic laser pulse. Altogether these developments underline how the particle-pusher problem needs careful study to ensure that particle-pusher algorithms can be trusted when employed to study the strongly relativistic and highly complex configurations encountered in ultra-intense laser-matter problems.

Despite these developments the methods of Vay and Higuerra-Cary are still only second order accurate methods. For problems where the overall behaviour of the system is quite 'regular' this means that they will be quite adequate in the majority of cases. What has not been given so much consideration is whether the dynamics can always be assumed to be sufficiently 'regular'. Some researchers have pointed out that some laser interaction problems will have a 'stochastic' nature [32, 75, 76], this terminology appears to actually mean that the dynamics are *chaotic* [77–79]. If the Lyapunov time is larger than the time-scale of interest then this is not a problem for numerical simulation. However if the Lyapunov time becomes much shorter than the time-scale of interest then the ability to predict future states of the system will be highly limited even with very sophisticated numerical solvers.

In this paper we present a relatively simple test problem for a single electron : two

plane EM Gaussian wave-packets that cross at an oblique angle and which are π out of phase. The electron is initially at rest and which sits 'off-axis' by a fraction of the vacuum wavelength. To the best of the authors' knowledge this problem does not have an analytic solution. We have studied the ability of a number of leapfrog pushers, RK4 method, and more sophisticated adaptive algorithms to solve the electron orbits in this problem. We have found that, in general, all of these solvers are only able to obtain converged orbits for a fraction (<20%) of the total problem duration (100-200 fs out of 1 ps). Complete converged orbits are only obtained in a few cases, and usually only the RK4 method (or better) is able to do this. A survey of the sensitivity to initial conditions was carried out, and it was found that there are regions of parameter space which exhibit extreme sensitivity to initial conditions. This indicates that this problem, however simple it may seem, in fact is *chaotic* in nature, as expected given earlier studies [32, 75, 76], however in this case it would appear that the chaotic dynamics is severly problematic for numerical integration. We suggest that this may have important ramifications for both Vacuum Laser Acceleration (VLA) [80–84] and Direct Laser Acceleration (DLA) [85–93].

2.3 Description of Model Problem

We consider a problem where two relativisitically-strong plane EM wave-packets intersect obliquely. We want to study the relativistic motion of an electron that is initially at rest. This can be described by the following formulae for the electric fields of the incident waves:

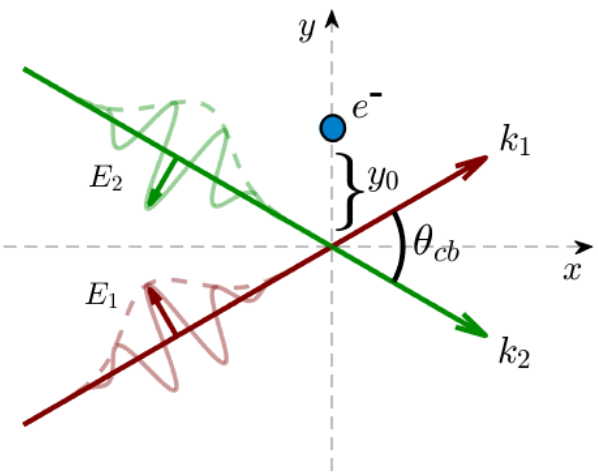

Figure 2.1: Schematic of the simulation set-up showing key parameters.

$$\mathbf{E} = \mathbf{E}_1 + \mathbf{E}_2, \tag{2.1}$$

$$\mathbf{E}_1 = E\cos\psi_1 f_{env,1}\left[-\sin(\theta_{cb}/2), \cos(\theta_{cb}/2), 0\right], \tag{2.2}$$

$$\mathbf{E}_2 = E\cos\psi_2 f_{env,2}\left[\sin(\theta_{cb}/2), \cos(\theta_{cb}/2), 0\right], \tag{2.3}$$

where $\psi_1 = \mathbf{k_1}.\mathbf{r} - \omega_L t + \phi_1$, $\psi_2 = \mathbf{k_2}.\mathbf{r} - \omega_L t + \phi_2$, $\mathbf{k}_1 = [\cos(\theta_{cb}/2), \sin(\theta_{cb}/2), 0]$, $\mathbf{k}_2 = [\cos(\theta_{cb}/2), -\sin(\theta_{cb}/2), 0]$. For the envelope functions, we use $f_{env} = \exp(-(\psi/k_L + 5c\tau_L)^2/(2c\tau_L))$. There are corresponding magnetic fields in the z-direction. This corresponds to two intersecting plane wave-packets that are aligned obliquely to the x-axis with the E-field polarized in the xy-plane in each case. The angle between the wavevectors of the two wave-packets is θ_{cb}. For our baseline problem we consider the case where $E = 5\omega_L m_e c/e$ (i.e. each plane wave-packet has $a_0 = 5$), θ_{cb} =40°, λ_L =1 μm, and τ_L =20 fs. The two wavepackets are π out of phase, i.e. $\phi_1 = 0$, $\phi_2 = \pi$. The electron is initially at rest at x =0,z =0, and $y = y_0$. A schematic of the problem is shown in fig.2.1.

Since this problem is quite close to that considered previously [32, 75, 76], we should expect that chaotic dynamics are likely to be encountered. A very significant difference

with earlier studies is that the value of the normalized vector potential in this case is significantly larger ($a > 5$ here). However since Mendonca's [94] criterion is $a_1 a_2 > 1/16$ we expect that chaotic dynamics will only be more prevalent in this problem.

2.4 Analysis with Standard Algorithms

In the first part of our study we have used the following solvers : (i) the Boris pusher [67], (ii) the Vay pusher [74], (iii) the Higuera-Cary pusher [72], and (iv) the 4th order Runge-Kutta (RK4) algorithm [95], to study this problem. Note that (i)–(iii) are formally 2nd order algorithms (although they differ in their treatment of the $\mathbf{E} \times \mathbf{B}$ velocity) , and only (iv) is formally 4th order. These were applied to study the baseline case (case 1). We shall not re-state the details of these here, and we refer the reader to the given references for further details. We have tested and checked our implementations, in particular by testing that they reproduce the motion in a single plane wave-packet. The baseline numerical integration is carried out over 18000 time steps with Δt =0.05 fs. To examine convergence, the time step is multiplied by a factor $1/M$, and the total number of time steps by M in order to keep the total duration of the integration constant. In general, we regard two trajectories as being converged if the variables in question are within 5% of one another. All of these solvers reproduce the analytic prediction for the single plane-wave problem with $M = 1$ and the solutions of each solver are practically identical.

For each solver we obtained solutions of M =1,2,4, and 8. The results for the Boris pusher, in terms of p_y are shown in fig.2.2. By following sequence of cases, we can see that the solution is not converging.

The behaviour of the Boris pusher is in sharp contrast with the RK4 algorithm. The results of the RK4 algorithm, also in terms of p_y, are shown in fig.2.3. Here the four curves almost perfectly overlap, showing clearly that there has been very good convergence,

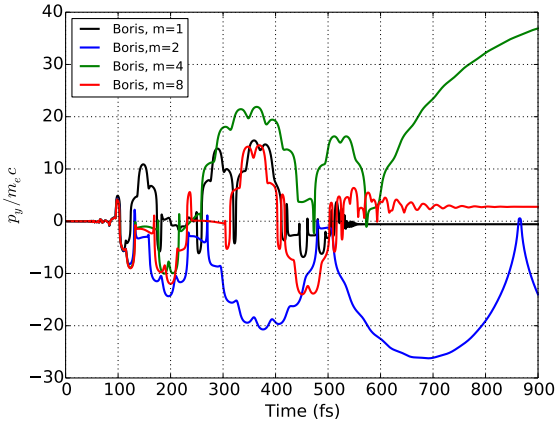

Figure 2.2: The results from the Boris Pusher for the baseline case. Value of M for each line is shown in the legend. Solution shows no sign of convergence with increasing M.

and that it has happened very rapidly.

The behaviour of both the Vay and Higuera-Cary pushers are shown in fig.s 2.4 and 2.5. By comparing fig.s 2.4 and 2.5 to fig. 2.3 we can see that, when M =8, both the Vay and the Higuera-Cary pushers come very close to the solution obtained by the RK4 algorithm. This should lead to confidence in the solution obtained by the RK4 solver. It is clearly good that both the Vay and Higuera-Cary pushers are able to eventually reach this solution, however the rate of convergence is rather slow, and it requires that one adopts a very small time (M =8) time step. In figure 2.6 we directly compare the Vay, Higuera-Cary, and RK4 solutions for M =8. As can be seen they all lie extremely close to one another, showing that the Vay and Higuera-Cary solvers are able to approach the RK4 solution, whereas the Boris solver cannot for $M \leq 8$.

In the second part of our study we extended this to multiple cases to see if these findings reflected a general trend. As is evident from fig.s 2.2–2.5, even when convergence is not obtained over the entire 900 fs, convergence in fact can occur over a time period that is a fraction of the total duration of the problem. When extending the study we instead looked at the fraction of the problem duration over which convergence was obtained

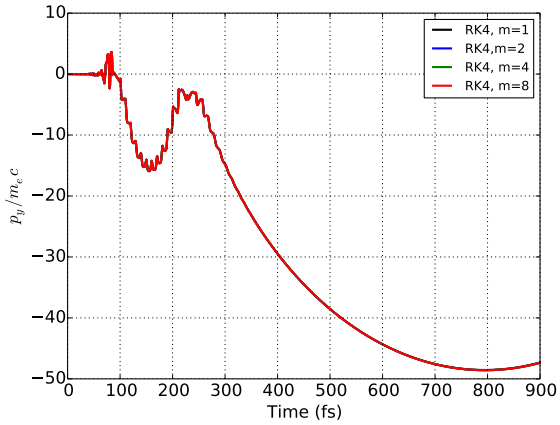

Figure 2.3: The results from the RK4 algorithm for the baseline case. Value of M for each line is shown in the legend. All four curves overlap almost perfectly, indicating extremely rapid convergence.

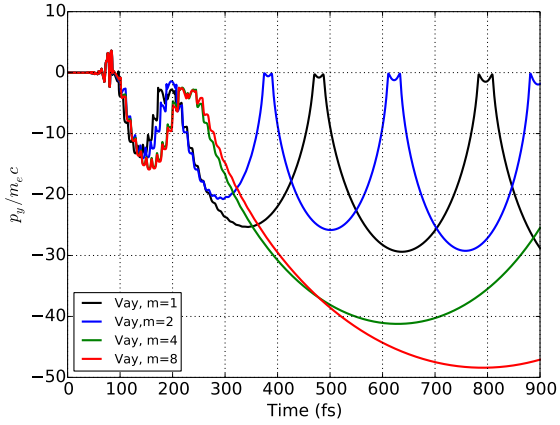

Figure 2.4: The results from the Vay Pusher for the baseline case. Value of M for each line is shown in the legend.

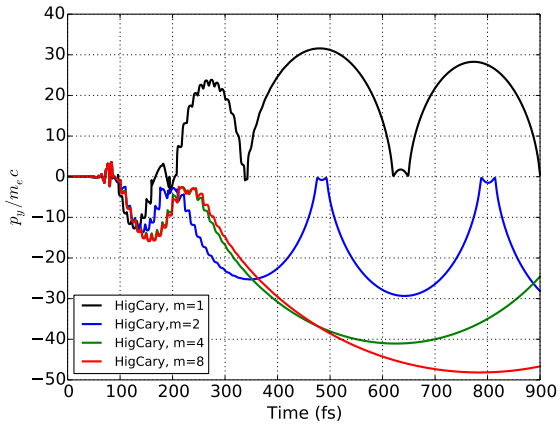

Figure 2.5: The results from the Higuera-Cary pusher for the baseline case. Value of M for each line is shown in the legend.

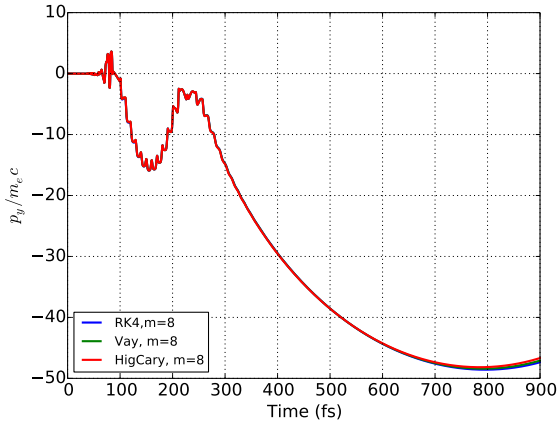

Figure 2.6: Comparison of the solutions from the Vay, Higuera-Cary, and RK4 pushers for M =8, showing that, in the M =8 case, convergence is obtained.

Table 2.1: Summary of results for different cases. Shown in the percentage of the total problem duration for which a given pusher is able to obtain convergence for $M \leq 8$. The special cases of the Vay and Higuera-Cary pushers in the baseline case are noted by an asterisk.

Case	Boris	Vay	Hig.-Cary	RK4
1.a_0 =5, $y_0 = \lambda/4$, $\theta_{cb} = 40°$	14.7	100*	100*	100
2.a_0 =5, $y_0 = \lambda/2$, $\theta_{cb} = 40°$	11.1	11.0	9.1	12.1
3.a_0 =10, $y_0 = \lambda/2$, $\theta_{cb} = 40°$	12.8	13.3	12.9	100.0
4.a_0 =10, $y_0 = \lambda/4$, $\theta_{cb} = 40°$	10.2	10.2	11.3	17.8
5.a_0 =5, $y_0 = \lambda/8$, $\theta_{cb} = 40°$	10.9	11.6	11.6	17.6
6.a_0 =10, $y_0 = \lambda/8$, $\theta_{cb} = 40°$	10.8	11.9	11.9	17.1
7.a_0 =5, $y_0 = \lambda/4$, $\theta_{cb} = 60°$	11.6	11.9	11.7	14.0
8.a_0 =5, $y_0 = \lambda/4$, $\theta_{cb} = 80°$	9.3	9.3	9.8	16.6
9.a_0 =5, $y_0 = \lambda/4$, $\theta_{cb} = 20°$	14.8	14.8	14.8	41.3
10.a_0 =5, $y_0 = \lambda/4$, $\theta_{cb} = 10°$	48.7	48.3	49.0	62.5

(instead of whether or not *total* convergence was obtained). The results are summarized in table 2.1, which shows the convergence obtained for each case as a percentage of the total problem duration (900 fs), and for each solver tried. The special cases of the convergence obtained by the Vay and Higuera-Cary pushers in the baseline case are noted by an asterisk.

From Table 2.1 we find that the baseline case unfortunately represents a rather optimistic one from the point of view of numerically solving this problem. In general we found that even the RK4 pusher was unable to produce converged solutions for more than 18% of the problem duration. Converged solutions over the full duration were only obtained by the RK4 solver in a couple of cases. Also as the approach angle, θ_{cb}, becomes very small, it is much easier to obtain convergence.

All the leapfrog solvers perform less well than the RK4 pusher. The differences between the three are usually rather small (again suggesting that the baseline case, happens to be a special case). It therefore appears that, in general, the enhanced leapfrog solvers are not substantially better at the crossed beam problem than the Boris pusher.

We have also examined the effect that the different solvers have on distributions

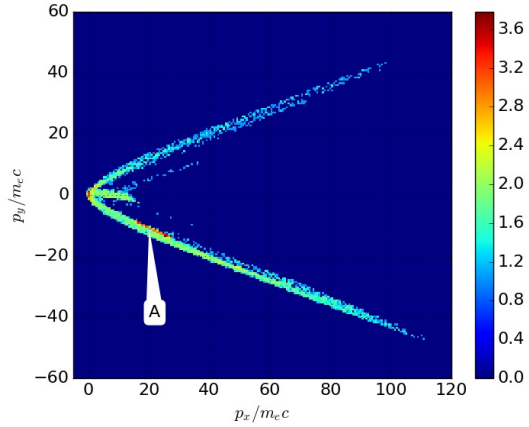

Figure 2.7: Distribution at 450 fs of ensemble calculation (see text) for the case of the Boris solver.

arising from an ensemble of different initial conditions. This was done for 10000 different particles initialized at rest with the initial x-position spanning -0.5 to $+0.5\lambda_L$ ($y_{init} = \lambda_L/4$). The problem was run up to 450 fs with M =1. Otherwise the problem corresponds to the baseline case. We compared the distributions that arose from using the Boris and the RK4 solvers, which are shown in fig.s 2.7 and 2.8 respectively.

In the case of the RK4 solver we see that there is a very strong spike at high energy, denoted as 'B' in fig. 2.8. This feature is absent in fig. 2.7, and instead we see a different feature denoated as 'A' in this figure. Given that the strongest accumulations of particles are completely different for different solvers applied to the same ensemble/problem, we can conclude that the issues observed with single trajectories will lead to significant differences in particles distributions as well.

It therefore appears to be the case that the crossed beam problem presented here represents a far harder test than the single plane wave of single electron trajectory calculation. To the best of the author's knowledge this is currently the hardest test case, at least specifically for laser-plasma studies, as the conventional particle pushers tested here are known to capable of producing fully converged solutions (for $M \leq 8$) over the full

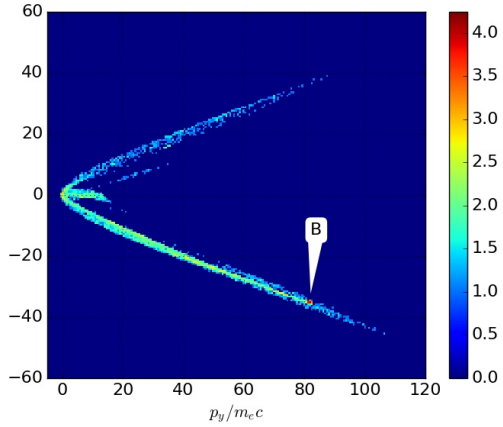

Figure 2.8: Distribution at 450 fs of ensemble calculation (see text) for the case of the RK4 solver.

duration. This is certainly the case for the single plane wave problem. More importantly the results presented in Table 2.1 already indicate the most likely reason as to why this problem is so challenging : namely that the dynamics has become chaotic. We see that, in the general case, a converged solution can only be obtained for a short period of time. We also see that there are strange isolated cases where a full converged solution can be obtained. The observation of these features motivated a more detailed study of the problem.

2.5 Parameter Scans with Advanced Algorithms

In the second phase of this study, another class of solvers was used, namely the MATLAB suite of ODE solvers. In broad terms, applying these solvers to the problem lead to results similar to those presented in Sec. 2.4, with convergence only obtained over a limited period of time and for a small angle between the beams. Out of the entire suite, ODE113 performed the best. This solver is a variable-step, variable-order (VSVO) Adams-Bashforth-Moulton Predictor-Corrector solver of order 1 to 13. It was found that convergence was reliably obtained when the angle between the beams was limited to no more than $\theta_{cb} = 30°$. We have cross-checked the results obtained with ODE113 against the

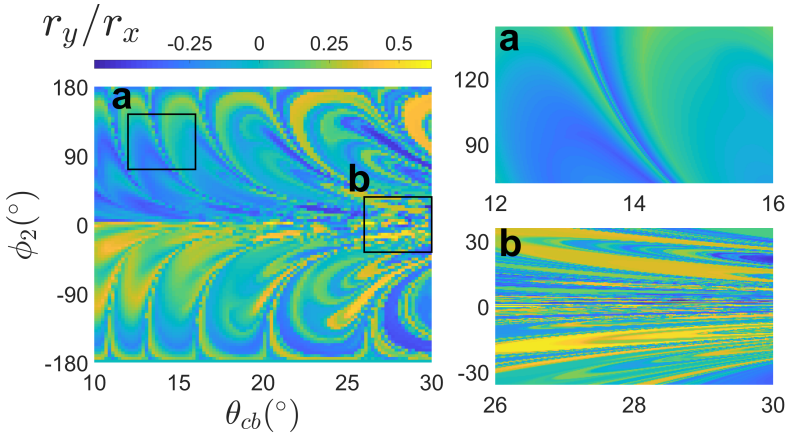

Figure 2.9: Results from parameter scan over ϕ_2 and θ_{cb} in terms of r_y/r_x. Main plot is a coarse scan, with fine scans as sub-plots a and b.

RK4 algorithm, and found good agreement between the two.

In order to study the sensitivity to the initial conditions, parameters scans were then carried out by varying θ_{cb}, ϕ_1, and ϕ_2. For each set of initial conditions a calculation was run up to 200 fs. Two outputs were recorded : (a) the ratio of the final displacement in y to that in x (r_y/r_x), and (b) the time at which the maximum γ occurred ($\tau_{\gamma,max}$, normalized to the laser period). Two types of scans were carried out, *coarse* and *fine*. For the coarse scans, 100 points were used for each parameter over a large range : $\pm\pi$ for phases and 10–30° for θ_{cb}. For the fine scans, a fraction of each range was used and 200 points were then used for each parameter. In all other respects, the calculations are the same as the baseline calculation described in Sec. 2.3. By moving from the analysis of Sec. 2.4 where we looked at 10 cases to these parameter scans where we look at 10000-40000 cases per scan, we can obtain a much clearer idea of how sensitive this problem can be to the initial conditions.

In Fig.s 2.9 and 2.10 we show the results from a coarse parameter scan of θ_{cb} and ϕ_2 with ϕ_1 held fixed at 0°. The sub-figures show plots of fine parameter scans in the regions indicated.

What we observe from these extensive parameters scans is that the parameter space

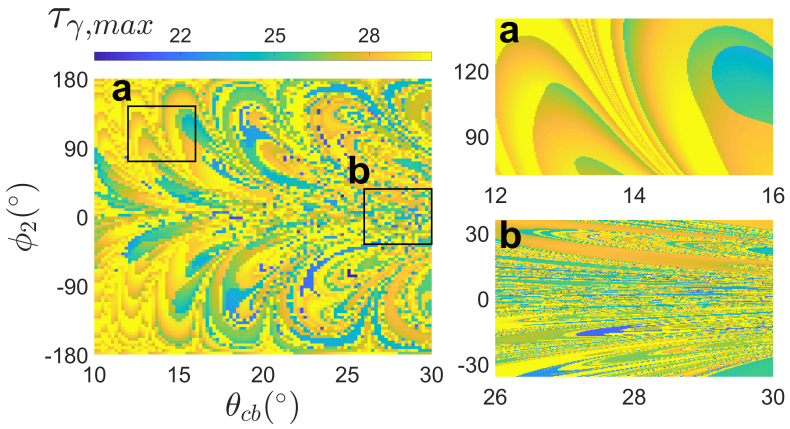

Figure 2.10: Results from parameter scan over ϕ_2 and θ_{cb} in terms of $\tau_{\gamma,max}$. Main plot is a coarse scan, with fine scans as sub-plots a and b.

appears to consist of two types of regions. There are regions where the results of the calculations vary (relatively) slowly and smoothly as the initial conditions are changed. Examples of these are shown in the 'a' sub-figures in both fig. 2.9 and fig. 2.10. There are also regions where small variations of the initial conditions leads to gross changes in the results including rapid changes in sign. Examples of these sub-regions are shown in the 'b' sub-figures in both fig. 2.9 and fig. 2.10.

As we were observing strong point-to-point changes in fig. 2.10(b) along $\theta_{cb} = 28^\circ$ we repeated this set of calculations at twice the resolution in ϕ_2 (i.e. now with 400 points in ϕ_2 across the 'fine' range). The results are shown in fig. 2.11. It can be seen that there is no improvement in terms of being able to 'resolve' the detail in this region.

We can summarize the results from this second phase of the study as follows : (i) we have done an extensive parameter scan of the initial conditions / problem parameters using an advanced ODE solver, (ii) this reveals regions in parameter space that are very sensitive to the initial conditions / problem parameters, (iii) we are not able to 'resolve' this sensitivity by successively refining the set of points over which we scan. These observations suggest that we are actually looking at a system that exhibits chaotic dynamics, as we expected from earlier studies.

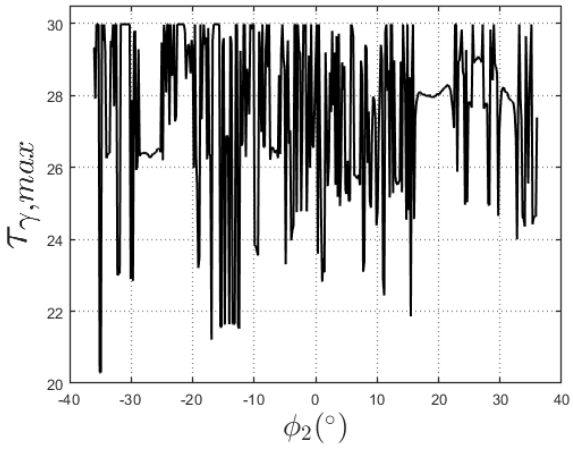

Figure 2.11: Line-out of Fig.2.10(b) along $\theta_{cb} = 28^\circ$

2.6 Conclusions

In this paper we have examined an apparently simple model problem in relativistic single electron motion relevant to ultra-intense laser-plasma interactions, involving two obliquely intersecting plane wave-packets. The findings for this model problem, which are presented herein can be summarized as follows:

1. Under a wide range of conditions converged solutions cannot be obtained for a 1 ps period using a wide range of different solvers including the Boris method, 4th order Runge-Kutta, and the MATLAB suite of ODE solvers.

2. Converged solutions appear to occur in isolated ranges of problem parameters.

3. Converged solutions can, in general, only be obtained over quite short durations, especially compared to benchmarks such as the single plane-wave problem where this is not an issue.

4. When extensive parameter scans are carried out across initial conditions / problem parameters, it is found that regions in parameter space exist where there is a very high degree of sensitivity to these initial conditions (or problem parameters).

5. Progressively increasing the resolution of these sensitive regions does not lead to any improved resolution of the highly sensitive region.

Our findings have, in the authors' view, two main consequences. Firstly, great care needs to be taken when using PIC codes to study laser-plasma interactions. Prior to this study it was generally assumed that algorithms such as the Boris pusher would produce reasonably accurate results irrespective of the field configuration under consideration. In light of this study, we no longer think this can be assumed. We suggest that PIC simulations are accompanied by complementary studies of the single particle motion to ensure that converged orbits can be obtained.

Secondly, these findings suggest that the root cause of both the issues of convergence and the sensitivity to initial conditions is at the very least indicative of extreme nonlinearity, but it quite strongly suggests that the dynamics of this problem are *chaotic*. This is entirely consistent with earlier studies [32, 75, 76], however these results now indicate that it is quite easy for the Lyapunov time to become sufficiently short that numerical integration is inhibited. This would explain the very limited ability of nearly all methods to obtain converged solutions, and it also explains the very high sensitivity to initial conditions. We do not claim to provide any rigorous proof that the dynamics of this system are chaotic, only to submit the results of numerical calculations that show that this might be the case, and that further investigation should be carried out. We do however draw the attention of the reader to earlier studies where such detailed analysis was carried out [94]. If this simple model problem is indeed shown to have chaotic dynamics then this could have quite profound implications for the field of ultra-intense laser-plasma interactions, as it would then imply that a number of laser-target configurations where there are interfering laser fields would have the potential for chaotic dynamics.

2.7 Acknowledgements

Chapter 2, in full, is a reprint of the material as it appears in A. P. L. Robinson, K. Tangtartharakul, K. Weichman, and A. V. Arefiev, "Extreme nonlinear dynamics in vacuum laser acceleration with a crossed beam configuration", *Physics of Plasmas* **26**, 093110 (2019), with the permission of AIP Publishing. The dissertation author contributed methodology, supervised visualization, and assisted in writing the paper.

The work of K.T. and A.V.A was supported by the National Science Foundation (PHY 1632777). K.W. was supported in part by the DOE Office of Science under Grant No. DE-SC0018312 and in part by the DOE Computational Science Graduate Fellowship under Grant No. DE-FG02-97ER25308.

Chapter 3

Laser reflection as a catalyst for direct laser acceleration in multipicosecond laser-plasma interaction

3.1 Abstract

We demonstrate that laser reflection acts as a catalyst for superponderomotive electron production in the preplasma formed by relativistic multipicosecond lasers incident on solid density targets. In 1D particle-in-cell simulations, high energy electron production proceeds via two stages of direct laser acceleration, an initial stochastic backward stage, and a final non-stochastic forward stage. The initial stochastic stage, driven by the reflected laser pulse, provides the pre-acceleration needed to enable the final stage to be non-stochastic. Energy gain in the electrostatic potential, which has been frequently considered to enhance stochastic heating, is only of secondary importance. The mechanism underlying

the production of high energy electrons by laser pulses incident on solid density targets is of direct relevance to applications involving multipicosecond laser-plasma interactions.

3.2 Introduction

Laser-plasma interaction (LPI) at relativistic intensities ($> 10^{18}$ W/cm^2) provides an efficient, compact source of energetic charged particles, neutrons, and radiation useful for applications in accelerator science [12, 13], imaging [10, 11], laboratory astrophysics [9], and inertial confinement fusion [96]. Often, the production of accelerated ions [17, 18], neutrons [19], or high energy X-rays [20, 21] is driven indirectly by the laser through the production of high energy electrons. Understanding the mechanisms of electron heating via LPI is therefore crucial for a variety of applications.

In low density plasma, there are several routes for electron acceleration, including direct laser acceleration (DLA) [97] and wakefield acceleration [12], capable of producing electrons with energies of MeV or greater. A laser pulse incident on a solid density plasma reflects from the surface where the electron density $n_e \approx \gamma_0 n_{cr}$ (the critical density $n_{cr} = \omega^2 m_e / 4\pi e^2$ is adjusted by the relativistic factor $\gamma_0 \approx (1 + a_0^2)^{1/2}$ associated with transverse oscillations in the laser, which has normalized amplitude $a_0 = eE_0/m_e c\omega$ [31]), producing an electric field that can be interpreted as a standing wave close to the surface and counter-propagating pulses further away. Energy gain mechanisms at a sharp laser-solid interface for a laser pulse at normal incidence include j×B heating [98] and standing wave acceleration [99, 100], and typically generate peak electron energy near the ponderomotive limit $E_p = m_e c^2 (1 + a_0^2/2)$ and a slope temperature for the electron energy distribution consistent with the ponderomotive scaling $T_p = [(1 + a_0^2)^{1/2} - 1] m_e c^2$ [101].

When the interface between the vacuum and the opaque plasma is not sharp, superponderomotive electron acceleration in excess of tens to hundreds of MeV with $a_0 < 10$

is possible via a variety of mechanisms [33, 85, 102]. In particular, the generation of high energy electrons in the presence of the counter-propagating incident and reflected laser components produced by incomplete laser absorption has generated significant interest in stochastic heating [94, 103] as a source of highly energetic, superponderomotive ($\gamma \gg 1 + a_0^2/2$) electrons in long scale-length plasma [32–35].

The development of a large region of low density plasma in front of an opaque target is virtually unavoidable for relativistically intense pulses with picosecond duration. Picosecond pulses incident on solid-density targets evolve an initial exponential preplasma density distribution towards a long, relatively flat subcritical plateau jumping up sharply to overcritical density [33, 34, 104, 105]. The preplasma produced in this way can have a quasi-1D geometry when the laser spot size is large, as is available from existing high power laser facilities such as LFEX [4], LMJ-PETAL [5], NIF ARC [3], and OMEGA EP [2]. While higher-dimensional effects can somewhat alter the electron and ion dynamics, for instance reducing the reflectively of the opaque plasma surface [105, 106], 1D simulations present a useful platform for developing a conceptual understanding of picosecond laser-solid interaction under experimentally relevant conditions.

While substantial progress has been made in understanding possible routes to energetic electron production by picosecond pulses, the electron acceleration process observed in portions of the parameter space remains to be fully explained. Concurrent with the development of the characteristic preplasma "shelf" and solid density "wall" plasma profile in Ref. 104 was the observation that high energy electrons originate in the wall and follow a trajectory consisting of initial backward propagation along the shelf, followed by reflection to forward propagation, during which strong DLA occurs. It can be deduced from the dephasing rate and the laser work done on the characteristic high energy electrons shown in Ref. 104 (Appendix 3.8 includes a demonstration of this analysis) that high energy electrons were accelerated *without* slipping substantially in the phase they experience in

the forward-propagating component of the laser, which is inconsistent with the high phase slip characteristic of stochastic heating. While it has been suggested that a sufficient electrostatic potential well in the ion shelf region may serve to "lock" the electron in phase with the co-propagating laser, enhancing electron energy in a multi-bounce process [34], the energy gain observed in Ref. 104 occurs with only a *single* bounce and is *substantially in excess* of the well depth (the maximum beam energy produced by this mechanism for a finite potential well [107]).

The purpose of the present work is to demonstrate that the reflected component of the laser pulse enables non-stochastic electron acceleration to high energy along a single bounce trajectory in the ion shelf-wall density profile characteristic of picosecond laser-solid interactions. For $a_0 = 5$ and an underdense plasma shelf of 50 μm, we observe electron acceleration via direct laser acceleration in excess of 75 MeV, more than 10 times the vacuum ponderomotive limit. It will be shown that the production of such high energy electrons during the forward DLA requires accounting for electron energization by the backward-propagating reflected component of the laser pulse and that this pre-acceleration enables non-stochastic energy gain in excess of what can be produced by stochastic heating. In contrast with previous work where the electron energy gain was found to correspond to stochastic heating or the electrostatic potential played an important role in reducing phase slip, we find that a DLA-plus-bounce model in which the only contribution of the electrostatic potential is to reflect energetic electrons is sufficient to reproduce the observed pre-acceleration and final non-stochastic energy gain.

The outline of this paper is as follows. Section 3.3 introduces a simulation in which we observe strong electron acceleration by DLA processes which exhibit different character during backward and forward propagation and do not appear to require energy gain from the electrostatic potential (Section 3.4). In Section 3.5, we demonstrate that DLA in counter-propagating pulses can produce the observed behavior and we identify

the backward and forward acceleration processes as corresponding to stochastic and non-stochastic DLA, respectively, explaining the vital role of laser reflection in high energy electron production.

3.3 Electron acceleration model

We model electron acceleration in the characteristic subcritical plateau ("shelf") and overcritical density ("wall") preplasma profile formed by multipicosecond pulses in 1D using the EPOCH paricle-in-cell (PIC) code [71]. The preplasma consists of a 50 μm long 5% critical density ($0.05n_{cr}$) shelf in front of a solid density plasma wall modeled by 10 times the critical density, as shown conceptually in Figure 3.1a and numerically in Figure 3.1b. The wall extends to the far boundary of the simulation domain, which is sized such that a light speed object originating at the vacuum boundary of the simulation and being reflected from the far boundary could not make a second transit of the wall surface during the simulation. The vacuum boundary is located 100 μm from the shelf edge. Into this system is introduced a semi-infinite laser pulse with a rapid 100 fs HWHM rise time, which is short compared to the time it takes electrons to be accelerated. The electric field of the laser is linearly polarized in y and propagates in the x-direction.The simulation is allowed to run for 2.2 ps after the peak of the laser pulse hits the solid density plasma, which we find is sufficient for the electron energy spectrum to saturate.

The resolution of the simulation is 150 cells/μm, which gives 7.5 cells per skin depth (c/ω_{pe}) in the solid density plasma. This resolution ensures direct laser acceleration is well-resolved [108]. The plasma is modeled by 3000 macroparticles per cell in both the shelf and the wall, for both electrons and ions. The ions are singly charged and treated as immobile.

The choice of a semi-infinite laser pulse and immobile ions allows us to study the

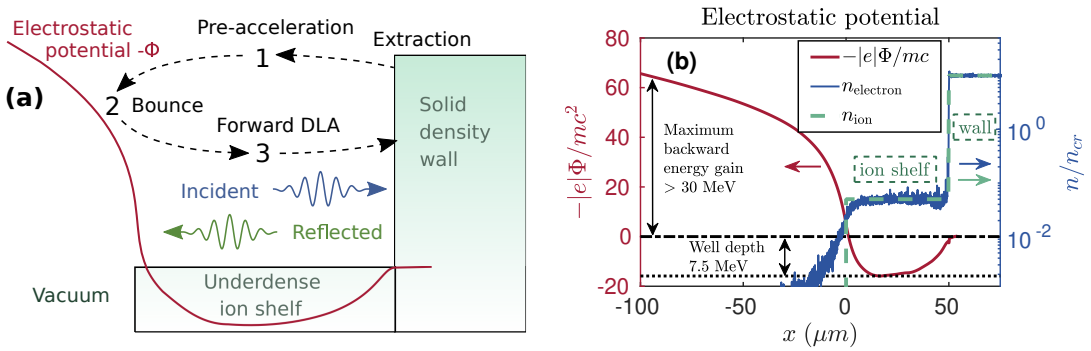

Figure 3.1: PIC simulation setup and electrostatic potential. (a) Conceptual diagram of simulation setup and electron acceleration process. (b) Time-averaged electron density and electrostatic potential relative to the wall surface, with (immobile) ion density, from 1D PIC simulation.

electron dynamics occurring near the peak of a multipicosecond laser pulse. The semi-infinite pulse duration is appropriate for studying the electron acceleration process in multipicosecond pulses provided electrons are accelerated on a sub-ps timescale, which we find to be the case (discussed in Sections 3.4 and 3.5). Using immobile ions allows us to isolate the effect of the presence of the shelf and wall ion density profile that arises in self-consistent multipicosecond simulations on electron dynamics from effects related to the time evolution of this profile, such as its initial establishment. As we will demonstrate in Section 3.6, the key conclusions of our work remain valid with mobile ions, even when the ion density evolves on the picosecond scale. A 1D simulation with immobile ions may also artificially increase the plasma reflectivity at the critical density surface and thereby may artificially increase the amplitude of the reflected wave compared to 2D simulations [106]. The intent of this work is to describe the energy gain mechanism we observe in the 1D simulations and provide a framework for evaluating energy gain in higher-dimensional simulations. As we will discuss in Section 3.6, the mechanism we observe in our 1D simulations is still conceptually valid in systems with lower reflectivity.

We capture the time history of the position, momentum, and other properties of the individual (macro)electrons extracted from the wall and accelerated over the shelf region.

The collected information includes a diagnostic for the longitudinal and transverse work done on each particle. It is well-known that the energetic electrons produced by relativistic laser pulses interacting with plasma are predominantly forward-directed (momentum $|p_x| \gg |p_y|$, i.e. p_y does not contribute substantially to the energy) despite the laser only doing transverse work (W_y) in 1D. We therefore use the work diagnostic to separate the contributions to the forward-directed momentum from the plasma-generated longitudinal electric field (E_x) and the laser electric field (E_y),

$$W_{x,y} = -|e| \int_0^t dt' v_{x,y} E_{x,y}. \tag{3.1}$$

3.4 Direct laser acceleration in PIC simulation

We begin by outlining the results of our PIC simulation. Key features of the simulation setup and electron trajectory are illustrated in Figure 3.1a. As we will show, the reflection of the incident (forward-propagating) laser pulse from the critical density surface is particularly important, and in 1D occurs with minimal absorption.

Over the course of the simulation, the laser removes electrons from the immobile ion shelf and fosters the development of a substantial electrostatic (electron) potential well in the ion shelf region (Figure 3.1b). The potential well develops over a few hundred fs and reaches a depth comparable to the ponderomotive potential. The development of a similarly deep potential well in picosecond laser-solid interaction is also observed in simulations with mobile ions [33, 104] (see also Section 3.6). The maximum magnitude of the potential in the vacuum region, to the left of the ion shelf in Figure 3.1b, is far in excess of the magnitude at the wall surface. This asymmetry in the potential substantially exceeds the initial kinetic energy of electrons entering the shelf region from the wall surface (the maximum value it could have in a purely electrostatic system) and indicates that electrons

undergo substantial backward-directed energy gain from non-electrostatic sources.

The incident and reflected (backward-propagating) components of the laser accelerate electrons to high energies in a characteristic single-bounce trajectory (Figure 3.1a). The majority of high energy electrons originate in the solid density wall and either begin close to the surface or are brought to the surface as return current. The surface oscillates under the influence of the reflecting laser pulse [109, 110] and ejects electrons into the shelf region. Electrons extracted from the surface of the wall are then (1) initially accelerated backwards through the underdense preplasma, (2) reflected off of the electrostatic potential in the vicinity of the shelf-vacuum interface, and (3) re-accelerated forwards through the ion shelf and re-injected into the overdense wall. Steps 1-3 take around 500 fs on average.

During Step 1 (backward propagation), electrons gain energy from the longitudinal electric field of the plasma and the transverse electric fields of the counter-propagating incident and reflected components of the laser pulse. We probe the correlation between acceleration during backward propagation and the electron's final (forward-propagating) energy by binning electrons by their final energy and averaging the maximum backward W_x and W_y of electrons in each final energy bin. The result is shown in Figure 3.2a. No correlation is seen between the electron's final energy and the maximum work done by the longitudinal electric field of the plasma during backward propagation. The maximum backward W_x is approximately equal to the energy with which the electron is initially extracted from the wall surface plus the depth of the time-averaged electrostatic potential well. In contrast, higher final (forward-moving) energy is on average associated with higher backward DLA energy gain (W_y). We further observe that the majority of the backward DLA energy gain occurs while the longitudinal electric field is decelerating for electrons.

Like the backward acceleration stage, the forward electron acceleration of Step 3 is also strongly DLA-dominated. A net energy accounting for the electrons (Figure 3.3a) reveals the longitudinal electric field contributes on average less than 20% of the final

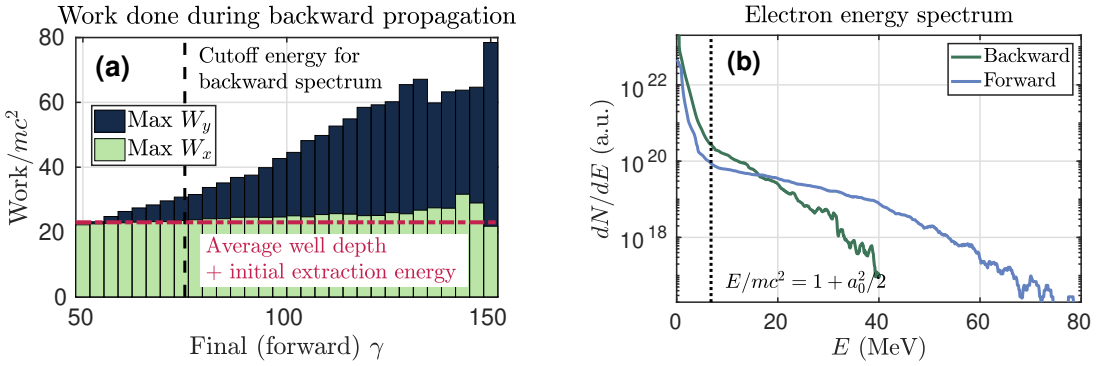

Figure 3.2: Work done on backward-moving electrons and comparison of backward- and forward-moving energy spectra. (a) Maximum work done during backward propagation by the longitudinal (x, plasma) and transverse (y, laser) electric field components, binned by the electron's final (forward-moving) energy. (b) Comparison of backward- and forward-moving electron energy spectra, evaluated at the end of the simulation.

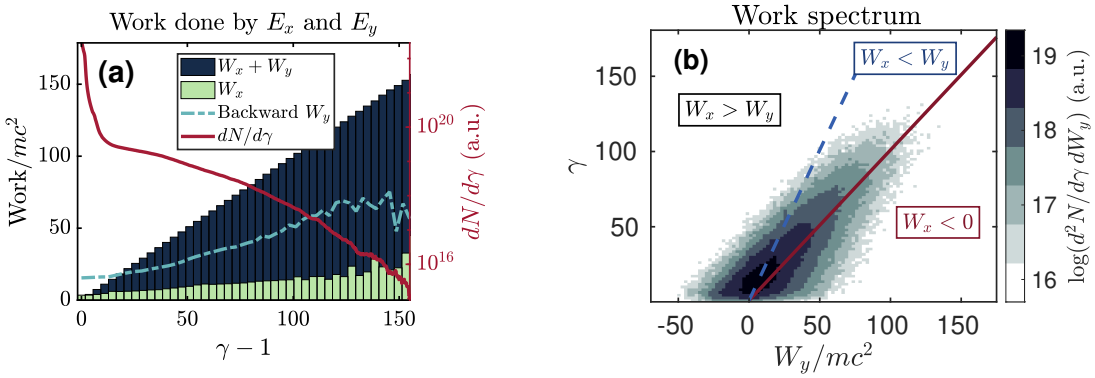

Figure 3.3: Work done on electrons by the the longitudinal (x, plasma) and transverse (y, laser) electric field components, evaluated at the final time the electron is in the shelf region. (a) Electron energy spectrum and average work, binned by energy, with maximum W_y from backward propagation (Figure 3.2a). (b) Spectral distribution of the work done by the laser field.

electron energy and is substantially smaller than the energy contribution from backward DLA. The longitudinal electric field does net negative work for a substantial fraction of the high energy electrons (Figure 3.3b).

There is a notable difference in the electron spectra (Figure 3.2b) and the character of the acceleration during backward and forward propagation. We observe a significant difference in the ability of electrons to maintain phase in the co-propagating component of the laser pulse, exemplified by the characteristic high energy electron trajectory shown in Figure 3.4. During the forward propagation stage, the phase electrons experience in

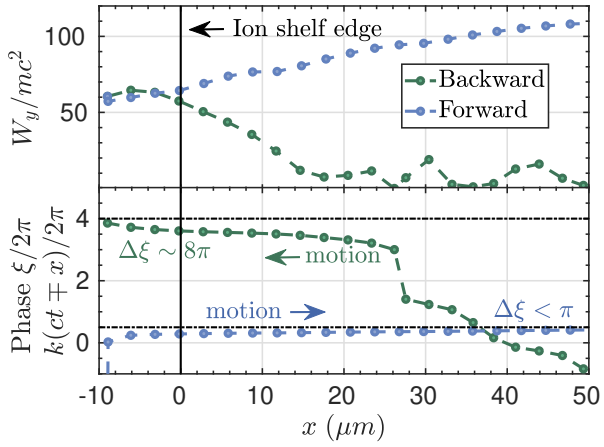

Figure 3.4: Representative high energy electron trajectory from PIC simulation with (top) the work done on the electron by the laser electric field and (bottom) the phase slip the electron experiences in the co-propagating laser.

the incident (forward-propagating) laser pulse changes by less than one period over the entire propagation over the shelf, whereas during the backward propagation stage, the electrons slip in phase by at least several periods with respect to the reflected (backward-propagating) part of the pulse (Figure 3.4, bottom). The work done on electrons by the laser electric field (Figure 3.4, top) reflects this phase slip, with W_y changing smoothly during forward propagation, but exhibiting cycles of rapid energy gain and loss during backward propagation.

To summarize, we find electron acceleration proceeds in two stages corresponding to forward and backward propagation. Although the character of the stages is different, both stages appear to correspond to DLA alone, without a substantial synergistic contribution from the longitudinal electric field. As will be discussed in more detail in Sections 3.5 and 3.6, the character of the forward acceleration and the non-involvement of the longitudinal electric field are in contrast with previous explanations for energy gain in multipicosecond laser-solid interaction [33–35, 75, 107, 111]. In Section 3.5, we will demonstrate that DLA alone is capable of reproducing the observed acceleration characteristics, including the

difference in character between the backward and forward energy gain.

3.5 Electron acceleration in counter-propagating laser pulses

We found in Section 3.4 that electron acceleration proceeds in two distinct DLA stages, neither of which appear to rely on a net energy contribution from the longitudinal electric field. In this Section, we will explain these observations using a model for direct laser acceleration in counter-propagating laser pulses.

The equations of motion of an electron in counter-propagating linearly y-polarized laser pulses in vacuum are (in 1D)

$$\begin{aligned} \frac{dx}{dt} &= \frac{p_x}{\gamma m} \\ \frac{dp_x}{dt} &= -|e|E_x - \frac{|e|p_y}{\gamma mc}B_z \\ \frac{dp_y}{dt} &= -|e|E_y + \frac{|e|p_x}{\gamma mc}B_z. \end{aligned} \tag{3.2}$$

where the choice of y-polarization has specified $E_z = B_y = 0$, and we have taken $B_x = 0$ and $p_z = 0$ for consistency with our PIC simulation setup. We then separate E_y and B_z associated with the laser field into separate $+x$- and $-x$-directed components, denoted with subscripts 1 and 2, respectively.

We relate $B_{z,1,2}$ to $E_{y,1,2}$ via Maxwell's equations by allowing the laser propagation to correspond to vacuum (i.e. setting the phase velocity equal to the speed of light, which is appropriate based on the phase velocity we observe in the PIC simulation, see Appendix 3.8), and express them in terms of the normalized vector potential $\boldsymbol{a}_{1,2}$, with $\boldsymbol{a}_{1,2} = a_{1,2}\hat{y}$. We take a_1 and a_2 to be functions of $t - x/c$ and $t + x/c$ for the $+x$- and $-x$-directed pulses,

respectively, and define $a_{1,2}$ by

$$\begin{aligned} E_{y,1,2} &= -\frac{mc}{|e|}\frac{\partial}{\partial t}a_{1,2} \\ B_{z,1,2} &= \frac{mc}{|e|}\frac{\partial}{\partial x}a_{1,2}. \end{aligned} \tag{3.3}$$

Substituting these expressions in Equations 3.2, we readily obtain an integral of the motion (as per Ref. 112)

$$\frac{d}{dt}\left(\frac{p_y}{mc} - a_1 - a_2\right) = 0. \tag{3.4}$$

We take $E_x = 0$ for the purposes of our analysis. An accelerating longitudinal electric field dynamically reduces the electron dephasing rate in a single laser pulse [93] and it has been suggested that E_x could play an important role in electron acceleration by picosecond pulses [34]. However, we find no evidence for a substantive synergistic energy gain from E_x during either backward propagation (see Section 3.4). In this model, we treat E_x as contributing to the initial longitudinal momentum to determine what effect, if any, it can have on the electron energy gain.

Combining Equations 3.2, 3.3, and 3.4, the equations of motion for an electron in this system are

$$\begin{aligned} \frac{dx}{dt} &= \frac{p_x}{\gamma m} \\ \frac{dp_x}{dt} &= \frac{p_y}{\gamma}\left(\frac{da_1}{d\left(t - x/c\right)} - \frac{da_2}{d\left(t + x/c\right)}\right) \\ p_y &= p_{y,0} + a_1 mc + a_2 mc - a_{1,0} mc - a_{2,0} mc \\ a_{1,2} &= a_0 \sin\left(ck\left[t \mp x/c\right] + \phi_{1,2}\right). \end{aligned} \tag{3.5}$$

The electron is injected into the counter-propagating pulses at $x = 0$, $t = 0$ with a starting phase in each laser pulse given by $\phi_{1,2}$. We take the initial longitudinal momentum $p_{x,0} \geq 0$ to probe the importance of pre-acceleration. We also allow for an initial $p_{y,0}$ to represent

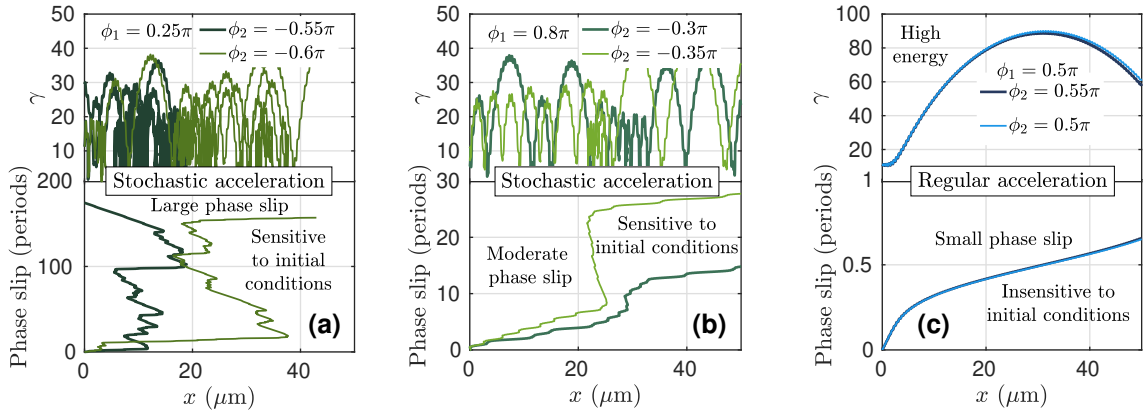

Figure 3.5: Example electron trajectories for initial longitudinal momentum $p_{x,0} = 10$ and transverse momentum $p_{y,0} = 5$. The two trajectories in each figure were obtained by fixing the initial phase in one pulse (ϕ_1) and varying the other (ϕ_2) by 0.05π. (a) Stochastic acceleration consistent with stochastic heating (large phase slip). (b) Stochastic acceleration with moderate phase slip. (c) Regular acceleration.

the modulation of the transverse momentum by the counter-propagating laser pulses during pre-acceleration. $p_{x,0} \geq 0$ is also suitable to probe backward propagation due to the symmetry of Equations 3.5 as $(x, \boldsymbol{p}) \rightarrow (-x, -\boldsymbol{p})$ (with suitable modification of the initial laser phases). In the backward case, the range of initial $p_{x,0}$ and $p_{y,0}$ represents the initial extraction of the electron from the surface and acceleration by the electrostatic potential. We perform scans over $\phi_{1,2}$, $p_{x,0}$ and $p_{y,0}$ to explore the range of initial conditions electrons may experience in the PIC simulation.

The electron position and momentum are evolved according to Equations 3.5 for a time of 200 laser periods using MATLAB's ode113 solver with relative error tolerance of 10^{-13}. We find that electron acceleration is accomplished in two distinct regimes. Certain initial conditions lead to stochastic motion of the electron (e.g. Figures 3.5a and 3.5b), while others produce motion which appears regular (e.g. Figure 3.5c). Stochastic electron trajectories are difficult to compute exactly [113] and it was not possible to achieve convergence for some of the initial conditions leading to stochastic motion. The intent of modeling stochastic motion in this work is not to present exact trajectories, but to obtain

characteristic values for the maximum γ-factor of electrons and the amount the electron slips in phase in each laser pulse over the shelf length. For the purposes of the subsequent analysis, we have verified that the solver preserves key physical features of electron motion in counter-propagating pulses. Over our range of initial conditions, the solver is converged for the regular trajectories, exhibits the phase space filling behavior needed to capture the maximum γ-factor and the rapid divergence of neighboring trajectories in the stochastic regime, and preserves the phase-space separation between stochastic and regular motion we expect on the basis of Poincaré surface of section plots (as shown, e.g. in Ref. 94).

We distinguish the stochastic regime from the regular regime in this work on the basis of the motion of the electron, not as $t \to \infty$, as would formally define chaotic/stochastic behavior, but over a propagation distance corresponding to the shelf length. The whole of the electron bounce trajectory in the PIC simulation (both backward and forward motion) takes on average 500 fs (150 laser cycles). In this section, we model electron acceleration in counter-propagating systems for up to 667 fs (200 laser cycles), which is sufficient for electrons to be displaced by more than the shelf length for nearly all the initial conditions we evaluate. In contrast, past treatments of stochastic heating have typically been based on conditions where electrons interact with the counter-propagating electromagnetic waves over a relatively long time to allow electrons to explore the full range of accessible phase space (corresponding to hundreds to thousands of laser periods worth of phase slip, for example References 33, 75, 114).

In our model, electrons slip anywhere from more than one hundred to less than one period in the co-propagating laser over the shelf length. We find that the hallmarks of stochasticity (e.g. the divergence of neighboring orbits signified by the sensitive dependence on initial conditions shown in Figures 3.5a and 3.5b) are associated with electrons which slip by tens of more of periods in phase. The usual stochastic heating picture is clearly applicable to electrons which slip by hundreds of laser periods in phase (e.g. for trajectories

in Figure 3.5a), but may not be for electrons which only slip tens of periods in phase slip (e.g. Figure 3.5b). We term both of these cases "stochastic," and contrast them with "regular" electrons. In the regular regime, trajectories do not depend sensitively on the initial conditions, electrons slip in phase by at most a few laser periods over the shelf length, and the peak energy can be higher (e.g. Figure 3.5c).

The distinct characteristics of the stochastic and regular regimes are easy to identify in a scan over the initial phases ϕ_1 and ϕ_2. Figure 3.6a shows the γ-factor as the electron crosses $x = 50$ μm for the initial momentum conditions $p_{x,0}/mc = 10$, $p_{y,0}/mc = 5$. We see that for $\phi_1 \gtrsim 0$ and $\phi_2 \lesssim 0$, both γ and the phase of the electron in the co-propagating laser (shown in Figure 3.6b) vary from pixel to pixel in our calculation (one pixel corresponds to $\Delta\phi/\pi = 0.05$), revealing the sensitive dependence on initial conditions characteristic of the stochastic regime. By contrast, the γ-factor and the phase slip vary smoothly in the regular regime (the remainder of the phase scan). We find that the highest energy electrons correspond to the regular regime. These electrons have begun to decelerate by the time they reach $x = 50$ μm, which suggests that additional pre-acceleration can improve the electron energy.

We repeat the scan over the starting $\phi_{1,2}$ for different values of $p_{x,0}$ and $p_{y,0}$ and find that the regular regime is made accessible through sufficient pre-acceleration, though regularity also requires the electron to have favorable initial phases in the two pulses (as can be seen, for example, in Figure 3.6b). When the electron has initial forward momentum $p_{x,0}/mc \lesssim a_0 = 5$, the motion is stochastic for all initial choices of $\phi_{1,2}$, while for $p_{x,0}/mc \gtrsim a_0$, as shown in Figures 3.5 and 3.6b, certain initial choices in $\phi_{1,2}$ produce stochastic behavior, while others result in regular acceleration. The range of initial conditions producing regular acceleration increases with increasing $p_{x,0}$.

We also find that sufficient pre-acceleration enables the regular regime to produce higher electron energy at $x = 50$ μm than the stochastic regime. Figures 3.7a and 3.7b

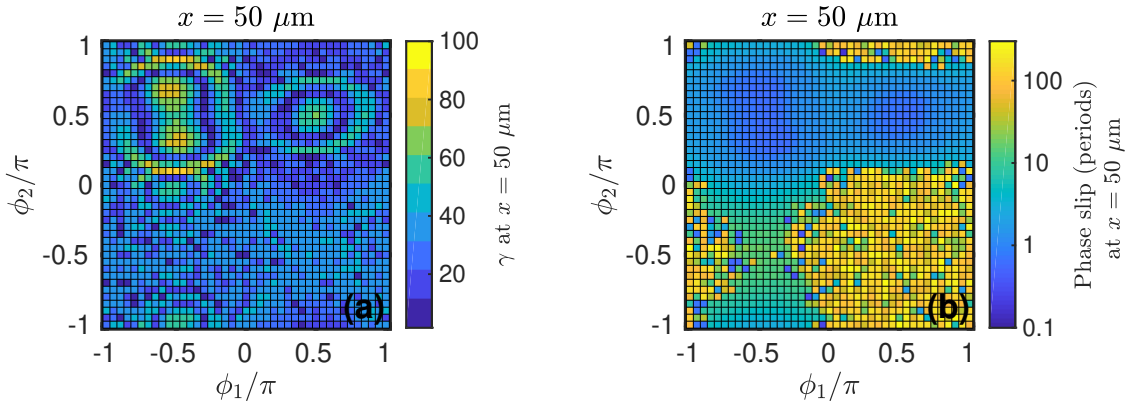

Figure 3.6: Evaluation of electron trajectories in counter-propagating lasers after propagation over the shelf length ($x = 50$ μm), scanning over the initial laser phases ϕ_1 and ϕ_2, with initial longitudinal momentum $p_{x,0}/mc = 10$ and transverse momentum $p_{y,0}/mc = 5$. (a) γ-factor after propagation over the shelf length and (b) corresponding phase slip of the electron in the $+x$-propagating laser.

show the maximum γ-factor and associated phase slip in the forward pulse obtained after propagation over the shelf length, compiled by evaluating over 40,000 electron trajectories ($\Delta\phi = 0.1$ for the scan over $\phi_{1,2}$). The maximum achievable γ-factor in this system corresponds to regular acceleration with small phase slip ($\Delta\xi/2\pi \lesssim 0.5$) and requires $p_{x,0}/mc \gtrsim 15$ for our range of initial $p_{y,0}$. We also see that pre-acceleration only systematically reduces phase slip and increases the maximum electron energy in the regular regime, and does not in the stochastic regime.

We now compare qualitatively the stochastic and regular acceleration predicted by our counter-propagating DLA model to the PIC simulation results. The backward acceleration stage exhibits features of stochastic acceleration, including rapid cycles of energy gain and loss with a corresponding multi-period phase slip. Furthermore, stochasticity would explain the lack of correlation between the backward DLA energy gain and the backward pre-acceleration provided by the longitudinal electric field. The forward acceleration stage, on the other hand, agrees well with regular acceleration. High energy electrons exhibit minimal phase slip in the forward-propagating laser over the shelf length and higher final

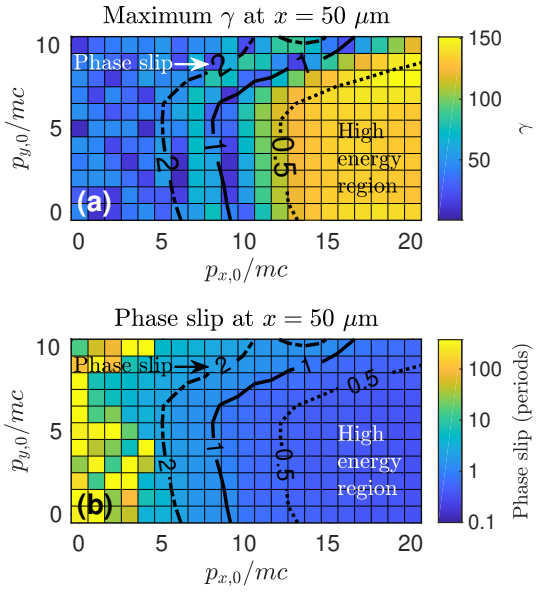

Figure 3.7: Highest energy electron trajectories in counter-propagating lasers evaluated after after propagation over the shelf length ($x = 50$ μm) for a range of initial longitudinal ($p_{x,0}$) and transverse ($p_{y,0}$) momenta. (a) Maximum achievable γ-factor at $x = 50$ μm and (b) corresponding phase slip in the $+x$-propagating laser for different starting momenta. Black contours on both (a) and (b) indicate the phase slip in periods.

energy is associated with higher pre-acceleration by backward DLA.

The electron energy gain process we observe in the simulation can be summarized as follows. Electrons are extracted from the solid density plasma surface and backward accelerated by the electrostatic potential well and by stochastic DLA. This is not a synergistic process and DLA is the dominant contributor to the energy gain. Next, the electron bounces in the electrostatic potential and the backward energy gain is transformed into a forward pre-acceleration. The backward DLA energy gain can be sufficient for the electron to then be forward accelerated by non-stochastic DLA. When the forward acceleration is non-stochastic, electrons can gain higher energy than is produced by stochastic heating. In this single-bounce process, the only important role of the electrostatic potential is to reflect electrons during the bounce. We find the key to energetic electron production is laser reflection from the critical density surface.

3.6 Summary and Discussion

We investigated the production of high energy electrons in a system representative of the plasma and laser conditions produced by multipicosecond laser-solid interaction. In particle-in-cell simulations designed to isolate the electron dynamics occurring near the peak of a multipicosecond laser pulse, we observed high energy electron production via a two-stage acceleration process involving an initial backward phase and a final forward phase, which we demonstrated are consistent with stochastic and non-stochastic direct laser acceleration, respectively. The only required role of the electrostatic potential in this process is to reflect high-energy electrons between the backward and forward stages.

Previous work on electron heating by multipicosecond laser pulses incident on solid density targets has focused on stochastic heating [33, 75], requires multiple bounces in the electrostatic potential [107], or involves a substantive energy contribution from the electrostatic potential [34, 35, 111]. We have demonstrated electron acceleration can be achieved in a two-stage, *single*-bounce DLA process in which *only one* stage is stochastic and the longitudinal electric field is *not required* to explain the observed energy gain. The conclusion we draw is that, for our model conditions, the key factor driving the acceleration of electrons to high energy is reflection of the laser pulse from the dense plasma surface.

The intent of this work is to provide a framework for future analysis. To this end, we have neglected several potentially important aspects of the physics of picosecond laser-solid interaction which should be included in future models to evaluate the applicability of the two-stage acceleration process we describe in more complex situations. While performing an in-depth analysis is beyond the scope of this work, we now discuss briefly the robustness of the acceleration process we describe to some of these additional considerations.

First, we expect the backward pre-acceleration required to enable high energy forward regular acceleration to depend on the laser intensity and the shelf length, both of which will evolve over the course of a multipicosecond laser pulse. Conceptually, we

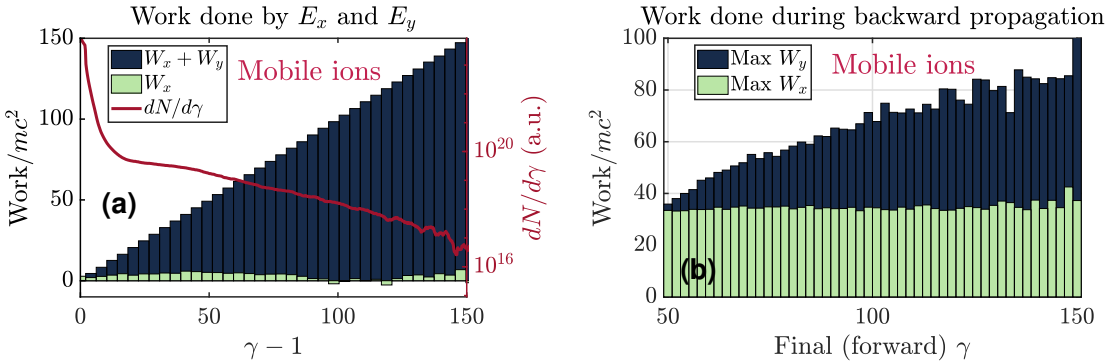

Figure 3.8: Work done on electrons by the the longitudinal (x, plasma) and transverse (y, laser) electric field components, evaluated at the final time the electron is in the shelf region for the case with mobile ions. (a) Electron energy spectrum and average work, binned by energy. Compare to Figure 3.3a. (b) Maximum work done during backward propagation, binned by final energy. Compare to Figure 3.2a

require that the stochastic energy gain be sufficient to enable the forward acceleration to access the regular regime and that the regular regime be able to deliver higher electron energy than the stochastic regime over an acceleration distance corresponding to the shelf length. We demonstrate the feasibility of this process for an additional set of conditions in Appendix 3.9. We expect our acceleration mechanism to be conceptually valid over some portion of the parameter space, within which it may be possible to optimize the preplasma for electron heating. Experimentally, one could consider using one laser pulse to generate the preplasma and begin the shelf formation and another to perform electron acceleration, akin to the approach used in Refs. 115, 116.

Second, we note that 1D geometry and ion immobility can artificially suppress laser absorption at the wall surface [105, 106]. Similar to the analysis of Appendix 3.9, we have verified that the electron acceleration process we observe remains feasible even with relatively high absorption, for example, with the $\sim 75\%$ absorption (50% reduction in $a_{\text{reflected}}$) observed in Ref. 106. The dominance of this energy gain process should be checked in systems with higher absorption.

Third, ion immobility and the temporally semi-infinite profile are most applicable

under conditions where the ion shelf evolution does not substantially change the character of electron acceleration. To demonstrate that the two-stage character of electron acceleration is robust to ion mobility, we conduct an additional PIC simulation where we allow the ions to be mobile, fully ionized aluminum. In this simulation, the ion shelf density drops by approximately a factor of 2 over 1 picosecond, but the time-averaged electrostatic potential and the forward-moving electron energy spectrum are not substantially affected. While in-depth analysis of the effects of ion mobility is beyond the scope of this work, we verify that key features of the acceleration are unchanged. High energy electrons are still predominantly DLA-accelerated (Figure 3.8a) through two stages of DLA where the final forward stage exhibits non-stochastic character. Additionally, high final electron energy is still correlated with high backward DLA energy gain, while there is still no correlation between energy gain from the longitudinal electric field and energy gain during either DLA stage (Figure 3.8b).

We additionally note that 1D geometry is most applicable to conditions under which the preplasma shelf is short compared to its transverse extent, as may be produced by the large focal spot size available from high-power laser facilities including LFEX [4], LMJ-PETAL [5], NIF ARC [3], and OMEGA EP [2]. In 2D and 3D geometry, the laser pulse may generate a plasma channel, introducing an additional timescale associated with the time it takes for an electron to transit the channel transversely. For the non-stochastic DLA we observe during forward motion, the electron motion is predominantly forward-directed and we expect the limited transverse size to introduce only secondary effects on the forward DLA process if the spot is sufficiently large. The backward DLA process should be re-evaluated in the context of 2D and 3D simulations.

As a final note, the two-stage DLA process we have described relies on the phase of electrons being either randomized or favorably preserved during the transition from the stochastic backward DLA to the regular forward DLA. However, if the electric field

is sufficiently strong, the electrostatic potential appears as a hard wall and the electron phases are not randomized during the bounce, which could in principle result in electrons never being injected into a favorable phase for regular acceleration. This analysis, as well as an analysis of the conditions under which stochastic heating may occur during the bounce itself, will be the subject of a follow-up publication.

3.7 Acknowledgements

Chapter 3, in full, is a reprint of the material as it appears in K. Weichman, A. P. L. Robinson, F. N. Beg, and A. V. Arefiev, "Laser reflection as a catalyst for direct laser acceleration in multipicosecond laser-plasma interaction", *Physics of Plasmas* **27**, 013106 (2020), with the permission of AIP Publishing. The dissertation author was the primary investigator and author of the paper.

This research was supported in part by the DOE Office of Science under Grant No. DE-SC0018312. K. Weichman was supported in part by the DOE Computational Science Graduate Fellowship under Grant No. DE-FG02-97ER25308. Particle-in-cell simulations were performed using EPOCH [71], developed under UK EPSRC Grant Nos. EP/G054940, EP/G055165, and EP/G056803. This work used HPC resources of the Texas Advanced Computing Center (TACC) at the University of Texas at Austin and the National Energy Research Scientific Computing Center (NERSC), a U.S. Department of Energy Office of Science User Facility operated under Contract No. DE-AC02-05CH11231. Data collaboration was supported by the SeedMe2 project [117] (http://dibbs.seedme.org).

3.8 Appendix: Phase velocity

In this Appendix, we demonstrate that the phase velocity is sufficiently close to the speed of light that it is appropriate to take $v_\phi = c$ for the purposes of our analysis.

First, we determine the upper limit on the phase velocity we can reasonably neglect. It is important for the electron trajectory analysis in Section 3.4 (Figure 3.4) and for highest energy electrons in the DLA model in Section 3.5 (Figure 3.7) that we capture accurately whether a high energy electron has transitioned from the accelerating to the decelerating phase in its co-propagating laser pulse, i.e. the maximum error in the phase slip we can tolerate is 1/4 laser period.

The phase of an electron in the $+x$-directed laser pulse incorporating and neglecting the phase velocity are given by

$$\begin{aligned} \xi_{v_\phi} &= k\left(v_\phi t - x\right) \\ \xi_c &= k\left(ct - x\right), \end{aligned} \tag{3.6}$$

respectively. The difference in phase introduced by neglecting the phase velocity as an electron travels over the shelf distance is therefore

$$\xi_{v_\phi} - \xi_c = k\left(v_\phi - c\right)t < \pi/2. \tag{3.7}$$

In the PIC simulation, electrons traverse the shelf in less than 500 fs on average, therefore we require $v_\phi/c - 1 \lesssim 10^{-3}$.

Next, we estimate the phase velocity of the forward-propagating laser in the PIC simulation, which we find differs substantially from the cold neutral plasma value. Established graphical methods for directly measuring the phase velocity in PIC simulation [87, 118] are challenging to apply and interpret in the presence of interference patterns, such as results from the strong laser reflection in our simulation. Instead, we constrain the phase velocity by examining the laser work (W_y) done on high energy electrons as they slip in phase.

The basis of this approach is that an electron injected into an initially accelerating phase in the forward-propagating laser will reach a maximum energy and then begin to

decelerate once the electron slips in phase by 1/4 period. Whether a transition from acceleration to deceleration is visible in W_y for a high energy electron indicates whether the electron slips by more or less than 1/4 laser period. We can simultaneously calculate the phase slip based on the particle position and time and determine whether it agrees with W_y.

For convenience, the following analysis is based on the electron trajectory of Figure 3.4, though other electron trajectories from the simulation may serve to more tightly constrain v_ϕ. We see based on W_y that this electron does not experience a transition from accelerating to decelerating phase, therefore we consider the actual phase slip to be less than 0.25 laser period. Simultaneously, we calculate the phase slip over the course of the acceleration (starting from $x = -5$ μm in Figure 3.4) to be ~ 0.15 laser period, occurring over a time of ~ 55 laser cycles. The maximum error in phase we introduce by neglecting v_ϕ is therefore

$$\xi_{v_\phi} - \xi_c = k(v_\phi - c)t \lesssim 0.6. \tag{3.8}$$

Solving for the phase velocity gives us $v_\phi/c - 1 < 2 \times 10^{-3}$.

On the basis of this calculation and the good agreement between calculated phase and W_y seen for the electrons (Figure 3.4, and others), we therefore consider it suitable to neglect the difference between the phase velocity and the speed of light in this work.

3.9 Appendix: Robustness of two-stage DLA model to alternate parameters

In this Appendix, we demonstrate that the two-stage acceleration process we identify in simulations remains conceptually valid for an alternate choice of parameters, which suggests the process may be robust to changes in the shelf length and laser intensity. Figure

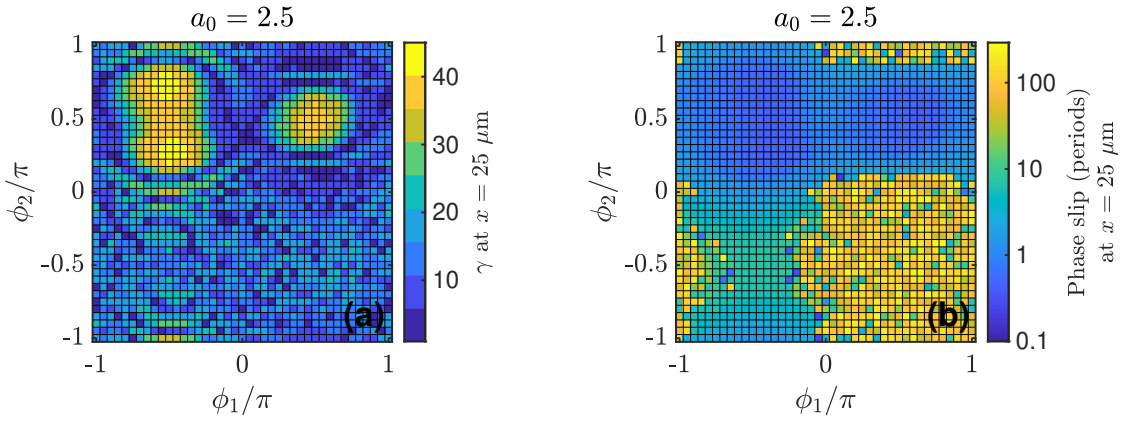

Figure 3.9: Evaluation of electron trajectories in counter-propagating lasers for $a_0 = 2.5$, shelf length $x = 25$ μm, and initial longitudinal momentum $p_{x,0}/mc = 5$ and transverse momentum $p_{y,0}/mc = 2.5$. Akin to Figure 3.6, we scan over the initial laser phases ϕ_1 and ϕ_2. (a) γ-factor after propagation over the shelf length and (b) corresponding phase slip of the electron in the $+x$-propagating laser.

3.9 shows the result of repeating the scan over initial phases done to produce Figure 3.6 with $a_0 = 2.5$, where we have also reduced the initial electron momenta and the shelf length by a factor of 2.

We can see from Figure 3.9 that the key requirements can still be satisfied for the initial stochastic backward acceleration stage to enable a subsequent non-stochastic, higher energy forward acceleration stage. In particular, we observe that:

1. The regular regime, which we can easily identify by the lack of sensitivity to initial conditions seen in Figure 3.9b produces higher peak energy over the shelf length than the stochastic regime for sufficient pre-acceleration (for instance, the pre-acceleration $p_{x,0}/mc = 5$ used to generate Figure 3.9).

2. The stochastic regime can produce high enough energy to enable the regular acceleration (the peak stochastic energy gain is substantially above the initial $p_{x,0}$).

While there are also additional considerations which could be important in the context of a full PIC simulation, our semi-analytic model calculation shows that the

acceleration process we observe under our original conditions is still conceptually valid for these new conditions.

Chapter 4

Magnetic enhancement of direct laser acceleration in relativistic picosecond laser-plasma interaction

4.1 Abstract

We demonstrate that a weak transverse magnetic field can facilitate substantially enhanced direct laser acceleration (DLA) by a modestly relativistic picosecond laser pulse under experimentally relevant conditions. While it has long been known that the addition of a magnetic field may enhance the acceleration of an already-relativistic electron in vacuum, the generation of a sufficient collection of such hot electrons is challenging. First, we demonstrate using 1D particle in cell simulations in a preheated plasma that the magnetically assisted DLA can still be observed in the presence of charge separation-associated electric fields. Second, we formulate a scenario using 2D simulations in which magnetically assisted DLA can be observed starting from a cold underdense plasma. This approach leverages the transverse ponderomotive force of a modestly relativistic femtosecond

duration laser pulse to catalyze electron acceleration by a modestly relativistic picosecond duration laser pulse and can deliver electron energy in excess of 10 times the ponderomotive limit of the long pulse, using a 100 T-level, experimentally accessible magnetic field. The high electron energy is additionally retained after the lasers have passed through the plasma, which could make magnetically assisted direct laser acceleration an attractive approach to the production of relativistically hot low density plasma.

4.2 Introduction

The production of high energy density plasma by relativistic laser-plasma interactions provides a convenient platform for investigations in laboratory astrophysics [6–9], imaging [10, 11], accelerator science [12, 13], and inertial confinement fusion [14–16]. Laser-produced plasma is capable of producing charged particles [17, 18], neutrons [19], and high energy X-rays [20, 21]. However, the generation of these energetic particles and radiation is usually driven indirectly by the direct production of high energy electrons. Understanding and optimizing the production of energetic electrons in laser-plasma interaction is therefore crucial to the practical application of laser-plasma physics.

In situations where a relativistic intensity ($I_0 \gtrsim 10^{18}$ W/cm^2 for 1 μm wavelength) laser pulse interacts with a low density plasma, electrons can gain energy while oscillating in the laser electric and magnetic fields. Typically, the energy gain of electrons by this direct laser acceleration is limited by the phase slip of electrons out of the accelerating phase in the laser pulse [97]. The rate of phase slip is given in terms of the dephasing

parameter R by [93]

$$\frac{\mathrm{d}\left(t - x/v_\phi\right)}{\mathrm{d}t} = \frac{R}{\gamma} \tag{4.1}$$

$$R = \gamma\left(1 - \frac{v_x}{v_\phi}\right), \tag{4.2}$$

which depends on the electron's velocity in the laser propagation direction (here, taken to be v_x) and the phase velocity of the laser v_ϕ. For direct laser acceleration by a plane wave in vacuum (i.e. $v_\phi = c$), R is a conserved quantity and the peak energy an electron can obtain is given by [93, 97]

$$\gamma_p = \frac{1 + R^2 + (a + p_{y0})^2}{2R}, \tag{4.3}$$

where $a \equiv |e|E/m_e c\omega$ is the normalized vector potential associated with a laser pulse with instantaneous electric field amplitude E and frequency ω, p_{y0} is the initial electron momentum in the laser polarization (y) direction, and we have assumed for the sake of simplicity that $a = 0$ initially and $p_z = 0$. When the electron begins from rest, Eq. 4.3 reduces to the well-known cold ponderomotive electron energy $\gamma_c = 1 + a^2/2$. Based on Eq. 4.3, it is readily apparent that one can exceed γ_c by reducing the dephasing R by increasing v_x, for example by pre-accelerating electrons in the forward direction or imposing an accelerating electric field [93, 119].

However, it has also long been known that high electron energy can also be produced in systems with larger dephasing, where the electron velocity makes a larger angle with the laser propagation direction [85, 102]. The addition of a static, uniform magnetic field B_0 transverse to both the direction of laser propagation and the polarization direction serves to rotate electron the momentum in and out of the forward direction. While this momentum rotation seems undesirable from the standpoint of dephasing, it has been demonstrated to enhance the direct laser acceleration of electrons [120] and to facilitate energy retention

after a laser pulse passes through an underdense plasma [121].

Previous work in the area of the effects of transverse magnetic fields on direct laser acceleration has concerned theoretical treatments (i.e. single electrons in vacuum) [120, 122, 123], laser pulse durations corresponding to only a fraction of a cyclotron orbit [121], or acceleration in the self-generated fields of a plasma channel with highly relativistic laser pulses [124]. In contrast, it has yet to be investigated how direct laser acceleration can be affected by the addition of a transverse magnetic field in the regime of modestly relativistic picosecond laser pulses. Such pulses enable the use of 100 T-level applied magnetic fields. 100 T-level magnetic field generation over length and time scales suitable for picosecond laser-plasma interaction ($> 100\,\mu$m and > 10 ps) has been demonstrated experimentally at a number high-power laser facilities worldwide [23–26, 29]. As we will demonstrate, picosecond pulses with 100 T-level applied magnetic fields can enable electrons to undergo direct laser acceleration over the course of multiple cyclotron orbits during the pulse duration, producing a strong effect on the electron energy. An investigation of direct laser acceleration in the relativistic picosecond regime is therefore desirable in terms of its immediate experimental accessibility and potential to verify theoretical and simulation predictions.

In this work, we present a practical demonstration of magnetically enhanced direct laser acceleration by relativistic picosecond laser-plasma interaction. First, in Section 4.3 we illustrate the basic physics of enhanced direct laser interaction in the presence of strong magnetic fields. Then, in Section 4.4 we demonstrate using particle-in-cell simulations that relativistic picosecond laser pulses have the potential to deliver dramatic heating in a preheated underdense plasma. Finally, in Section 4.5 we replace the preheating of electrons by a second laser pulse, demonstrating that 100 T-level magnetic fields are capable of facilitating significantly enhanced electron heating under experimentally relevant conditions.

4.3 Direct laser acceleration with a transverse magnetic field

In this work, we will consider the direct laser acceleration (DLA) of electrons in the presence of an applied magnetic field both in vacuum and in low density plasma. In this Section, we outline the fundamentals of how an applied magnetic field is able to assist in electron acceleration via DLA and can deliver high energy to an electron undergoing multiple cyclotron orbits over the course of a picosecond laser pulse.

The dynamics of an electron in the presence of electric and magnetic fields is in general given by

$$\begin{aligned} \frac{d\vec{p}}{dt} &= -|e|\vec{E} - \frac{|e|\vec{p}}{\gamma m_e c} \times \vec{B} \\ \frac{d\vec{x}}{dt} &= \frac{\vec{p}}{\gamma m_e}. \end{aligned} \tag{4.4}$$

In this work, we consider electron motion in a y-polarized laser pulse propagating in the x-direction with and without a z-directed externally applied magnetic field. With the choice of an initial momentum $p_z = 0$, this results in 2D motion in the x-y plane.

In this Section, we consider the acceleration of single electrons, ignoring charge separation-induced electric fields. In the limit that the phase velocity $v_\phi = \omega/k$ is close to the speed of light (as we will later show is appropriate), this reproduces the dynamics of electrons in vacuum. With these simplifications, the motion of an electron in this system is

described by

$$\begin{aligned}
\frac{\mathrm{d}p_x}{\mathrm{d}t} &= -\frac{|e|p_y}{\gamma m_e c}\left(B_L + B_0\right) \\
\frac{\mathrm{d}p_y}{\mathrm{d}t} &= -|e|E_L + \frac{|e|p_x}{\gamma m_e c}\left(B_L + B_0\right) \\
\frac{\mathrm{d}x}{\mathrm{d}t} &= \frac{p_x}{\gamma m_e} \\
\frac{\mathrm{d}y}{\mathrm{d}t} &= \frac{p_y}{\gamma m_e},
\end{aligned} \tag{4.5}$$

where E_L and B_L are the laser electric and magnetic fields and B_0 is the applied magnetic field (in the z-direction). For a plane wave laser pulse with frequency ω and phase velocity v_ϕ, E_L and B_L can be expressed in terms of the normalized vector potential a as

$$\begin{aligned}
E_L &= -\frac{m_e c\omega}{|e|}\frac{\mathrm{d}a}{\mathrm{d}s} \\
B_L &= -\frac{m_e c\omega}{|e|}\frac{c}{v_\phi}\frac{\mathrm{d}a}{\mathrm{d}s} \\
s &\equiv \omega t - \omega x/v_\phi,
\end{aligned} \tag{4.6}$$

where a is a function of the phase variable s. In what follows, we will consider a to have the form $a = a_0 \sin s$.

Following the work of Ref. 121, we rewrite the time derivatives in Eqs. 4.5 in terms of derivatives in the phase variable s to obtain

$$\begin{aligned}
R\frac{\mathrm{d}R}{\mathrm{d}s} &= p_y\left(\left[1 - \frac{c^2}{v_\phi^2}\right]\frac{\mathrm{d}a}{\mathrm{d}s} + \frac{c}{v_\phi}\frac{\omega_{c0}}{\omega}\right) \\
R\frac{\mathrm{d}p_x}{\mathrm{d}s} &= p_y\left(\frac{c}{v_\phi}\frac{\mathrm{d}a}{\mathrm{d}s} - \frac{\omega_{c0}}{\omega}\right) \\
R\frac{\mathrm{d}p_y}{\mathrm{d}s} &= Rm_e c\frac{\mathrm{d}a}{\mathrm{d}s} + p_x\frac{\omega_{c0}}{\omega},
\end{aligned} \tag{4.7}$$

where $R \equiv \gamma - p_x/m_e v_\phi$ is the dephasing parameter and $\omega_{c0} \equiv |e|B_0/m_e c$ is the cyclotron

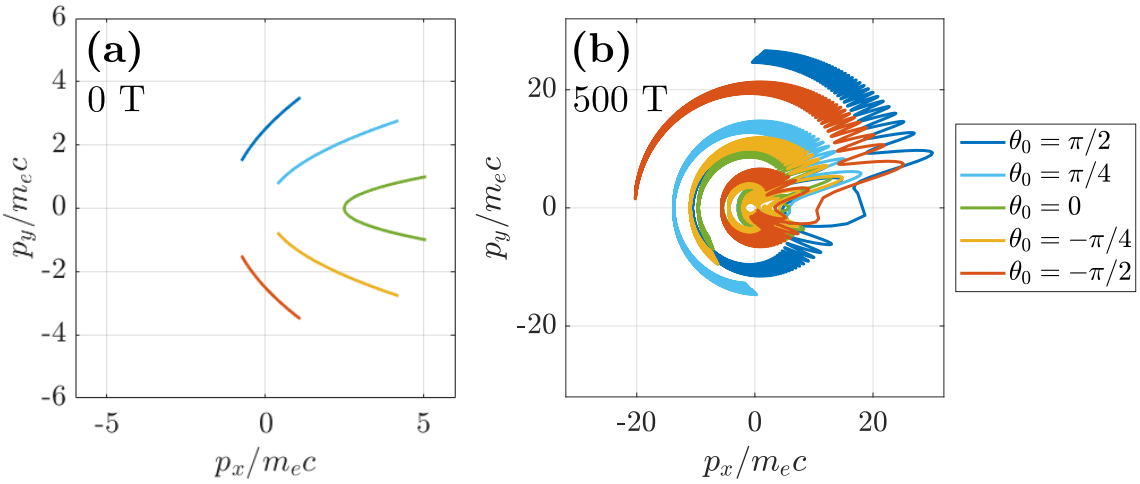

Figure 4.1: Illustration of difference between non-magnetized and magnetically assisted direct laser acceleration. Momentum space trajectories for electrons in vacuum interacting with a plane wave laser pulse with $a_0 = 1$ for 1 ps with (a) no magnetic field and (b) 500 T magnetic field ($\omega_{c0}/\omega \approx 0.05$). In all cases, the electron is initialized with $|p| = 2.5 m_e c$ into a laser phase where $a = 0$. θ_0 is the initial angle between the electron momentum and the forward direction ($\tan\theta_0 = p_y/p_x$).

frequency associated with B_0. The solution of these equations describes the electron trajectory. Eqs. 4.7 suggest that even a weak magnetic field with $\omega_{c0} \ll \omega$ may fundamentally alter the electron dynamics. With the addition of the magnetic field, the quantities R and $p_y - a$, which (in the limit that $v_\phi \to c$) are constants of the motion are no longer conserved. In addition, Eqs. 4.7 are no longer symmetric with respect to $p_y \to -p_y$ and $a \to -a$.

An example of how the addition of a magnetic field can fundamentally alter DLA is shown in Fig. 4.1, where we have solved Eqns. 4.7 using MATLAB's ode113 solver for several initial conditions with the same starting energy. The addition of a magnetic field can deliver a cyclotron rotation-like path in momentum space punctuated by distinct kicks in the electron energy, during which the electron momentum maintains a near-constant angle with with p_x-axis. Each kick promotes the electron to a higher energy and suggests the possibility that the addition of a weak magnetic field can facilitate significant plasma heating.

To illustrate how the magnetic field facilitates enhanced energy gain via DLA, it is

useful to consider the evolution of the electron energy and the angle the electron momentum makes with the forward direction θ. Similar to the approach of Ref. 120, we obtain

$$\frac{\mathrm{d}\gamma}{\mathrm{d}s} = \frac{1}{R}\frac{p_y}{m_e c}\frac{\mathrm{d}a}{\mathrm{d}s} = \frac{1}{R}\left(\gamma\beta\sin\theta\frac{\mathrm{d}a}{\mathrm{d}s}\right) = \frac{\beta\sin\theta}{1-\dfrac{c}{v_\phi}\beta\cos\theta}\frac{\mathrm{d}a}{\mathrm{d}s} \tag{4.8}$$

$$\frac{\mathrm{d}\theta}{\mathrm{d}s} = \frac{1}{R}\left(\frac{\omega_{c0}}{\omega} + \left[\frac{1}{\beta}\cos\theta - \frac{c}{v_\phi}\right]\frac{\mathrm{d}a}{\mathrm{d}s}\right) = \frac{\dfrac{\omega_{c0}}{\omega} + \dfrac{1}{\beta}\left[\cos\theta - \dfrac{c}{v_\phi}\beta\right]\dfrac{\mathrm{d}a}{\mathrm{d}s}}{\gamma\left(1-\dfrac{c}{v_\phi}\beta\cos\theta\right)}. \tag{4.9}$$

In the absence of a magnetic field, $\mathrm{d}\theta/\mathrm{d}s = 0$ for an angle θ_* given by

$$\cos\theta_* = c\beta/v_\phi. \tag{4.10}$$

This angle represents a stable solution of Eq. 4.9 during the accelerating phase of the laser pulse. Furthermore, θ_* maximizes the rate of energy gain in Eq. 4.8. In the limit that $v_\phi \to c$, we use the invariants R and $p_y - a$ to compare the actual momentum angle during acceleration, $\cos\theta_R = p_x/|p|$, to the prediction that $\cos\theta_* = \beta$. In the small angle limit, this results in

$$\begin{aligned} \theta_R^2 &\approx \frac{4R^2\left(\left[a+p_{y0}\right]^2 - R + R^2\right)}{\left(\left[a+p_{y0}\right]^2 + 1 - R\right)^2} \\ \frac{\theta_R^2 - \theta_*^2}{\theta_R^2} &\approx -\frac{\left[a+p_{y0}\right]^2\left[1+R^2\right] + 1 - R - R^2 - R^3 + 2R^4}{\left(\left[a+p_{y0}\right]^2 + 1 - R - 2R^2\right)\left(\left[a+p_{y0}\right]^2 - R + R^2\right)}, \end{aligned} \tag{4.11}$$

where we have assumed p_{y0} corresponds to a time when $a = 0$. We therefore observe an angle during the acceleration which is approximately θ_* in the limit where $a_0 \gg 1$ and $R \ll a_0$. These observations suggest θ_* can be an important property of non-magnetized acceleration. However, it is important to note that θ_* is not actually constant over the course of the acceleration, but changes as the energy changes ($\sin\theta_* \approx \theta_* = \sqrt{1-\beta^2} = 1/\gamma$).

In the presence of a magnetic field, the momentum angle which is a stable solution of Eq. 4.9 is instead

$$\cos\theta = \frac{c\beta}{v_\phi} - \left(\beta\frac{\omega_{c0}}{\omega}\right) / \left(\frac{\mathrm{d}a}{\mathrm{d}s}\right). \tag{4.12}$$

Eq. 4.12 suggests there is asymmetry between the two halves of the laser cycle, i.e. whether a constant value of θ can be achieved depends on the sign of $\mathrm{d}a/\mathrm{d}s$. Without loss of generality, we have assumed that the magnetic field is $+z$-directed, i.e. $\omega_{c0} > 0$. In the case where electrons are fairly relativistic and the phase velocity is only slightly above the speed of light (quantified below), we can only achieve a constant value of θ for $\mathrm{d}a/\mathrm{d}s > 0$. This further suggests that the magnetically assisted acceleration occurs only for $\theta > 0$, i.e. $p_y > 0$. To obtain an estimate for θ, we further proceed by approximating $\mathrm{d}a/\mathrm{d}s \sim a_0$. In the small angle limit, we have approximately [120]

$$\theta \approx \sqrt{2\left(1 - \frac{c\beta}{v_\phi}\right) + 2\beta\frac{\omega_{c0}}{a_0\omega}} = \sqrt{\theta_*^2 + \theta_m^2}, \tag{4.13}$$

where we define $\theta_m = \sqrt{(2\beta\omega_{c0}/a_0\omega)}$.

The stable angle which may be obtained during acceleration is only increased appreciably relative to θ_* if the θ_m is at least comparable to θ_*. This implies that observing the effect of the magnetic field on the acceleration requires

$$1 - \frac{c\beta}{v_\phi} \gtrsim \frac{\beta\omega_{c0}}{a_0\omega}. \tag{4.14}$$

In Sections 4.4 and 4.5, we consider plasmas which are low density and only moderately relativistic, such that $1-\beta \gg v_\phi/c - 1$, on which basis we safely set $v_\phi = c$ for the remainder of this work. The requirement that $\theta_m > \theta_*$ can then be recast in terms of a minimum

requirement on the electron energy for the effect of the magnetic field to be observed,

$$\gamma \gtrsim \sqrt{\frac{a_0}{2}\frac{\omega}{\omega_{c0}}}, \tag{4.15}$$

where the above expression was obtained in the limit of a weak magnetic field ($\omega_{c0}/a_0\omega \ll 1$).

Eq. 4.15 suggests the plasma may need to be preheated in order to observe the effect of the magnetic field. In this work, we consider weak magnetic fields ($\omega_{c0}/\omega \sim 0.01$-$0.05$) and modestly relativistic laser pulses ($a_0 \sim 1$). Under these conditions, Eq. 4.15 predicts a substantially superponderomotive energy ($\gamma \gtrsim 7 > 1 + a_0^2/2$, for $\omega_{c0}/a_0\omega = 0.01$) is required to observe the effect of the magnetic field on the acceleration. While this estimate is a slight overprediction (see Fig. 4.2a), it successfully illustrates the need for preheating to observe the effect of the magnetic field. This preheating can also enhance energy gain by non-magnetized DLA, however in this case the energy gain is highly sensitive to the initial conditions (for example, the angle the electron momentum makes with the forward direction, which is encapsulated in R) and can be lower than in the magnetized case (e.g. Fig. 4.1).

The near-constant angle we predict in Eq. 4.12 is a distinguishing feature of the magnetically assisted DLA process. For an electron which starts with $\theta > \theta_m$, the rate of energy gain increases as θ decreases. We can therefore expect the highest energy gain from electrons with $\theta \sim \theta_m$. Similar to Ref. [120], we approximate the maximum energy gain by substituting θ_m in Eq. 4.8 and integrating over a half laser cycle ($\Delta s = \pi$) with $\beta \to 1$. This is appropriate because for $\theta \sim \theta_m$ the rate of energy gain is not sensitively dependent on the energy. In the small angle approximation, this gives a maximum energy gain of approximately

$$\Delta\gamma \sim 2^{3/2} a_0^{3/2} \sqrt{\frac{\omega}{\omega_{c0}}}. \tag{4.16}$$

Importantly, the plasma preheating needed to achieve a constant angle during the

acceleration also allows the electron to retain the energy it gains from the laser, which is fundamentally different than non-magnetized DLA. In deriving an expression for θ_m, we specified the half of the laser cycle with $\mathrm{d}a/\mathrm{d}s > 0$, as was required to achieve a constant value of θ. During the following half of the cycle, the electron cannot obtain a constant momentum angle. In Eq. 4.9, we observe that the contribution to the momentum rotation by the laser in $\mathrm{d}\theta/\mathrm{d}s$ is unable to cancel out the momentum rotation provided by the magnetic field, i.e. we have

$$\frac{\omega_{c0}}{\omega} > \frac{1}{\beta}(1-\beta)\left|\frac{\mathrm{d}a}{\mathrm{d}s}\right|, \tag{4.17}$$

which is guaranteed by the preheating assumption we made in order to satisfy $\theta_m > \theta_*$. This suggests a net rotation of the electron momentum over the course of this half laser cycle. Correspondingly, as θ increases, the ability of the laser to exchange energy with the plasma decreases (based on Eq. 4.8), which means the laser is unable to undo the full acceleration it provided during the half of the cycle with $\mathrm{d}a/\mathrm{d}s > 0$. During the subsequent accelerating phase, the electron is again able to gain some energy, however, the acceleration now starts with $\theta > \theta_m$ and is thereby less efficient.

This alternation between accelerating and decelerating phases with decreasing energy change over each half-cycle continues as the electron undergoes a net cyclotron drift in momentum space. Eventually, the electron becomes mostly backward-directed ($p_x < 0$), which effectively terminates the energy gain. As the electron continues to rotate in momentum space, however, its momentum becomes favorable again for acceleration and the energy gain and loss over each laser cycle increases once more. Eventually, the electron can again reach the favorable momentum conditions ($p_x > 0$, p_y just slightly above 0) to receive a large energy kick from the laser with $\theta \sim \theta_m$, which can promote the electron to a yet-higher energy orbit (for example, the 500 T case in Fig. 4.2b).

We verify our predictions for the energy gain and angle of magnetically assisted DLA by numerically integrating the equations describing the electron motion (Eqs. 4.7)

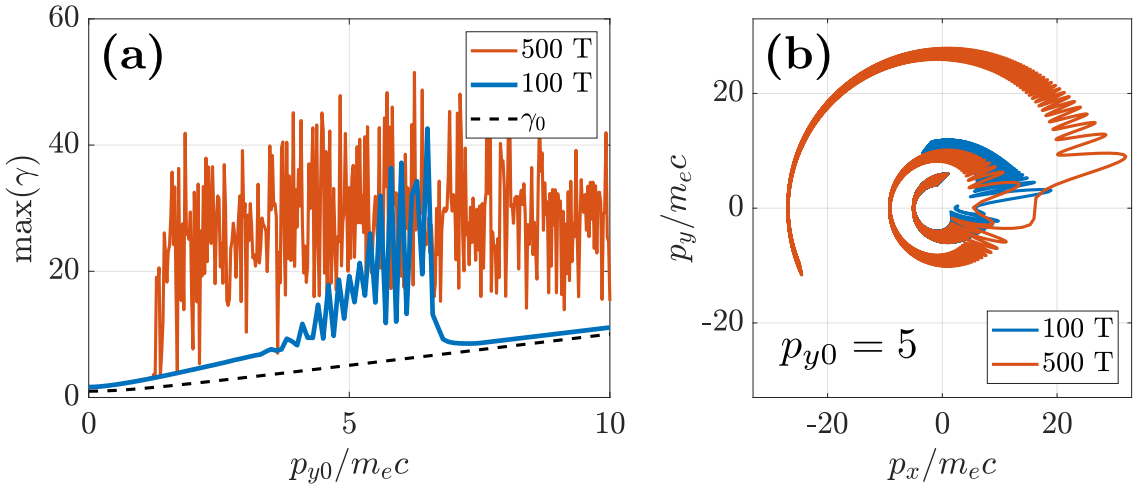

Figure 4.2: Onset of magnetically assisted direct laser acceleration and illustration of multiple energy kicks. (a) Maximum energy achieved in 660 laser cycles (2 ps plane wave pulse) versus initial momentum p_{y0} for a laser pulse with $a_0 = 1$. In the calculation, $p_{x0} = 0$ and the electron starts in a laser phase with $a = 0$. The sharp decrease for $p_{y0} \gtrsim 7$ in the 100 T case (blue line) occurs because the cyclotron period becomes too long for the electron to reach the acceleration conditions. (b) Example trajectories from the parameter scan, with $p_{y0} = 5$. In the 500 T case, the electron is able to experience multiple cyclotron orbits during the pulse duration.

using MATLAB's ode113 solver. First, we verify the prediction that preheating the electron is required to observe substantial energy gain in the presence of the magnetic field. We consider magnetically assisted DLA with a plane wave laser pulse with $a_0 = 1$ in the presence of a 100 T magnetic field ($\omega_{ce}/\omega = 0.0093 \approx 0.01$). We initialize the electron with $p_{x0} = 0$ and a varying value of $p_{y0} > 0$ and allow the electron to propagate with the laser for 660 laser cycles (corresponding to a 2 ps pulse duration), recording the maximum γ-factor which is achieved during the acceleration. The result is shown in the blue lines in Fig. 4.2. We observe a significant increase in the energy gain for $p_{y0} \gtrsim 4$ in the 100 T case. In this case, the electron is only able to undergo one major energy kick by the laser and we observe energy gain which is consistent with the prediction of Eq. 4.16 ($\Delta\gamma \lesssim 29$ for the 100 T case).

Next, we demonstrate net energy retention and the possibility for the electron to obtain multiple kicks from a sufficiently long laser pulse. The cyclotron period of an electron

is given by $2\pi/\omega_{c0} \approx 0.4\ \text{ps} \times \gamma/(B_0/100\ \text{T})$. This is also the approximate timescale for electrons to complete a full orbit in momentum space in magnetically assisted DLA. With the values of ω_{c0}/ω we consider, electrons are able to obtain $\gamma > 10$ in a single momentum kick. For a 100 T magnetic field, this implies that multipicosecond to tens of picosecond long pulses are required in order for the electron to obtain multiple momentum kicks. While such pulses are experimentally available, they are computationally challenging to model. Instead, we demonstrate that electron energy can be retained over multiple momentum kicks by increasing the applied magnetic field to 500 T.

Figures 4.1b and 4.2b show examples of magnetically assisted direct laser acceleration with a 500 T magnetic field over the course of 330 and 660 laser cycles (corresponding to 1 ps and 2 ps pulses), respectively. In these examples, we observe that the energy gained during each kick is retained and the electron is continuously accelerated to higher energies as it continues to interact with the laser. Electrons may also sometimes loose energy in the interaction with the laser. In the limit of a very long laser pulse (substantially longer than the pulses we consider), this results in a stochastic heating process [122].

The dramatic energy increase we predict from even modestly relativistic laser pulses suggests magnetically assisted direct laser acceleration may provide an efficient method to heat plasma to substantially relativistic energies. However, these theoretical predictions neglect important aspects of the laser-plasma interaction which are important in actual experiments, such as effects of the plasma density and charge separation-induced electric fields and multidimensional effects. It is also not immediately clear whether one can practically achieve the substantial preheating required to observe magnetically assisted DLA. In the remainder of this work, we will demonstrate that substantial electron heating by magnetically assisted DLA is indeed feasible under realistic conditions. This suggests a promising new approach to generating relativistically hot low-density plasma.

4.4 Energy gain in a preheated plasma

In the previous Section, we outlined a process via which a transverse magnetic field can facilitate direct laser acceleration of preheated electrons in vacuum. In this Section, we demonstrate using 1D particle-in-cell simulations that this process can indeed be observed in a low density preheated plasma, and is only slightly modified as the plasma density is scanned over several orders of magnitude. This robustness of the acceleration mechanism to plasma density and the electric fields associated with charge displacement is crucial to the two-dimensional simulations we will show in Section 4.5.

We conduct one-dimensional simulations of a modestly relativistic picosecond-duration laser interacting with a preheated millimeter-scale plasma slab using the open-source particle-in-cell (PIC) simulation code EPOCH [71]. The laser pulse has a $\sin^2$ temporal shape with a FWHM duration of 1.5 ps and a peak normalized vector potential $a_0 = |e|E_0/m_e c\omega = 1$, where E_0 and ω are the peak electric field strength and frequency of the laser. The plasma consists of a 2.7 mm long slab with a uniform density varied between $10^{-4}\, n_{cr}$ and $10^{-2}\, n_{cr}$, where $n_{cr} = 1.1 \times 10^{21}$ cm^{-3} is the critical density for the reflection of the laser pulse. The plasma is initialized hot with a 2D water-bag distribution in the initial kinetic energy ($p_z = 0$ and constant $\mathrm{d}N/\mathrm{d}\varepsilon$) up to the cutoff momentum $|p|/m_e c \leq 5$ ($\varepsilon \leq 2.1$ MeV). Ions are held immobile in the nominal case. Additional simulation parameters are given in Table 4.1.

The simulations we conduct in this Section differ from the case of direct laser acceleration in a vacuum by introducing charge separation-related longitudinal electric fields. In the context of a plasma slab, longitudinal electric fields typically form at the plasma-vacuum interface due to the high mobility of electrons relative to ions. Within the bulk of the slab, the laser can also drive plasma waves which have associated longitudinal electric fields. Sufficiently strong longitudinal electric fields can affect direct laser acceleration by dynamically increasing or decreasing the electron's forward momentum, changing

Table 4.1: Nominal 1D PIC simulation parameters. The plasma is initialized hot with a 2D water-bag distribution ($p_z = 0$ and constant $\mathrm{d}N/\mathrm{d}\varepsilon$), up to the momentum cutoff $|p|/m_e c \leq 5$.

Laser parameters	
Wavelength	$\lambda_0 = 1$ μm
Laser propagation direction	$+x$
Laser polarization	y
Peak intensity	1.4×10^{18} W/cm^2 ($a_1 = 1$)
Duration ($\sin^2$, electric field FWHM)	1.5 ps
Other parameters	
Applied magnetic field ($\mathbf{B} = B_0 \hat{\mathbf{z}}$)	$B_0 = 500$ T
Plasma slab thickness	2.7 mm
Initial electron density	$n_e = 10^{-4}\, n_{cr}$
Initial electron momentum cutoff	$|p|/m_e c \leq 5$
Ion mobility	Immobile
Spatial resolution	50 cells/μm
Macroparticles per cell, electron	100
Macroparticles per cell, ion	50
Position and time reference	
Location of the front of the plasma slab	$x = 0$
Time when peak of pulse reaches $x = 0$	$t = 0$

the dephasing parameter and the maximum energy gain [93, 119]. We initially conduct simulations with immobile ions to maximize these sources of electric fields.

We first consider the case of a cold plasma. The direct laser acceleration of initially cold electrons in vacuum (i.e. ignoring any longitudinal electric fields) produces a cutoff electron energy given by the cold ponderomotive maximum $\gamma_c = 1 + a_0^2/2 = 1.5$ (Eq. 4.3 with $R = 1$). Additionally, because DLA is a reversible process, electrons in vacuum cannot retain energy after the laser pulse has passed. Following the analysis presented in Section 4.3, we do not expect a 100-500 T magnetic field to significantly affect these results. To test whether the longitudinal electric fields present in low-density plasma can change these expectations, we consider a cold plasma with a density of $10^{-4}\, n_{cr} \approx 1.1 \times 10^{17}$ cm^{-3}. As shown in Fig. 4.3a, although a small population of electrons is able to slightly exceed γ_c through acceleration by the longitudinal electric field at the plasma-vacuum interface, overall we

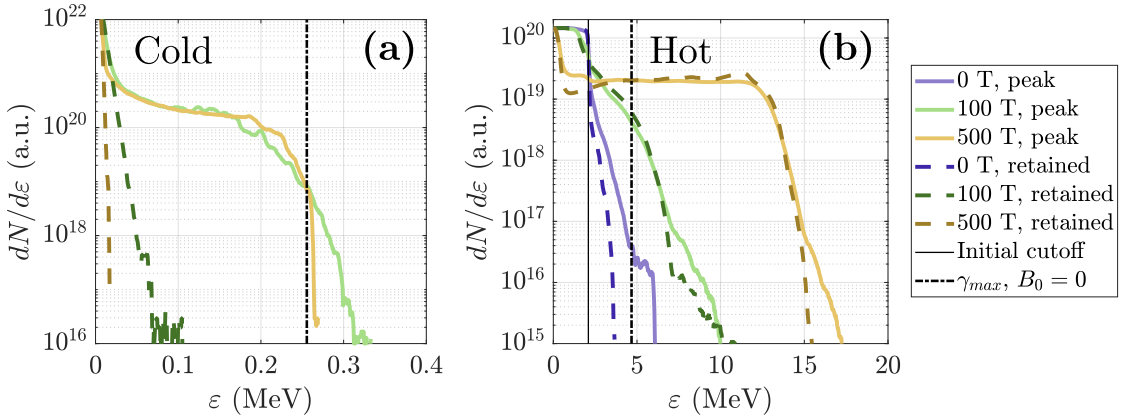

Figure 4.3: Electron energy spectra for magnetically assisted DLA in 1D simulations. (a) Cold plasma case. (b) Hot plasma case (water-bag energy distribution, see Table 4.1). The peak energy (solid colored lines) occurs while the laser is still in the plasma slab in all cases. The dash-dotted lines represent the maximum energy predicted from non-magnetized DLA theory in both the hot and cold cases. The solid black line in (b) represents the maximum energy in the initial distribution.

observe good agreement with the ponderomotive limit. In addition, minimal energy is retained by the plasma after the laser has exited the plasma slab. These results indicate that the longitudinal electric field does not significantly perturb the usual non-magnetized acceleration process for a plasma with a density of $10^{-4}\, n_{cr}$.

Next, we heat the plasma to examine whether the magnetically assisted DLA process can be observed in a finite-density plasma. As discussed in more detail in Table 4.1, we initialize plasma electrons with momentum $|p| = \sqrt{p_x^2 + p_y^2} \leq 5 m_e c$. This choice of initial energy corresponds to $|p|/m_e c \gg a_0$, and is above the threshold to trigger substantial magnetically assisted DLA (based on Fig. 4.2 in Section 4.3). In the non-magnetized case, we predict the preheating to increase the maximum ponderomotive electron energy to 5.2 MeV ($\gamma_p = 10.1$, based on $p_{x0} = 5 m_e c$ and $p_{y0} = 0$ in Eq. 4.3). This prediction is in good agreement with the simulation results (purple solid and black dash-dotted lines in Fig. 4.3b). We additionally observe a substantial drop in the electron energy within the plasma slab as the laser pulse exits the plasma, which is again consistent with ordinary non-magnetized DLA.

As shown in Fig. 4.3b, the addition of a 100-500 T magnetic field both increases the electron energy above γ_p and enables near-complete energy retention by the plasma. We additionally find robust agreement between the electron acceleration process we observe in the simulation and magnetically assisted DLA theory. Figure 4.4 shows the average trajectories of randomly selected electrons with final γ above either 10 (100 T case) or 20 (500 T case). These trajectories are in good agreement with the trajectories we obtain by solving Eqs. 4.7 starting from an initial electron momentum of $|p|/m_e c = 5$. The addition a 500 T magnetic field is especially effective at heating the plasma. In this case, electrons are able to undergo multiple cyclotron orbits during the laser pulse duration, which facilitates several distinct energy kicks by the laser pulse. As was true for the cold plasma case, a minority of the hot electrons are able to experience some additional acceleration by the longitudinal electric field at the plasma-vacuum boundary. However, on the whole, the longitudinal electric field does not make a significant contribution to the electron energy (Fig. 4.5b). We additionally find that there is no change in the electron energy spectrum upon substituting mobile protons for the originally immobile ions.

Increasing the plasma density can introduce two potentially competing effects on the electron energy gain. First, as we have mentioned, increasing the plasma density modifies the longitudinal electric field and specifically increases the electric field strength at the plasma-vacuum boundary, which could increase the energy of electrons interacting with the boundary and make this population more important to the overall energy spectrum. Second, increasing the plasma density can increase the phase velocity, which can affect the ability of electrons to gain energy via magnetically assisted DLA, as discussed in Sec. 4.3 and also Ref. 120.

For an applied magnetic field of 500 T, as the plasma density is increased from 10^{-4} to $10^{-2}\ n_{cr}$, we observe a slight ($\sim 10\%$) increase in the peak electron energy (Fig 4.5a). At the same time, the slope of the high energy tail ($\varepsilon > 10$ MeV) increases, indicating

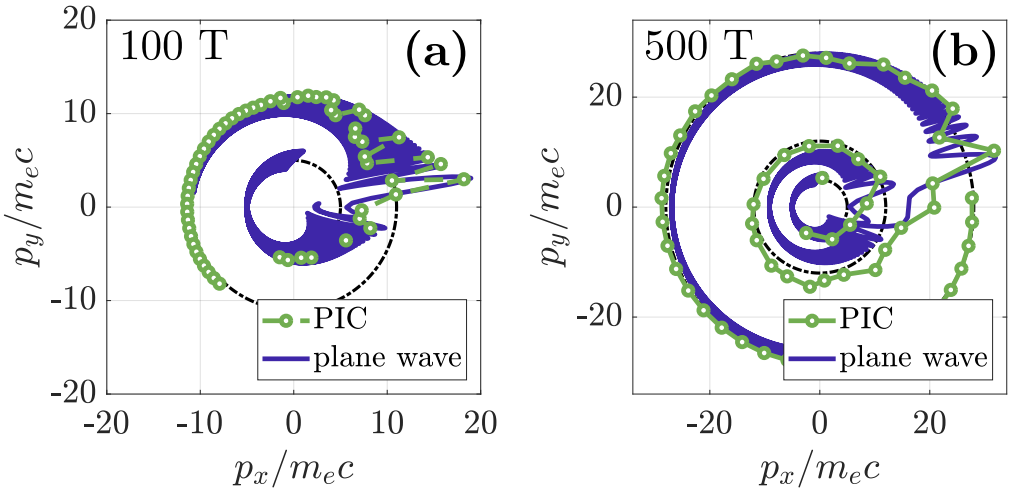

Figure 4.4: Characteristic electron trajectories for magnetically assisted DLA in 1D simulations with (a) 100 T and (b) 500 T. Green lines: randomly chosen electron with $\gamma > 10$ (100 T case, (a)) or $\gamma > 20$ (500 T case, (b)). Blue lines: trajectory calculated from plane wave simulation of 3.3 ps laser pulse starting from $p_{y0} = 5$ and $p_{x0} = 0$.

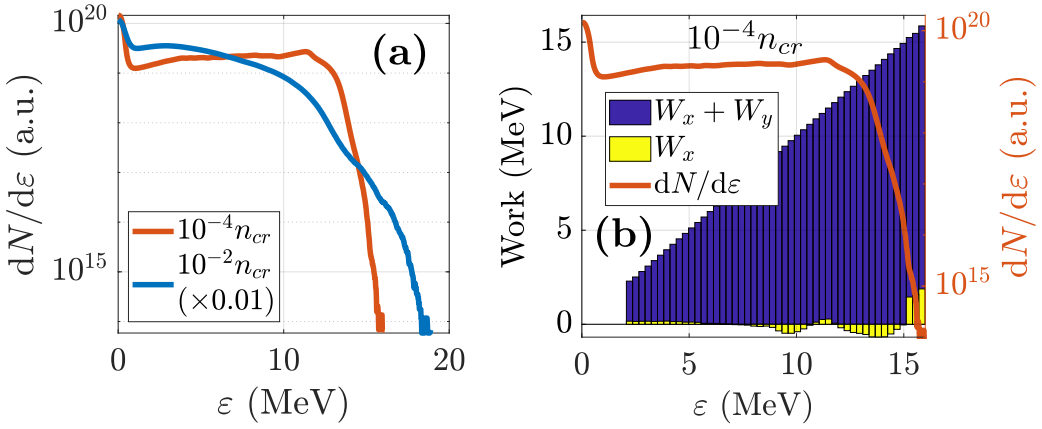

Figure 4.5: Effect of plasma density and work done on hot electrons in 1D simulations. (a) Comparison of electron density spectra for plasma densities $10^{-4}\, n_{cr}$ and $10^{-2}\, n_{cr}$. The spectra for $10^{-2}\, n_{cr}$ has been multiplied by 0.01 for the sake of comparison. (b) Work done on electrons and electron energy spectrum at the end of the simulation with $10^{-4}\, n_{cr}$. The total kinetic energy (height of blue bar) is the sum of the work done by the longitudinal (yellow bar) and transverse electric fields. Each bar represents the average work done on electrons within that energy bin.

that although electrons may obtain higher peak energy, overall fewer electrons are able to obtain this peak energy. On the whole, however, the change in the electron energy pertains mostly to the electrons which interact with the plasma-vacuum boundary and suggests that magnetically assisted direct laser acceleration is still likely to be seen even with relatively high (gas jet-level as opposed to gas cell-level) plasma density.

4.5 Energy gain facilitated by a second laser pulse

In Sections 4.3 and 4.4, we considered magnetically assisted direct laser acceleration in idealized 1D geometry with an already-relativistic preheated plasma. The electron starting energies we considered ($\gamma \sim 5$) could be quite challenging to produce experimentally, and it is therefore desirable to demonstrate that the DLA process we discuss can actually be achieved starting from a cold plasma in multidimensional geometry. In this Section, we show that magnetically assisted DLA can indeed produce comparable energy to analytic predictions in 2D PIC simulations, with the addition of a second, short laser pulse to catalyze the energy gain.

In this Section, we conduct 2D PIC simulations using EPOCH. We again consider laser irradiation of a finite (now 200 μm thick) plasma slab with a low density ($10^{-4}\, n_{cr}$). However, we now take the plasma to be a cold, initially neutral hydrogen plasma and consider the laser irradiation to consist of two temporally and spatially Gaussian pulses: a picosecond pulse with low intensity ($a_1 = 1$) and a large spot size and a femtosecond pulse with somewhat higher intensity ($a_2 = 3$) and a small spot size. The picosecond laser pulse has a 1 ps duration and a 50 μm spot size and the femtosecond pulse has a 50 fs duration and a 8 μm spot size (all given in terms of the FWHM in $|E|$). The pulses are co-propagating and are timed such that the peak of the femtosecond pulse is located on the leading edge of the picosecond pulse where the electric field falls off to 1/e of its peak

Table 4.2: Nominal 2D PIC simulation parameters. The initial plasma temperature is set as zero.

Laser parameters	
Wavelength	$\lambda_0 = 1\ \mu$m
Laser propagation direction	$+x$
Laser polarization	y
Picosecond laser	
Peak intensity	1.4×10^{18} W/cm^2 ($a_1 = 1$)
Duration (Gaussian, electric field FWHM)	1 ps
Spot size (Gaussian, electric field FWHM)	50 μm
Femtosecond laser	
Peak intensity	1.2×10^{19} W/cm^2 ($a_2 = 3$)
Duration (Gaussian, electric field FWHM)	50 fs
Spot size (Gaussian, electric field FWHM)	8 μm
Delay of peak relative to picosecond pulse	-0.6 ps
Other parameters	
Applied magnetic field ($\mathbf{B} = B_0\hat{\mathbf{z}}$)	$B_0 = 500$ T
Plasma slab thickness	200 μm
Initial electron density	$n_e = 10^{-4}\ n_{cr}$
Ion mobility	Mobile protons
Spatial resolution	30 cells/μm
Macroparticles per cell, electron	40
Macroparticles per cell, ion	20
Size of simulation box ($x \times y$, μm)	400×300
Position and time reference	
Location of the front of the plasma slab	$x = 0$
Time when peak of picosecond laser reaches $x = 0$	$t = 0$

value. The temporal separation of the peaks of the pulses is $\Delta t = 600$ fs ($c\Delta t = 180\ \mu$m). The simulation is run until both pulses exit the simulation domain. Additional details of the simulation setup are given in Table 4.2.

We observe a strong enhancement to the electron energy upon the addition of a 500 T magnetic field (Figs. 4.6a vs b). As we observed in the 1D simulations, without the applied magnetic field, the electron energy is in good agreement with the ponderomotive energy (cold ponderomotive limit for the femtosecond pulse $\gamma_c = 1 + a_2^2/2 \approx 5.5$) while the laser pulses are in the plasma slab and very little energy is retained after they leave the slab.

In contrast, in the case with the magnetic field, electrons are able to obtain significantly higher energy ($\gamma > 20$), and the majority of this energy is retained even after the laser pulses have left the plasma (Fig. 4.6b).

The electron energy gain process also shows good agreement with the magnetically assisted DLA process we outlined in Section 4.3. Figure 4.6 shows the the momentum space trajectories of 30 randomly selected electrons with a final γ greater than 20. The trajectory is in good agreement with the predicted trajectory from 1D theory (Sec. 4.3) for an electron with initial momentum $|p|/m_e c = 3.4 \sim a_2$ accelerated by a 1 ps duration plane wave laser pulse. Spatially, we both predict and observe that the energy gain occurs near the laser axis, which corresponds to the minimum y-value of the cyclotron-like orbit (where p_y changes sign). This allows electrons to be accelerated by a laser pulse with a spot size smaller than the Larmor radius.

The dramatic electron energy gain we observe with the applied magnetic field requires both the picosecond and femtosecond laser pulses. As was the case in our 1D simulations with cold plasma, the maximum electron energy remains in agreement with $\gamma_c = 1 + a^2/2$ in 2D simulations with a single laser pulse regardless of the applied magnetic field (Fig. 4.6c).

The role of the femtosecond laser pulse is to catalyze the magnetically assisted direct laser acceleration process by providing electrons with an initial momentum kick. As the femtosecond pulse propagates through the plasma, it expels electrons transversely through the ponderomotive force and in the process imparts net momentum to the electrons ($|p| \sim a_2$). This initial momentum kick provides the preheating needed to trigger the magnetically assisted DLA process.

As shown directly in Fig. 4.7c, the electron energy gain in the simulations with the magnetic field is attributable to work done by the transverse (as opposed to longitudinal) electric field, which is consistent with energy gain by the ponderomotive force followed

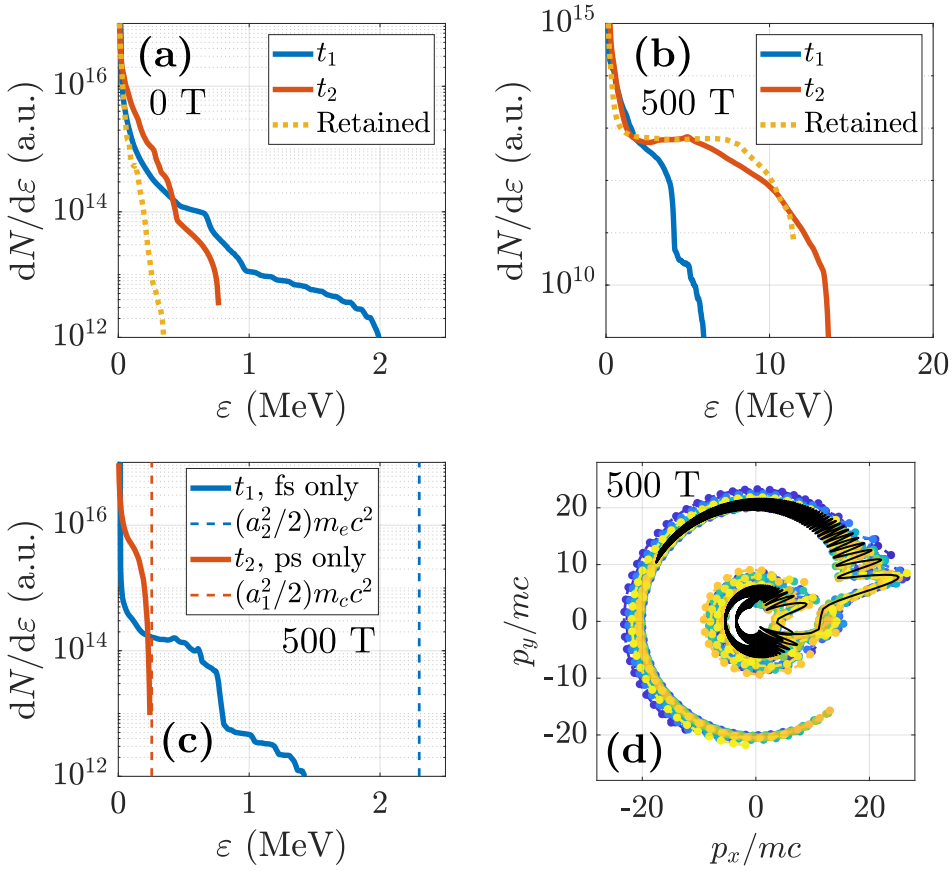

Figure 4.6: Magnetically assisted DLA in 2D simulations using a two pulse scheme. (a-c) Electron energy spectra for (a) non-magnetized case with both pulses, (b) 500 T case with both pulses, and (c) 500 T case with only the picosecond pulse or the femtosecond pulse. t_1 and t_2 denote when the peak of the femtosecond and picosecond pulses are halfway through the plasma slab, respectively. The energy retained was evaluated when the picosecond pulse has fallen to 1/e of its peak electric field value at the right edge of the slab. (d) Colored lines: electron trajectories in momentum space for 30 randomly selected electrons with final $\gamma > 20$. Black line: electron trajectory calculated from theory starting with $p_{y0} = 3.4 m_e c$ and $p_{x0} = 0$.

by direct laser acceleration. Ordinarily, i.e. with $B_0 = 0$, the propagation of a sufficiently intense femtosecond laser pulse through low density plasma drives longitudinal plasma waves, which can also trap and accelerate electrons via laser wakefield acceleration [12, 13, 125]. However, this acceleration process requires long distances to accelerate electrons when the plasma density is low and is not able to deliver energy in excess of the ponderomotive energy over the distance we consider in our simulations (e.g. Fig. 4.6). Additionally, the application of the magnetic field is likely detrimental to the wakefield acceleration of electrons when the characteristic Larmor radius of ponderomotively expelled electrons ($\rho_L \equiv |cp/eB| \sim a_2 m_e c^2/|e|B_0 \sim 10\ \mu$m) is smaller than the usual wakefield bubble size ($\sim \lambda_{pe} = 2\pi c/\omega_{pe} \sim 100\ \mu$m, where ω_{pe} is the electron plasma frequency). As shown in Figs. 4.7a and 4.7b, the applied magnetic field is able to substantially alter the formation of the plasma wake by rotating the momentum of electrons and preventing electrons from moving away from the axis. While the momentum rotation of electrons is detrimental from the standpoint of wakefield acceleration because it prevents charge separation, it benefits magnetically assisted DLA by keeping the hot electrons near the axis, which helps facilitate the subsequent interaction with the picosecond pulse.

4.6 Summary

In summary, we predict that dramatic plasma heating can be achieved under experimentally relevant conditions by magnetically assisted direct laser acceleration. The observation of magnetically assisted DLA in a plasma requires several conditions to be met. First, as we discuss in Section 4.3, noticeable rotation of the electron momentum must occur during the acceleration process, which requires the electron to be preheated prior to interacting with the DLA pulse. Second, electric fields associated with charge separation in a finite-density plasma must not overwhelm the acceleration process. As we demonstrate in

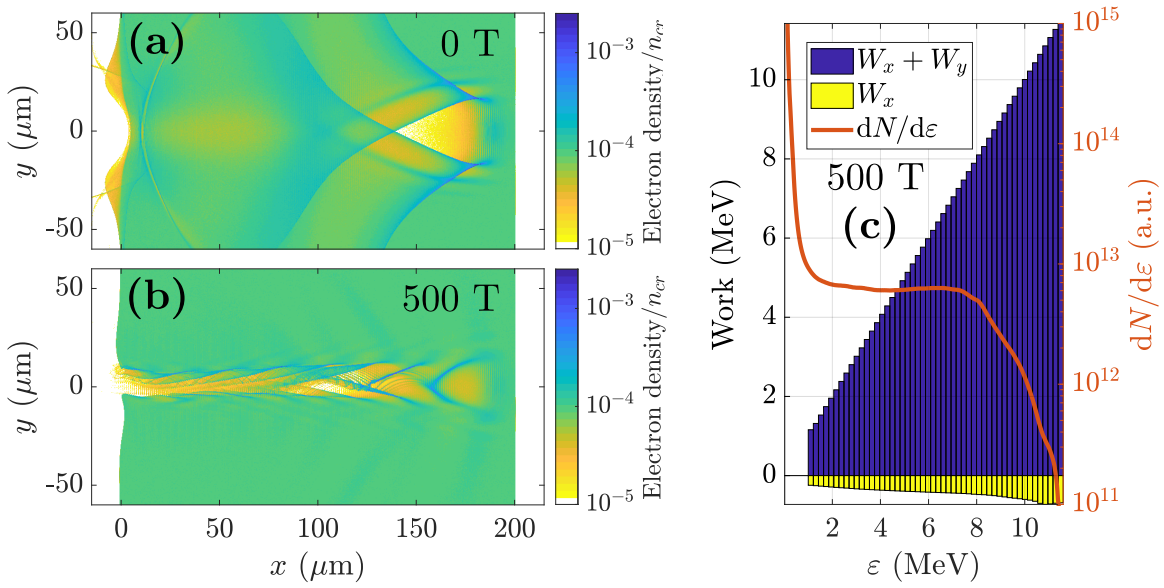

Figure 4.7: Magnetic confinement and work done on hot electrons. (a,b) Electron density profile with (a) no magnetic field, and (b) 500 T magnetic field. (c) Work done on electrons and electron energy spectrum at the end of the simulation. The total kinetic energy (height of blue bar) is the sum of the work done by the longitudinal (yellow bar) and transverse electric fields. Each bar represents the average work done on electrons within that energy bin.

Section 4.4, the second criterion is easily met by plasma with densities relevant to both gas jets and gas cells ($\sim 10^{-4}\, n_{cr}$ to $10^{-2}\, n_{cr}$). However, achieving a relativistically preheated plasma can be challenging and it is therefore desirable to formulate a scenario in which magnetically assisted DLA is possible starting from a cold plasma. In Section 4.5, we introduced one such scenario, in which a small spot size femotosecond duration pulse is used to catalyze the direct laser acceleration process for a large spot size picosecond duration pulse. In this example, we were able to produce copious electrons with $\gamma > 20$ using a femtosecond pulse with $a_0 = 3$ and a picosecond pulse with $a_0 = 1$ and an applied magnetic field of 500 T. This dramatic heating in excess of 10 times the ponderomotive limit of the long pulse is retained after the pulses have left the plasma, suggesting magnetically assisted direct laser acceleration may be an avenue to producing relativistically hot plasmas, and may be desirable for further experiments.

4.7 Acknowledgements

Chapter 4, in part, is currently being prepared for submission for publication of the material. K. Weichman and A. V. Arefiev. The dissertation author was the primary investigator and author of this material.

This research was supported by the DOE Office of Science under Grant No. DE-SC0018312. Particle-in-cell simulations were performed using EPOCH [71], developed under UK EPSRC Grant Nos. EP/G054940, EP/G055165, and EP/G056803. This work used HPC resources of the Texas Advanced Computing Center (TACC) at the University of Texas at Austin and the Extreme Science and Engineering Discovery Environment (XSEDE) [126], which is supported by National Science Foundation grant number ACI-1548562. Data collaboration was supported by the SeedMe2 project [117] (http://dibbs.seedme.org).

Chapter 5

Generation of focusing ion beams by magnetized electron sheath acceleration

5.1 Abstract

We present the first 3D fully kinetic simulations of laser driven sheath-based ion acceleration with a kilotesla-level applied magnetic field. The application of a strong magnetic field significantly and beneficially alters sheath based ion acceleration and creates two distinct stages in the acceleration process associated with the time-evolving magnetization of the hot electron sheath. The first stage delivers dramatically enhanced acceleration, and the second reverses the typical outward-directed topology of the sheath electric field into a focusing configuration. The net result is a focusing, magnetic field-directed ion source of multiple species with strongly enhanced energy and number. The predicted improvements in ion source characteristics are desirable for applications and suggest a route to experimentally confirm magnetization-related effects in the high energy density regime.

We additionally perform a comparison between 2D and 3D simulation geometry, on which basis we predict the feasibility of observing magnetic field effects under experimentally relevant conditions.

5.2 Introduction

Recent advances in all-optical magnetic field generation have made experimentally accessible new regimes of magnetized high energy density physics (HEDP) relevant to applications including inertial fusion energy [14–16] and laboratory astrophysics [8, 9, 127]. In particular, the introduction of laser-driven coil targets [23–26, 30] capable of generating nanosecond-duration, hundreds of Tesla to kilotelsa-level magnetic fields over 100's of microns at currently-existing large laser facilities including LFEX/GEKKO XII at ILE [23], LULI [24, 30], and OMEGA [25, 26] introduces new possibilities in magnetized, relativistic laser-produced plasma. The understanding of the impact of strong magnetic fields on HEDP is rapidly evolving and has spurred research in areas including electron beam transport [128, 129], laser-produced magnetic reconnection [7], and ion acceleration [130–132].

In particular the ion acceleration induced by the expansion of a laser-heated electron sheath into vacuum [36,37] presents an attractive platform for the study of magnetic field effects in laser-produced plasmas. Following its initial demonstration [38–40], non-magnetized sheath-based ion acceleration has been extensively studied [133], including in configurations compatible with experimental magnetic field generation platforms. Improvements in the ion source characteristics, including efforts to generate a focusing ion beam [134–136] and increase the energy [137–139], are additionally desirable for applications including isochoric heating [41] and ion fast ignition [42]. It is therefore advantageous to elucidate the mechanism via which applied magnetic fields can beneficially alter sheath-based ion acceleration, particularly in the context of realistic magnetic field strengths.

Given the computational expense associated with 3D simulations, it would seem desirable to study the effect of the applied magnetic field in the context of 2D simulations. The limitations of using 2D simulations to represent 3D physics are well known in the target normal sheath acceleration (TNSA [140]) regime (i.e. without an applied magnetic field), with, for example, the conclusion that 2D simulations over-predict both the acceleration time and the maximum ion energy (e.g. Refs. 141, 142). However, the addition of the magnetic field as a new element in sheath-based ion acceleration requires re-evaluating the appropriateness of 2D simulations (such as those presented in Refs. 30, 130) to study what is inherently a 3D phenomenon.

In this study, we present the first 3D fully kinetic simulations of sheath-based ion acceleration with a kilotesla-level applied magnetic field. We demonstrate that the magnetization of hot electrons creates a two-stage ion acceleration process consisting of enhanced energy gain and later focusing, resulting in a focusing, magnetic field-directed ion source of multiple species with strongly enhanced energy and number. We show that electron magnetization is tied to the balance of thermal to magnetic pressure in the hot electron sheath (plasma β_e), which changes over the course of the acceleration. The change in magnetization drives a fundamental change in the topology of the sheath electric field and reverses the usual outwardly diverging ion motion into focusing. We additionally find that the beneficial effects of the applied magnetic field are substantially downplayed in 2D simulations, on which basis we predict the feasibility of observing the acceleration mechanism we describe under experimentally relevant conditions.

5.3 Results

We simulate a relativistically intense laser pulse interacting with the preplasma in front of an opaque plastic target with and without an applied magnetic field in 2D

and 3D using the particle-in-cell code EPOCH [71] (see Methods). The magnetic field strength and laser spot size were chosen to make 3D simulations tractable below machine-scale, which necessitated a 2000 T magnetic field. We also investigate the ability of 2D simulations to reproduce the magnetic field benefits observed in 3D at 2000 T. Following this analysis, we conduct additional 2D simulations with a 400 T field and larger laser spot to probe the relevance of the ion acceleration process we observe in 3D under experimentally realizable conditions. Unless explicitly stated, all simulation results were obtained from 3D simulations.

The simulation setup is shown schematically in Fig. 5.1a. The laser pulse is linearly y-polarized, propagates in the x (target normal) direction, and is spatially and temporally Gaussian with 3 μm FWHM spot size and 150 fs FWHM duration (both given in terms of the intensity). The wavelength is 1.06 μm and the the peak intensity is 2×10^{19} W/cm^2. The plastic (CH) target is 5 μm thick with a 1.5 μm preplasma scale length. We apply a static uniform magnetic field of $B_0 = 2000$ T at either target normal incidence (0°, $B_x = B_0$) or angled upward at 10° in the x-y plane. For convenience, $t = 0$ denotes the time when the peak of the laser pulse would impact the front target surface and $x = 0$ is the location of the rear surface. See Methods for additional details of the simulation setup.

5.3.1 Magnetic field-associated benefits to ion acceleration

Sheath-based ion acceleration is the transfer of electron thermal energy to ion energy mediated by a quasi-static electric field. When the laser interacts with the front surface preplasma, it generates a population of hot electrons. These electrons stream through the target and establish a sheath field on the rear surface, which then accelerates ions.

We find that the applied magnetic field has negligible impact on the laser production of hot electrons and does not substantially alter the laser-produced electron energy or angular spectrum (Fig. 5.1f). In our cases, the applied magnetic field is weak compared to

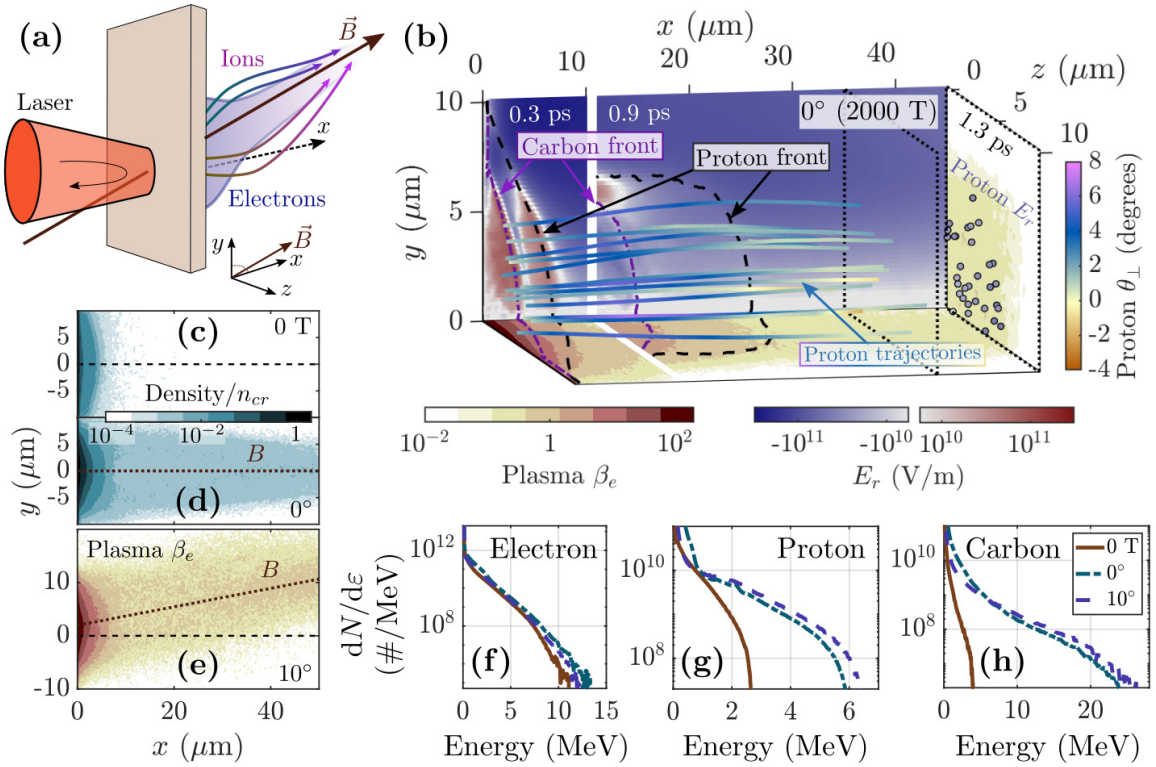

Figure 5.1: Ion acceleration with a strong applied magnetic field. (a) Schematic of simulation setup and ion acceleration. (b) Illustration of two-stage acceleration process for target-normal 2000 T magnetic field: (top) radial electric field, (bottom, right side) plasma β_e, and (trajectories) $\theta_\perp$, the angle the proton momentum makes with the x-axis, plotted along the trajectories of randomly selected protons. The protons shown have final energy above 4 MeV. Dashed lines indicate the proton and carbon ion front locations. The 3 times shown represent the first stage of the acceleration (0.3 ps), the beginning of the second stage (0.9 ps), and late into the second stage (1.3 ps). The slice in β_e at $t = 1.3$ ps corresponds to $x = 35$ μm (dotted plane). (c,d) Electron density at $t = 0.3$ ps for (c) TNSA (no magnetic field) and (d) 2000 T target normal magnetic field. (e) Plasma β_e at $t = 0.3$ ps calculated from the density with 2000 T magnetic field directed at 10° in the $x - y$ plane. (f) Energy spectra for electrons at $t = 0.3$ ps. (g,h) Final energy spectra for (g) protons and (h) carbon ions. (g,h) capture all ions with $p_x > 0$.

the peak laser magnetic field and the electron gyro-frequency is low compared to the laser frequency, which precludes the resonant heating effect observed at substantially higher magnetic field strength [119, 131, 132].

Although there is no apparent difference in the laser-produced hot electrons, we find that the accelerated ion energy and number, especially for the heavier ion species, are substantially enhanced by the application of the 2000 T field (Figs. 5.1g and 5.1h). This enhancement occurs because the magnetic field restricts the transverse spread of hot electrons within the target, enhancing the sheath electric field. Guiding of electrons within a target by a strong magnetic field has also been observed experimentally (for example, in Ref. 129).

The guiding effect of the magnetic field is expected to be important when the magnetic field is able to substantially affect the transverse spread of hot electrons. For our simulation parameters, the laser spot size is comparable to the hot electron Larmor radius $\rho_L = cp_\perp/eB$, where we estimate $cp_\perp \sim T$ by the slope temperature $T \approx 0.8$ MeV ($\mathrm{e}^{-\varepsilon/T}$ fit). The magnetic field reduces the hot electron transport across field lines and thereby increases the sheath electron density (e.g. Fig. 5.1c versus Fig. 5.1d) and the accelerating electric field, which increases the accelerated ion energy and number.

We additionally find that the magnetic field fundamentally changes the electric field configuration of the sheath *through the magnetization of hot electrons*, resulting in high energy ions which are 1) magnetic field-directed (the angular spectrum peaks along the field direction), and 2) magnetic field-focusing (coming to a focus along the field line).

5.3.2 Role of electron magnetization in the sheath

Qualitatively, electrons are magnetized when the magnetic force dominates the electric force perpendicular to the field lines, i.e.

$$|e\mathbf{v}\times\mathbf{B}|/c > |e\mathbf{E}_\perp|, \tag{5.1}$$

which requires at a minimum $B > E_\perp$. We estimate the sheath electric field generated by hot electrons as

$$E_\perp \approx 4\pi|e|n_e\lambda_{De} = \sqrt{4\pi n_e T}, \tag{5.2}$$

where $\lambda_{De} \equiv \sqrt{T/4\pi e^2 n_e}$ is the hot electron Debye length corresponding to the local electron density n_e. We estimate $B \approx B_0$ for the magnetic field (the diamagnetic effect does not change the order of magnitude of B).

The relative strength of the electric and magnetic fields in the sheath is therefore approximately

$$E_\perp/B \sim \rho_L/\lambda_{De} \sim \sqrt{\beta_e}, \tag{5.3}$$

where $\beta_e \equiv 8\pi n_e T/B^2$ is the ratio of thermal to magnetic pressure. Thus we monitor β_e, which is associated with the collective processes of sheath formation and magnetic pressure, to infer the electron magnetization in the sheath.

Close to the target surface and during the initial stage of acceleration, ions see an electron population with $\beta_e \gg 1$. During this stage, the ions quickly gain the majority of their final energy, which is enhanced by the addition of the magnetic field. However, there is no change to the electric field direction relative to a typical unmagnetized sheath.

Farther from the target surface and during the second stage of acceleration, high energy protons and carbon ions encounter an electron population with $\beta_e < 1$. This population is magnetic field-following (i.e. magnetized), which we demonstrate directly

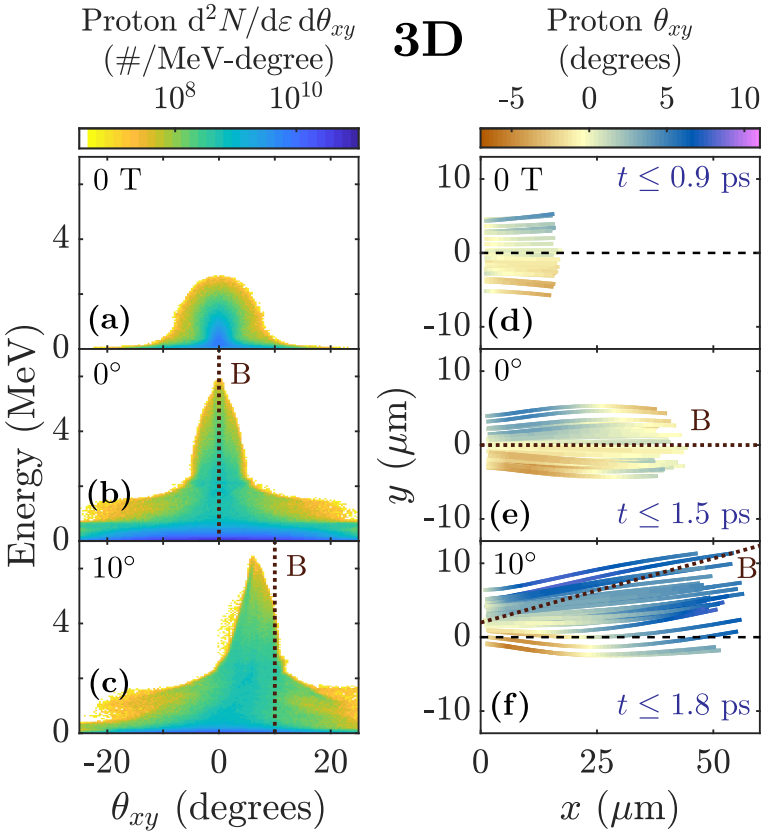

Figure 5.2: Ion focusing and deflection with applied magnetic field. (a)-(c) Angularly resolved proton energy spectrum corresponding to the cases shown in Fig. 5.1g. (d)-(f) θ_{xy}, the angle between the proton's forward momentum (p_x) and p_y, plotted along the trajectories of randomly selected protons. The protons shown have final energy above 2 MeV (0 T case) or 4 MeV (2000 T cases). (a,d) TNSA (no magnetic field). (b,e) Target normal 2000 T magnetic field. (c,f) 2000 T magnetic field directed at 10° in the $x-y$ plane.

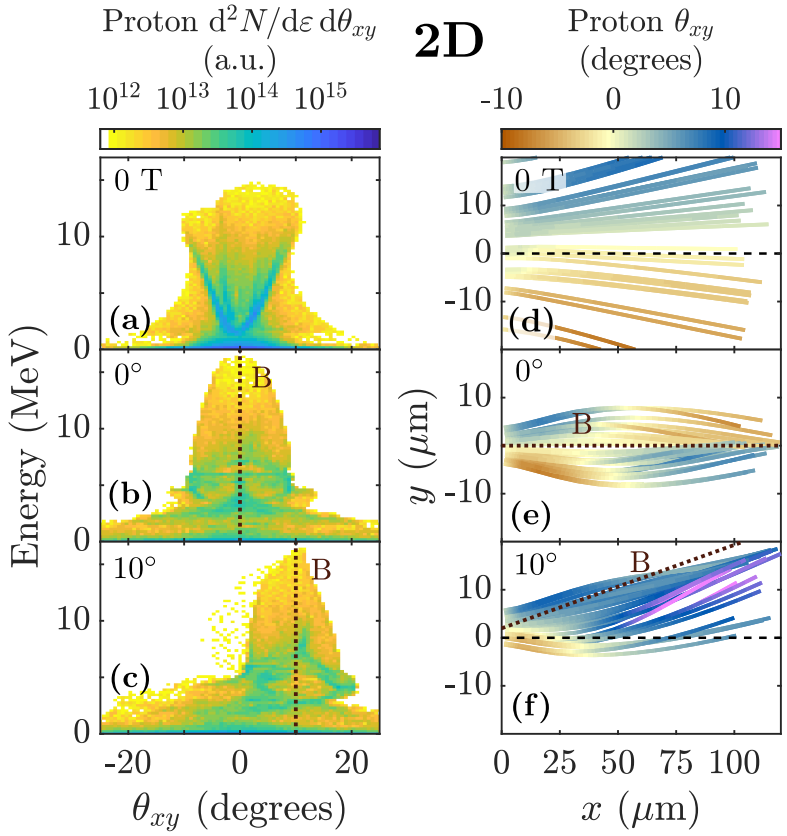

Figure 5.3: Ion focusing and deflection in 2D simulations. (a)-(c) Angularly resolved proton energy spectrum. (d)-(f) θ_{xy}, the angle between the proton's forward momentum (p_x) and p_y, plotted along the trajectories of randomly selected protons. The protons shown have final energy above 10 MeV. (a,d) TNSA (no magnetic field). (b,e) Target normal 2000 T magnetic field. (c,f) 2000 T magnetic field directed at 10° in the $x-y$ plane. The angularly integrated energy spectra for the cases in (a,b) are shown in Fig. 5.4a.

by tilting the magnetic field by 10° in the x-y plane, e.g. in Fig. 5.1e. We find that the net deflection of electrons from the target-normal direction in the 10° case causes the high energy ion population to be deflected as well (Figs. 5.2c and 5.2f). While the protons are still in the process of deflecting toward the field lines at the end of our 3D simulation, 2D simulations demonstrate that the high energy ion population becomes fully magnetic field-directed (Fig. 5.3c).

The magnetization of hot electrons additionally induces ion focusing about the magnetic field lines (e.g. Fig. 5.2e). The target-transverse, outward directed electric field

experienced by ions during the initial, unmagnetized stage of the acceleration ($t \lesssim 0.5$ ps, e.g. $x < 10$ μm in Fig. 5.1b) results from the higher mobility of electrons than ions. The relative mobility of the hot electron population allows them to expand past the ions in both the target-normal and target-transverse directions and creates an initial outward expansion of the ions which is similar to the case with no magnetic field ($x \lesssim 10$ μm in Figs. 5.2d-f).

In contrast, in the magnetized sheath, the magnetic pressure exceeds the electron thermal pressure and the electrons become less mobile than the ions in the magnetic field-transverse direction, reversing the transverse sheath configuration. We find that as ions pass $\beta_e \lesssim 0.5$, the electric field becomes magnetic field-focusing ($t \gtrsim 0.5$ ps, e.g. $x > 10$ μm in Fig. 5.1b). This focusing effect persists over a long time and visibly pulls high energy ions toward the field lines (e.g. Figs. 5.1b and 5.2e,f). It also reduces the angular spread of high energy ions relative to the 0 T case (Fig. 5.2a-c).

This sheath-field-reversal induced focusing may also help explain astrophysical jet formation in an axial magnetic field. Jet formation has previously been studied in sub-100 T level magnetic fields, where several mechanisms have been proposed to explain ion collimation, including shocks [8], gradients in magnetic pressure [143], and pinching [144]. While these studies employed magnetohydrodynamic modeling due to the relatively large spatial (∼mm) and time (∼ns) scales involved, in our study the high magnetic field and short laser pulse duration create spatial (~ 100 μm) and time (∼ps) scales conducive to 3D kinetic modeling. As a result, we are able to separate the dynamics of the fully kinetic electrons from the ions. This approach has already enabled the discovery of novel astrophysically relevant ion acceleration-related phenomena under other conditions, for example in the colliding flows considered in Ref. 127. In our regime of relativistic intensity short pulse lasers and kilotesla-level magnetic fields, ion focusing is mediated by the ions transversely overshooting magnetized electrons from the high energy tail of the distribution and requires a fully kinetic treatment in lieu of single fluid magnetohydrodynamics.

5.3.3 Necessity of 3D simulations

Although we observe the magnetic field-deflecting and magnetic field-focusing effects of electron magnetization in 2D simulations (Fig. 5.3), we find that 3D simulations are required to accurately capture the benefits of adding the magnetic field. This may be due in part to fundamental differences in physical processes which affect the strength of the sheath electric field in 2D versus 3D geometry. First, in 3D the hot electron sheath expands in two transverse directions, while in 2D it only expands in one, meaning the accelerating electric field drops less in 2D than in 3D for expansion over the same distance. Second, in 3D the electrostatic potential well created by charge separation has finite depth and allows sufficiently hot electrons to carry kinetic energy out of the system, while in 2D, the electrostatic potential does not converge as the hot electrons move away from the ions. As a result, in 2D even very hot electrons can transfer their full kinetic energy into sheath potential energy, while in 3D some of this energy would be lost. The effect of these differences can be seen even in TNSA (no magnetic field), where it is well-known that 2D simulations over-predict the ion energy (see, for instance the difference in peak energy in Figs. 5.2a and 5.3a).

The addition of a sufficiently strong magnetic field modifies both the transverse expansion of the hot electron sheath and the behavior of the (now magnetized) electrons escaping the potential well, and clearly degrades the fidelity of 2D simulations. 2D geometry also fails to capture the 3D nature of cyclotron orbits. In a series of otherwise identical 2D simulations (same magnetic field strength, laser spot size, etc as the 3D cases), we observe that 2D simulations downplay the beneficial effects of the applied magnetic field. 2D simulations fail to reproduce the substantial energy enhancement observed in 3D simulations, e.g. the factor of 2 and 5 increases in the peak ion energy shown for proton and carbon ions in Figs. 5.1g,h, respectively. Instead, 2D simulations predict almost no enhancement in the peak proton energy and only a moderate increase in the peak carbon

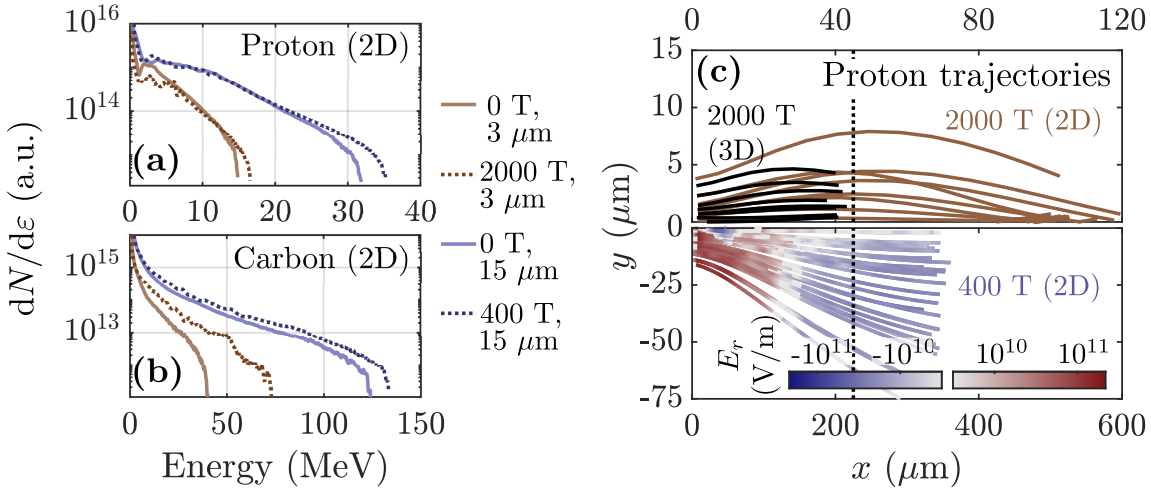

Figure 5.4: Ion acceleration in 2D simulations with target normal magnetic field and comparison with 3D. (a,b) Energy spectra in 2D simulations for 2000 T case (3 μm focal spot) and 400 T case (15 μm focal spot) for (a) protons, and (b) carbon ions. (c, top) 2000 T: comparison of proton trajectories in 2D and 3D. (c, bottom) 400 T: radial electric field experienced by randomly selected protons, plotted along their trajectories. Dotted lines in (c) denote (top) $x = 45$ μm, roughly where p_y changes sign in the 2000 T 2D case, and (bottom) $x = 5 \times 45 = 225$ μm. The protons shown have final energy above 4 MeV (3D case), 10 MeV (2D, 2000 T), or 25 MeV (2D, 400 T).

energy (brown lines in Figs. 5.4a,b). Additionally, we find that 2D simulations substantially over-predict the distances ions must propagate to be deflected towards the magnetic field lines and subsequently focused (e.g. Fig. 5.4c,top).

When 3D simulations are not tractable, for example at lower magnetic field strength, we can leverage the property that 2D simulations downplay the effects of the applied magnetic field to predict whether the magnetic field can still beneficially impact ion acceleration. Fig. 5.4c,bottom shows the transverse component of the electric field experienced by high energy protons in a 2D simulation where we have decreased the magnetic field strength and increased the laser spot size by a factor of 5 ($B_x = 400$ T, 15 μm FWHM; keeping the ratio between the spot size and the Larmor radius roughly fixed). The transition from radially outward to radially inward electric field associated with the electron magnetization occurs later and the focal length is longer in the 400 T case

than the 2000 T case, even when the distances are scaled by a factor of 5 (as in the visual comparison between the top and bottom panels of Fig. 5.4c). However, the transition to a focusing electric field still clearly occurs and the focusing field persists for long enough to visibly alter the direction of the ion momenta, on which basis we expect the benefits of adding the magnetic field to be observable in 3D at experimentally relevant field strengths.

5.4 Discussion

In summary, the net result of adding a strong magnetic field is a magnetic field-directed, magnetic field-focusing ion source of multiple species with enhanced energy and number. The ion acceleration process features a fundamental change in the sheath dynamics mediated by the electron magnetization and occurs in two stages, an initial target normal stage with high energy gain and high divergence driven by electrons which are unmagnetized in the sheath but transversely confined through magnetization in the target, followed by a subsequent stage of ion deflection and focusing in the magnetic field direction driven by magnetized electrons. We term this two stage ion acceleration process magnetized electron sheath acceleration (MESA). We have additionally demonstrated that the benefits of adding the magnetic field are downplayed in 2D simulations, on which basis we predict the relevance of MESA under experimentally relevant conditions.

5.5 Methods

We simulate a relativistically intense laser pulse interacting with the preplasma in front of an opaque plastic (CH) target with and without an applied magnetic field in 2D and 3D geometry using the open source particle-in-cell code EPOCH [71]. The laser pulse has a wavelength of 1.06 μm, is spatially and temporally Gaussian with a 150 fs FWHM duration and a 3 μm FWHM spot size (both given in terms of the intensity), and has a

peak intensity of 2×10^{19} W/cm^2. The preplasma has an exponential profile with a scale length ($1/e$ density falloff) of 1.5 μm. This preplasma scale length was chosen to deliver robust TNSA-dominated acceleration in the case with no applied magnetic field. We model the target as a 5 μm thick slab of fully ionized proton and carbon plasma with electron number density $n_e = 70\, n_{cr}$, where $n_{cr} \equiv m_e \omega_0^2 / 4\pi e^2$ is the critical density associated with the reflection of a laser pulse with frequency ω_0. The plasma is initialized cold. The laser is linearly polarized in the y-plane, propagates in the x-direction, and is focused onto the front target surface. We apply a static uniform magnetic field of $B_0 = 2000$ T at either target normal incidence (0°, $B_x = B_0$) or angled upward at 10° in the x-y plane.

In 3D, the simulation domain is $90 \times 37 \times 24$ μm for the largest simulation, which we resolve with 30 cells/μm in x and 20 cells/μm in y and z. The target rear surface, which we have defined as $x = 0$, is located 25 μm from the simulation boundary. Electrons, protons, and carbon ions are represented by 10, 5, and 5 cubic B-spline macroparticles per cell through most of the domain, with 20 macroparticles per cell for protons and carbon ions within 0.5 μm of the target rear surface to better resolve the ion spectra. The use of high order particle shape such as cubic B-spline has been demonstrated to mitigate numerical heating (for example, in EPOCH [71]), and in our simulations delivers robust energy conservation. The simulation is run until the highest energy protons begin to leave the simulation box. The field and density quantities shown in figures were temporally averaged over 5 laser cycles (18 fs) and spatially averaged over 0.3 μm.

In the 2D simulations we conduct to compare with the 3D cases, the simulation domain is 170×80 μm for the ordinary TNSA ($B_0 = 0$) case. In the cases with a 15 μm spot size, simulation domain is 550×200 μm for the largest simulation ($B_0 = 400$ T), which we resolve with 30 cells/μm in both x and y. In this simulation, the target rear surface, which we have defined as $x = 0$, is located 55 μm from the simulation boundary. Electrons, protons, and carbon ions are represented by 50, 25, and 25 cubic B-spline macroparticles

per cell through most of the domain, with 150 macroparticles per cell for protons and carbon ions within 0.5 μm of the target rear surface. The simulation cost for the 400 T case was approximately the same as the 3D simulations.

5.6 Acknowledgements

Chapter 5, in full, is a reprint of the material as it appears in K. Weichman, J. J. Santos, S. Fujioka, T. Toncian, and A. V. Arefiev, "Generation of focusing ion beams by magnetized electron sheath acceleration", *Scientific Reports*, **10**, 18966 (2020). The dissertation author was the primary investigator and author of the paper.

This research was supported in part by the DOE Office of Science under Grant No. DE-SC0018312. K.W. was supported in part by the DOE Computational Science Graduate Fellowship under Grant No. DE-FG02-97ER25308. J.J.S. acknowledges the support of the "Investments for the future" program IdEx Bordeaux LAPHIA (ANR-10-IDEX-03-02). Particle-in-cell simulations were performed using EPOCH [71], developed under UK EPSRC Grant Nos. EP/G054940, EP/G055165, and EP/G056803. This work used HPC resources of the Texas Advanced Computing Center (TACC) at the University of Texas at Austin and the National Energy Research Scientific Computing Center (NERSC), a U.S. Department of Energy Office of Science User Facility operated under Contract No. DE-AC02-05CH11231. Data collaboration was supported by the SeedMe2 project [117] (http://dibbs.seedme.org).

Chapter 6

Strong surface magnetic field generation in relativistic short pulse laser-plasma interaction with an applied seed magnetic field

6.1 Abstract

While plasma often behaves diamagnetically, we demonstrate that the laser irradiation of a thin opaque target with an embedded target-transverse seed magnetic field B_{seed} can trigger the generation of an order-of-magnitude stronger magnetic field with opposite sign at the target surface. Strong surface field generation occurs when the laser pulse is relativistically intense and results from the currents associated with the cyclotron rotation of laser-heated electrons transiting through the target and the compensating current of cold electrons. We derive a predictive scaling for this surface field generation, $B_{\text{gen}} \sim -2\pi B_{\text{seed}} \Delta x/\lambda_0$ (in the large spot size limit), where Δx is the target thickness and

λ_0 is the laser wavelength, and conduct 1D and 2D particle-in-cell simulations to confirm its applicability over a wide range of conditions. We additionally demonstrate that both the seed and surface-generated magnetic fields can have a strong impact on application-relevant plasma dynamics, for example substantially altering the overall expansion and ion acceleration from a μm-thick laser-irradiated target with a kilotesla-level seed magnetic field.

6.2 Introduction

Relativisitic laser-plasma interaction with applied magnetic fields presents an opportunity to study the effects of magnetic fields in the high energy density regime. Both applied and self-generated magnetic fields can strongly influence plasma behavior, and make laser-plasma a convenient platform both for investigating the fundamental physics of magnetized plasmas, for example laboratory astrophysics [6, 7, 9], and for exploring potential improvements to laser-plasma applications, such as inertial fusion energy [14–16].

Plasma has a reputation for being diamagnetic and often acts to exclude magnetic fields. However, in the laser-plasma context, there is growing interest in scenarios where laser-plasma interactions have the potential to self-generate strong magnetic fields or to amplify weak applied magnetic fields [43, 54, 145–148]. Such an objective is desirable to augment experimentally available magnetic fields from laser-driven coil [23–26] or pulsed power sources [27–29] and push the study of magnetized high energy density physics into new regimes. Most of the previous work has relied on instability-seeded growth [6, 148], flux compression [54], or circularly polarized or Laguerre-Gaussian [145, 149] laser pulses, which limits these laser-driven magnetic field generation techniques to specific experimental facilities. However, it has recently been shown that the more ubiquitous Gaussian linearly polarized laser pulses also have the potential to amplify a target-normal seed magnetic

field in a thin overdense (i.e. opaque) target [150].

In this work, we demonstrate that an embedded target-transverse magnetic field can also trigger the generation of a strong surface magnetic field lasting longer than the pulse duration. We find that the generation of a non-azimuthal large-amplitude magnitude field at the rear target surface results from the localized production of electrons at the laser-irradiated surface and requires relativistic laser intensity. We additionally construct a predictive scaling based on the physical processes driving the magnetic field generation. This scaling is robust over a wide range of laser and target conditions.

We further demonstrate the validity of our predictive scaling and the importance of surface magnetic field generation in applications. As an example, we consider the effect of the seed and surface-generated magnetic fields on the dynamics of target expansion and ion acceleration from a laser-irradiated target. Both the applied and plasma-generated fields can become sufficiently large to modify ion acceleration from the target surfaces. As we will demonstrate, the surface-generated magnetic field can become sufficiently strong to restrict the expansion of the rear target surface. Meanwhile, the seed field can facilitate ion acceleration from the laser-irradiated surface, in some cases even causing the front-surface acceleration to outperform the rear-surface acceleration.

The outline of this paper is as follows. In Section 6.3, we conduct 1D simulations and demonstrate that strong surface field generation is tied to cyclotron rotation of the hot and cold electron return currents generated by laser-plasma interaction in an embedded magnetic field. In Section 6.4, we estimate the magnitude of the rear surface field and show that the surface field generation is robust over a wide parameter range. In Section 6.5, we demonstrate with 1D and 2D simulations that the generation of strong surface fields can initiate electron confinement near the target surfaces and that this confinement can strongly impact the expansion and acceleration of ions from a laser-irradiated target. In Section 6.6, we summarize and discuss possible extensions of this work.

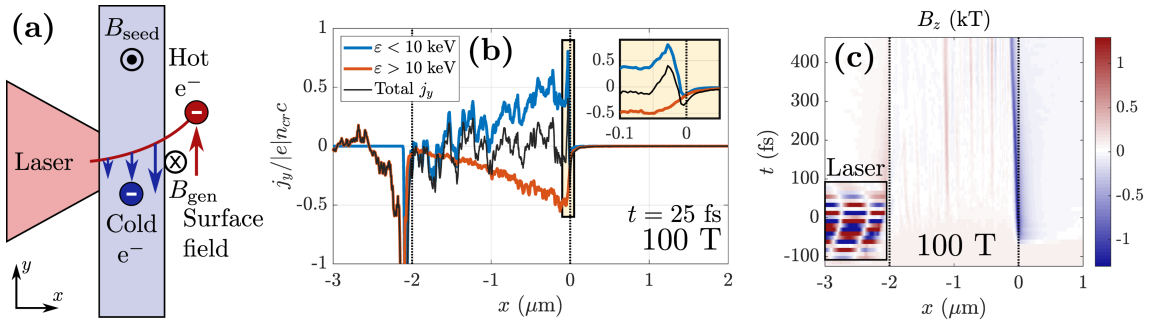

Figure 6.1: Surface magnetic field generation in laser-irradiated targets. (a) Hot electrons streaming through the target gain transverse momentum in the presence of B_{seed}, inducing a counter-streaming current in the cold target population and generating a surface magnetic field. (b) Current density j_y generated by electrons in 1D PIC simulation, $B_{\text{seed}} = 100$ T. Inset: current near the target rear surface. The spike near the front surface is associated with electron motion in the laser and does not contribute significantly to the time-averaged magnetic field generation. (c) Surface-tangent magnetic field B_z generated in 1D PIC simulation with $B_{\text{seed}} = 100$ T. The pattern associated with the laser at the front surface (black box) is an artifact of the time averaging (see Table 6.1) and the data output frequency. Dotted lines in (b) and (c) indicate the initial target surfaces.

6.3 Surface magnetic field generation

In this Section, we will discuss how laser-irradiation of an opaque target with an embedded target-transverse magnetic field is able to produce strong surface magnetic fields. We will initially demonstrate this using 1D particle-in-cell simulations.

We simulate a relativisitcally intense laser pulse interacting with a plastic (CH) target with an embedded target-transverse magnetic field. We conduct collisionless simulations using the open-source particle-in-cell code EPOCH [71]. The target is represented by a quasineutral CH plasma with a short scale length preplasma and peak density $n_e = 50\, n_{cr}$, where $n_c = 1.75 \times 10^{21}$ cm^{-3} is the critical density corresponding to the laser wavelength. The simulation parameters for our nominal case are given in Table 6.1. The simulation setup is shown schematically in Fig. 6.1.

We observe the generation of surface magnetic fields with 10-15 times the magnitude of the original seed (for example, Fig. 6.1c). In 1D simulations, the strongest field is generated at the rear target surface ($x = 0$) and a weaker field of opposite sign is generated

Table 6.1: Nominal 1D PIC simulation parameters. The initial plasma temperature is set as zero. The simulation setup is shown schematically in Fig. 6.1a.

Laser parameters	
Wavelength	$\lambda_0 = 0.8$ μm
Peak intensity	1×10^{19} W/cm^2
Duration (Gaussian, electric field FWHM)	100 fs
Laser propagation direction	$+x$
Laser polarization	y
Other parameters	
Seed magnetic field ($\mathbf{B} = B_{\text{seed}}\hat{\mathbf{z}}$)	$B_{\text{seed}} = 100$ T
Target thickness	$\Delta x = 2$ μm
Preplasma scale length (1/e dropoff)	0.1 μm
Peak electron density	$n_e = 50\, n_{cr}$
Preplasma density cutoff (minimum)	$0.05\, n_{cr}$
Spatial resolution	200 cells/λ_0
Macroparticles per cell, electron	400
Macroparticles per cell, ion	200
Time interval for averaging B_z in figures	10 fs
Position and time reference	
Location of the rear of the foil	$x = 0$
Time when peak of laser would reach $x = 0$	$t = 0$

near the laser-irradiated surface ($x = -2$ μm). These fields rise quickly (on the order of the 100 fs pulse duration) and persist for hundreds of femtoseconds after the laser pulse has been fully reflected by the target. In the rest of this work, we will focus primarily on the rear-surface field. Unlike the front surface field, the rear surface field can have high amplitude and is also present in higher dimensional simulations (e.g. Sec. 6.5).

The rear-surface field is produced as a consequence of the cyclotron rotation of the laser-heated and cold (return current) electrons propagating through the target. As shown both schematically and quantitatively in Fig. 6.1, the current which creates this field can be separated into contributions from the hot and cold electron populations.

We choose the division between hot and cold in Fig. 6.1 to be 10 keV to fully capture the contribution of each population. However, in spite of this seemingly low energy, we do not expect collisions (which are not included in our simulations) to disrupt the surface magnetic field generation. The small angle collisional scattering time ($1/\nu_{ei}$) is approximately

$$\begin{aligned} 1/\nu_{ei} &\approx \frac{m_e^2 v_0^3}{8\pi Z^2 e^4 n_i} \left(\ln \frac{m_e v_0^2}{2Ze^2 n_i^{1/3}} \right)^{-1} \\ &= 1.3\,\mathrm{ns} \cdot \frac{(v_0/c)^3}{Z^2} \left(11 + \ln \frac{(v_0/c)^2}{Z} \right)^{-1}, \end{aligned} \tag{6.1}$$

where v_0 is the velocity of hot electrons, Z is the charge state of the ions, in the Coulomb logarithm ($\ln r_{\max}/r_{\min}$) we have approximated $r_{\max}$ by the ion spacing $n_i^{-1/3}$, and in the second expression we have used $n_i = n_e/7 = 1.25 \times 10^{22}$ cm^{-3}. The majority of the hot electron current is carried by electrons with energy above 25 keV ($v_0/c \sim 0.3$), which corresponds to a small angle collisional scattering time for carbon ions ($Z = 6$) of approximately 150 fs. This is much longer than both the transit time of the electron through the target and the rise time of the surface magnetic field (both ~ 30 fs).

The transverse currents responsible for the surface magnetic field generation are

driven by the travel of hot electrons through the magnetized target. Hot electrons are generated at the front target surface by the interaction of the laser with the preplasma. These electrons then stream through the target with a net $+x$-directed velocity, during which time the embedded $+z$-directed seed magnetic field B_{seed} rotates their momentum such that they exit the rear target surface carrying a net transverse current $j_y < 0$ (red line in Fig. 6.1b). In response, the cold electrons in the target obtain a compensating $j_y > 0$ which prevents the embedded magnetic field from decreasing (blue line in Fig. 6.1b). However, only hot electrons are able to enter the rear target sheath, resulting in an uncompensated current in the sheath (hot electrons) and in response at the rear surface (cold electrons), as shown in the inset in Fig. 6.1b. This current double layer generates a strong magnetic field at the rear target surface (Fig. 6.1c). This magnetic field persists for as long as the physical configuration of hot electrons streaming through a cold electron background persists, which exceeds the laser pulse duration (see also Sec. 6.5).

The localized production of electrons near the target surface and the initial magnetization of the target are both crucial to the high amplitude surface magnetic field generation. Such a large surface field is produced because electrons undergo cyclotron rotation during the course of their transit of the target. This will be shown directly by the estimate for the rear surface magnetic field we construct in the following Section.

6.4 1D scaling of rear surface magnetic field

In this Section, we obtain a qualitative picture for cyclotron rotation-mediated surface field generation. We will additionally demonstrate the robustness of the field generation mechanism in 1D simulations to the choice of laser intensity, target thickness, and the strength of the seed magnetic field and predict an optimum range for field generation. Over a large range of parameters, we find that the surface field is well-predicted by a simple

scaling.

The rear surface return current arises to screen the target from the hot electron current in the sheath and has approximately equal magnitude to the sheath current. We estimate the sheath current density as

$$j_y \sim -|e| v_y n_s, \tag{6.2}$$

where n_s is the number density and v_y is the average y-directed velocity of hot electrons entering the sheath. v_y is produced by the rotation of the electron momentum during the transit of the target. Given that the magnetic field within the target remains approximately equal to the applied field ($B_z \approx B_{\text{seed}}$), and assuming the electrons are relativistic with longitudinal (x-directed) velocity $v_x \sim c$, the transverse velocity is approximately

$$v_y \sim v_x \sin\left(\frac{\omega_{c0}}{\gamma}\Delta t\right) \sim \frac{|e| B_{\text{seed}} \Delta x}{\gamma m_e c}, \tag{6.3}$$

where $\omega_{c0} \equiv |e| B_{\text{seed}}/m_e c$ is the non-relativistic cyclotron frequency associated with B_{seed}, Δx is the target thickness, γ is taken as a characteristic value for the hot electrons, and we have assumed the overall momentum rotation is small ($\omega_{c0}\Delta t/\gamma \ll 1$).

We now estimate the magnetic field generated by this current. The sheath size is approximately given by the electron Debye length, $\lambda_{De} \equiv \sqrt{T_e/4\pi e^2 n_s}$. For a relativistic plasma, we have $T_e \approx (\gamma - 1) m_e c^2$, which we substitute in the Debye length to give $\lambda_{De} \approx \sqrt{(\gamma-1) m_e c^2/4\pi e^2 n_s}$. Approximating the current density as constant over λ_{De}, the magnetic field generated at the target surface is approximately $B_{\text{gen}} \sim 4\pi j_y \lambda_{De}/c$. Combining this with Eqs. (6.2) and (6.3), the magnetic field generated at the rear target

surface can be approximated as

$$\frac{B_{\text{gen}}}{B_{\text{seed}}} \sim -\sqrt{\frac{4\pi\left(\gamma-1\right)e^2 n_s \Delta x^2}{\gamma^2 m_e c^2}} \approx -\frac{\Delta x}{\lambda_{De}}, \tag{6.4}$$

where the last expression assumes the plasma is sufficiently relativistic that $\gamma - 1 \approx \gamma$.

The surface magnetic field generation is inherently a kinetic effect and can be thought of as an overshoot of the diamagnetic effect. This can be seen directly through an alternate approach to deriving this equation. The diamagnetic effect occurs when charged particles undergo cyclotron motion in a magnetic field which results in a net current that acts to reduce the field. Normally, the cyclotron motion and the net current are co-located, i.e. the rotation of the charged particles occurs in the same spatial region as the net current. This is the only possibility if the plasma is described as a single fluid in lieu of a kinetic description. However, the target we consider is conductive and inhibits changes to the embedded magnetic field. Although hot electrons undergo rotation in the target, they are only able to generate a magnetic field in the sheath. This magnetic field grows until the plasma-generated field in the sheath is able to undo the momentum rotation of electrons transiting the target, based on which we expect

$$\frac{\omega_{c1}\Delta t_s}{\gamma} \approx \frac{\omega_{c0}\Delta t}{\gamma}, \tag{6.5}$$

where ω_{c1} is the non-relativistic cyclotron frequency associated with B_{gen} and Δt_s is the time the electron spends in the sheath. Assuming the electron motion is relativistic and $\Delta t_s \sim \lambda_{De}/c$, Eq. (6.5) gives the same result as Eq. (6.4). This analysis also confirms what we stated at the end of Sec. 6.3: the localized production of hot electrons at the front target surface and the embedded magnetic field are both key to producing a strong rear surface field.

6.4.1 Estimate for sheath density in a laser-irradiated target

As written, Eq. (6.4) involves the sheath density n_s and the characteristic hot electron γ-factor, both of which should in principle be measured from simulations. However, to obtain a simple predictive scaling, we now specifically consider the case of a short scale length preplasma (scale length $<$ laser wavelength) and a reasonably short laser pulse (~ 100 fs). Under these conditions, we estimate the sheath density as roughly $n_s \sim \gamma n_{cr} \sim a_0 n_{cr}$.

The origin of this estimate can be seen straightforwardly by considering the transfer of laser energy into hot electrons in the short scale length preplasma. In what follows, we predict the hot electron density which can be produced by the transfer of laser energy to hot electron energy over half of a laser cycle. This model is expected to capture the approximate magnitude of the hot electron density, and was motivated by the success of other single-cycle-based models, for example, the vacuum heating model developed in Ref. 151.

The maximum number of electrons the laser can interact with and accelerate in half a laser cycle can be estimated from the condition where the laser transfers a substantial fraction of its energy to electrons. In 1D this energy balance is given by

$$\begin{aligned}(\gamma - 1)\, m_e c^2 N &\simeq \frac{c}{8\pi\omega_0} \int_0^\pi \left(E^2 + B^2\right) \mathrm{d}\left(\omega_0 t\right) \\ &= \frac{E_0^2 c}{8\omega_0} = a_0^2 \frac{m_e^2 c^3 \omega_0}{8e^2},\end{aligned} \tag{6.6}$$

where N is the number of electrons the laser accelerates per unit area during the half-cycle and $a_0 \equiv |e|E_0/m_e c\omega_0$ is the normalized vector potential for the laser pulse with maximum amplitude E_0 and frequency ω_0. The maximum number density of hot electrons streaming

through the target into the sheath for this half-cycle is thus approximately

$$n_s^{\text{half}} \lesssim 2N/\beta\lambda_0 = \frac{a_0^2}{\beta\,(\gamma-1)}\frac{n_{cr}}{2}, \tag{6.7}$$

where we have divided N by $\beta\lambda_0/2$ with $\beta = v/c$ to approximate the hot electrons being distributed within the target over the full half-cycle. This may introduce an underestimate for the density as the electrons are often observed to be more strongly bunched (for example, in Ref. 101).

For a sufficiently short laser pulse and preplasma scale length, it is well established that the electron energy roughly follows the ponderomotive scaling regardless of the exact acceleration mechanism [98, 99, 101, 152]. In this parameter regime, long pulse effects such as stochastic heating [32, 94] are not important. In the ponderomotive limit, and the limit where $a_0^2 \gg 1$, we have

$$\gamma \approx \sqrt{1+a_0^2} \approx a_0, \tag{6.8}$$

which gives the hot electron density which can be produced in a half laser cycle as

$$n_s^{\text{half}} \lesssim \frac{\sqrt{1+a_0^2}}{\sqrt{1+a_0^2}-1}\frac{a_0 n_{cr}}{2} \approx \frac{a_0 n_{cr}}{2}. \tag{6.9}$$

While Eq. (6.9) represents the maximum transfer of laser energy to hot electrons in a single half-cycle, we still expect the prediction it provides to retain the correct order of magnitude even when electrons can undergo multiple interactions with the laser pulse. That is, we expect the sheath density to be given by

$$n_s \sim \eta\frac{a_0 n_{cr}}{2} \sim a_0 n_{cr}, \tag{6.10}$$

where we have introduced the factor η to account for the possibility hot electrons may obtain more net energy than the half-cycle estimate suggests and to provide a fitting parameter for the simulation results. The approximation $n_s \sim a_0 n_{cr}$ in Eq. (6.10) leads to a good fit for the predicted magnetic field. This estimate is also consistent with the expectation that the laser interacts with electrons in a preplasma up to the relativistically adjusted critical density (γn_{cr}).

Equation (6.10) represents a 1D estimate, which we expect to be consistent with higher dimensional simulations in the limit that the laser spot size is sufficiently large. For smaller laser spot size, Eq. (6.10) can be extended to multidimensional geometry by incorporating the effect of the transverse expansion of hot electrons on the sheath density. Following the geometric expansion model employed, for example, in Ref. 153, we consider the hot electron population to expand with a characteristic angle α, where typically $\alpha \sim 25-45^\circ$ (e.g. Refs. 22, 44, 153). In this model, the hot electron population generated within the laser spot FWHM w_0 at the front surface expands to a larger diameter $w_0 + 2\Delta x \tan\alpha$ at the back surface. For a D-dimensional simulation, we thereby approximate the hot electron density within the sheath as

$$n_s(D) \sim a_0 n_{cr} \left(\frac{w_0}{w_0 + 2\Delta x \tan\alpha} \right)^{D-1} \sim \frac{a_0 n_{cr}}{\left(1 + \dfrac{2\Delta x}{w_0} \right)^{D-1}}, \tag{6.11}$$

where the final expression approximates $\tan\alpha \sim 1$.

6.4.2 Scaling and limit on maximum generated field strength

For the case of a short scale length preplasma and a reasonably short laser pulse, we therefore take Eqs. (6.8) and (6.11) as order-of-magnitude estimates for γ and n_s in Eq. (6.4), based on which we expect the strength of the generated magnetic field in a

D-dimensional simulation to scale as roughly

$$\begin{aligned}\frac{B_{\text{gen}}}{B_{\text{seed}}} &\sim -\sqrt{\frac{4\pi e^2 n_{cr}\Delta x^2}{m_e c^2\left(1+\frac{2\Delta x}{w_0}\right)^{D-1}}} \\ &\sim -\sqrt{\frac{4\pi e^2 n_{cr}\Delta x^2}{m_e c^2}} = -\frac{2\pi\Delta x}{\lambda_0},\end{aligned} \tag{6.12}$$

where the second line represents the large spot size limit ($\Delta x/w_0 \to 0$). We will consider a perfectly 1D case for the remainder of this Section. The effects of 2D geometry and finite spot size are discussed in more detail in Sec. 6.5).

We now additionally estimate the maximum surface magnetic field which can be produced. While Eq. (6.12) provides a good prediction of the generated magnetic field strength over a wide range of conditions (see Fig. 6.2), this scaling breaks down if the seed magnetic field is sufficiently strong for electrons to undergo a significant fraction of a cyclotron rotation within the target. We roughly estimate the maximum surface magnetic field which can be produced by estimating $v_y \sim c$, which occurs when the target thickness is equal to the Larmor radius $\rho_e \equiv cp_x/|e|B_{\text{seed}}$. Estimating $cp_x \sim \sqrt{\gamma^2-1}m_e c^2$ and setting $\rho_e = \Delta x$ gives

$$B^*_{\text{seed}} \sim \frac{\sqrt{\gamma^2-1}m_e c^2}{|e|\Delta x} \approx \frac{a_0 m_e c^2}{|e|\Delta x}, \tag{6.13}$$

where we have approximated $\sqrt{\gamma^2-1} \approx a_0$ as discussed in Sec. 6.4.1. The maximum amplitude of the magnetic field that can be generated is roughly (employing $v_y \sim c$ in Eq. (6.2) and retaining $B_{\text{gen}} \sim 4\pi j_y \lambda_{De}/c$),

$$B^*_{\text{gen}} \sim -\sqrt{4\pi\gamma n_s m_e c^2} \approx -a_0\sqrt{4\pi n_{cr} m_e c^2}. \tag{6.14}$$

For a 0.8 μm laser wavelength and a 2 μm thick target, we therefore predict the maximum magnetic field amplitude that can be generated to be $B^*_{\text{gen}} \approx 13\,a_0$ kT occurring

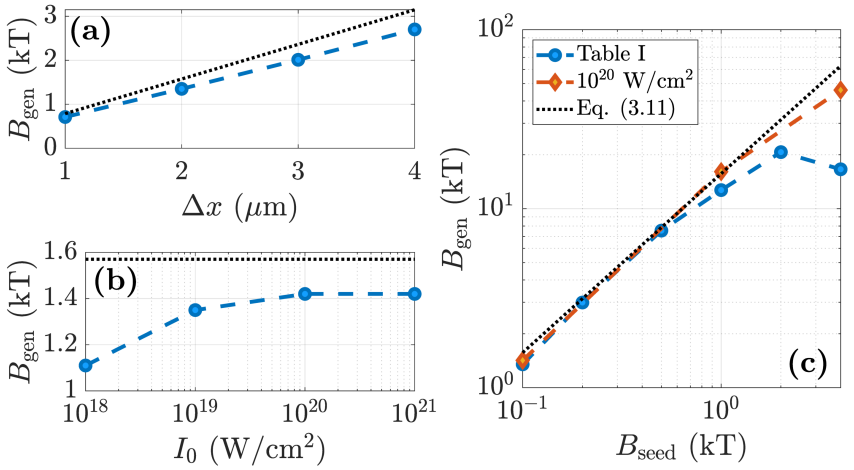

Figure 6.2: Maximum rear surface magnetic field in 1D parameter scans. (a) Scan over target thickness. (b) Scan over peak intensity. (c) Scan over seed magnetic field strength. The simulation parameters not scanned over are as given in Table 6.1. The black dotted lines correspond to Eq. (6.12).

at an initial seed amplitude of $B^*_{\mathrm{seed}} \approx 0.85\, a_0$ kT. Due to the nature of the estimate we performed, Eqs. (6.13) and (6.14) are undoubtedly overestimates, nevertheless, they establish the optimum seed magnetic field for surface field generation to be on the order of kT for few-μm-thick targets with $a_0 \lesssim 10$. Such fields are rapidly becoming experimentally relevant [29, 30].

Below B^*_{seed}, based on Eq. (6.12), we expect the plasma-generated magnetic field strength B_{gen} to be insensitive to the laser intensity, and to increase linearly with the target thickness and the seed magnetic field strength. Fig. 6.2 shows how B_{gen} scales with these parameters. Overall, we find good agreement between the predicted scaling and 1D PIC simulation results over a wide range of parameters, including in the approximate magnitude of $|B_{\mathrm{gen}}/B_{\mathrm{seed}}|$, which for the nominal case we predict to be ~ 16 based on Eq. (6.12) and observe in 1D PIC simulation to be 14-16.

The assumptions made to obtain Eq. (6.12) break down if the electron motion becomes sub-relativistic. Correspondingly, we find that the magnitude of the rear surface magnetic field is insensitive to laser intensity for $I_0 \gtrsim 10^{19}$ W/cm^2, but begins to drop

below this threshold as the electron motion in the laser becomes less relativistic, as shown in Fig. 6.2b.

We also find that the magnetic field generation is reduced relative to the prediction of Eq. (6.12) as the seed magnetic field strength approaches B^*_{seed}, corresponding to the regime where the electrons complete a noticeable fraction of a cyclotron rotation within the target. For the parameters given in Table 6.1, when $B_{\text{seed}} \gtrsim 1$ kT, the generated magnetic field begins to deviate from the predicted value based on Eq. (6.12). As shown in Fig. 6.2c, the maximum magnitude of the surface magnetic field is approximately 19 kT corresponding to a seed field of 2 kT. Our observed B^*_{gen} and B^*_{seed} agree with the predictions of Eqs. (6.14) and (6.13) to within a factor of 1.5. For $B_{\text{seed}} \gtrsim B^*_{\text{seed}}$, the generated magnetic field is reduced relative to B^*_{gen}.

As we have discussed, the strongest surface generated magnetic field is produced for $B_{\text{seed}} \sim B^*_{\text{seed}}$. In this regime, both the surface generated and the seed magnetic fields can have a notable and application-relevant effect on the plasma dynamics. In the following section, we consider the effect of the seed and surface-generated magnetic fields on a laser-irradiated target in 2D. For $B_{\text{seed}} \gtrsim B^*_{\text{seed}}$, the magnetic field can substantially alter target expansion and the associated ion acceleration.

6.5 Plasma expansion with a strong applied magnetic field

In this Section, we discuss the regime in which the seed and plasma-generated surface magnetic fields are sufficiently strong to affect the overall expansion of the laser-irradiated target. For $B_{\text{seed}} \gtrsim B^*_{\text{seed}}$, electrons become trapped near the target surfaces, restricting the rear surface expansion and associated ion acceleration. At the same time, the front surface expansion is enhanced, increasing the energy of backward-accelerated ions. For

sufficient B_{seed}, the energy and number of ions accelerated backward by the expanding front surface can exceed those accelerated from the rear surface, an unusual situation for thin laser-irradiated targets with a preplasma [154].

In Sections 6.3 and 6.4, we conducted 1D simulations to illustrate the magnetic field generation process. However, 1D geometry neglects higher-dimensional effects such as the finite laser spot size and the transverse escape of electrons, which in more realistic (e.g. 2D) simulations can affect the magnitude and duration of the surface field. The finite spot size also leads to the generation of azimuthal magnetic fields [22, 44, 147] which could potentially compete with the $-z$-directed non-azimuthal surface magnetic field generation.

First, we demonstrate using 2D simulations that the surface magnetic field generation can disrupt the development of the usual rear-surface azimuthal field and can produce a stronger, non-azimuthal magnetic field at the rear target surface. Sufficiently strong azimuthal magnetic fields have been shown to impair ion acceleration via target normal sheath acceleration [22]. Second, we demonstrate that the presence of the seed magnetic field and the generation of the non-azimuthal surface field can exacerbate this effect. While the rear-surface expansion can be dramatically reduced, the front-surface expansion is enhanced and can even produce higher accelerated ion number than ordinary ($B_{\text{seed}} = 0$) rear-surface target normal sheath acceleration (TNSA).

6.5.1 Surface field generation in 2D simulations

We conduct 2D simulations with a finite laser spot size of 3 μm FWHM (Gaussian, electric field) and peak intensity $I_0 = 10^{19}$ W/cm^2. Additional parameters which differ from the 1D simulations of Secs. 6.3 and 6.4 are given in Table 6.2. We begin with the case of $B_{\text{seed}} = 0$ (no applied magnetic field). As the laser-heated electrons stream through the target, they generate an azimuthal field with maximum magnitude of approximately 3.8 kT (Fig. 6.3a). This field is associated with the outward radial streaming of electrons

Table 6.2: Nominal 2D PIC simulation parameters with a planar target which differ from the 1D parameters given in Table 6.1. The number of macroparticles per cell for the ions is increased to 120 within 0.2 μm of rear surface.

Laser parameters	
Spot size (Gaussian, electric field FWHM)	$w_0 = 3\ \mu$m
Other parameters	
Seed magnetic field ($\mathbf{B} = B_{\text{seed}}\hat{\mathbf{z}}$)	$B_{\text{seed}} = 1$ kT
Spatial resolution	50 cells/λ_0
Macroparticles per cell, electron and ion	60
Size of simulation box ($x \times y$, μm)	35×70
Time interval for averaging B_z in figures	20 fs

in the sheath [44].

For $B_{\text{seed}} > 0$, the angular distribution of electrons entering the sheath is altered by the cyclotron rotation of electrons in the target. The magnetic field resulting from this offset becomes evident if B_{seed} is sufficiently large to produce B_{gen} at least comparable to the peak azimuthal magnetic field of the $B_{\text{seed}} = 0$ case. We can roughly estimate the minimum value of B_{seed} needed to produce a visible B_{gen} by considering the case when the cyclotron rotation in the target becomes comparable to the characteristic divergence angle α of hot electrons, i.e. $\rho_e \sin\alpha = \Delta x$. As mentioned in Sec. 6.4.1, $\alpha \sim 25 - 45^\circ$ such that $\sin\alpha \sim 1/2$, which implies that in general surface magnetic field generation will be observed in 2D and 3D geometry when

$$B_{\text{seed}} \gtrsim \frac{B^*_{\text{seed}}}{2} \sim \frac{a_0 m_e c^2}{2|e|\Delta x}, \tag{6.15}$$

where B^*_{seed} is the seed field where we predict the generated field to be maximized (Eq. 6.13).

The prediction of Eq. 6.15 is in fairly good agreement with simulations. We observe that a seed field of at least 500 T is needed to substantially modify the surface field profile and increase the (negative) magnetic field amplitude relative to the $B_{\text{seed}} = 0$ case. As B_{seed} is increased, the azimuthal magnetic field at the rear target surface is suppressed and

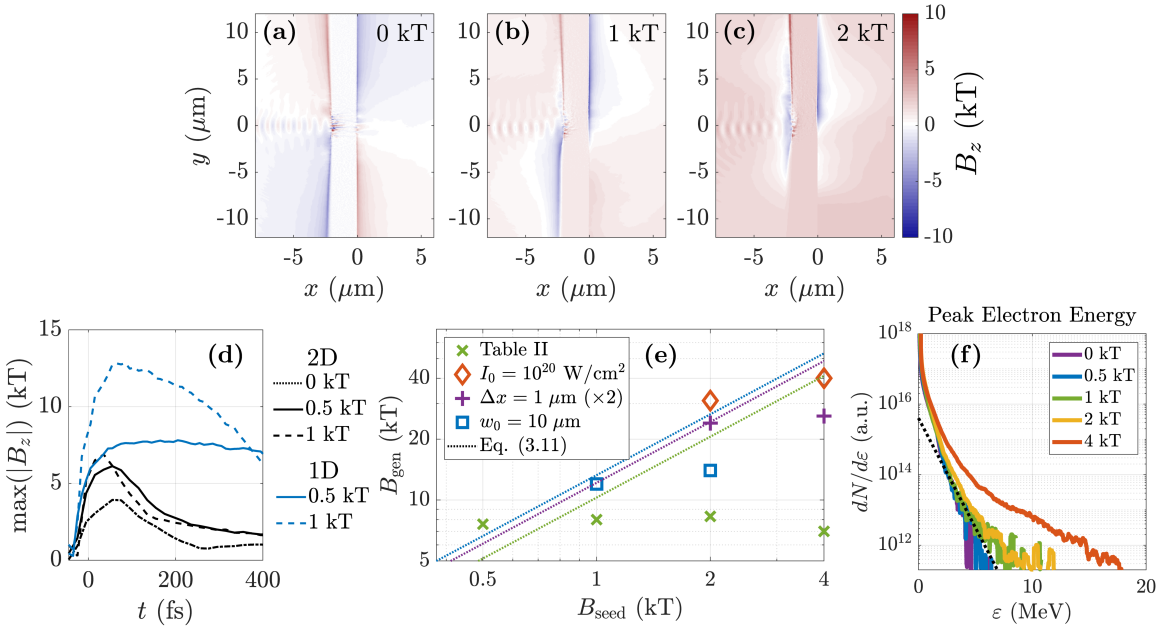

Figure 6.3: Surface magnetic field generation in 2D PIC simulations. (a)-(c) Magnetic field profile at $t = 75$ fs for scan over B_{seed} with other parameters as given in Table 6.2, (a) without an applied magnetic field, (b) with $B_{\text{seed}} = 1$ kT, and (c) with $B_{\text{seed}} = 2$ kT. (d) Temporal evolution of the magnitude of the surface field in 2D and corresponding 1D simulations. Parameters other than B_{seed} are as given in Tables 6.2 and 6.1. (e) Peak surface magnetic field in parameter scans. The legend indicates parameters which differ from the setup given in Table 6.2. Colored dotted lines represent the prediction of Eq. (6.12) corresponding to each of the cases shown with colored markers. The results with $\Delta x = 1$ μm and the purple line have been multiplied by a factor of 2 for the sake of comparison. The prediction for $I_0 = 10^{20}$ W/cm^2 (red) is the same as for Table 6.2 (green). (f) Electron energy spectrum in scan over B_{seed} (other paramters as given in Table 6.2). Dotted line: pondermotive temperature $T_p = 0.7$ MeV.

eventually overcome by the non-azimuthal surface field generation (e.g. Figs. 6.3b,c). As the field profile becomes more non-azimuthal, the generated magnetic field saturates at a peak value of approximately -7 kT for $B_{\text{seed}} \gtrsim 500$ T (Fig. 6.2c). This value is roughly 2 times the peak magnetic field produced in the $B_{\text{seed}} = 0$ case.

As we would expect based on the ability of electrons to move transversely in multidimensional simulations, the magnitude of the magnetic field in 2D simulations is somewhat lower than what we observe in 1D (e.g. Fig. 6.3d). The transverse motion of hot electrons also causes the field to drop more rapidly in 2D than in 1D (FWHM ~ 150 fs in 2D vs ~ 400 fs in 1D for the $B_{\text{seed}} = 1$ kT cases). In 2D, the surface magnetic field persists over roughly the same duration as the azimuthal magnetic field which is produced in the $B_{\text{seed}} = 0$ case (Fig. 6.3d). The magnitude and duration of the surface field should in the future be revisited with 3D simulations.

In 2D simulations, the value of B_{seed} needed to modify the surface magnetic field and the saturation value of B_{gen} depends on the peak laser intensity, the target thickness, and to a lesser extent the laser spot size. We have conducted additional simulations with, separately, $I_0 = 10^{20}$ W/cm^2, $\Delta x = 1$ μm, and $w_0 = 10$ μm (Fig. 6.3e). The maximum amplitude of the azimuthal magnetic field produced in the $B_{\text{seed}} = 0$ case varies with these parameters due to changes in the hot electron population streaming through the rear target surface, as does the minimum B_{seed} required for the surface field to become non-azimuthal. At the value of B_{seed} where B_{gen} becomes distinctly visible (left-most points in Fig. 6.3e), the generated surface field is generally in good agreement with the prediction of Eq. (6.12). In all cases, B_{gen} saturates at approximately this value, which is approximately 2 times the peak magnetic field produced with $B_{\text{seed}} = 0$. In the remainder of this work, we will analyze the case given in Table 6.2.

In principle, the application of a seed magnetic field may also increase the electron energy if the magnetic field is sufficiently strong to rotate the electron momentum towards

the laser polarization direction during direct laser acceleration [120], which could affect the generated surface field. However, for $B_{\text{seed}} \lesssim 2$ kT, the seed field does not substantially change the number of accelerated electrons or the bulk of the electron energy spectrum (Fig. 6.3f). For $B_{\text{seed}} \lesssim 1$ kT, the hot electron temperature remains in good agreement with the ponderomotive scaling [101] ($T_p = [(1+a_0^2)^{1/2} - 1]m_e c^2 \approx 0.7$ MeV, black dotted line in Fig. 6.3f), and only a slight increase in the energy of the hottest part of the spectrum occurs for $B_{\text{seed}} \leq 2$ kT. As the seed magnitude is further increased to $B_{\text{seed}} = 4$ kT, the electron is substantially increased. However, at this seed amplitude the Larmor radius is smaller than the target thickness and electrons can be prevented from transiting all the way through the target (see Section 6.5.2), and the surface field generation is actually reduced.

6.5.2 Effect on target expansion and ion acceleration

In the regime we are considering, both the seed and surface-generated magnetic fields can become sufficiently strong to inhibit the transport of electrons, resulting in electron trapping near the target surfaces and altering the target expansion and ion acceleration process. To illustrate the effect of this trapping on the hot and return current electrons, we divide electrons into three populations based on their energy. For convenience, we perform this analysis based on 1D simulations. When the applied magnetic field is below the kilotesla level (e.g. $B_{\text{seed}} = 100$ T in Fig. 6.4a), the electrons in all three energy bins become uniformly distributed throughout the target. However, with a 1 kT applied field (e.g. Fig. 6.4b), only the high energy electrons ($\varepsilon > 100$ keV) become uniformly distributed. Electrons in the low energy bin ($\varepsilon < 10$ keV) show a significant buildup at the rear target surface, while those in the middle energy bin (10 keV$< \varepsilon <$ 100 keV) are trapped near the front surface.

While the front surface trapping can be attributed to the strong seed magnetic field preventing the transit of moderate energy electrons through the target (which have a

Larmor radius comparable to the target thickness), the rear surface buildup of electrons is more surprising. In the usual target normal sheath acceleration case with $B_{\text{seed}} = 0$, the transit of hot electrons through the target and compensating return current lead to the development of a thin ion-dominant layer at the rear target surface. With no applied magnetic field or with a weak applied magnetic field, this ion layer is rapidly accelerated by the hot electron sheath, quickly reducing, but not entirely eliminating, the charge separation and associated electric field (Fig. 6.4e). In this case, hot electrons remain free to transit the target and provide a continual acceleration of ions from the rear target surface as the target expands (e.g. Fig. 6.4c).

However, when the seed magnetic field is sufficiently strong ($B_{\text{seed}} \gtrsim 1$ kT), the plasma-generated magnetic field in the rear sheath becomes comparable in strength to the sheath electric field (green contour in Fig. 6.4f), substantially altering the motion of electrons within the sheath and terminating the acceleration of ions from the target (Fig. 6.4d). This leads to a maintained ion density spike at the rear target surface, which eventually acts to attract the surrounding cold electrons, producing the density spike in the cold electron population seen in Fig. 6.4b.

This surface trapping has several consequences. First, from a modeling perspective, the localized production of electrons near the front target surface is a critical component of accurately modeling the surface trapping. Care must be taken in simulations of target expansion which substitute hot electrons for the laser-plasma interaction [155, 156] to account for this spatial localization. We have demonstrated in Section 6.4 that the initial spatial localization of hot electrons plays a substantial role in the generation of strong, asymmetric surface magnetic fields, and in this section we have shown that electrons do not eventually become uniformly distributed through the target in the presence of a strong seed field.

Second, the termination of target expansion as the sheath magnetic field begins to

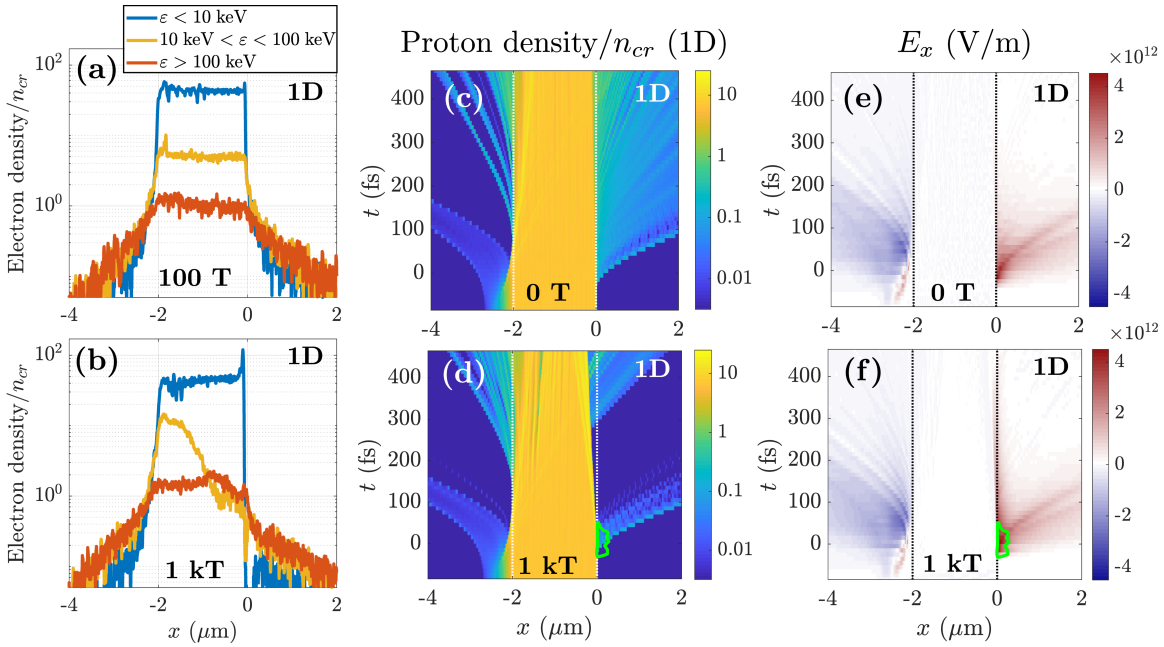

Figure 6.4: Modification of target expansion in 1D simulations by applied magnetic field. (a),(b) Electron trapping near surfaces with (a) $B_{\text{seed}} = 100$ T, and (b) $B_{\text{seed}} = 1$ kT, at $t = 175$ fs. (c)-(f) Target expansion with (c),(e) $B_{\text{seed}} = 0$, and (d),(f) $B_{\text{seed}} = 1$ kT. (c),(d) Proton density. (e),(f) Electric field E_x. With $B_{\text{seed}} = 1$ kT, the rear surface expansion is terminated following the initial burst of ion acceleration once $|E_x|$ drops below $|B_z|$ (green contours in (d) and (f) denote where $|E_x|$ equals the maximum surface magnetic field magnitude at that time). Dotted lines in (c)-(f) denote initial target position.

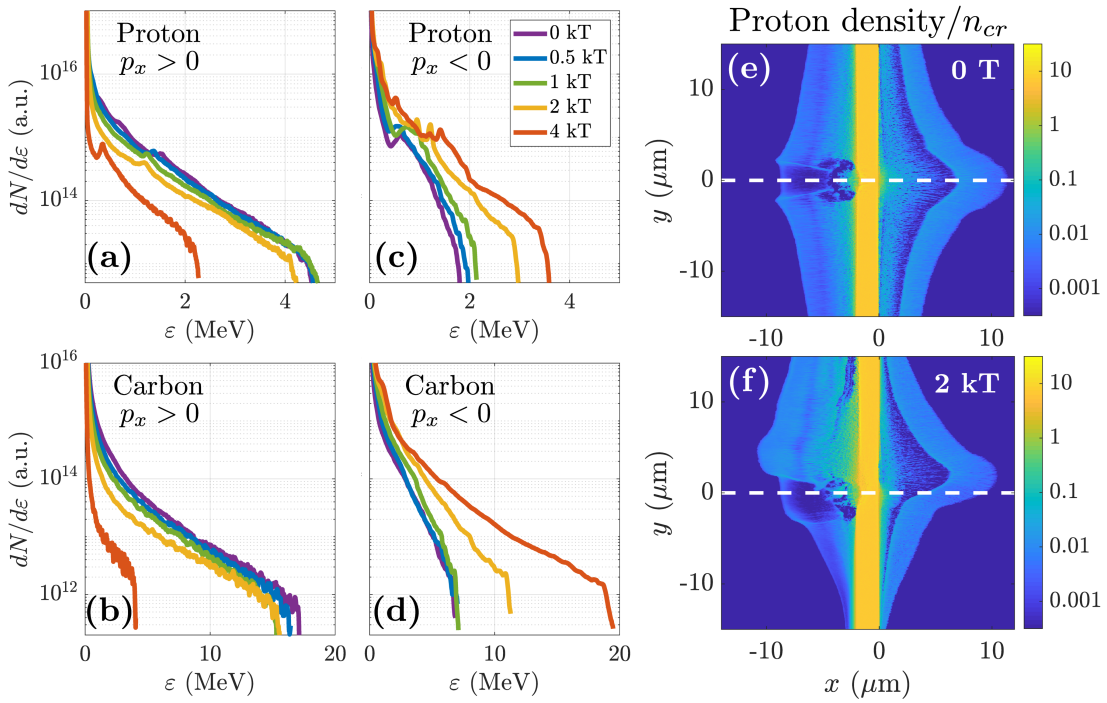

Figure 6.5: Modification of target expansion and ion energy in 2D PIC simulations by applied magnetic field. Ion energy spectra for (a),(c) protons and (b),(d) carbon ions. (a),(b) Ions accelerated in the $+x$-direction, corresponding to ordinary rear-surface TNSA. (c),(d) Ions accelerated in the $-x$-direction from the laser-irradiated surface. Spectra were evaluated at $t = 430$ fs; the cutoff energy changes by less than 10% over the preceding 100 fs for all cases. (e),(f) Proton density at $t = 430$ fs for (e) $B_{\text{seed}} = 0$, and (f) $B_{\text{seed}} = 2$ kT. The dashed line indicates the laser axis.

dominate over the electric field can substantially reduce the energy of ions accelerated from the rear surface. As shown for our 2D simulations in Figure 6.5a,b, both the peak energy and the total number of accelerated ions with momentum $p_x > 0$ are strongly impacted by adding a seed magnetic field of $B_{\text{seed}} \gtrsim 2$ kT.

At the same time, we observe a substantial increase in the energy and number of ions accelerated from the front surface ($p_x < 0$; Fig. 6.5c,d). This increased ion acceleration is attributable to the trapping and deflection of moderate energy electrons near the front surface. Ordinarily, i.e. with $B_{\text{seed}} = 0$, ion acceleration from the front surface is suppressed by the radiation pressure exerted by the laser pulse, which initially causes front surface ions to be drawn into the target. This visibly digs a hole in the accelerated ion density

on the laser axis (Fig. 6.5e). However, for $B_{\text{seed}} > 0$, the hot electron cloud formed by the laser pulse is deflected transversely away from the laser axis and can accelerate ions from outside the laser spot (Fig. 6.5f). This deflection, combined with the electron trapping near the front surface (e.g. Fig 6.4b) enhances the ion acceleration from the front surface. For the 4 kT seed field, the ion energy may also be increased by the increased electron energy (see Fig. 6.3f). In this case, the carbon energy and number are enhanced beyond the $B_{\text{seed}} = 0$ value (Fig. 6.5d).

6.6 Summary

We have shown that laser-irradiated targets with an embedded target-transverse magnetic field do not behave purely diamagnetically when the laser is relativistically intense, but are instead able to generate strong surface magnetic fields lasting longer than the pulse duration. These surface magnetic fields result from the cyclotron rotation of the laser-heated and cold electron populations within the target and are fundamentally linked to the spatial localization of hot electron production by the laser pulse. This mechanism is robust over a range of laser and target parameters and produces surface field strengths on the order of 10-15 times the seed strength. We have formulated a simple predictive scaling in good agreement with both 1D and 2D particle-in-cell simulations, $B_{\text{gen}} \sim -2\pi B_{\text{seed}} \Delta x/\lambda_0$ (in the large spot size limit), and have demonstrated the relevance of surface field generation to applications. The applied seed and surface-generated surface fields can enact substantial electron trapping and visibly reduce and increase accelerated ion energies from the rear and front target surfaces, respectively. Both the changes in ion energy and the fields generated in these configurations may be experimentally visible, offering a potential route to experimental verification.

6.7 Acknowledgements

Chapter 6, in full, is a reprint of the material as it appears in K. Weichman, A. P. L. Robinson, M. Murakami, and A. V. Arefiev, "Strong surface magnetic field generation in relativistic short pulse laser-plasma interaction with an applied seed magnetic field", *New Journal of Physics*, **22**, 113009 (2020). The dissertation author was the primary investigator and author of the paper.

This research was supported by the DOE Office of Science under Grant No. DE-SC0018312. Particle-in-cell simulations were performed using EPOCH [71], developed under UK EPSRC Grant Nos. EP/G054940, EP/G055165, and EP/G056803. This work used HPC resources of the Texas Advanced Computing Center (TACC) at the University of Texas at Austin and the Extreme Science and Engineering Discovery Environment (XSEDE) [126], which is supported by National Science Foundation grant number ACI-1548562. Data collaboration was supported by the SeedMe2 project [117] (http://dibbs.seedme.org).

Chapter 7

Generation of megatesla magnetic fields by intense-laser-driven microtube implosions

7.1 Abstract

A microtube implosion driven by ultraintense laser pulses is used to produce ultrahigh magnetic fields. Due to the laser-produced hot electrons with energies of mega-electron volts, cold ions in the inner wall surface implode towards the central axis. By pre-seeding uniform magnetic fields on the kilotesla order, the Lorenz force induces the Larmor gyromotion of the imploding ions and electrons. Due to the resultant collective motion of relativistic charged particles around the central axis, strong spin current densities of $\sim$ peta-ampere/cm^2 are produced with a few tens of nm size, generating megatesla-order magnetic fields. The underlying physics and important scaling are revealed by particle simulations and a simple analytical model. The concept holds promise to open new frontiers in many branches of fundamental physics and applications in terms of ultrahigh magnetic fields.

7.2 Introduction

Laboratory generation of strong magnetic fields have been intensively studied [23, 24, 54, 157–171], because such fields may realize new experimental tools for fundamental studies and support diverse applications. Examples include plasma and beam physics [21, 22, 129, 130, 172, 173], astro- [174, 175] and solar-physics [176, 177], atomic and molecular physics [178], and materials science [179, 180]. Magnetic field reconnection [176, 177], generation of collisionless shock [172], gamma-ray and pair production [181–183], and fusion application in a strongly magnetized plasma [30, 184–186] are receiving increased attention. Although laser−solid interactions numerically predict magnetic fields $\lesssim$ a few hundreds kT [21, 22, 171], the highest magnetic field experimentally observed to date is on the kilotesla (kT) order [23, 168].

Here we propose a novel concept called a microtube implosion (MTI), which generates megatesla (MT) magnetic fields utilizing a structured target and intense laser pulses. Suppose that a long-stretched cylindrical target contains a coaxial hollow cylindrical space with an inner radius of $R_0 \sim 1 - 10$ μm (Fig. 7.1a). Irradiating the target by ultraintense femtosecond laser pulses with an intensity of $I_{\rm L} \sim 10^{19} - 10^{22}$ Wcm^{-2} generates hot electrons with temperatures of $T_{\rm e} \sim 1-$ a few 10's mega-electron volts (MeV) according to the ponderomotive scaling [140]. Note that the ponderomotive scaling does not resemble the true dynamics of electrons on a solid surface with a steep density gradient, where the prerequisites for decoupling the quiver and envelope motion of electrons do not hold. Hot electrons ionize the target material to produce a plasma of atomic mass number A and initial ion density $n_{\rm i0} \sim 10^{23}$ cm^{-3} to ionization state Z.

The hot electrons are so energetic that some of them exit the target wall and enter the cavity. Therein the electron pressure and the electrostatic force balance with each other to form an electron sheath on the plasma/vacuum interfaces. The surface ions are accelerated inward (implosion, Fig. 7.1b) through expansion into a vacuum by the sheath

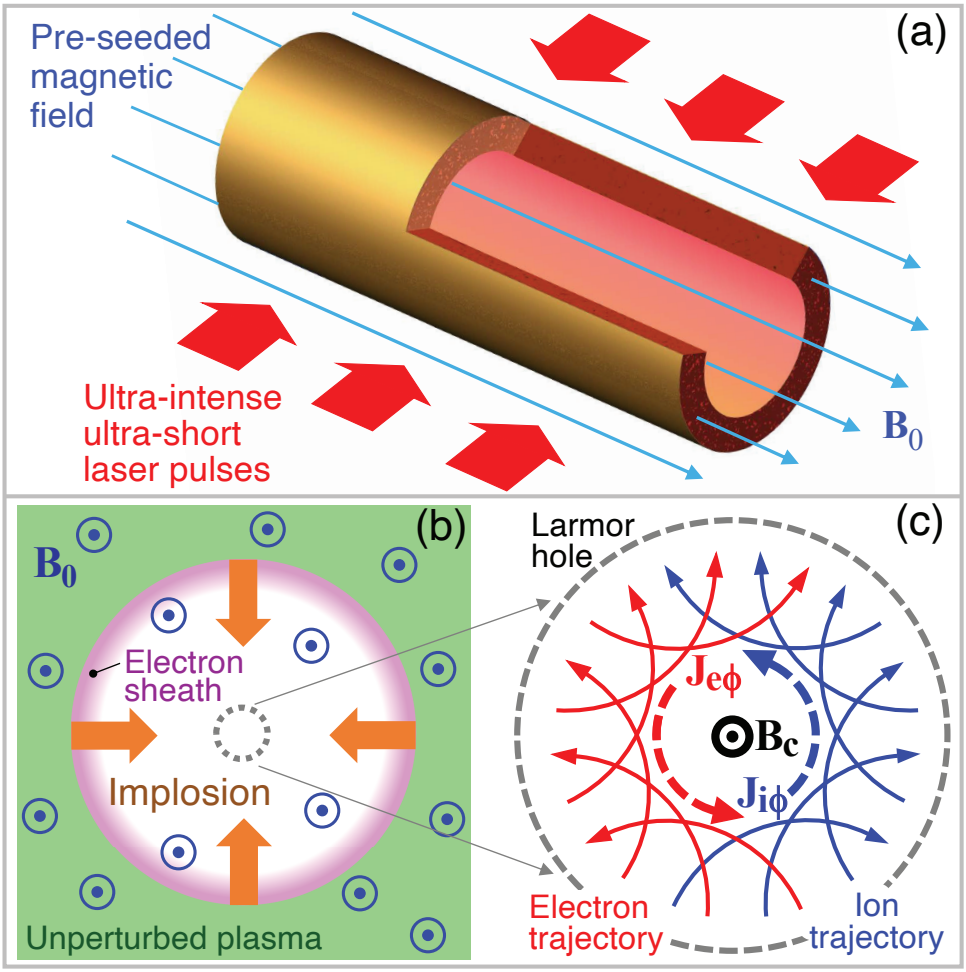

Figure 7.1: (a) Perspective view of a microtube irradiated by ultraintense laser pulses (laser configuration is just schematic). Uniform external magnetic field $\mathbf{B}_0$ is pre-seeded prior to main laser illumination. (b) Top view of the inner plasma dynamics. Laser-produced hot electrons drive isothermal expansion of the inner-wall plasma into vacuum. (c) Ultrahigh magnetic field $\mathbf{B}_c$ is generated at the center due to the collectively formed currents by ions and electrons, which are deflected in opposite directions by $\mathbf{B}_0$.

electric field [37, 101, 153, 187, 188]. In the ideal situation where a system has a perfect axial symmetry, the temporal evolution of the imploding and exploding plasma should also be axially symmetric. In this configuration, a magnetic field does not evolve. However, if a pre-seeded magnetic field is introduced into the system, an extraordinary magnetic field can be generated at the center with a $2-3$ orders of magnitude larger magnification factor.

A uniform magnetic field $\boldsymbol{B}_0$ on the kT order, which is parallel to the cylindrical axis (z-axis), is pre-seeded by an external laser-plasma device such as a capacitor coil [23, 24, 160, 167]. Using a ns-long laser, such a seed field quickly rises on the sub-ns time scale and diffuses into the MTI target nearly simultaneously, and then slowly decays on time scales $\gtrsim 10$ ns, which are characterized by impedance of the capacitor-coil. Thus, the lifetime of such a pre-seeded magnetic field $\gtrsim 10$ ns is much longer than the characteristic time scale of MTI ~ 100 fs. During the implosion, the Lorenz force deflects ions and electrons clockwise and anticlockwise, respectively, gaining azimuthal momentum, as depicted in Fig. 7.1c. The ion trajectories draw circles with Larmor radii $\sim 0.1-1$ mm for typical laser and target parameters in MTI. In particular, the envelope of the ion paths forms a nanometer-scale hole at the center (hereafter called the "Larmor hole"). Since electrons are negatively charged, the resultant direction of the electron current $\boldsymbol{J}_{\mathrm{e}\phi}$ is anticlockwise, which is the same as that of the ion current $\boldsymbol{J}_{\mathrm{i}\phi}$. Then ultraintense spin currents on the order of 10^{15} Acm^{-2} run around the Larmor hole. Consequently, the currents from the ions and electrons work together to generate MT-order magnetic field $\boldsymbol{B}_{\mathrm{c}}$ at the center.

Compared with other conventional approaches, the most innovative point of the current concept lies in the geometrically unique plasma flow. A cylindrically converging flow composed of relativistic electrons and ions, which are infinitesimally twisted by the pre-seeded magnetic field in opposite directions, can effectively produce ultrahigh spin currents and consequently, ultrahigh magnetic fields. In addition, the current geometry may be better suited for many practical purposes.

For over 50 years, researchers have strived to realize high magnetic fields. Many approaches have been employed, including high explosives [157, 158], electromagnetic implosions [159, 163], high-power lasers [54, 166], and Z pinches [161, 162]. The principal physical mechanism of these works is based on magnetic flux compression (MFC) using hollow cylindrical structures and pre-seeded magnetic fields. The present scheme also uses a similar physical configuration. However, MTI differs from MFC because the ultrahigh magnetic fields in MTI are generated by the spin currents induced by collective Larmor gyromotions.

7.3 Results

7.3.1 Two-dimensional particle simulation

To demonstrate the expected behavior of MTI, we perform 2D (x, y) PIC simulations using the open-source fully relativistic code EPOCH [71]. In this first part of EPOCH simulations (v.4.10.17), we employ rather simple and ideal physical conditions to effectively extract the salient features of the underlying MTI physics. First, the simulation uses the periodic boundary conditions for particles and fields, where the hollow cylindrical volume is placed at the middle of the square computational domain. This configuration simulates collective targets with multiple equally spaced microtubes inside a heated material. We set 100 particles/cell for carbon ions and 200 particles/cell for electrons. The lengths for the unit cell size and full span of each side of the square domain are 6.25 nm and 10 μm, respectively. Therefore, the whole computational domain size is 1600×1600 mesh^2. The initial inner radius of the microtube is $R_0 = 3$ μm.

Second, since hot-electron average energy $\mathcal{E}_{\text{he.av}}$ spans the relativistic regime for the parameters of interest, we use the Maxwell-Jüttner (M-J) distribution [189] rather than the Maxwell-Boltzmann (M-B) distribution for the non-relativistic regime. The

M-J distribution defines the hot electron population in terms of the Lorenz factor γ as $f(\gamma) = \frac{\gamma^2\beta}{\Theta K_2(1/\Theta)} \exp(-\frac{\gamma}{\Theta})$, where $\beta = v/c = \sqrt{1-1/\gamma^2}$ and $\Theta = T_\mathrm{e}/m_\mathrm{e}c^2$ with T_e, m_e, and c being the electron temperature, the electron rest mass, and the speed of light, respectively; K_2 is the modified Bessel function of the second kind. The relation between $\mathcal{E}_\mathrm{he.av}$ and T_e significantly differs between the two distributions. That is, $\mathcal{E}_\mathrm{he.av} = \frac{3}{2}T_\mathrm{e}$ for the M-B distribution ($\mathcal{E}_\mathrm{he.av} \ll m_\mathrm{e}c^2$) while $\mathcal{E}_\mathrm{he.av} \simeq 3T_\mathrm{e} - m_\mathrm{e}c^2$ for the M-J distribution ($\mathcal{E}_\mathrm{he.av} \gg m_\mathrm{e}c^2$).

It should be noted that on such an ultrashort timescale as femtoseconds, there is insufficient time for electrons to be thermalized [190, 191]. In this sense, employing the M-J distribution, which is characterized by a specific temperature, may not be legitimate. However, high-energy-tail electrons, whose population decreases exponentially with energy, predominantly influence the energy transport and thus the dynamics of the overall system [188]. In fact, both the M-J and M-B distributions have such an exponential dependence in their functional forms. For this reason, employing the M-J distribution is an acceptable choice. Actually, simulations have confirmed that the same value of $\mathcal{E}_\mathrm{he.av}$ yields a similar result for the implosion dynamics and the generation of the magnetic field for both energy distributions. Therefore, $\mathcal{E}_\mathrm{he.av}$ rather than T_e is employed below as a principal parameter. Note that we later provide another set of simulation results as a proof-of-principle, using more practical conditions that take the laser−matter interactions into account, where the electron population is not approximated by the M-J distribution.

Figure 7.2 shows the temporal evolution of the normalized densities of ions, $\tilde{n}_\mathrm{i} = n_\mathrm{i}/n_\mathrm{i0}$, and electrons, $\tilde{n}_\mathrm{e} = n_\mathrm{e}/n_\mathrm{e0}$, under $n_\mathrm{e0} = Zn_\mathrm{i0}$ for a fully ionized carbon plasma with $A = 12$ and $Z = 6$. The solid and dashed curves indicate the EPOCH results and the model prediction, respectively. The model is described later. Initially, the inside of the tube is empty, and the remaining volume is filled with uniform ions with $T_\mathrm{i} = 10$ eV and $n_\mathrm{i0} = 1 \times 10^{23}$ cm^{-3} and uniform electrons with $\mathcal{E}_\mathrm{he.av} = 5$ MeV. The pre-seeded magnetic

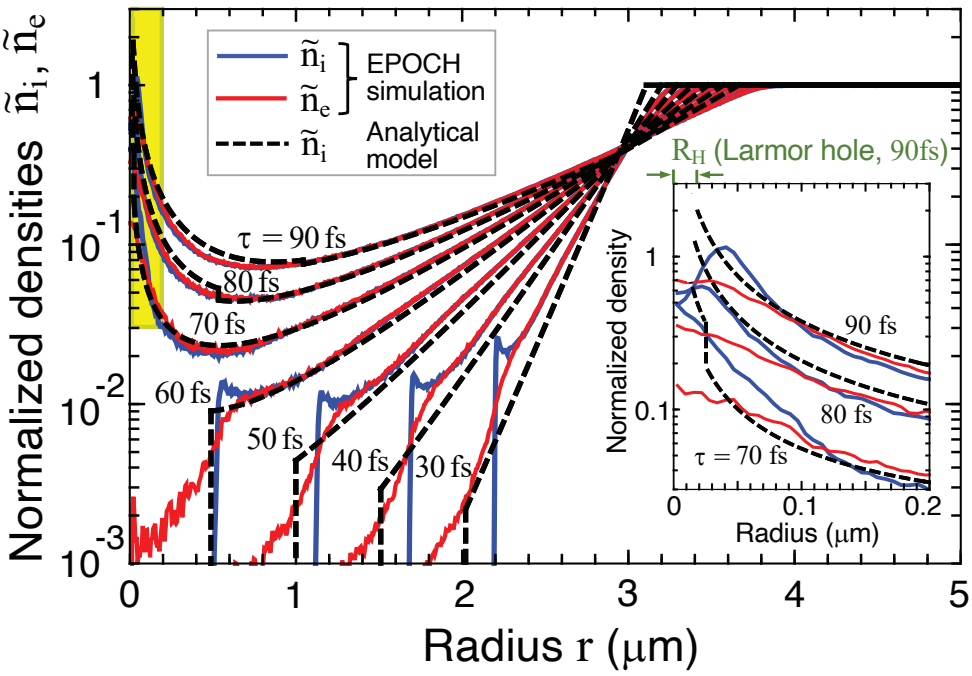

Figure 7.2: Temporal evolution of the normalized densities of ions $\tilde{n}_\mathrm{i} = n_\mathrm{i}/n_\mathrm{i0}$ and electrons $\tilde{n}_\mathrm{e} = n_\mathrm{e}/n_\mathrm{e0}$ under charge neutrality $n_\mathrm{e0} = Zn_\mathrm{i0}$ with $Z = 6$ (fully ionized carbon plasma). Other fixed parameters are $R_0 = 3\,\mu$m, $n_\mathrm{i0} = 1\times10^{23}$ cm^{-3} (i.e., 2 g cm^{-3}), $B_0 = 4$ kT, and $\mathcal{E}_\mathrm{he.av} = 5$ MeV. Dashed curves are obtained by the model lines for constant velocities (Fig. 7.4b) and the density given by Eq.(7.3). Inset shows a magnified view of the yellow-painted area.

field $B_0 = 4$ kT is distributed uniformly over the entire computational domain.

After launching the plasma expansion into a vacuum at $\tau = 0$, the implosion phase is observed for a period, $\tau \lesssim 70$ fs (Fig. 7.2). The implosion velocity of the innermost ions remains nearly constant at $v_\mathrm{i} \simeq 6\times10^9$ cm/s before the cavity collapse. Macroscopically, ions and electrons in the imploding plasma layer move together and maintain charge neutrality. The electron sheath thickness at the plasma/vacuum interface is roughly equal to the local electron Debye length $\lambda_\mathrm{De} = (T_\mathrm{e}/4\pi n_\mathrm{e}e^2)^{1/2} \sim 150$ nm, where e denotes the elementary charge, $T_\mathrm{e} \approx 1.8$ MeV ($\mathcal{E}_\mathrm{he.av} = 5$ MeV with the M-J distribution), and $n_\mathrm{e} \approx 6\times10^{21}$ cm^{-3} (Fig. 7.2).

Upon cavity collapse, the head group of imploding ions passes the target center at the Larmor hole radius $r = R_\mathrm{H}$ and expands outward. The mean-free-path of ion-ion

collisions is roughly given by $\ell_{\rm ii} \sim T_{\rm e}^2/4\pi n_{\rm i} Z^2 e^4$, which amounts to ~ 4 cm $\gg R_0$ under $T_{\rm e} = 2$ MeV, $Z = 6$, and $n_{\rm i} = 10^{23}$ cm^{-3}. Hence, these ions collisionlessly intersect other ions, which are still imploding toward the center. Meanwhile, the central density increases to the same order as its initial value due to the geometrical accumulation effect (Fig. 7.2, inset). The Larmor hole radius, $R_{\rm H} \approx 20$ nm, indicated at the top of the inset corresponds to the analytical prediction at $\tau = 90$ fs [Eq.(7.5)]. The Larmor hole is also seen in the simulation result as the one-humped structure, but the simulated one grows more quickly than the model and expands outward. This is attributed to the fact that a highly compressed ion sphere is created at the center and the strong electrostatic field radially pushes the ions outward.

Figure 7.3 shows snapshots taken from the dominant period of the magnetic field generation, $\tau \approx 80 - 120$ fs: (a) the normalized ion density $\tilde{n}_{\rm i} = n_{\rm i}/n_{\rm i0}$, (b) the normalized electron density $\tilde{n}_{\rm e} = n_{\rm e}/n_{\rm e0}$, (c) the azimuthal electron current $J_{{\rm e}\phi}$, and (d) the magnetic field $B_{\rm z}$. Comparing Figs. 7.3a and 7.3b provides insight on how the core plasma develops. The one-humped structure forms in the central region and oscillates at the ion-plasma frequency $\omega_{\rm pi} = (4\pi n_{\rm i} Z^2 e^2/m_{\rm i})^{1/2}$ to emit compression waves outward at sound speed $c_{\rm s} = (ZT_{\rm e}/m_{\rm i})^{1/2}$. Applying the numbers used in Fig. 7.3 (i.e., $n_{\rm i} = 1 \times 10^{23}$ cm^{-3} and $T_{\rm e} = 1.8$ MeV) yields $c_{\rm s} \simeq 9 \times 10^8$ cm/s and the cycle $\tau_{\rm cyc} = 2\pi/\omega_{\rm pi} \simeq 9$ fs ($\nu \equiv \tau_{\rm cyc}^{-1} \simeq 110$ THz), which agree well with the simulation result.

According to Ampere's law, $c\nabla \times \boldsymbol{B} = 4\pi \boldsymbol{J} + \dot{\boldsymbol{E}}$, the azimuthal current distribution, $J_\phi = J_{{\rm e}\phi} + J_{{\rm i}\phi}$, directly contributes to the magnetic field $B_{\rm c}$ generated at the center. The azimuthal electron current density $J_{{\rm e}\phi}$ dynamically evolves around the center over the distance approximately equal to the local Debye length $\lambda_{\rm De} \sim 100 - 150$ nm (Fig. 7.3c). According to Faraday's law, $c\nabla \times \boldsymbol{E} = -\dot{\boldsymbol{B}}$, when $B_{\rm c}$ reaches its peak, the displacement current ($\propto \partial E_\phi/\partial t$) becomes substantially small. Then, $B_{\rm c}$ is given as the sum, $B_{\rm c} = B_{\rm ce} + B_{\rm ci}$, where $B_{\rm ce} = (4\pi/c)\int_0^\infty J_{{\rm e}\phi} {\rm d}r$ and $B_{\rm ci} = (4\pi/c)\int_0^\infty J_{{\rm i}\phi} {\rm d}r$ are the contributions

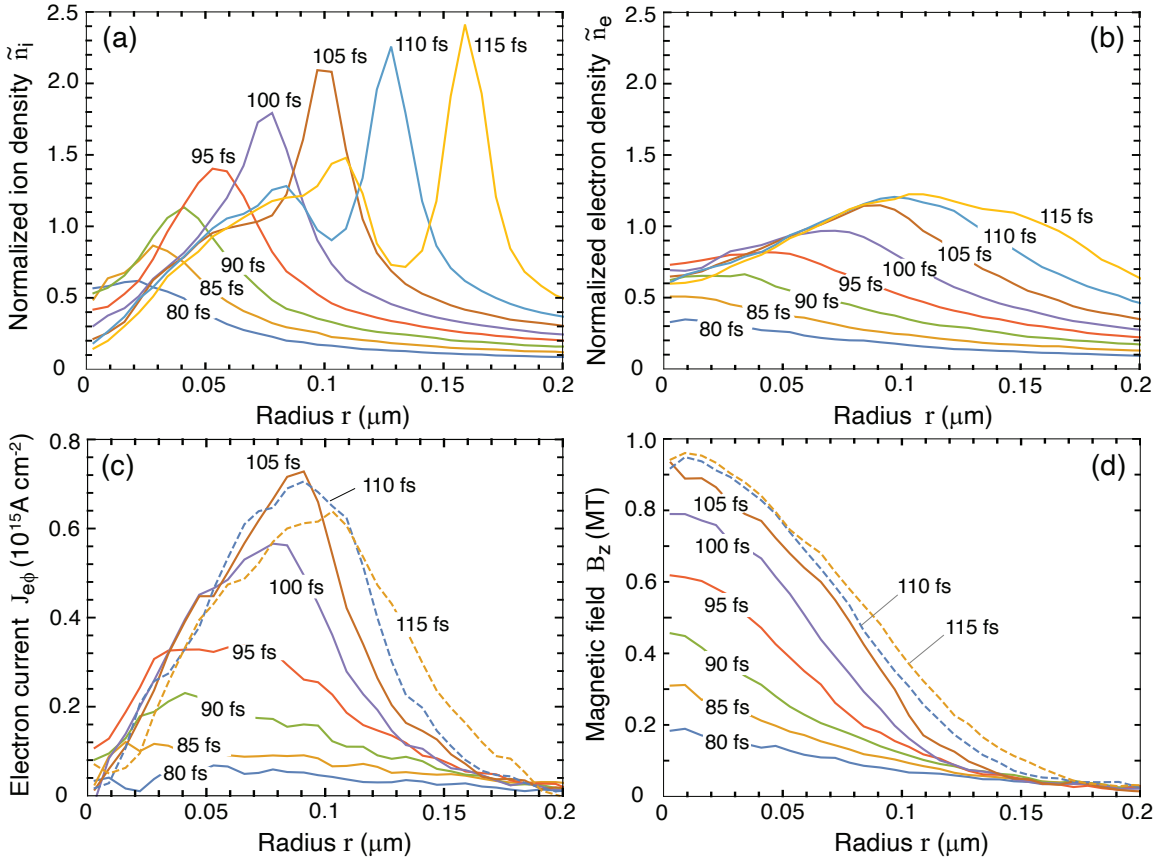

Figure 7.3: Snapshots taken from the dominant period for the magnetic field generation, $\tau \approx 80-120$ fs. Fixed parameters are the same as those in Fig. 7.2. (a) Normalized ion density $\tilde{n}_i = n_i/n_{i0}$, (b) normalized electron density $\tilde{n}_e = n_e/n_{e0}$, (c) azimuthal electron current $J_{e\phi}$, and (d) magnetic field B_z.

from electrons and ions, respectively. Due to the high mobility of electrons, the effect of electron currents on the magnetic field generation dominates over that of ion currents. MTI simulations indicate that $B_{\rm ce}/B_{\rm ci} \sim 3-4$ or equivalently $B_{\rm c}/B_{\rm ci} \sim 4-5$ is kept nearly constant. For example, $B_{\rm c} \simeq 0.95$ MT and $B_{\rm ce} \simeq 0.71$ MT are derived at $\tau = 105$ fs from Fig. 7.3c,d, which correspond to $B_{\rm c} \simeq 4B_{\rm ci}$.

7.3.2 Model

Here, we describe the ion dynamics in terms of a semi-analytical model and demonstrate that it forms the basis of the whole system. The time origin matters when comparing the model to the simulation results. To avoid confusion, hereafter, we employ the time variable, t, instead of τ used for the simulation. Suppose that a planar plasma is held at rest in a half-infinitely stretched region $-\infty < x \leq 0$ for $t \leq 0$, which is composed of uniform cold ions and hot electrons with densities $n_{\rm i}$ and $n_{\rm e}$, respectively. We postulate that the plasma is charge neutral, i.e., $Zn_{\rm i} = n_{\rm e}$. In addition, hot electron temperature $T_{\rm e}$ is assumed to be constant both spatially and temporally due to the high conductivity. Once the boundary between the vacuum and plasma is set free at $t = 0$, the plasma begins to expand into the vacuum. The ion motion is governed by the following hydrodynamic system describing the mass and momentum conservation as

$$\frac{\partial n_{\rm i}}{\partial t} + \frac{\partial}{\partial x}(n_{\rm i} v_{\rm i}) = 0, \tag{7.1}$$

$$\frac{\partial v_{\rm i}}{\partial t} + v_{\rm i}\frac{\partial v_{\rm i}}{\partial x} = -\frac{c_{\rm s}^2}{n_{\rm i}}\frac{\partial n_{\rm i}}{\partial x}, \tag{7.2}$$

where $n_{\rm i}(x,t)$ and $v_{\rm i}(x,t)$ are the number density and the velocity of the ions, respectively. Grevich *et al.* [36] found a self-similar solution to the above system, where the physical quantities are expressed in terms of a single dimensionless coordinate defined by $\xi = x/c_{\rm s}t\,(\geq -1)$ in the forms of $n_{\rm i} = n_{\rm i0}{\rm e}^{-\xi-1}$ and $v_{\rm i} = (\xi+1)c_{\rm s}$. Under the self-similar solution, the

plasma expands to the right supersonically for $x > 0$ or $\xi > 0$, while the rarefaction wave propagates to the left at the sound speed $c_{\rm s}$, corresponding to the path, $\xi = -1$.

The two physical ingredients, collisionless ions and isothermal electrons, provide insight to harness Grevich's self-similar solution as a useful approximation and to describe the kinetic behavior of the ions. To accomplish this, a geometrical modification needs to be added to the self-similar solution. The resultant system behaves such that individual fluid elements can penetrate each other in cylindrically converging and diverging processes.

Suppose that an ion with mass $m_{\rm i}$ and ionization state Z is moving at a constant speed $v_{\rm i}$ on the xy-plane in a uniform magnetic field $\boldsymbol{B}_0$, which is parallel to the z-axis. The ion draws a circular orbit with a Larmor radius $R_{\rm L} = m_{\rm i} v_{\rm i} c/ZeB_0$, where $B_0 = |\boldsymbol{B}_0|$. If the position and velocity of the ion are specified at $t = 0$ to be $(x, y) = (R_0, 0)$ and $(\dot{x}, \dot{y}) = (-v_{\rm i}, 0)$, respectively, the ion moves on the circle, $(x - R_0)^2 + (y - R_{\rm L})^2 = R_{\rm L}^2$.

Here, it is useful to introduce cylindrical coordinates, $r = \sqrt{x^2 + y^2}$ and $\phi = \tan^{-1}(y/x)$. The ion path s along its Larmor circle is measured with the distance from the initial point $(x, y) = (R_0, 0)$ or with the polar angle $\theta = \sin^{-1}[(R_0 - x)/R_{\rm L}]$ pivoting around the guiding center $(x, y) = (R_0, R_{\rm L})$, as illustrated in Fig. 7.4a. It should be noted that Fig. 7.4a is not to scale. The dimensionless coordinate of the self-similar solution is then redefined in terms of s and θ as $\xi = s/c_{\rm s}t = R_{\rm L}\theta/c_{\rm s}t$. Note that $v_{\rm i}$ and $R_{\rm L}$ are functions of ξ. Consequently, Grevich's self-similar solution for a planar system is reformed for a cylindrical system as

$$n_{\rm i} = n_{\rm i0} \frac{R_0}{r} {\rm e}^{-\xi - 1}, \tag{7.3}$$

$$\left(v_{\rm ir}, v_{{\rm i}\phi}\right) = \frac{(\xi + 1) c_{\rm s}}{r} \left(\pm\sqrt{r^2 - R_{\rm H}^2}, R_{\rm H}\right), \tag{7.4}$$

where $v_{\rm ir}$ and $v_{{\rm i}\phi}$ denote the radial and azimuthal component of the ion velocity, respectively. The reformed set, Eqs. (3) and (4), rigidly satisfies the mass conservation law for a cylindrical

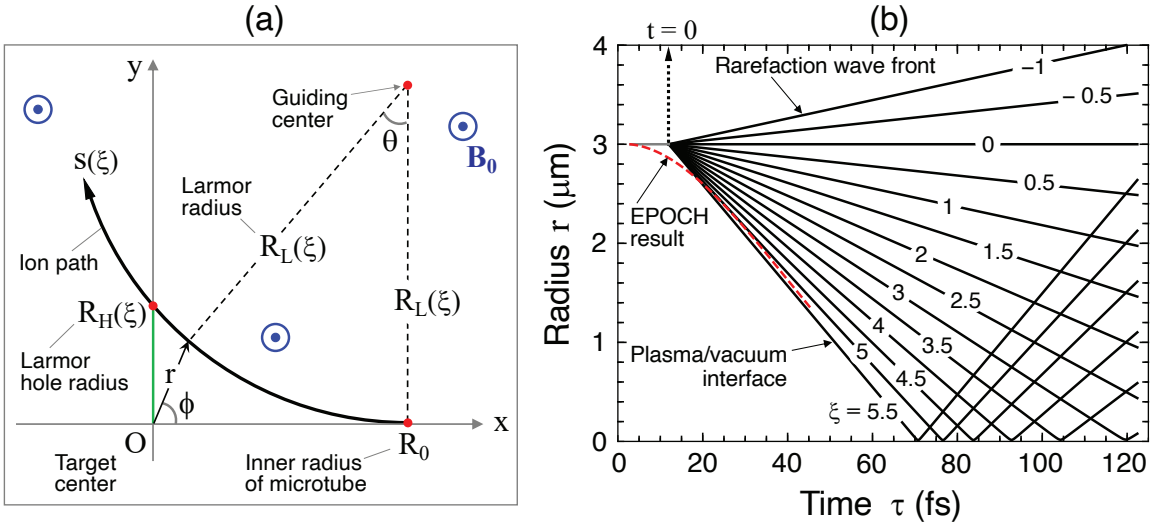

Figure 7.4: Analytical model: (a)Schematic explaining the relation between the key parameters (not to scale). Curve with its coordinate s stands for an ion path, on which the ion implodes at a constant speed as a function of ξ. In most practical cases, $R_{\rm H}(\mathrm{nm}) \ll R_0(\mu\mathrm{m}) \ll R_{\rm L}(\mathrm{mm})$. (b)Radius−time diagram of ξ-contour lines under the same parameters as in Figs. 7.2 and 7.3. Temporal evolution of the density profile shown in Fig. 7.2 is directly obtained from this diagram coupled with Eq. (7.3). The time lag of 12 fs between $\tau = 0$ and $t = 0$ is fixed such that the timing of the cavity collapse coincide for both the simulation and the model.

geometry such that the factor R_0/r in Eq. (7.3) explains the geometrical accumulation effect. The minus and plus signs of the double sign in Eq. (7.4) correspond to the converging and diverging phases, respectively. The relation between $v_{\rm ir}$ and $v_{{\rm i}\phi}$ can be understood by considering the simplified physical picture of a single fast ion approaching the center along a straight line, $y = R_{\rm H}$, with a constant speed v_0 at $r = \infty$, i.e., $(v_{\rm ir}, v_{{\rm i}\phi}) = (-v_0, 0)$. The ion passes the origin $(x, y) = (0, 0)$ at the shortest distance $r = R_{\rm H}$, when the velocities replace each other, i.e., $(v_{\rm ir}, v_{{\rm i}\phi}) = (0, v_0)$. Therefore, the higher the implosion velocity of an ion, the higher the current and resultant magnetic fields around the center, i.e., $B_{\rm z} \propto J_{{\rm i}\phi} = Zev_0R_{\rm H}/r$.

Although Grevich's solution gives a simple physical picture of plasma expansion into a vacuum, it lacks important information such as the location of ion front $x_{\rm f}$. In fact, Grevich's solution gives an infinite propagation speed of the ion front, i.e., $\dot{x}_{\rm f} \to \infty$ as $\xi \to \infty$. Assuming that the plasma expands adiabatically, a reasonable approximation

for the dimensionless coordinate of the ion front $\xi_{\rm f}$ is obtained such that the plasma front expands at the speed $\dot{x}_{\rm f} = 2(\gamma-1)^{-1}c_{\rm s}$ [192], where γ denotes the adiabatic index. Meanwhile, the self-similar solution based on the isothermal assumption gives the speed of a fluid element at $\xi = \xi_{\rm f}$ as $\dot{x}_{\rm f} = (\xi_{\rm f}+1)c_{\rm s}$. Equating the two speeds gives $\xi_{\rm f} = (3-\gamma)/(\gamma-1)$. In particular, the adiabatic index for the relativistic electrons is $\gamma = 4/3$ [192], yielding $\xi_{\rm f} = 5$. This result well explains $\xi_{\rm f} \simeq 5.5$ obtained from the simulation (Figs. 7.2 and 7.4b).

Figure 7.4b shows the $r-t$ diagram obtained from the reformed self-similar system, under the conditions in Figs. 7.2 and 7.3, where the curves correspond to different values of ξ. The time origin of the model corresponding to $\tau = 12$ fs is chosen such that the cavity-collapse timings coincide with each other on the horizontal axes. This can be confirmed by the red dashed curve, which shows the trajectory of the innermost ions at an early stage of implosion according to the EPOCH simulation (Fig. 7.2). Combining the curves in Fig. 7.4b and the density profile given by Eq. (7.3) leads to the dashed curves in Fig. 7.2 as the model predictions.

The Larmor hole radius $R_{\rm H}$ is obtained from the geometrical consideration under $R_{\rm H} \ll R_0 \ll R_{\rm L}$ to be $R_{\rm H} \simeq R_0^2/2R_{\rm L}$, which is explicitly rewritten as

$$\frac{R_{\rm H}(t)}{1{\rm nm}} \simeq 43\frac{Z}{A}\left(\frac{B_0}{1{\rm kT}}\right)\left(\frac{R_0}{3\mu{\rm m}}\right)^2\left(\frac{(\xi_{\rm c}(t)+1)c_{\rm s}}{10^9{\rm cm/s}}\right)^{-1}, \tag{7.5}$$

where $\xi_{\rm c}(t) = R_0/c_{\rm s}t$ corresponds to the ions passing by the target center at time t. The azimuthal ion current, $J_{{\rm i}\phi} = Zen_{\rm i}v_{{\rm i}\phi}$, is then given with the help of Eqs. (7.3) and (7.4) by

$$J_{{\rm i}\phi}(r,t) = \left(\frac{R_{\rm H}}{r}\right)^2 J_{\rm H}(t), \quad r \geq R_{\rm H}, \tag{7.6}$$

$$J_{\rm H}(t) = (R_0/R_{\rm H})Zen_{\rm i0}c_{\rm s}(\xi_{\rm c}+1){\rm e}^{-\xi_{\rm c}-1}. \tag{7.7}$$

The spatial profile of the ion current has a maximum $J_{\rm H}(t)$ at the Larmor hole rim $r = R_{\rm H}$ to spatially decay at the rate r^{-2} for $r \geq R_{\rm H}$.

In Eq. (7.7), the factor $R_0/R_{\rm H}$ explains the cylindrical accumulation effect. Consequently, the ion current contribution to the central magnetic field follows $B_{\rm ci}(t) = (4\pi/c)\int_{R_{\rm H}}^{\infty} J_{{\rm i}\phi}(r,t){\rm d}r = (4\pi/c)R_{\rm H}J_{\rm H}(t)$. The space-integrated quantity $B_{\rm ci}(t)$ is independent of $R_{\rm H}$ itself. With time t, the numerical factor, $(\xi_{\rm c}+1){\rm e}^{-\xi_{\rm c}-1}$, in Eq. (7.7) monotonically increases, and $\xi_{\rm c}(t)$ decreases from its initial value $\xi_{\rm c}(\tau = 70\ {\rm fs}) = \xi_{\rm f} = 5.5$. Although the factor asymptotically approaches its maximum, ${\rm e}^{-1} = 0.37$, with $t \to \infty$ or $\xi_{\rm c} \to 0$, a cut-off value of $\xi_{\rm c}$ exists for the physical reason described below.

According to the EPOCH simulations, after the cavity collapse at $\tau = \tau_{\rm c} (\simeq 70$ fs), the magnetic field grows at the center for a period of $4-6$ ion-oscillations, i.e., $\Delta\tau \sim (4-6)\times\tau_{\rm cyc} \sim 40-60$ fs with the cycle $\tau_{\rm cyc} = 2\pi/\omega_{\rm pi} \approx 10$ fs for the case in Figs. 7.2 and 7.3. This corresponds to $\tau \sim 110-130$ fs or $\xi_{\rm c} \sim 3$ (Fig. 7.4b). After the duration $\Delta\tau$, the core periodically emits outgoing density waves at a frequency $\omega_{\rm pi}$. These waves carry a portion of the central plasma energy, as seen in the double-humped structure of the ion density profile for $\tau = 110-115$ fs in Fig. 7.3a. In fact, $B_{\rm c}(t)$ begins to decay coherently with the first emission of the density wave (Fig. 7.3a,d). Since the model does not consider this emission process, we estimate the maximum magnetic field by limiting the growth at the peak time $\tau_{\rm peak} = \tau_{\rm c} + \Delta\tau$. This corresponds to $\xi_{\rm c} \sim 3$. Recalling the observed constancy, $B_{\rm c} \simeq 4B_{\rm ci}$, leads to its maximum value $B_{\rm c.max}$ as

$$\frac{B_{\rm c.max}}{1\,{\rm MT}} = \Psi \equiv \frac{(Z/6)^{3/2}}{(A/12)^{1/2}}\left(\frac{n_{\rm i0}}{10^{23}\,{\rm cm}^{-3}}\right)\left(\frac{R_0}{3\,\mu{\rm m}}\right)\sqrt{\frac{\mathcal{E}_{\rm he.av}}{6\,{\rm MeV}}}. \tag{7.8}$$

Thus, $B_{\rm c.max}$ is proportional to the total ion flux emitted from the inner surface of the microtube, i.e., $B_{\rm c.max} \propto Zn_{\rm i0}c_{\rm s}R_0$ (recall $c_{\rm s} \propto \sqrt{ZT_{\rm e}/A}$).

Figure 7.5 shows the results of about three dozen EPOCH simulations (solid circles) for $B_{\rm c.max}$ as a function of Ψ defined in Eq. (7.8). The straight black line denotes the model prediction. Each simulation result corresponds to a subset with the key parameters,

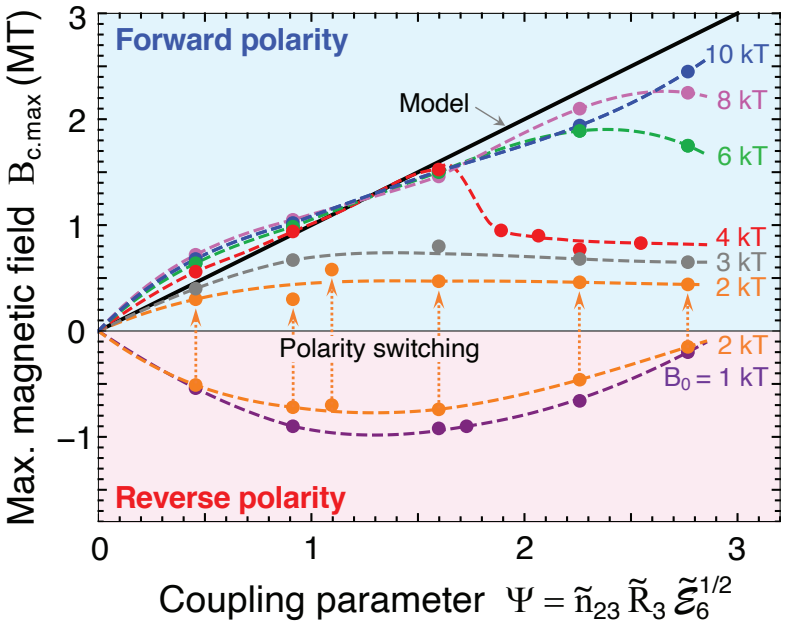

Figure 7.5: Maximum magnetic field as a function of coupling parameter Ψ [Eq. (7.8)], where $\tilde{n}_{23} = n_{i0}/10^{23}\text{cm}^{-3}$, $\tilde{R}_3 = R_0/3\mu\text{m}$, and $\tilde{\mathcal{E}}_6 = \mathcal{E}_{\text{he.av}}/6\text{MeV}$ denote normalized values for the initial ion density, inner radius of the microtube, and average electron energy, respectively. $Z = 6$ and $A = 12$ are fixed assuming a fully ionized carbon plasma. Solid circles are EPOCH results, which are linked by the dashed curves to smoothly guide the readers' eye.

$(B_0, n_{i0}, R_0, \mathcal{E}_{\text{he.av}})$. Their composition is chosen rather randomly over the ranges, $B_0 = 1-10$ kT, $n_{i0} = 5\times10^{22} - 2\times10^{23}$ cm^{-3}, $R_0 = 1-3\,\mu$m, and $\mathcal{E}_{\text{he.av}} = 5-15$ MeV, while $A = 12$ and $Z = 6$ are fixed. Despite the random choices, the overall simulation results are smoothly linked in a systematic manner by the dashed curves parameterized by B_0. This demonstrates the physical significance of the parameter Ψ as an essential measure of the magnetic-field generation in the present scheme

There is a threshold relation between B_0 and Ψ such that the simulation results and the model line agree well. For example, for $B_0 \gtrsim 6$ kT and $\Psi \lesssim 2.5$, the model well reproduces the overall behavior of the simulation results. The physical reason why these curves overlap with the model line is as follows. Although the individual trajectories of charged particles are deformed to radially shift outward due to higher B_0 and smaller Larmor radius R_L (Fig. 7.4a), the integrated currents and consequently the magnetic field,

$\int J_{i\phi} dr \propto \int J_{e\phi} dr \propto B_c$, are unchanged.

With $B_0 = 4$ kT, the difference between the simulation and the model begins to increase for $\Psi \gtrsim 1.6$. Moreover, for $B_0 < 3$ kT, the behaviors of the simulation results are unpredictable by the model. In particular, with $B_0 = 2$ kT, the temporal evolution of the system becomes unstable. Although it initially behaves in the reverse polarity regime ($B_{c.max} < 0$), it eventually turns into the forward polarity regime ($B_{c.max} > 0$). This phenomenon is labeled as "polarity switching" in Fig. 7.5. The polarity switching suddenly occurs on the timescale of several femtoseconds, when the electron current distribution surrounding the target center evolves very quickly in a complex manner. One of the potential causes for this phenomenon seems to be the existence of an electron-rich space at the center, which is omitted in the model assuming that R_H is so large [Eq. (7.5)] that electrons are evacuated from the Larmor hole.

7.3.3 Practical simulation with laser-plasma interaction

In this section, we perform proof-of-principle EPOCH simulations to demonstrate that strong magnetic fields can still be produced, when the uniform hot electron population previously assumed by the M-J distribution is replaced with a realistic laser-plasma interaction [71]. These simulations reproduce salient features of the MTI process described in the previous sections. Note that although the EPOCH code used here is somewhat customized with the same core modules as recent releases, the results provided below should be reproducible using the latest release.

We consider an isolated target, which consists of an initially cold, fully ionized charge-neutral carbon−electron plasma with an initial ion density $n_{i0} = 3 \times 10^{22}$ cm^{-3} and electron density $n_{e0} = 6 n_{i0}$. We have reduced the target density by a factor of ~ 3 relative to the case given in Figs. 7.2 and 7.3 to mitigate the computational cost associated with PIC simulations of the laser−plasma interaction. The target's outer cross-section is a

square with 12-μm-long sides. The inner radius of the microtube is $R_0 = 3\,\mu$m. This target is irradiated on each of the four outer sides by a large-spot (spatially plane wave) laser pulse with a wavelength of $\lambda_\mathrm{L} = 0.8\,\mu$m, a total duration ($\sin^2$ temporal shape in $|E|$) of $\tau_\mathrm{L} = 100$ fs, and a peak intensity of $I_\mathrm{L} = 10^{21}$ W/cm^2. The pulses are co-timed such that the peaks of all four pulses interact with the target surface simultaneously. The plasma is modeled with a resolution of 100 cells/μm and 200 particles/cell for carbon ions and 400 particles/cell for electrons, using the cubic B-spline particle shape included in EPOCH. The full size of the simulation box is 22 μm $\times$ 22 μm.

In practical laser-driven configurations, the laser−plasma interaction causes the hot electron population driving the implosion to depart from the conditions of spatial uniformity and temperature isotropy, which are assumed in the derivation of the maximum magnetic field given in Eq. (7.8). The energetic electron spectrum has multiple energy components and differs from a single-temperature M-J distribution (Fig. 7.6a). Despite this departure from the conditions assumed in the previous sections, we still observe strong magnetic field generation with similar features to the single-temperature case. Due to the spatial non-uniformities, strong magnetic fields with spatially varying signs can be generated in small regions of the implosion volume even without the presence of any seed magnetic field. However, the addition of a seed magnetic field ($B_0 = 6$ kT) increases both the maximum amplitude of the magnetic field produced and the spatial volume over which it maintains the same sign (Fig. 7.6b).

Figure 7.7 shows the detailed temporal evolution of the physical quantities, which are summarized in Fig. 7.6b. The magnetic field generation in the laser-driven case occurs in two stages, where the majority of the magnetic field generation occurs during the first stage. During the implosion, substantial anisotropy in the ion current crossing through the center of the microtube generates a strong magnetic field around the center ($r < 0.3\,\mu$m, Stage 1 in Fig. 7.7a,c). In the simulations, the magnitude of this magnetic field increases by

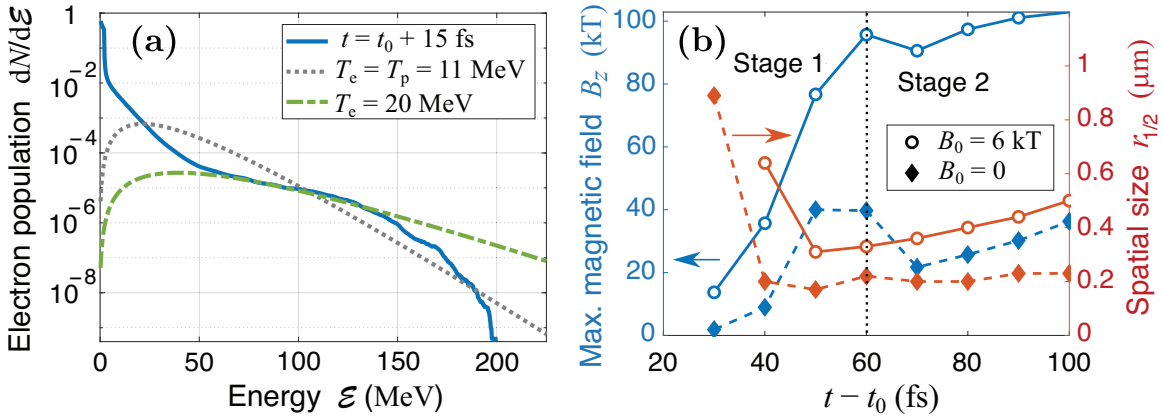

Figure 7.6: Electron energy spectrum and magnetic field growth in laser-driven targets ($\lambda_L = 0.8\,\mu$m, $I_L = 10^{21}$ W/cm^2, $\tau_L = 100$ fs). (a) Blue-line: Laser-produced electron energy spectrum under $B_0 = 6$ kT, normalized such that $\int(dN/d\mathcal{E})d\mathcal{E} = 1$. Grey dotted line: M-J fit to the spectrum using the ponderomotive temperature $T_p \equiv (1+a_0^2)^{1/2} m_e c^2 \approx 11$ MeV, where $a_0 \equiv |e|E_0/m_e c\omega$ for a laser with maximum electric field amplitude E_0 and frequency ω. Green dash-dotted line: M-J fit to the mid-energy part of the spectrum, provided for comparison. (b) Maximum magnetic field and radius at which the field falls to half its maximum value ($r_{1/2}$), obtained by azimuthally averaging the magnetic field; t_0 is the time when the peaks of the laser pulses reach either $x = 0$ or $y = 0$.

a factor of $\gtrsim 2$ upon applying $B_0 = 6$ kT through the MTI process (Fig. 7.7a). Later, this central magnetic field is further amplified by electrons undergoing $E \times B$-directed motion as the central ion population explodes outward (Stage 2 in Fig. 7.7a,c). Unlike Stage 1, which occurs over approximately 30 fs and agrees well with the MTI process described earlier, Stage 2 can persist for well over 100 fs. Figure 7.7 does not capture the end of this stage due to the computational cost of these simulations. However, simulations performed with plastic targets suggest the magnetic field can be slowly amplified over hundreds of femtoseconds. In the presence of the 6-kT seed, the first stage, which includes the MTI amplification process, generates a ~ 100 kT magnetic field over $r \lesssim 0.3\,\mu$m in approximately 20 fs, while the second stage amplifies this magnetic field to ~ 120 kT over approximately 50 fs and increases the size of the central spot to a radius of $\sim 0.5\,\mu$m.

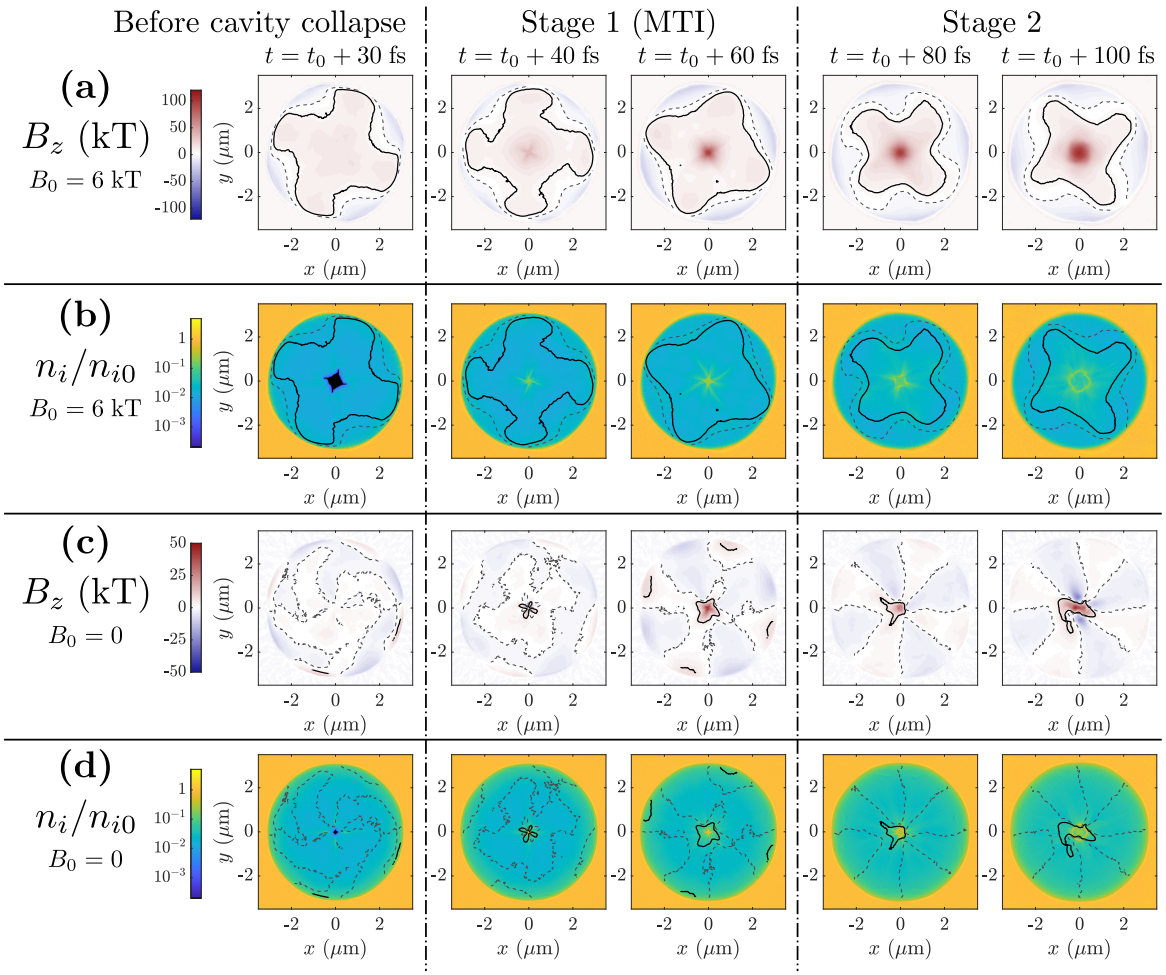

Figure 7.7: Detailed temporal evolution of the magnetic field B_z and the normalized ion density n_i/n_{i0} of laser-driven MTI. Summary plots are given in Fig. 7.6. (a),(b) results with $B_0 = 6$ kT. (c),(d) results with $B_0 = 0$. (a),(c) Magnetic field in the microtube. (b),(d) Density of carbon ions during the implosion. The black solid and grey dashed contours indicate $B = 6$ kT and $B = 0$, respectively. The first time snapshot ($t = t_0 + 30$ fs) corresponds to a moment immediately before the cavity collapse.

7.4 Discussion

We here briefly discuss laser requirements for MTI. To achieve MT-order magnetic fields experimentally, a rough estimate assuming a pulse duration of ~ 30 fs suggests that a laser system with a pulse energy of $0.1-1$ kJ and a total power of $10-100$ PW is required. Such high-power laser performance is accessible by today's laser technology [1,193]. Meanwhile, fundamental studies, including proof-of-principle experiments, should be feasible using substantially smaller laser systems. Unlike for ultrathin targets with nm-scale thicknesses, MTI targets are significantly less sensitive to laser contrast due to the micron-thick wall, while beam co-timing should be within $10-20$ fs for implosions with a timescale of ~ 100 fs.

Detecting MT-order magnetic fields inside a plasma presents a challenge for conventional techniques that rely on charged particle sources. In anticipation of achieving ultrahigh magnetic fields, there have been efforts to develop other techniques to infer the existence of strong B-fields inside a dense plasma in use of, for example, an XFEL photon beam with Faraday rotation effect [130, 170, 173] and spin-polarized neutrons [194].

We roughly estimate the minimum number of beams $n_{\rm B}$ from a uniformity point of view. For simplicity our discussion here is limited to the cross-sectional dimensions. Nonuniformity of the imploding ion front is directly influenced by that of hot electron density, which comprises the local electron sheath (Fig. 7.1b). Hot electrons produced on the laser-irradiated surface go back and forth between the target surface and the cavity wall with an in-between distance $\Delta R = R_1 - R_0$, where R_1 is the initial target radius. This hot electron transport is regarded as a kind of random-walk diffusion process. The nonuniformity on the outer surface should diminish on the cavity wall via this diffusion process along the lateral direction. As is well documented, the diffusion distance is given by $L_{\rm d} \sim \sqrt{N}\Delta R$, where $N \sim c\Delta t/\Delta R$ stands for the reflection number between the two surfaces during the implosion time Δt. Consequently, $n_{\rm B} \gtrsim 2\pi R_0/2L_{\rm d} \sim 2$ (i.e., two-sided

illumination) when employing for example $R_0 = 3\,\mu$m, $\Delta R = 2\,\mu$m, and $\Delta t \sim 50$ fs (Fig. 7.2). It should be noted that controlling both the temporal and spacial profiles of the incident laser pulses also plays a crucial role to improve the implosion uniformity [195, 196].

In summary, we propose a novel concept called MTI, which produces MT-order magnetic fields using intense laser pulses. Key physical elements of MTI are imploding ion fluxes with quasi-relativistic speeds and the resultant ultrahigh spin currents running around the nanometer-scale Larmor hole at the center. The spin currents are due to the collective motion of the imploding ions and the accompanying relativistic electrons. The pre-seeded magnetic field B_0 significantly influences the magnetism of the plasma. For example, the forward (reverse) polarity appears in the domain of higher (lower) B_0. Polarity switching is an extraordinary phenomenon, which requires further investigation. The scaling law for the maximum magnetic field $B_{\mathrm{c.max}}$ is obtained as a function of B_0 and the total ion flux emitted from the inner surface of microtube Ψ. With the realistic laser-plasma interaction taken into account, strong magnetic field generation has been demonstrated as a proof-of-principle of MTI.

7.5 Acknowledgments

Chapter 7, in full, is a reprint of the material as it appears in M. Murakami, J. J. Honrubia, K. Weichman, A. V. Arefiev, and S. V. Bulanov, "Generation of megatesla magnetic fields by intense-laser−driven microtube implosions", *Scientific Reports* **10**, 16653 (2020). The dissertation author contributed simulations, figures, and writing to the paper.

M.M. was supported by the Japan Society for the Promotion of Science (JSPS). J.J.H. was supported by the EUROfusion grant ENR-IFE19.CCFE-01-T001-D001 and the research grant RTI2018-098801-B-I00 of the Spanish Ministry for Research. J.J.H. thankfully acknowledges the computer resources at MareNostrum and the technical support

provided by the Barcelona HPC of the Spanish Supercomputing Network and the CeSViMa HPC of the UPM. The work by S.V.B. was supported by the project High Field Initiative (No. CZ.02.1.01/0.0/ 0.0/15_003/0000449) from the European Regional Development Fund. The work by K.W. and A.V.A was supported by the DOE Office of Science under Grant No. DE-SC0018312 and used HPC resources of the Texas Advanced Computing Center (TACC) at the University of Texas at Austin and the Extreme Science and Engineering Discovery Environment (XSEDE) [126], which is supported by National Science Foundation grant number ACI-1548562. Data collaboration was supported by the SeedMe2 project [117] (http://dibbs.seedme.org).

Chapter 8

Sign reversal in magnetic field amplification by relativistic laser-driven microtube implosions

8.1 Abstract

We demonstrate and explain the surprising phenomenon of sign reversal in magnetic field amplification by the laser-driven implosion of a structured target. Relativistically intense laser pulses incident on the outer surface of a microtube target consisting of thin opaque shell surrounding a μm-scale cylindrical void drive an initial ion implosion and later explosion capable of generating and subsequently amplifying strong magnetic fields. While the magnetic field generation is enhanced and spatially smoothed by the application of a kilotesla-level seed field, the sign of the generated field does not always follow the sign of the seed field. One unexpected consequence of the amplification process is a reversal in the sign of the amplified magnetic field when, for example, the target outer cross section is changed from square to circular. Using 2D particle-in-cell simulations, we demonstrate that sign

reversal is linked to the stability of the surface magnetic field of opposite sign from the seed which arises at the target inner surface during laser irradiation. The stability of the surface magnetic field and consequently the sign of the final amplified field depends sensitively on the target, laser, and seed magnetic field conditions, which could be leveraged to make laser-driven microtube implosions an attractive platform for the study of magnetic fields in high energy density plasma in regimes where sign reversal either is or is not desired.

8.2 Sign reversal in magnetic field amplification

The emergence of new magnetic field generation techniques [23–26,29] and structured target fabrication capabilities [45, 47, 49, 50] coupled with the continual development of relativistic short pulse lasers [1] is rapidly enabling new regimes of magnetized high energy density (HED) physics. The combination of a strong magnetic field and HED plasma offers the opportunity to observe new magnetization-related phenomena in areas such as laboratory astrophysics [6, 7, 9] and to obtain improvements in applications including inertial fusion energy [14–16] and ion acceleration [130–132, 197]. In addition, the increasing availability of structured targets has opened up new possibilities for manipulating laser-plasma interaction to achieve desirable goals including enhanced energetic particle production [45–47, 49], radiation sources [48, 50, 51], and magnetic field generation [52, 53].

Concurrently, there is growing interest in scenarios where HED plasma generates or amplifies magnetic fields [54, 55, 150, 198, 199]. In particular, magnetic field amplification is desirable to extend the experimentally accessible magnetic field beyond what is currently available via vacuum field generation techniques. One such platform for field amplification is laser-driven implosions. In the context of 100 μm-scale implosions driven by ns-duration sub-relativistic-intensity lasers, magnetic fields can be amplified via flux compression [54, 55]. However, field amplification is also possible in the implosion of a μm-scale structured

microtube target driven by sub-ps relativistic laser pulses, where the amplification occurs both during and after the ion implosion phase [199].

Lasers irradiating a microtube target consisting of a thin opaque shell surrounding a small cylindrical void are capable of driving strong ion acceleration via a two stage process consisting of an initial ion implosion and later explosion [200, 201]. It has recently been demonstrated that this process can also generate strong magnetic fields, which are enhanced by the application of a kilotesla-level seed magneic field [199]. In the proof-of-principle demonstration presented in Ref. 199, the observed strong magnetic field generated within the void had the same direction as the applied seed field. However, as we will show in this work, a similarly strong magnetic field with peak amplitude in excess of 40 times the seed can also be generated with opposite sign from the seed field.

Magnetic field amplification in microtube targets is a multi-stage process involving field generation by both electron and ion currents. The addition of a seed field also causes the production of a surface magnetic field with opposite sign from the seed at the inner target surface [198], which we find under certain conditions can be amplified in lieu of the applied seed. As we will demonstrate in this work, the sign of the strong magnetic field produced by the implosion is influenced by the stability of this surface magnetic field and can be reversed through changes to the target, laser, and seed magnetic field conditions.

We conduct 2D simulations of an imploding microtube target driven by 4 laser pulses using the open source particle-in-cell code EPOCH [71]. As shown schematically in Fig. 8.1a,b, the target consists of a thin fully ionized plastic (CH) shell which is either completely cylindrical or has a square outer cross section with the same central cylindrical hole. The minimum thickness of this shell is nominally 3 μm with a 3 μm radius hole. We nominally apply a seed magnetic field in the direction out of the simulation plane (z) of $B_{\text{seed}} = 3$ kT. The 4 laser pulses are spatially and temporally Gaussian with a peak intensity of 10^{21} W/cm^2, a 25 fs FWHM pulse duration, and a varying spot size w_0. The majority of

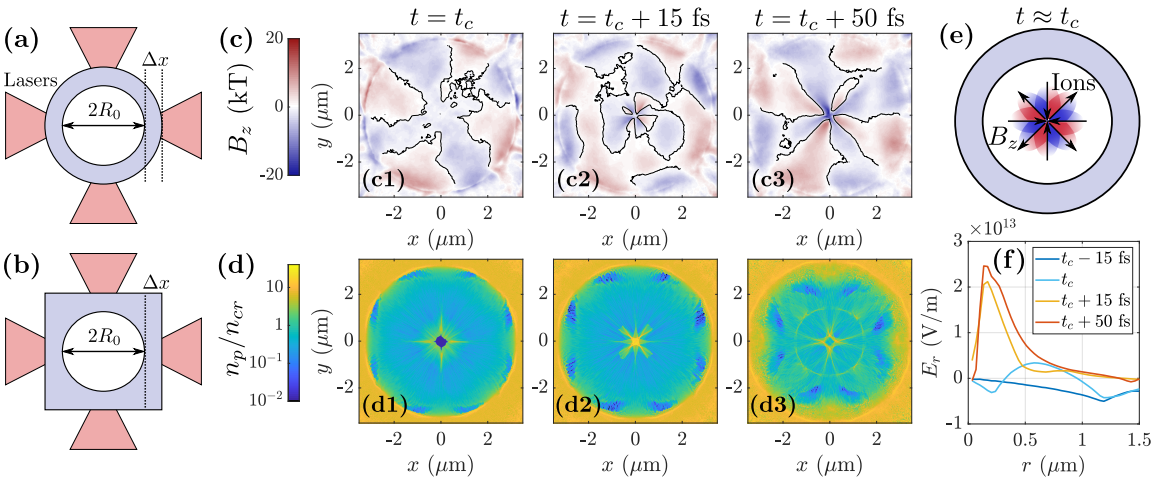

Figure 8.1: Magnetic field generation and amplification with $B_{\text{seed}} = 0$ in an imploding target. Schematic of target configuration for (a) circular and (b) square outer cross section. (c) Field generation and (d) proton density for circular case with $w_0 = 15$ μm. The black contours in (c) denote $B_z = 0$. (e) Schematic of B_z generated by imploding ion current. (f) Azimuthally averaged radial electric field $E_r(r)$ for the circular case with $w_0 = 15$ μm. $t = t_c$ is just before ions reach the center (here, $t_c = 50$ fs).

the simulations we conduct correspond to a laser spot size which is large compared to the microtube target size, under which conditions we expect 2D simulations to feature similar implosion dynamics as would be observed near the laser axis in 3D. Additional details of the simulation setup are given in Table 8.1.

The essential dynamics of the implosion are as follows [200] and are qualitatively unchanged by the addition of the seed magnetic field. The laser pulse interacting with the outer target surface generates hot electrons which stream into the inner target void and drive a strong ion implosion towards the target center (Fig. 8.1d). This implosion is driven by the radially inward electric field associated with the net excess of electron charge within the void ($t \lesssim t_c$ in Fig. 8.1f, where t_c is the time ions first reach the target center). After ions arrive at the target center, the radial electric field is reversed and acts to re-accelerate ions outward during a subsequent explosion phase ($t \gtrsim t_c$ in Fig. 8.1f). This process can generate high plasma density at the target center and produce high ion energy from the explosion [200, 201]. In the cases we will consider, the laser produces hot electrons with a

Table 8.1: Implosion simulation parameters. The inner target cross section is circular with either a circular or square outer cross section. The initial plasma temperature is set as zero and the target surface is sharp (no preplasma). t_c is measured to within 5 fs.

Laser parameters	
Wavelength	$\lambda_0 = 0.8$ μm
Peak intensity	1×10^{21} W/cm^2
Duration (Gaussian, electric field FWHM)	25 fs
Spot size (Gaussian, electric field FWHM)	$w_0 = 15$ μm
Laser polarization	x or y
Other parameters	
Seed magnetic field ($\mathbf{B} = B_{\text{seed}}\hat{\mathbf{z}}$)	$B_{\text{seed}} = 3$ kT
Target inner radius	$R_0 = 3$ μm
Minimum target thickness	$\Delta x = 3$ μm
Peak electron density	$n_e = 50\, n_{cr}$
Spatial resolution	100 cells/λ_0
Macroparticles per cell, electron	200
Macroparticles per cell, ion	100
Size of simulation box ($x \times y$, μm)	48×48
Time interval for averaging B_z in figures	5 fs
Time reference	
Time when peak of laser would reach void	$t = 0$
Time just before ions reach center (varies)	$t = t_c$

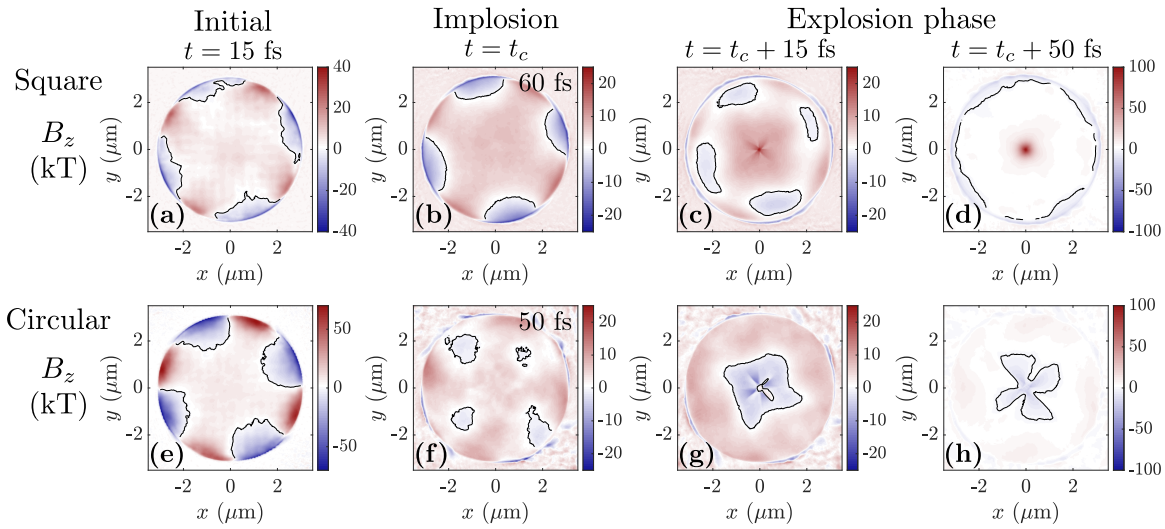

Figure 8.2: Time history of magnetic field amplification with $w_0 = 15$ μm and $B_{\text{seed}} = 3$ kT. (a)-(d) Square outer cross section target. (e)-(h) Circular outer cross section target. t_c is just before ions cross through the center of the target.

temperature T_e of 5-20 MeV ($e^{-\varepsilon/T_e}$ fit) and ion energies of 10's of MeV for protons and $\gtrsim 100$ MeV for carbon ions.

Even with no initial seed magnetic field ($B_{\text{seed}} = 0$), the departure from cylindrical symmetry introduced by the 4 laser spots produces a strong $\pm z$-directed magnetic field. This magnetic field initially has two components, a hot-electron-generated component near the edge of the target void which is visible early in time (near $r = 3$ μm in Fig. 8.1c1), and a later ion-generated component near the target center ($r \lesssim 1$ μm in Fig. 8.1c2). Electron-generated magnetic fields are also common near the surface of planar targets [22, 198], albeit with different orientation due to the difference in target geometry. The ion-generated magnetic field is driven by the strong spatial non-uniformity in the imploding ion density (Fig. 8.1d), which produces the 8-lobed magnetic field profile shown schematically in Fig. 8.1e. During the subsequent explosion ($E_r > 0$) phase, the net flow of electrons towards the target center produces a net $-E_r \times B_z$-directed current, and amplifies the ion-generated magnetic field. In the case of $B_{\text{seed}} = 0$, this process results in an amplified magnetic field profile with sub-μm-scale structure including both positive and negative lobes (Fig. 8.1c3).

The addition of $B_{\text{seed}} = 3$ kT leads to the generation of a field which is stronger and more spatially uniform than the field generated with $B_{\text{seed}} = 0$ (e.g. Fig. 8.2d vs Fig. 8.1c), but otherwise has little effect on the implosion process (the magnetic field remains too weak to magnetize the imploding ions, and only becomes strong enough to affect the dynamics of individual electrons late in time). With the seed field, the magnetic field can be amplified by the imploding ions (within 10-30 fs of t_c) in addition to the later amplification by $E \times B$ electron current [199]. This amplified field persists in excess of 100 fs in all the cases we have considered. Importantly, the magnetic field which is amplified by this process is the *locally present* magnetic field. The locally present field is the seed field in part of the parameter space, for example under the conditions shown in Fig. 8.2a-d, and in Ref. [199]. However, the application of the the seed magnetic field also triggers the production of a strong magnetic field with opposite sign at the inner target surface [198]. This surface-generated magnetic field can under other conditions reach the target center and be amplified in lieu of the seed, for example in Fig. 8.2e-h, reversing the sign of the amplified field.

Surface magnetic field generation and the processes leading to sign reversal lead to a significant dependence of the amplified magnetic field on the target, laser, and seed magnetic field conditions. A surprising consequence of this parameter dependence is shown in Fig. 8.3, where we show, for example, that the sign of the amplified magnetic field can in some cases be reversed by changing the outer cross section of the target from square to circular. The amplified magnetic field can even obtain the same magnitude in spite of the sign reversal (for example, the greater than 40-fold amplification relative to the seed shown in Cases d and h in Fig. 8.3). This is distinctly different than what would be expected from the geometric flux compression observed in 100 μm-scale implosions driven by sub-relativistic laser pulses [54, 55], and may be a unique feature of magnetic field amplification in μm-scale relativistic laser-driven implosions.

Whether the seed or the surface-generated magnetic field is amplified depends on

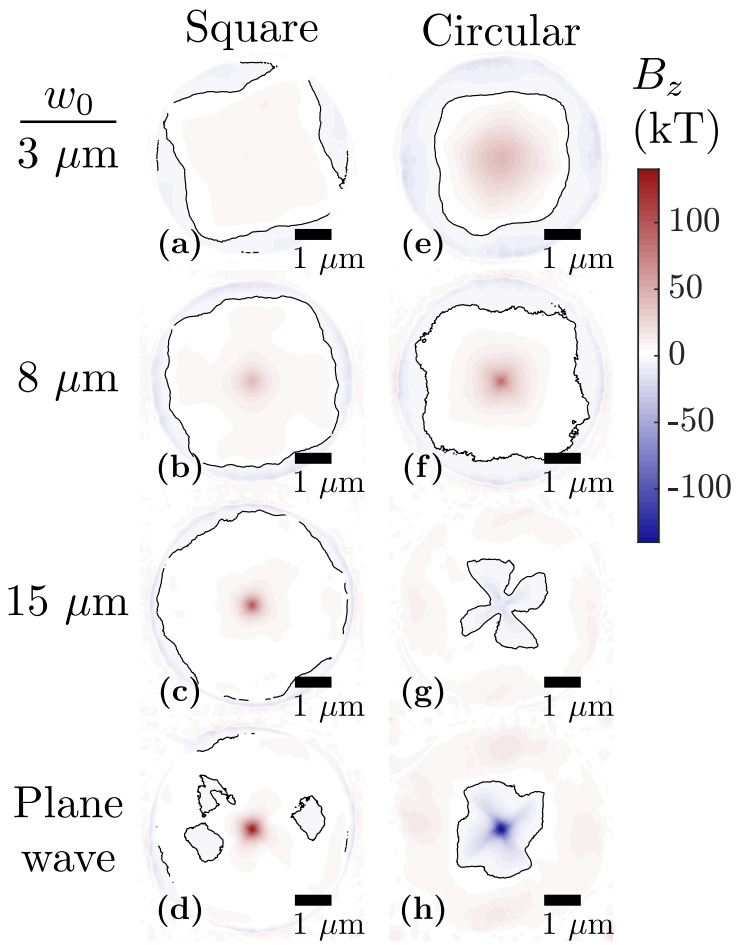

Figure 8.3: Comparison of magnetic field produced by imploding target with different target outer shapes (see Figs. 8.1a,b) and laser spot size with $B_{\text{seed}} = 3$ kT. The magnetic field is shown well after the implosion phase ($t = t_c + 50$ fs). The black contours denote $B_z = 0$.

the stability of the magnetic field at the target surface around the time ions first pass through the target center. The surface magnetic field arises due to the cyclotron rotation of laser-heated electrons transiting radially through the target [198] (shown conceptually in Fig. 8.4a). The current associated with the cyclotron rotation of these hot electrons and the compensating return current in the target create a double current layer near the surface (e.g. Fig. 8.4b), which produces the surface magnetic field. The surface-generated field competes with and can also suppress the electron-associated field [198], and is visible in the dominance of the $-z$-directed field close to (within ~ 0.1 μm of) the target inner surface in Figs. 8.2a,e.

We observe that the surface current is disrupted if the magnetic field within the target bulk changes substantially during the implosion. The four laser pulses driving the implosion seed a periodic structure in the plasma density and magnetic field at the outer target surface. These initial perturbations combined with the ongoing streaming of hot electrons through the relatively cold target produce a growing filamentary magnetic field structure within the target itself (Figs. 8.4e,f). The penetration of these filaments deep into the target significantly alters the momentum of hot electrons streaming through the target, disrupting the surface current generation process (for example Fig. 8.4d). The changing surface current launches regions of negative magnetic field into the target center, where they can be amplified, as shown for example in Fig. 8.2e-h, where Fig. 8.2f shows the field in transit towards the target center.

Amplification of the sign-reversed magnetic field only occurs, however, if the field is able to reach the target center before the seed field becomes substantially amplified, which requires the magnetic filaments to grow and the surface current to be disrupted before or only slightly after ions reach the target center. We find that whether the filaments are able to grow through the full target thickness in time to affect the magnetic field amplification depends on the target, laser, and seed magnetic field parameters. The filament growth is

in a nonlinear regime and may be challenging to predict analytically. However, in general we observe that the higher the population of hot electrons and the weaker the applied magnetic field, the faster the filaments grow.

In the context of the scan over the laser spot size and outer target shape shown in Fig. 8.3, we observe a larger population of recirculating hot electrons in the cases where the magnetic field within the target is disrupted before the ions reach the target center (Cases g-h) than in the other cases. More hot electrons are initially produced in these cases due to the large laser spot and the departure of the laser from normal incidence provided by the circular outer cross section (which allows for more efficient electron production from a sharp interface [202]).

The impact of this difference in the recirculating hot electron population on the magnetic field amplification process can be seen for example in the comparison of the circular and square outer cross section cases with $w_0 = 15\ \mu$m shown in Figs. 8.2 and 8.4. In the square case, the magnetic field within the target bulk remains mostly unperturbed (Fig. 8.4e) and the surface current is stable (Fig. 8.4c). The magnetic field near the target center maintains the same sign as the applied seed throughout the implosion and the final amplified magnetic field is positive (Fig. 8.2a-d). In contrast, in the circular case, the magnetic field filaments penetrate through the full target thickness by around $t = 45$ fs (Fig. 8.4f), disrupting the surface current (Fig. 8.4d). Before this time, the magnetic field in the void is qualitatively similar between the circular and square cases, albeit with somewhat different magnitude (Figs. 8.2a,e). After this time, however, the surface magnetic field in the circular case is broken up and regions of negative magnetic field are pushed into the target center (Fig. 8.2f). The timing of the disruption of the surface magnetic field is such that this negative, originally surface-generated field is present in the center during the explosion phase and is amplified in lieu of the seed field (Fig. 8.2g-h).

In addition to the target outer shape and laser spot size, the sign reversal of the

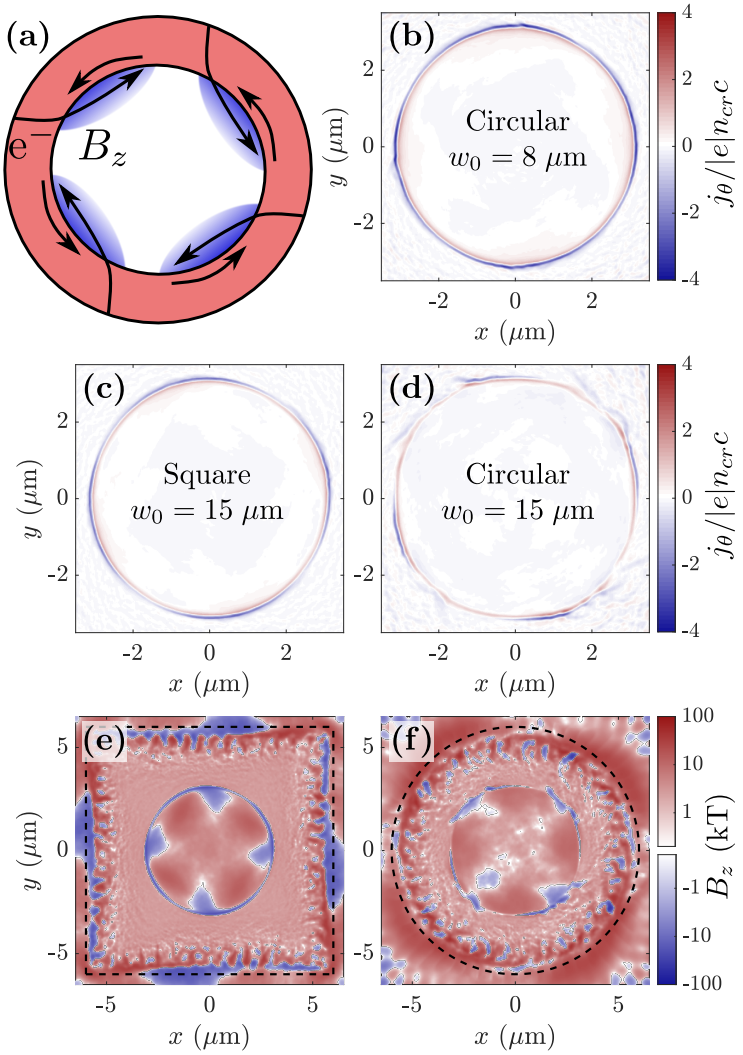

Figure 8.4: Formation and disruption of surface magnetic field. (a) Conceptual diagram of surface magnetic field generation. A surface field with opposite sign from the applied seed is driven by the azimuthal current. (b)-(d) Azimuthal current density j_θ at $t = 50$ fs for (b) circular target with 8 μm laser spot, (d) square target with 15 μm spot, (d) circular target with 15 μm spot. (e)-(f) Magnetic field in the 15 μm spot cases at $t = 45$ fs with (e) square and (f) circular outer cross section. Dashed lines indicate the initial target outer surface.

amplified magnetic field relative to the seed can depend on a number of other target, laser, and seed magnetic field parameters. In principle, any parameter which affects the timing of the implosion or the growth of the magnetic field filaments could affect the sign of the final generated field. To further illustrate this sensitivity, we have additionally scanned over the target thickness and seed magnetic field strength. Figure 8.5 summarizes how these parameters, as well as the target shape and laser spot size, affect the sign reversal of the amplified magnetic field.

First, we consider the effect of the target thickness. We have conducted additional simulations with a spatially plane wave laser pulse with the same FWHM pulse duration as given in Table 8.1 and a $\sin^2$ temporal shape in $|E|$ (to reduce the computational cost), scanning over the minimum target thickness Δx. For this parameter scan, we specifically consider the effect of Δx on the sign reversal in a target with outer circular cross section. The change of the temporal shape of the laser pulse from Gaussian to $\sin^2$ has negligible effect on the magnetic field observed in the target and the final magnetic field profile in the $\Delta x = 3\,\mu$m case is nearly identical to the result given in Fig. 8.3h.

We find that decreasing the target thickness relative to the nominal case (e.g. decreasing Δx from 3 μm to 1 μm) has no effect on the sign of the magnetic field. If, however, the target thickness is increased (e.g. $\Delta x = 6\,\mu$m), the magnetic filaments are unable to penetrate through the full target thickness before the implosion, the surface magnetic field is stable, and the final generated field has the same sign as the applied seed (Fig. 8.5d).

Second, we consider the effect of the seed magnetic field strength. We return to the conditions given in Table 8.1 (temporally Gaussian laser pulse with $\Delta x = 3\,\mu$m). We observe that increasing B_{seed} from 3 kT (the nominal case) to 6 kT changes the sign of the final generated field (Fig. 8.5e). In the 6 kT case, the increased B_{seed} prevents the magnetic field filaments from penetrating deep into the target and allows the surface-generated

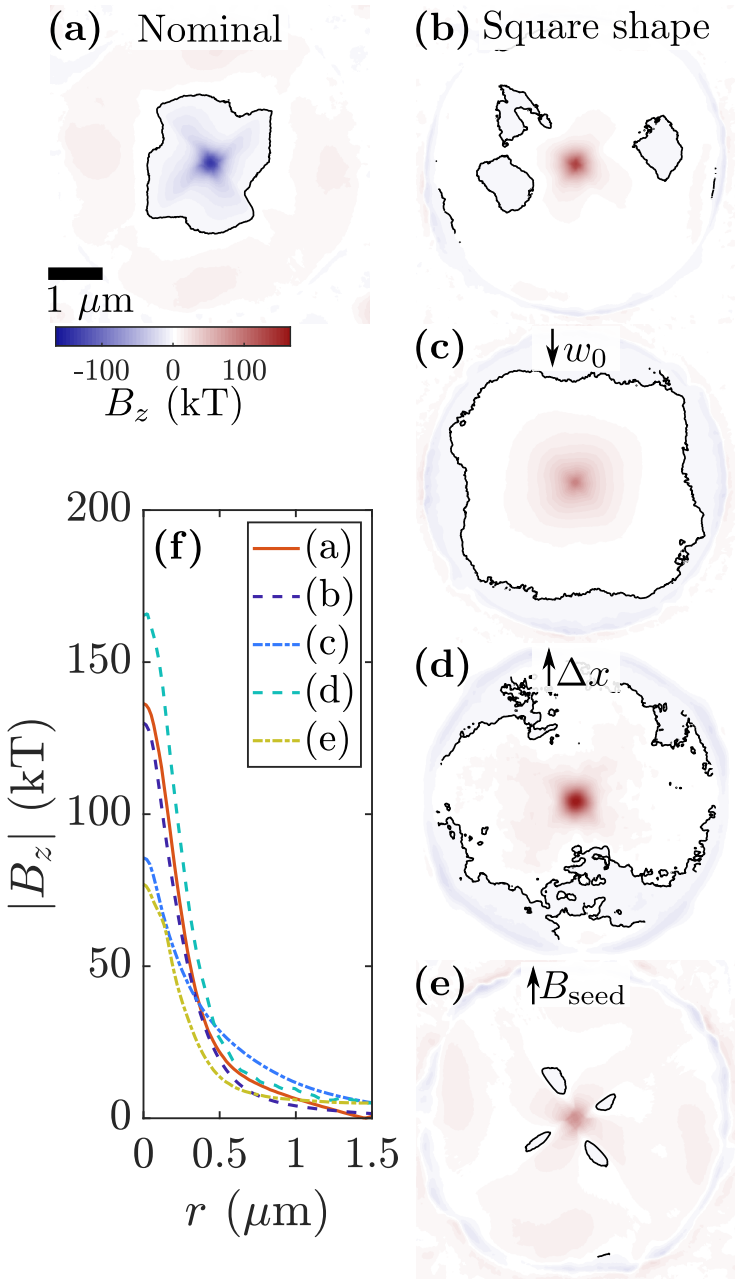

Figure 8.5: Dependence of the sign of the amplified magnetic field on key parameters. (a) Circular plane wave case, with other parameters as given in Table 8.1. (b)-(e) denote changes relative to the case given in (a), with (b) square outer cross section, (c) 8 μm laser spot size, (d) 6 μm thick target, and (e) $B_{\text{seed}} = 6$ kT. (f) Azimuthally averaged magnetic field $|B_z(r)|$ corresponding to (a)-(e). The time shown is $t = t_c + 50$ fs. Black contours in (a)-(e) denote $B_z = 0$.

magnetic field to be stable.

This dependence of the sign of the amplified magnetic field on B_{seed} was previously seen in Ref. 199, in simulations where the laser-plasma interaction was replaced by an initial distribution of hot electrons. The observed sign reversal of the magnetic field in the hot electron case may also be attributable to the destabilization of the surface-generated magnetic field. However, the inclusion of hot electrons throughout the target instead of their generation at the surface, as well as the lack of laser-imposed perturbations likely changes the dynamics of the surface field breakup.

As a final test, we have additionally considered the robustness of the sign reversal to pre-filling the target void with plasma. This partial filling of the void represents the initial inward expansion of the target which would under realistic conditions be driven by laser prepulse. In plane wave simulations otherwise matching the conditions given in Table 8.1, we find that although pre-fill may affect the magnitude of the amplified magnetic field, it does not have a significant effect on its sign or spatial profile, provided the pre-fill density remains below the hot electron density associated with the implosion ($\sim n_{cr}$). Although full verification will require modeling the prepulse directly, this preliminary result suggests the sign reversal phenomenon may still be observable under realistic laser conditions.

In summary, we have demonstrated that magnetic field amplification in imploding microtube targets can produce magnetic fields with amplitude in excess of 40 times an applied seed field with a polarity that either matches the seed or is opposite to it. Such a result is of interest within the field of magnetic field amplification, not only for the high magnetic field amplitude produced, but also the demonstrated reversal of the magnetic field polarity. In the context of an imploding microtube target, the potential to generate a strong magnetic field with either sign is related to the ability of the target to amplify the locally present magnetic field in the void and the production of a strong magnetic field at the inner target surface with opposite sign to the seed. Whether the applied

seed field or the surface field is amplified depends on the stability of the surface current, which is determined by the growth of laser-seeded magnetic filaments within the target. Consequently, we find that the sign of the generated magnetic field can be reversed by changes to the target, laser, and seed magnetic field configuration. This sensitivity of the magnetic field amplification process to effects which may not be considered in simple amplification models may be an important consideration in the design of future platforms for magnetic field generation. Additionally, the ability to controllably reverse the sign of the magnetic field with only small changes to the experimental configuration could make laser-driven microtube implosions an interesting platform for future study of the generation and effects of strong magnetic fields in high energy density plasma.

8.3 Acknowledgements

Chapter 8, in full, is a reprint of the material as it appears in K. Weichman, M. Murakami, A. P. L. Robinson, and A. V. Arefiev, "Sign reversal in magnetic field amplification by relativistic laser-driven microtube implosions", *Applied Physics Letters* (2020, accepted), with the permission of AIP Publishing. The dissertation author was the primary investigator and author of the paper.

This research was supported by the DOE Office of Science under Grant No. DE-SC0018312. Particle-in-cell simulations were performed using EPOCH [71], developed under UK EPSRC Grant Nos. EP/G054940, EP/G055165, and EP/G056803. This work used HPC resources of the Texas Advanced Computing Center (TACC) at the University of Texas at Austin and the Extreme Science and Engineering Discovery Environment (XSEDE) [126], which is supported by National Science Foundation grant number ACI-1548562. Data collaboration was supported by the SeedMe2 project [117] (http://dibbs.seedme.org).

Chapter 9

Magnetic field generation in a laser-irradiated thin collisionless plasma target by return current electrons carrying orbital angular momentum

9.1 Abstract

Magnetized high energy density physics offers new opportunities for observing magnetic field-related physics for the first time in the laser-plasma context. We focus on one such phenomenon, which is the ability of a laser-irradiated magnetized plasma to amplify a seed magnetic field. We performed a series of fully kinetic 3D simulations of magnetic field amplification by a picosecond-scale relativistic laser pulse of intensity 4.2×10^{18} W/cm^2 incident on a thin overdense target. We observe axial magnetic field

amplification from an initial 0.1 kT seed to 1.5 kT over a volume of several cubic microns, persisting hundreds of femtoseconds longer than the laser pulse duration. The magnetic field amplification is driven by electrons in the return current gaining favorable orbital angular momentum from the seed magnetic field. This mechanism is robust to laser polarization and delivers order-of-magnitude amplification over a range of simulation parameters.

9.2 Introduction

High energy density physics (HEDP) emerged as a new sub-field only about two decades ago, but has already substantially advanced our understanding of materials under extreme conditions and led to the development of several applications, such as those involving energetic particle beams. Much of this progress is due to breakthroughs in laser technology which have enabled drivers capable of depositing energy on a picosecond time scale and creating the high energy density state of matter [203]. Until recently, quasi-static magnetic fields have been of relatively low importance in HEDP research due to the technological challenges associated with generating sufficiently strong macroscopic fields at the laser facilities used for HEDP research.

The recent development of open-geometry, all-optical magnetic field generators [23, 24, 204] which are portable to any high-energy laser facility has opened up new regimes relevant to magnetized HEDP to exploration. It is now feasible to experimentally probe laser-plasma interactions with an embedded magnetic field that reaches hundreds of Tesla in strength. As a result, there has been an increased interest in laser-driven, high-energy-density systems embedded in strong magnetic fields. Such systems may deliver advances in inertial confinement fusion [14, 205, 206], particle sources [18, 130], and atomic physics [207].

Concurrently, limitations on the strength of externally applied magnetic fields have also stimulated research into mechanisms of magnetic field generation and amplification by

the laser-irradiated plasma itself. One such well-known method for generating quasi-static magnetic axial fields in an underdense plasma is the inverse Faraday (IF) effect enabled by circularly polarized light [145, 149, 208, 209]. An underdense plasma with net orbital angular momentum (OAM) can also be created using intense twisted laser beams rather than circularly polarized lasers [210–212]. Magnetic field generation has also been observed in solid density targets, including the generation of azimuthal surface and bulk magnetic fields due to the propagation of relativistic electron beams [146, 147, 213], and is beneficial for hot electron transport and electron beam collimation [145, 209, 214–217]. Magnetic field amplification has also been observed in laser-produced plasma, for example in shocks [148], colliding flows [218], implosions [168, 205, 219], and with twisted light [220].

In this paper, we introduce a novel method for the amplification of a seed axial magnetic field in the interaction of a picosecond-scale, relativistic intensity laser pulse with a thin overdense target. This mechanism persists for both linear and circular polarization and can amplify a seed axial magnetic field of 20-100 T by a factor of 10. This paper is organized as follows: In Section 9.3, we demonstrate magnetic field amplification for three choices of laser polarization, which distinguishes our amplification mechanism from the inverse Faraday effect. In Section 9.4, we show that the magnetic field amplification is associated with the azimulthal current we observe in simulations, which in Section 9.5 we identify as originating from the favorable orbital angular momentum electrons gain in the return current. In Section 9.6, we explore the robustness of the amplification mechanism to the choice of simulation parameters.

9.3 Observation of axial magnetic field amplification

We conduct 3D simulations of a picosecond-scale, relativistic intensity laser pulse interacting with a thin target of fully ionized hydrogen with an imposed uniform axial seed

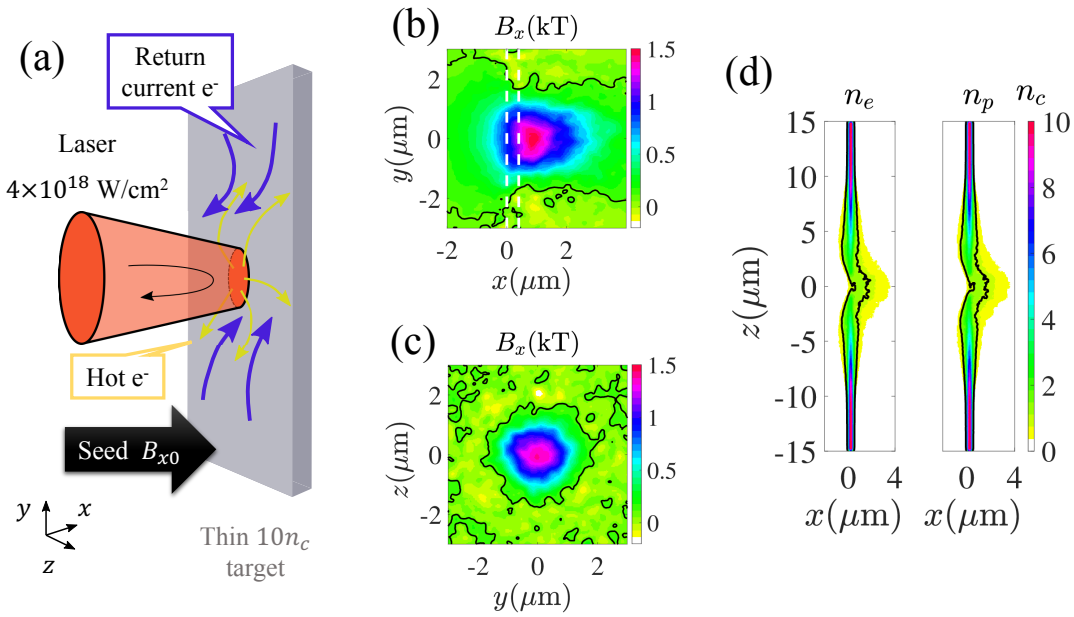

Figure 9.1: Magnetic field amplification in a thin laser-irradiated target. (a) Schematic of axial magnetic field amplification. Initially, the laser pondromotively expels electrons creating charge separation. Later, electrons in the return current gain favorable OAM in the seed magnetic field, creating an azimuthal current which amplifies the field. (b) and (c) Amplified axial magnetic field for the right hand circularly polarized case (Table 9.1) at $t = 340$ fs in the (b) x-y plane (z = 0 μm, dashed lines denote the original target position), and (c) y-z plane (x = 0.5 μm). The black contours denote $B_x = B_{x0}$. B_x is temporally (16 fs) and spatially averaged in the plane with stencil size 0.25 μm×0.25 μm. (d) Electron (left) and proton (right) density at $t = 340$ fs. The black contours denote the critical density n_c.

Table 9.1: 3D PIC simulation parameters. $n_c = 1.8 \times 10^{21}$ cm^{-3} is the critical density corresponding to the laser wavelength. The target is initialized without any preplasma. We confirmed that the resolution is adequate by conducting partial simulations with 4 particles per cell and 50 cells/μm. We have also conducted simulations with a smaller problem size with up to 20 particles per cell. These simulations further support the adequacy of our resolution.

Laser parameters	
Peak intensity	4.2×10^{18} W/cm^2
Normalized field amplitude	
Right hand circular polarization	$a_{y0} = a_{z0} = 1.0$
Wavelength	$\lambda = 0.8$ μm
Pulse duration ($\sin^2$ electric field)	$\tau_g = 600$ fs
Focal spot size (1/e electric field)	3 μm
Location of the focal plane	$x = -2$ μm
Laser propagation direction	$+x$
Other parameters	
Target thickness	0.4 μm
Electron density	$n_e = 10\, n_c$
Seed magnetic field strength	$B_{x0} = 0.1$ kT
Transverse size of simulation box	30 μm $\times$30 μm
Boundary conditions	open
Spatial resolution	40 cells/μm
Macroparticles per cell for each species	2
Position and time reference	
Location of the front of the target	$x = 0$
Time when peak of the laser is at $x = 0$	$t = 0$

magnetic field B_{x0}. We take the laser pulse to be either circularly or linearly polarized while keeping the same peak intensity. Simulations were carried out using the fully relativistic particle-in-cell code EPOCH [71]. Detailed parameters for the simulation are given in Table 9.1. Energy was well conserved in these simulations.

We observe magnetic field amplification for three different laser polarization configurations, right hand circularly polarized, left hand circularly polarized, and linearly y-polarized. The relative strengths of the amplified magnetic field are given in Table 9.2. In the right hand circularly polarized case, the seed magnetic field is amplified from the initial $B_{x0} = 0.1$ kT to a peak amplitude of $B_x = 1.5$ kT over a volume of 4 μm^3 in approximately 300 fs. Fig. 9.1(b) and (c) show the axial magnetic field in the x-z and y-z planes. The

Table 9.2: Amplified magnetic field strength for three laser polarizations with initial seed magnetic field $B_{x0} = 0.1$ kT and for right hand circular polarization with no seed magnetic field ($B_{x0} = 0$).

Polarization	**Peak magnetic field**	**Averaged magnetic field**
Right hand circular	1.5 kT	0.9 kT
Left hand circular	0.6 kT	0.38 kT
Linear	0.8 kT	0.45 kT
No seed magnetic field ($\mathbf{B_{x0} = 0}$)		
Right hand circular	0.4 kT	0.2 kT

dashed lines in Fig. 9.1(b) correspond to the initial position of the target. In contrast with the dramatic axial magnetic field amplification shown in Table 9.2, no substantial change is seen in the azimuthal magnetic field upon adding the axial seed magnetic field (see Appendix 9.12).

By probing different laser polarizations, we find that the observed magnetic field amplification clearly goes beyond the inverse Faraday (IF) effect. In the IF effect, the spin angular momentum of a circularly polarized laser [208] or the orbital angular momentum of a twisted laser [149] is transferred to electrons in the plasma, driving the generation of a magnetic field. In the absence of a seed magnetic field, the right hand circularly polarized laser pulse generates a peak magnetic field of $B_x = 0.4$ kT. A left circularly polarized laser would generate $B_x = -0.4$ kT. In all cases with a seed magnetic field, we see peak magnetic fields in the same direction as the seed significantly above this level. We additionally observe substantial magnetic field amplification with linear polarization keeping the same peak intensity, albeit with broken symmetry in the y-z plane (see Appendix 9.9), and with a left hand circularly polarized laser pulse, where the IF effect generates a magnetic field in the opposite direction from the initial seed. As shown in Table 9.2, the strongest magnetic field is generated with right hand circular polarization, followed by linear polarization and then left hand circular polarization. In light of these simulations, we find it likely that the high magnetic field amplitude we observe in the right hand circularly polarized simulation

represents a combination of magnetic field generation via the IF effect and magnetic field amplification via the novel mechanism we describe in this work. The remainder of this work will elucidate the magnetic field amplification process incorporating analysis of the right hand circularly polarized case.

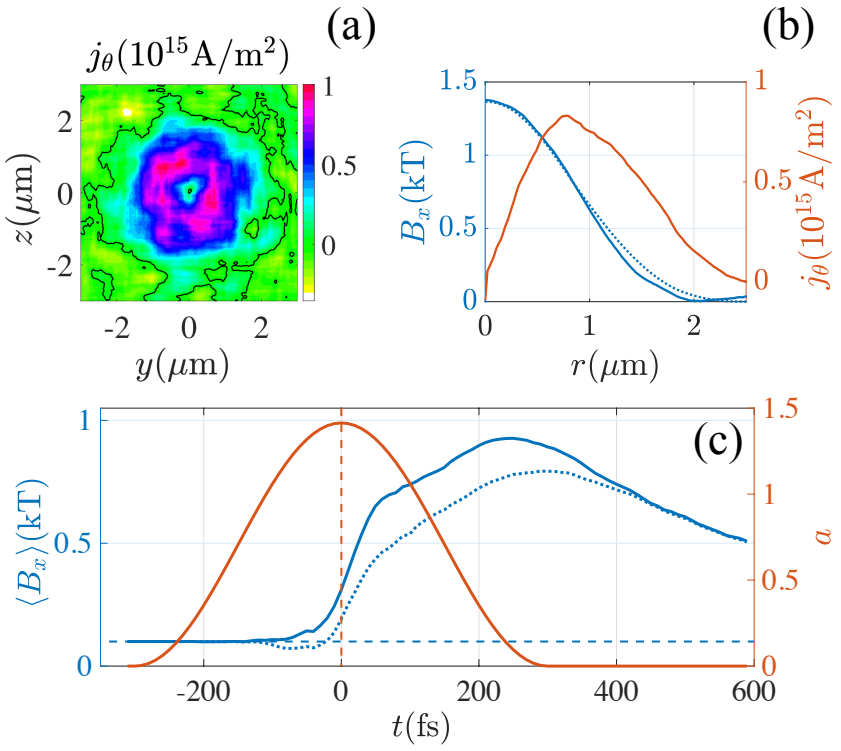

Figure 9.2: Azimuthal current density, axial magnetic field strength, and reference laser amplitude. (a) Slice of azimuthal current density at $t = 340$ fs and $x = 0.5$ μm. (b) Radial dependence of axial magnetic field and azimuthal current density at $t = 340$ fs, averaged over all θ and averaged in x over 0.4 μm $< x <$ 0.9 μm. Solid blue line: B_x measured from simulation. Dotted blue line B_x calculated from Ampère's law using the shown j_θ. The calculation was performed for $r <$ 2.5 μm with $B_x(r = 2.5\,\mu\mathrm{m}) = 0$. (c) Time evolution of axial magnetic field strength (blue curves, left axis), with reference laser amplitude a at the target surface (red line, right axis). Solid blue line: $\langle B_x\rangle$ averaged over the cylinder $r < 1$ μm, $0 < x < 1$ μm (the same volume as Table 9.2). Dotted blue line: average over a longer cylinder with the same radius ($r < 1$ μm, $0 < x < 2$ μm), to capture the initial diamagnetic plasma response. The red dashed line denotes $t = 0$, which is when the peak of the laser pulse would pass the front target surface in the absence of the plasma. The simulation parameters are as given in Table 9.1.

9.4 Relationship between magnetic field amplification and j_θ

We find that magnetic field amplification is driven by electrons in the return current that arises after the peak of the laser pulse hits the target surface. When the laser pulse interacts with the target, it expels electrons from the laser spot, creating charge separation which later induces a return current of electrons relaxing back towards the laser interaction volume to neutralise the space charge. This return current obtains orbital angular momentum (OAM) from the seed axial magnetic field (Fig. 9.1(a)). The corresponding azimuthal current j_θ (Fig. 9.2(a) and (b)) drives the amplification of the seed magnetic field.

In our simulations, magnetic field amplification is driven by the generation of an azimuthal current by electrons which gain favorable OAM. First, in this Section, we show that the observed magnetic field amplification can be explained quasistatically, and is tied to the azimuthal current. Then, in Section 9.5, we demonstrate how this azimuthal current can be generated by the electron return current and can persist over hundreds of femtoseconds.

We find that the azimuthal current j_θ is responsible for the magnetic field amplification. We demonstrate this in two ways. First, we perform an order of magnitude estimate for the maximum axial magnetic field based on the j_θ we observe in simulations. We see that a positive azimuthal current density $j_\theta \sim 10^{15}$ A/m^2 develops at small radius (e.g. Fig. 9.2(a) and (b)) during the amplification process. We estimate the maximum axial magnetic field generated from j_θ using the Biot-Savart law [221], which we simplify by assuming the current density is uniform over the radial extent R and the longitudinal

extent $2\Delta x$,

$$B_x^{\max} = \frac{\mu_0}{2}\int_0^R \int_{-\Delta x}^{\Delta x} j_\theta \frac{r^2}{(r^2+x^2)^{3/2}} \mathrm{d}x\mathrm{d}r = \mu_0 j_\theta \Delta x \,\mathrm{arsinh}(R/\Delta x). \tag{9.1}$$

We estimate $R = \Delta x \sim 1$ μm, which predicts a maximum magnetic field strength of $B_x^{\max} \sim 1$ kT, close to the peak magnetic field strength $\langle B_x \rangle = 0.9$ kT shown in Fig. 9.2(b), which was averaged over a cylindrical volume with radius and length of 1 μm.

Second, we calculate the magnetic field profile as a function of radius based on Ampère's law. The azimuthal current density and amplified magnetic fields we observe are fairly azimuthally symmetric (Figs. 9.1(c) and 9.2(a)). In the limit of perfect azimuthal symmetry, the axial magnetic field depends only on the azimuthal current density. We find good agreement between the axial magnetic field calculated from j_θ and the radial magnetic field profile in simulations (Fig. 9.2(b)). Thus, we find that the magnetic field amplification is magnetostatic and driven by j_θ.

We can also use the azimuthal current density to calculate the OAM density produced in this simulation. The OAM density of electrons as a function of position r can be written as $l_x = r m_e n_e v_\theta$, where m_e is the electron mass, n_e is the number density, and v_θ is the effective azimuthal velocity. The effective azimuthal velocity is related to the current density by $v_\theta = -j_\theta/(|e|n_e)$, which allows us to calculate the OAM density as $l_x = -r m_e j_\theta/|e|$. Using j_θ as given above and the electron density from simulations, $n_e \approx 10^{21}$ cm^{-3}, we find that the OAM density is $l_x = -0.02$ kg/m-s at $r = 1$ μm and $v_\theta \approx 0.02c$. In terms of the energy content, we find that the energy in the magnetic field ($\varepsilon_B = \int B^2/(2\mu_0) dV \approx 1$ μJ) remains small compared to the kinetic energy of electrons around the amplifying area (≈ 50 μJ).

9.5 Relationship between j_θ and the OAM of the return current

We now illustrate how the azimuthal current is produced by electrons which gain favorable OAM. When the laser pulse interacts with the target, the ponderomotive force expels electrons from the laser spot. Initially, this creates a net charge separation within the laser spot (see Appendix 9.10), which later induces a return current. This radially inward return current gains favorable OAM from the axial magnetic field and consequently provides the j_θ responsible for magnetic field amplification.

We use the trajectories of test electrons participating in the magnetic field amplification to illustrate the amplification process. During the amplification, we randomly select electrons at the sampling time t_s from the area in which the magnetic field is amplified ($0.5\ \mu\text{m} < x < 1.0\ \mu\text{m}$, $|y| < 3\ \mu\text{m}$, $|z| < 3\ \mu\text{m}$). We then track the full time history of these electrons to capture where they originated and demonstrate how they can obtain OAM.

The averaged trajectory of 344 electrons selected at time $t_s = 290$ fs is given in Fig. 9.3. By analyzing the individual (e.g. the movie in Appendix 9.11) and averaged transverse position of these electrons ($r_e(t)$, the blue line in Fig. 9.3(a)), we see that the majority of these electrons originate from radius $r_e > 10\ \mu$m, well outside the laser spot, and move inward to small radius during the falling edge of the laser pulse ($t > 0$). These observations identify these electrons as belonging to the return current.

We further see that inward motion of electrons can generate a negative average OAM ($l_{ex} < 0$) due to the axial seed magnetic field, which drives magnetic field amplification. The effect of the azimuthal magnetic field is already captured in the trajectory $r(t)$ and does not exert an azimuthal force on the electrons (see Appendix 9.12). The average radial velocity, $v_{er} \equiv \mathrm{d}r_e/\mathrm{d}t$, of the test electrons is shown in the red line in Fig. 9.3(a). In order to illustrate how the sign of the OAM can be favorable for magnetic field amplification,

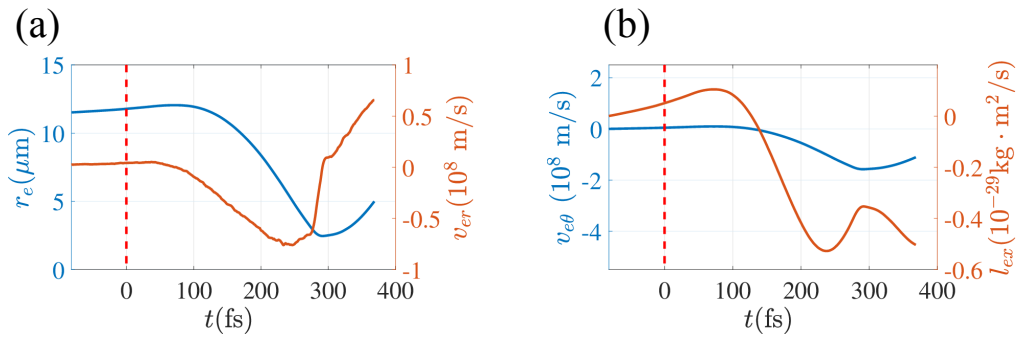

Figure 9.3: Average trajectory of 344 electrons participating in the amplification process. (a) Averaged radial position of electrons r_e (blue line, left axis) and radial velocity $v_{er} = \mathrm{d}r_e/\mathrm{d}t$ (red line, right axis). (b) Azimuthal velocity which would be expected based on interaction with the seed magnetic field $v_{e\theta} = \int |e| v_{er} B_{x0}/m_e \mathrm{d}t$ (blue line, left axis) and corresponding OAM per electron $l_{ex} = m_e v_{e\theta} r$ (red line, right axis). Red dashed lines indicate $t = 0$, the time when the laser pulse is at its peak at $x = 0$. Electrons were randomly chosen within the cubic volume $0 < x < 1$ μm, $|y| < 3$ μm, $|z| < 3$ μm at the sampling time $t_s = 290$ fs. The simulation parameters are as given in Table 9.1.

we consider the azimuthal velocity this radial velocity produces in conjunction with the seed field ($v_{e\theta} = \int |e| v_{er} B_{x0}/m_e dt$), and its corresponding OAM ($l_{ex} = m_e v_{e\theta} r_e$). Fig. 9.3(b) shows that the negative inward radial velocity associated with the return current can drive $v_{e\theta} < 0$ and $l_{ex} < 0$, which represents a net positive azimuthal current ($j_{e\theta} > 0$) for this group of electrons. The net rotation of electrons in the y-z plane is also immediately visible in the trajectories of the electrons, e.g. the movie in Appendix 9.11.

We replicate the above analysis for groups of electrons chosen at different sampling times, ($t_{s1} = 140$ fs, $t_{s2} = 190$ fs, $t_{s3} = 240$ fs, $t_{s4} = 290$ fs) and find a negative azimuthal velocity ($v_{e\theta} < 0$, Fig. 9.4) can be maintained in the region of magnetic field amplification over a long time, consistent with our observation that a positive azimuthal current density at $r = 0.5$ μm is maintained in the simulation over hundreds of femtoseconds (red line in Fig. 9.4). Looking earlier in time, we see that the azimuthal current density is negative around the time when the peak of the laser pulse impacts the target ($t = 0$, red dashed line in Fig. 9.4). This is consistent with our observation that it is the return current that drives magnetic field amplification.

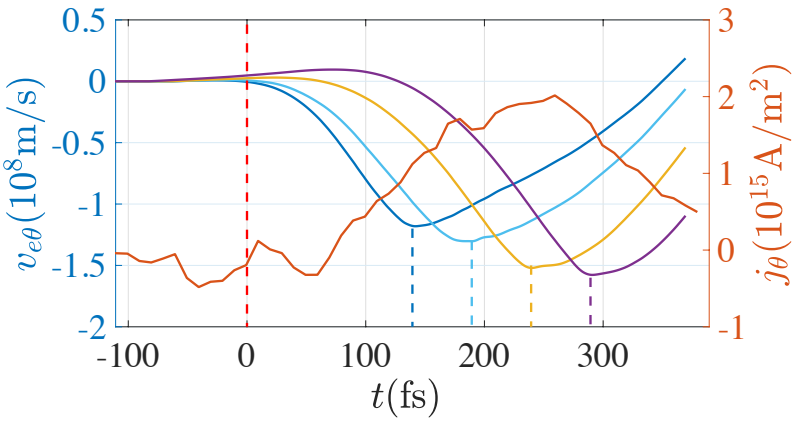

Figure 9.4: Azimuthal velocity for different sets of sampled electrons and azimuthal current density in the plasma. (a) Azimuthal velocity $v_{e\theta}$ (left axis) calculated as described in Fig. 9.3 for different sampling times ($t_{s1} = 140$ fs, $t_{s2} = 190$ fs, $t_{s3} = 240$ fs, $t_{s4} = 290$ fs), and azimuthal current density (red line, right axis) at location $x = 0.4$ μm and averaged over the circle defined by $r = 0.5$ μm. The red dashed line denotes the time when the laser intensity at the front target surface ($x = 0$) is maximum. The simulation parameters are as given in Table 9.1.

The net cycle-averaged inward force on an electron starting near rest (i.e. neglecting the magnetic force) encodes the competition between the ponderomotive force of the laser pushing the electron outward and the force due to charge separation pulling the electron inward. During the rising edge of the laser pulse ($t < 0$), electrons are pushed predominantly outward, and we see a small negative azimuthal current density, corresponding to the usual diamagnetic plasma response. We find that the diamagnetic response predominantly affects the axial magnetic field at the rear target surface, but does not have much effect on the magnetic field within the target (see the two blue curves in Fig. 9.2(c), which are averaged over different ranges in x). During the subsequent falling edge of the laser pulse (to the right of the red dashed line in Fig. 9.2(c)), the force associated with charge separation can overcome the ponderomotive force of the laser and a net return current is produced.

We find that the return current is able to drive magnetic field amplification during the falling edge of the laser pulse from $\langle B_x \rangle \approx B_{x0} = 0.1$ kT to $\langle B_x \rangle = 0.9$ kT. The amplification occurs over approximately 250 fs, which is comparable to both half the pulse

duration ($\tau_g/2 = 300$ fs) and the cyclotron period for an electron in the initial 0.1 kT seed field ($\tau_B = 340$ fs). The relationship between amplification and these timescales is discussed in more detail in Section 9.6. After $t = 240$ fs, by which time the laser pulse has mostly reflected from the target (see Fig. 9.2(c)), the magnetic field begins to slowly decay. Over the course of the amplification, the charge separation (which peaks around $t = 0$) substantially decreases, but does not return to zero (see Appendix 9.10) and we find that both the positive azimuthal current density (e.g. Fig. 9.4) and the amplified magnetic field (Fig. 9.2(c)) can persist for hundreds of femtoseconds.

9.6 Parameter scan

We now investigate the robustness of the amplification mechanism described in Sections 9.4 and 9.5 to the choice of simulation parameters. First, we scan the seed magnetic field strength B_{x0} holding all the other parameters the same as in Table 9.1 and investigate the balance of magnetic field amplification via our mechanism versus magnetic field generation via the IF effect. For a seed magnetic field strength below 20 T, the axial magnetic field becomes indistinguishable from the field produced in the absence of any seed magnetic field , as shown in Fig. 9.5(a). In other words, below 20 T no net magnetic field amplification is seen and the observed magnetic field can be attributed to magnetic field generation via the IF effect. In contrast, for a seed magnetic field strength above 20 T, we see that the seed magnetic field can be amplified by a factor of 10. The growth rate of the magnetic field during the initial linear rise increases as the seed field strength is increased (dashed lines in Fig. 9.5).

Second, we scan over the laser pulse duration τ_g at the original seed magnetic field strength ($B_{x0} = 0.1$ kT) to probe the impact of pulse duration on the magnetic field amplification. We see that the net amplification becomes weaker as the driving laser pulse

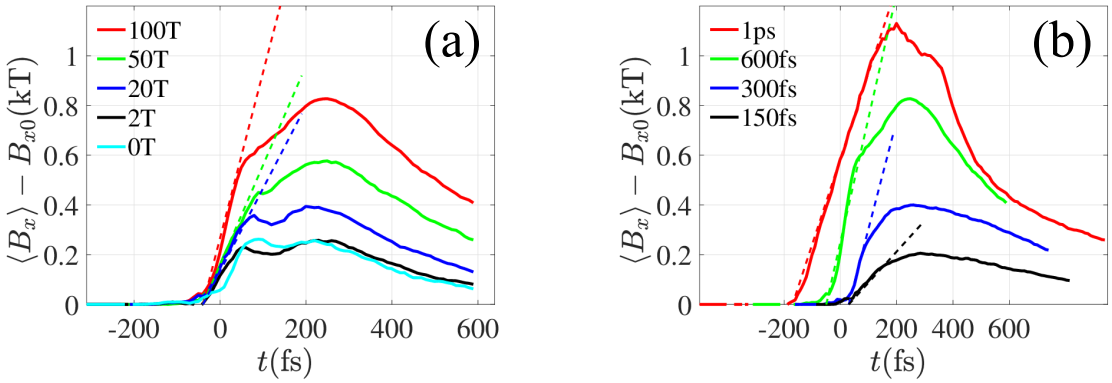

Figure 9.5: Net amplification of the axial magnetic field. (a) Scan over the seed magnetic field strength B_{x0}. (b) Scan over laser pulse duration. The parameters not scanned over are as given in Table 9.1. Only the net amplification, $\langle B_x \rangle - B_{x0}$, is shown. $\langle B_x \rangle$ is averaged over the cylinder $r < 1$ μm, $0 < x < 1$ μm. Dashed lines indicate the growth rate of the magnetic field during the initial, roughly linear phase.

duration becomes shorter and that the growth rate of the field during the initial linear rise is maximum for the 600 fs case, as shown in Fig. 9.5(b). We can obtain an average magnetic field as high as 1.1 kT for a pulse duration of 1 ps.

In conjunction with these first two parameter scans, we note that the period of electron Larmor precession in $B_{x0} = 0.1$ kT is around $\tau_B = 340$ fs and that for $B_{x0} = 20$ T, we have $\tau_B = 1700$ fs. This suggests that the amplification process requires the laser pulse duration to be sufficiently long that $\tau_g \gtrsim 0.5\,\tau_B$. This requirement on the pulse duration is consistent with our observation that the magnetic field amplification is driven by the return current. The return current rises and decays with the laser-induced charge separation, which decreases rapidly on the timescale of the pulse duration during the falling edge of the laser pulse (see Appendix 9.10). Thus, the primary return current timescale is the pulse duration. Over this time, electrons must undergo substantial momentum rotation to gain the orbital angular momentum needed to amplify the magnetic field, which sets the requirement that the pulse duration be at least on the order of the cyclotron period.

Third, we consider the robustness of the magnetic field amplification to the target

thickness. The use of a thin target (0.4 μm thickness) in our original simulations maintains the feasibility of having the seed axial magnetic field penetrate the target on a reasonable time scale. However, for thicker targets the experimental time scales for generating the seed field and allowing it to penetrate into the target must be accounted for. For example, experiments have shown that the capacitor coil target can produce an axial magnetic field in excess of 0.1 kT with a sub-nanosecond rise and slow decay in excess of 10 nanoseconds [23, 24, 30], which corresponds to approximately a 10 μm penetration depth into a copper-like conductive material. Without performing fully self-consistent simulations of the magnetic field penetration into the target, we are therefore limited to studying μm-scale target thickness. For the sake of demonstrating that magnetic field amplification is feasible in a thicker target, we consider a second case with 2 μm thickness. We see that kilotesla-level magnetic field amplification is still present, albeit over a smaller spatial scale and with a somewhat reduced amplitude (see Appendix 9.9).

9.7 Summary and discussion

We demonstrate a novel mechanism for magnetic field amplification by a short pulse laser interacting with a thin overdense target capable of amplifying a 0.1 kT seed to 1.5 kT over a spatial extent of several cubic microns and persisting for hundreds of femtoseconds longer than the laser pulse duration. We find that magnetic field amplification is driven by the return current arising during the falling edge of the laser pulse. Electrons in the return current gain orbital angular momentum in the presence of the seed magnetic field, driving an azimuthal current with favorable sign for magnetic field amplification. This amplification process is robust to the choice of simulation parameters and occurs for both linear and circular polarization. For a right hand circularly polarized pulse, we find that a seed magnetic field above 20 T delivers order-of-magnitude amplification from a 600 fs

pulse and increasing the pulse duration from 150 fs to 1 ps increases the amplified magnetic field by a factor of 5.

We have neglected electron collisions when examining the generation of the magnetic field. In order to demonstrate that this simplification is appropriate, we estimate the electron collision frequency based on our simulation results. Electron tracking shows that the characteristic energy of the return-current electrons is $\epsilon \approx 15$ keV. The electron-electron collision frequency is $\nu_{ee} \approx 5.8 \times 10^{-6} \epsilon^{-3/2} n_e \lambda_{ee}$, where n_e is the characteristic electron density in cm^{-3}, ϵ is the characteristic electron energy in eV, and $\lambda_{ee} \approx 10$ is the Coulomb logarithm. The magnetic field is generated over 400 fs, so the collisions can be considered as frequent only if $1/\nu_{ee} \ll 400$ fs. This corresponds to $n_e \gg 44 n_c$. In our simulations, the initial target density is $n_e = 10 n_c$, which indicates that it is reasonable to neglect electron collisions and explore the magnetic field generation using collisionless kinetic simulations. The target design considered in our work is experimentally feasible. Flat μm-thick hydrogen jets can be generated using cryogenic cooling [222]. The typical density is in the range of $20 n_c$.

9.8 Acknowledgements

Chapter 9, in full, is a reprint of the material as it appears in Y. Shi, K. Weichman, R. J. Kingham, and A. V. Arefiev, "Magnetic field amplification in a laser-irradiated thin collisionless plasma target by return current electrons carrying orbital angular momentum", *New Journal of Physics*, **22**, 073067 (2020). The dissertation author contributed conceptualization, methodology, and writing to the paper.

The work was supported by the DOE Office of Science under Grant No. DE-SC0018312. Y.S. acknowledges the support of Newton International Fellows Alumni follow-on funding. Simulations were performed using the EPOCH code (developed under

UK EPSRC Grants No. EP/G054940/1, No. EP/G055165/1, and No. EP/ G056803/1) using HPC resources provided by the TACC at the University of Texas and the ARCHER UK National Supercomputing Service. The authors would like to thank Dr. J. Santos and Dr. M. Wei for stimulating discussions.

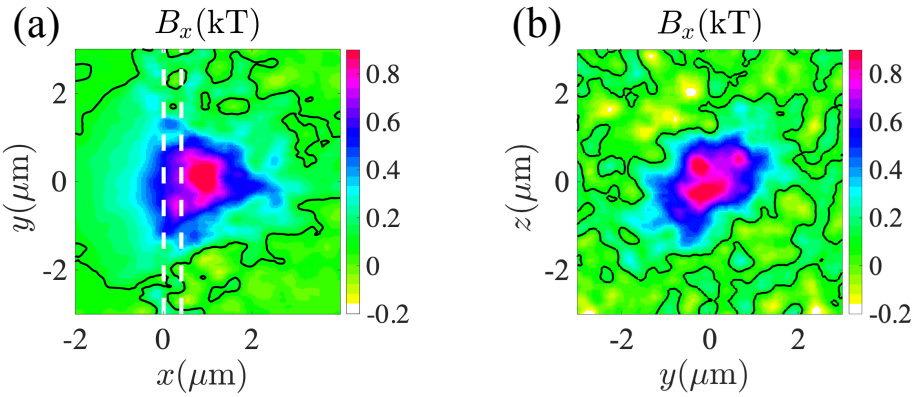

Figure 9.6: Magnetic field amplification driven by a linear polarized laser at $t = 340$ fs (other simulation parameters are as given in Table 9.1). (a) Axial magnetic field distribution in the x-y plane ($z = 0$, dashed lines denote the original target position). (b) Axial magnetic field distribution in the y-z plane ($x = 0.5$ μm). The black contours denote $B_x = B_{x0}$.

9.9 Appendix: Magnetic field amplification by a linearly polarized laser and in a thick target

In this Appendix, we show magnetic field amplification driven by two additional configurations. First, we consider a thin target irradiated by a linearly y-polarized laser pulse. Second, we demonstrate amplification in a thick target driven by a right hand circularly polarized pulse.

In the linear polarization case, we take $a_{y0} = 1.414$ to obtain the same peak intensity as the circularly polarized case. All other simulation parameters are the same as Table 9.1. Fig. 9.6 shows the amplified magnetic field we obtain at $t = 340$ fs. Compared to the right hand circularly polarized case (Fig. 9.1(b) and (c)), the magnetic field is weaker in the

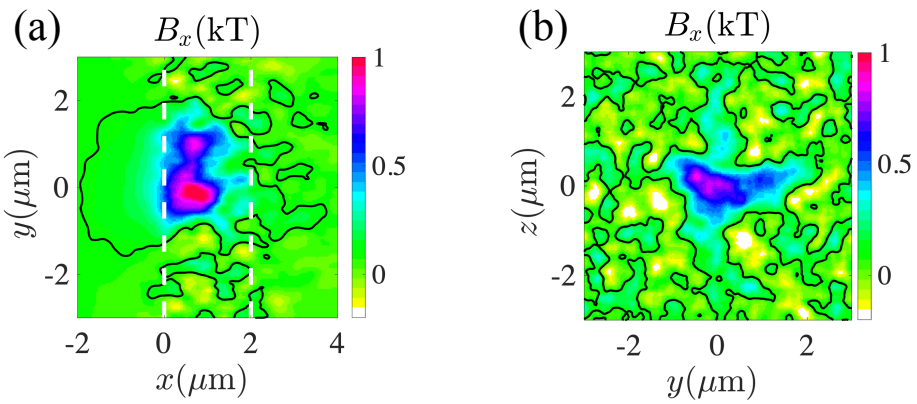

Figure 9.7: Magnetic field amplification driven by a circularly polarized laser pulse in a 2 μm thick target at $t = 340$ fs (other simulation parameters are as given in Table 9.1). (a) Axial magnetic field distribution in the x-y plane ($z = 0$, dashed lines denote the original target position). (b) Axial magnetic field distribution in the y-z plane ($x = 0.5$ μm). The black contours denote $B_x = B_{x0}$.

linearly polarized case. We also see that there is asymmetry in the y-z plane (Fig. 9.6(b)), which may be related to the polarization direction.

In the thick target case, we again consider a right hand circularly polarized laser, which is now incident on a 2 μm thick target. All other simulation parameters are as given in Table 9.1. The amplified magnetic field at $t = 340$ fs is shown in Fig. 9.7. Compared to the thin target case (Fig. 9.1(b) and (c)), the peak magnetic field strength is reduced with the thick target and the magnetic field is amplified over a smaller volume. However, the magnetic field is still amplified to the kilotesla level.

9.10 Appendix: Charge density, electron current density, and ion current density

In this Appendix, we present additional properties of the charge density and current present in the thin target in the right hand circularly polarized case with the simulation parameters given in Table 9.1. The blue curve in Fig. 9.8(d) shows the charge density distribution $\rho(t)/|e|$ averaged over 0.2 μm $< x <$ 0.4 μm and 1 μm $< r <$ 4 μm. During the

rising edge of the laser pulse, the charge density increases, indicating a net ponderomotive expulsion of electrons from the laser spot. After the peak of the laser pulse [vertical dashed line in Fig. 9.8(d)], the ponderomotive force on electrons in the target, $f_p(t) \propto -\partial a^2(t)/r\partial r$ decreases, and the charge density $\rho(t)$ also decreased, consistent with a net inward return current. The charge separation initially decreases substantially over the falling half of the laser pulse ($0 < t \lesssim 300$ fs), then transitions to a much slower decay at later times. In this simulation, the timescale for the charge separation to decrease is roughly comparable to the cyclotron period ($\tau_B = 340$ fs) and is far longer than the plasma period (~ 0.8 fs for a 10 n_c plasma).

Fig. 9.8(b) shows the azimuthal and radial electron current densities (blue and red curves, respectively) as a function of radius at time $t = 340$ fs, which is after the laser pulse has been fully reflected by the target. Figure 9.8(c) similarly shows the ion current densities. These densities have been averaged over $0.2\ \mu\text{m} < x < 0.4\ \mu\text{m}$. We see that the ion current density is much smaller than the electron current density, which suggests the ion motion in the transverse (y-z) plane can be ignored. We also note that the total current density is positive, i.e. there is a net inward electron return current.

9.11 Appendix: Movie: trajectories of traced electrons

Figure 9.9 shows the trajectory of one of the electrons we traced for the right hand circularly polarized case with the simulation parameters given in Table 9.1. Electrons oscillate longitudinally through the target (x-direction) while being pulled radially inward (left plot). The inward motion also corresponds to rotation in the transverse (y-z) plane (right plot). The movie further shows the trajectories of many traced electrons.

The movie shows clear cyclotron rotation of electrons, which is consistent with our

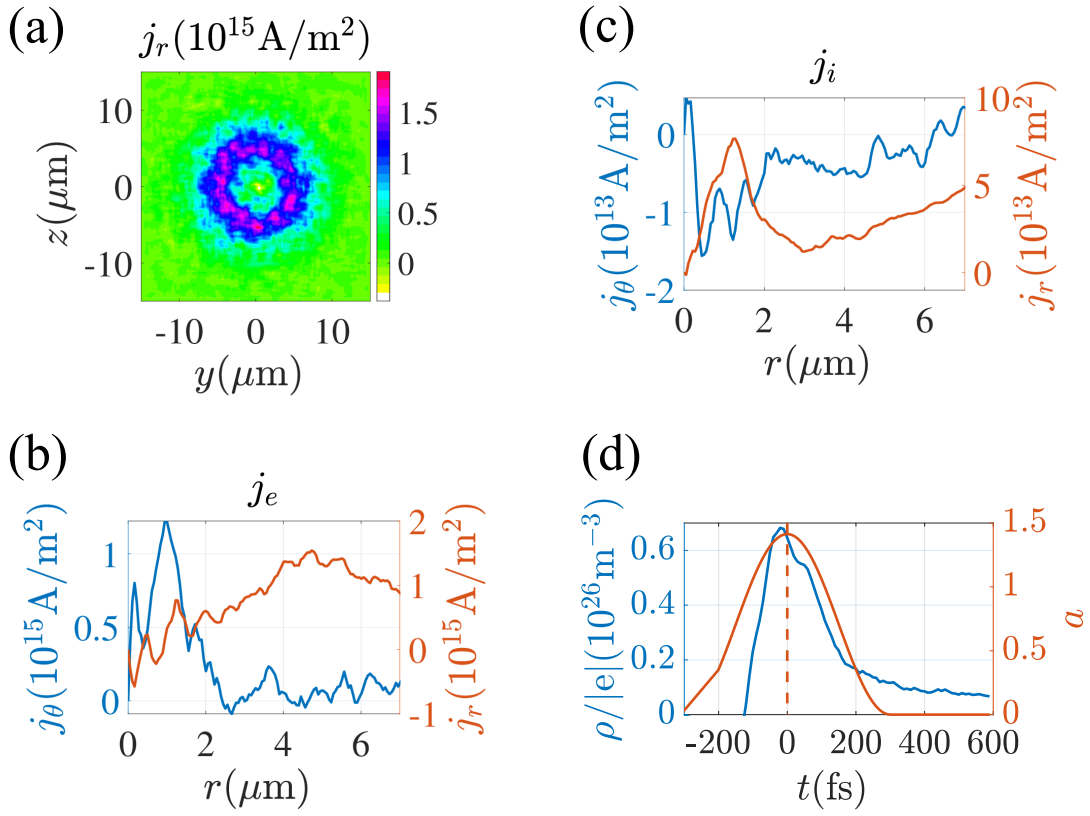

Figure 9.8: Charge density and per-species current density. (a) Total radial current density. (b) and (c) Azimuthal (blue, left axes), and radial (red, right axes) current densities for (b) electrons and (c) protons. (d) Charge density $\rho(t)/|e|$ (blue line, left axis) averaged over $0.2\ \mu\mathrm{m} < x < 0.4\ \mu\mathrm{m}$ and $1\ \mu\mathrm{m} < r < 4\ \mu\mathrm{m}$ as a function of time with reference laser amplitude $a(t)$ at the target surface (red line, right axis). The red dashed line corresponds to $t = 0$, when $a(t)$ is maximum. (a) - (c) are snapshots taken at ($t = 340$ fs) and averaged over $0.2\ \mu\mathrm{m} < x < 0.4\ \mu\mathrm{m}$. The simulation parameters are as given in Table 9.1.

expectations based on the electron cyclotron period ($\tau_B = 340$ fs for a 0.1 kT field). In this way, we can see directly that the return current electrons are magnetized. Ions, for which the cyclotron period is a factor of more than 1000 longer, are unmagnetized. We also see that as electrons approach small radius, the cyclotron motion can reverse direction. This is expected as electrons can overshoot the axis and begin to move radially outward (see, for example the dark blue group of electrons in Fig. 9.4). However, what we are showing in the movie is only a small subset of the electrons in the simulation and the overall azimuthal current density can still be positive (e.g. j_θ in Fig. 9.4).

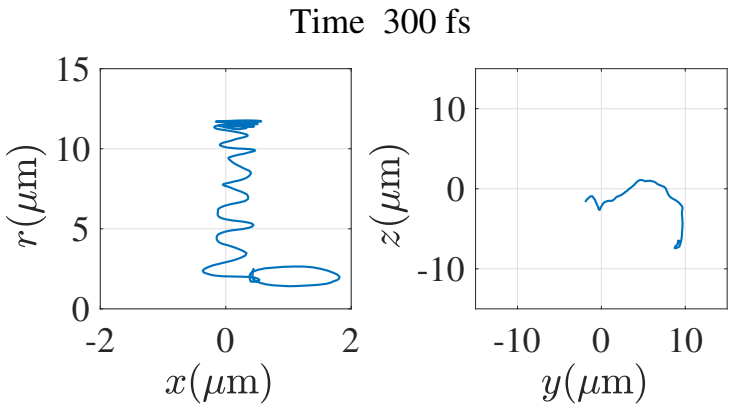

Figure 9.9: Trajectory of a representative electron shown from the beginning of the simulation to $t = 300$ fs. The electron oscillates longitudinally (in x) through the target while moving radially inward (left), and at the same time rotates in the transverse (y-z) plane (right). The simulation parameters are as given in Table 9.1.

9.12 Appendix: Azimuthal magnetic field

In this Appendix, we show the azimuthal magnetic field B_θ generated by the hot electron current in the right hand circularly polarized case both with and without the axial seed magnetic field. The simulation parameters are as given in Table 9.1. Figure 9.10 shows a slice of the azimuthal magnetic field in the y-z plane at $t = 340$ fs and $x = 0.4$ μm (the same time and roughly the same axial location as Fig. 9.1(c)). The strong azimuthal magnetic field field likely plays a role in the return current dynamics. As return currents are drawn radially inward, they oscillate longitudinally through the target (show in the trajectories in Appendix 9.11), which may be in part driven by B_θ.

However, the azimuthal magnetic field is expected to have the same effect on the return current both with and without the axial seed field. As shown in Figure 9.10, the difference in the azimuthal magnetic field with and without a 0.1 kT axial seed field is only 10-20%. The effect of the azimuthal field on the return current behavior is encapsulated in the $r(t)$ we extract from simulations in analysis given in Section 9.5. B_θ is aligned with the azimuthal current j_θ responsible for amplifying the axial magnetic field and does not affect j_θ directly. The biggest change in the return current dynamics is therefore associated with

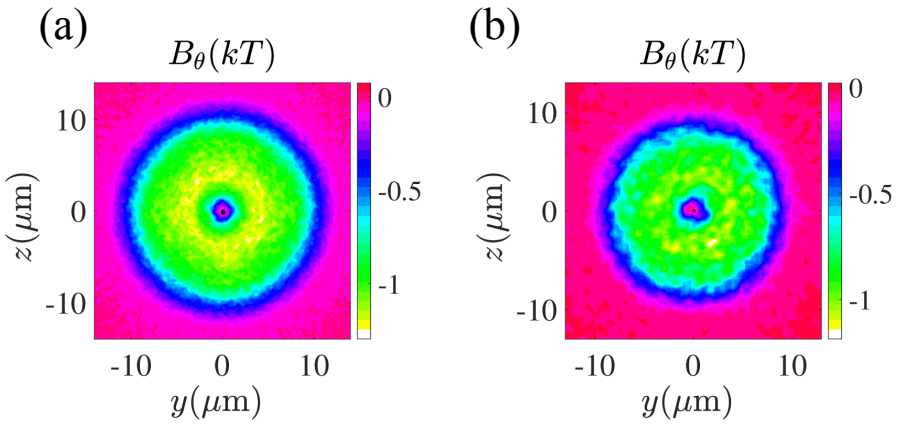

Figure 9.10: Azimuthal magnetic field generated by right hand circularly polarized laser pulse with (a) 0.1 kT axial seed magnetic field and (b) no seed magnetic field. Other simulation parameters are as given in Table 9.1. B_θ is shown at $t = 340$ fs and $x = 0.4$ μm and was temporally (16 fs) and spatially averaged in the plane with stencil size 0.25 μm$\times$0.25 μm. The azimuthal field is small at small radius, where the axial field is amplified.

the axial magnetic field, which increases by a factor of 5 upon adding a 0.1 kT seed field.

Chapter 10

Conclusions

In this dissertation, I have presented a number of scenarios highlighting the possible effects of a kilotesla-level applied magnetic field on relativistic laser plasma. These studies were motivated by the need to understand the role of magnetic fields in high energy density plasma both from the standpoint of fundamental physics and for the optimization of applications. My results suggest near-term experimentally relevant kilotesla-level applied fields are capable of introducing magnetized plasma phenomena in the relativistic laser-plasma regime and can provide both control and benefits for laser-plasma applications.

Chapters 2-4 considered possible routes to electron heating by picosecond pulses. The production of energetic electrons underlies most observable products of laser-plasma interaction and is crucial from an application standpoint. Chapter 2 demonstrated that standard computational techniques for laser-plasma modeling may fail to correctly capture the stochastic motion of electrons in crossed or counter-propagating laser pulses (as can be produced by laser reflection), indicating a need for the development of new computational schemes. In Chapter 3, I concluded that the energy gain mechanism for electrons in multipicosecond pulses incident on solid density targets can also be non-stochastic direct laser acceleration facilitated by laser reflection, which suggests an alternate approach to

optimizing hot electron production than stochastic heating. In Chapter 4, I introduced an applied magnetic field to relativistic laser-plasma interaction and demonstrated that the magnetic field can enable enhanced electron heating and energy retention through magnetically assisted direct laser acceleration under experimentally relevant conditions.

In Chapter 5, I demonstrated that the effects of an applied magnetic field can go beyond changes to the electron energy and can have a striking and desirable impact on application-relevant dynamics. In the context of sheath-based ion acceleration, I demonstrated that the magnetization of electrons in an expanding plasma can have a pronounced impact on the dynamics of plasma ions and can fundamentally alter the electric field topology. These changes are beneficial for the applications of ion acceleration and produce a focusing, magnetic field-directed ion source of multiple species with strongly enhanced energy and number.

Chapters 6-9 considered the potential of applied magnetic fields to trigger strong magnetic field generation in laser-irradiated solid targets. The generation of stronger magnetic fields could push the study of magnetized high energy density physics into regimes which are currently inaccessible using applied fields. In Chapter 6, I demonstrated that the generation of a strong surface magnetic field with opposite sign to the applied seed is a fundamental feature of the dynamics of laser-heated electrons within solid targets. Chapter 7 demonstrated the ability of microtube implosions to generate magnetic fields more than two orders of magnitude higher than an applied seed. In Chapter 8, I further demonstrated that the sign of the generated field is influenced by surface magnetic field production and can be controlled by changing the implosion parameters. Chapter 9 introduced an additional route to magnetic field generation driven by return current rather than hot electrons.

In conclusion, I have shown that kilotesla-level applied magnetic fields are capable of delivering desirable new physics effects in relativistic laser plasma. Such fields are rapidly becoming experimentally available at high-power laser facilities worldwide and could enable

near-term experimental verification of the ideas presented in this dissertation. Relativistic laser-plasma interaction with kilotesla-level applied magnetic fields is a rich new research area, and it is my hope that the physics concepts I have presented in this dissertation will help shape the direction of this evolving rapidly evolving field.

Bibliography

[1] C. N. Danson, C. Haefner, J. Bromage, T. Butcher, J.-C. F. Chanteloup, E. A. Chowdhury, A. Galvanauskas, L. A. Gizzi, J. Hein, D. I. Hillier, and et al., "Petawatt and exawatt class lasers worldwide," *High Power Laser Science and Engineering*, vol. 7, p. e54, 2019.

[2] D. N. Maywar, J. H. Kelly, L. J. Waxer, S. F. B. Morse, I. A. Begishev, J. Bromage, C. Dorrer, J. L. Edwards, L. Folnsbee, M. J. Guardalben, S. D. Jacobs, R. Jungquist, T. J. Kessler, R. W. Kidder, B. E. Kruschwitz, S. J. Loucks, J. R. Marciante, R. L. McCrory, D. D. Meyerhofer, A. V. Okishev, J. B. Oliver, G. Pien, J. Qiao, J. Puth, A. L. Rigatti, A. W. Schmid, M. J. Shoup, C. Stoeckl, K. A. Thorp, and J. D. Zuegel, "OMEGA EP high-energy petawatt laser: progress and prospects," *Journal of Physics: Conference Series*, vol. 112, p. 032007, may 2008.

[3] J. K. Crane, G. Tietbohl, P. Arnold, E. S. Bliss, C. Boley, G. Britten, G. Brunton, W. Clark, J. W. Dawson, S. Fochs, R. Hackel, C. Haefner, J. Halpin, J. Heebner, M. Henesian, M. Hermann, J. Hernandez, V. Kanz, B. McHale, J. B. McLeod, H. Nguyen, H. Phan, M. Rushford, B. Shaw, M. Shverdin, R. Sigurdsson, R. Speck, C. Stolz, D. Trummer, J. Wolfe, J. N. Wong, G. C. Siders, and C. P. J. Barty, "Progress on converting a NIF quad to eight, petawatt beams for advanced radiography," *Journal of Physics: Conference Series*, vol. 244, p. 032003, aug 2010.

[4] N. Miyanaga, H. Azechi, K.A. Tanaka, T. Kanabe, T. Jitsuno, J. Kawanaka, Y. Fujimoto, R. Kodama, H. Shiraga, K. Knodo, K. Tsubakimoto, H. Habara, J.Lu, G. Xu, N. Morio, S. Matsuo, E. Miyaji, Y. Kawakami, Y. Izawa, and K. Mima, "10-kj pw laser for the firex-i program," *J. Phys. IV France*, vol. 133, pp. 81–87, 2006.

[5] D. Batani, M. Koenig, J. L. Miquel, J. E. Ducret, E. d'Humieres, S. Hulin, J. Caron, J. L. Feugeas, P. Nicolai, V. Tikhonchuk, L. Serani, N. Blanchot, D. Raffestin, I. Thfoin-Lantuejoul, B. Rosse, C. Reverdin, A. Duval, F. Laniesse, A. Chancé, D. Dubreuil, B. Gastineau, J. C. Guillard, F. Harrault, D. Lebœuf, J.-M. L. Ster, C. Pès, J.-C. Toussaint, X. Leboeuf, L. Lecherbourg, C. I. Szabo, J.-L. Dubois, and F. Lubrano-Lavaderci, "Development of the PETawatt aquitaine laser system and new perspectives in physics," *Physica Scripta*, vol. T161, p. 014016, may 2014.

[6] C. M. Huntington, F. Fiuza, J. S. Ross, A. B. Zylstra, R. P. Drake, D. H. Froula, G. Gregori, N. L. Kugland, C. C. Kuranz, M. C. Levy, C. K. Li, J. Meinecke,

T. Morita, R. Petrasso, C. Plechaty, B. A. Remington, D. D. Ryutov, Y. Sakawa, A. Spitkovsky, H. Takabe, and H.-S. Park, "Observation of magnetic field generation via the weibel instability in interpenetrating plasma flows," *Nature Physics*, vol. 11, pp. 173–176, Feb 2015.

[7] G. Fiksel, W. Fox, A. Bhattacharjee, D. H. Barnak, P.-Y. Chang, K. Germaschewski, S. X. Hu, and P. M. Nilson, "Magnetic reconnection between colliding magnetized laser-produced plasma plumes," *Phys. Rev. Lett.*, vol. 113, p. 105003, Sep 2014.

[8] B. Albertazzi, A. Ciardi, M. Nakatsutsumi, T. Vinci, J. Béard, R. Bonito, J. Billette, M. Borghesi, Z. Burkley, S. N. Chen, T. E. Cowan, T. Herrmannsdörfer, D. P. Higginson, F. Kroll, S. A. Pikuz, K. Naughton, L. Romagnani, C. Riconda, G. Revet, R. Riquier, H.-P. Schlenvoigt, I. Y. Skobelev, A. Faenov, A. Soloviev, M. Huarte-Espinosa, A. Frank, O. Portugall, H. Pépin, and J. Fuchs, "Laboratory formation of a scaled protostellar jet by coaligned poloidal magnetic field," *Science*, vol. 346, no. 6207, pp. 325–328, 2014.

[9] S. V. Bulanov, T. Z. Esirkepov, M. Kando, J. Koga, K. Kondo, and G. Korn, "On the problems of relativistic laboratory astrophysics and fundamental physics with super powerful lasers," *Plasma Physics Reports*, vol. 41, pp. 1–51, Jan 2015.

[10] C. K. Li, F. H. Séguin, J. A. Frenje, J. R. Rygg, R. D. Petrasso, R. P. J. Town, P. A. Amendt, S. P. Hatchett, O. L. Landen, A. J. Mackinnon, P. K. Patel, V. A. Smalyuk, T. C. Sangster, and J. P. Knauer, "Measuring e and b fields in laser-produced plasmas with monoenergetic proton radiography," *Phys. Rev. Lett.*, vol. 97, p. 135003, Sep 2006.

[11] S. Kneip, C. McGuffey, F. Dollar, M. S. Bloom, V. Chvykov, G. Kalintchenko, K. Krushelnick, A. Maksimchuk, S. P. D. Mangles, T. Matsuoka, Z. Najmudin, C. A. J. Palmer, J. Schreiber, W. Schumaker, A. G. R. Thomas, and V. Yanovsky, "X-ray phase contrast imaging of biological specimens with femtosecond pulses of betatron radiation from a compact laser plasma wakefield accelerator," *Applied Physics Letters*, vol. 99, no. 9, p. 093701, 2011.

[12] T. Tajima and J. M. Dawson, "Laser electron accelerator," *Phys. Rev. Lett.*, vol. 43, pp. 267–270, Jul 1979.

[13] V. Malka, "Laser plasma accelerators," *Physics of Plasmas*, vol. 19, no. 5, p. 055501, 2012.

[14] D. J. Strozzi, M. Tabak, D. J. Larson, L. Divol, A. J. Kemp, C. Bellei, M. M. Marinak, and M. H. Key, "Fast-ignition transport studies: Realistic electron source, integrated particle-in-cell and hydrodynamic modeling, imposed magnetic fields," *Physics of Plasmas*, vol. 19, no. 7, p. 072711, 2012.

[15] S. Fujioka, Y. Arikawa, S. Kojima, T. Johzaki, H. Nagatomo, H. Sawada, S. H. Lee, T. Shiroto, N. Ohnishi, A. Morace, X. Vaisseau, S. Sakata, Y. Abe, K. Matsuo, K. F. Farley Law, S. Tosaki, A. Yogo, K. Shigemori, Y. Hironaka, Z. Zhang, A. Sunahara, T. Ozaki, H. Sakagami, K. Mima, Y. Fujimoto, K. Yamanoi, T. Norimatsu, S. Tokita, Y. Nakata, J. Kawanaka, T. Jitsuno, N. Miyanaga, M. Nakai, H. Nishimura, H. Shiraga, K. Kondo, M. Bailly-Grandvaux, C. Bellei, J. J. Santos, and H. Azechi, "Fast ignition realization experiment with high-contrast kilo-joule peta-watt lfex laser and strong external magnetic field," *Physics of Plasmas*, vol. 23, no. 5, p. 056308, 2016.

[16] S. Sakata, S. Lee, H. Morita, T. Johzaki, H. Sawada, Y. Iwasa, K. Matsuo, K. F. F. Law, A. Yao, M. Hata, *et al.*, "Magnetized fast isochoric laser heating for efficient creation of ultra-high-energy-density states," *Nature communications*, vol. 9, no. 1, p. 3937, 2018.

[17] M. Roth, T. E. Cowan, M. H. Key, S. P. Hatchett, C. Brown, W. Fountain, J. Johnson, D. M. Pennington, R. A. Snavely, S. C. Wilks, K. Yasuike, H. Ruhl, F. Pegoraro, S. V. Bulanov, E. M. Campbell, M. D. Perry, and H. Powell, "Fast ignition by intense laser-accelerated proton beams," *Phys. Rev. Lett.*, vol. 86, pp. 436–439, Jan 2001.

[18] A. Macchi, M. Borghesi, and M. Passoni, "Ion acceleration by superintense laser-plasma interaction," *Rev. Mod. Phys.*, vol. 85, pp. 751–793, May 2013.

[19] I. Pomerantz, E. McCary, A. R. Meadows, A. Arefiev, A. C. Bernstein, C. Chester, J. Cortez, M. E. Donovan, G. Dyer, E. W. Gaul, D. Hamilton, D. Kuk, A. C. Lestrade, C. Wang, T. Ditmire, and B. M. Hegelich, "Ultrashort pulsed neutron source," *Phys. Rev. Lett.*, vol. 113, p. 184801, Oct 2014.

[20] J. D. Kmetec, C. L. Gordon, J. J. Macklin, B. E. Lemoff, G. S. Brown, and S. E. Harris, "Mev x-ray generation with a femtosecond laser," *Phys. Rev. Lett.*, vol. 68, pp. 1527–1530, Mar 1992.

[21] D. J. Stark, T. Toncian, and A. V. Arefiev, "Enhanced multi-mev photon emission by a laser-driven electron beam in a self-generated magnetic field," *Phys. Rev. Lett.*, vol. 116, p. 185003, May 2016.

[22] M. Nakatsutsumi, Y. Sentoku, A. Korzhimanov, S. Chen, S. Buffechoux, A. Kon, B. Atherton, P. Audebert, M. Geissel, L. Hurd, *et al.*, "Self-generated surface magnetic fields inhibit laser-driven sheath acceleration of high-energy protons," *Nature communications*, vol. 9, no. 1, p. 280, 2018.

[23] S. Fujioka, Z. Zhang, K. Ishihara, K. Shigemori, Y. Hironaka, T. Johzaki, A. Sunahara, N. Yamamoto, H. Nakashima, T. Watanabe, *et al.*, "Kilotesla magnetic field due to a capacitor-coil target driven by high power laser," *Scientific reports*, vol. 3, p. 1170, 2013.

[24] J. J. Santos, M. Bailly-Grandvaux, L. Giuffrida, P. Forestier-Colleoni, S. Fujioka, Z. Zhang, P. Korneev, R. Bouillaud, S. Dorard, D. Batani, M. Chevrot, J. E. Cross, R. Crowston, J.-L. Dubois, J. Gazave, G. Gregori, E. d'Humières, S. Hulin, K. Ishihara, S. Kojima, E. Loyez, J.-R. Marquès, A. Morace, P. Nicolaï, O. Peyrusse, A. Poyé, D. Raffestin, J. Ribolzi, M. Roth, G. Schaumann, F. Serres, V. T. Tikhonchuk, P. Vacar, and N. Woolsey, "Laser-driven platform for generation and characterization of strong quasi-static magnetic fields," *New Journal of Physics*, vol. 17, p. 083051, aug 2015.

[25] L. Gao, H. Ji, G. Fiksel, W. Fox, M. Evans, and N. Alfonso, "Ultrafast proton radiography of the magnetic fields generated by a laser-driven coil current," *Physics of Plasmas*, vol. 23, no. 4, p. 043106, 2016.

[26] C. Goyon, B. B. Pollock, D. P. Turnbull, A. Hazi, L. Divol, W. A. Farmer, D. Haberberger, J. Javedani, A. J. Johnson, A. Kemp, M. C. Levy, B. Grant Logan, D. A. Mariscal, O. L. Landen, S. Patankar, J. S. Ross, A. M. Rubenchik, G. F. Swadling, G. J. Williams, S. Fujioka, K. F. F. Law, and J. D. Moody, "Ultrafast probing of magnetic field growth inside a laser-driven solenoid," *Phys. Rev. E*, vol. 95, p. 033208, Mar 2017.

[27] O. Portugall, N. Puhlmann, H. U. Müller, M. Barczewski, I. Stolpe, M. Thiede, H. Scholz, M. von Ortenberg, and F. Herlach, "The design and performance of a transportable low-cost instrument for the generation and application of megagauss fields," *Journal of Physics D: Applied Physics*, vol. 30, pp. 1697–1702, jun 1997.

[28] O. Portugall, N. Puhlmann, H. U. Müller, M. Barczewski, I. Stolpe, and M. von Ortenberg, "Megagauss magnetic field generation in single-turn coils: new frontiers for scientific experiments," *Journal of Physics D: Applied Physics*, vol. 32, pp. 2354–2366, sep 1999.

[29] V. V. Ivanov, A. V. Maximov, K. J. Swanson, N. L. Wong, G. S. Sarkisov, P. P. Wiewior, A. L. Astanovitskiy, and A. M. Covington, "Experimental platform for investigations of high-intensity laser plasma interactions in the magnetic field of a pulsed power generator," *Review of Scientific Instruments*, vol. 89, no. 3, p. 033504, 2018.

[30] J. J. Santos, M. Bailly-Grandvaux, M. Ehret, A. V. Arefiev, D. Batani, F. N. Beg, A. Calisti, S. Ferri, R. Florido, P. Forestier-Colleoni, S. Fujioka, M. A. Gigosos, L. Giuffrida, L. Gremillet, J. J. Honrubia, S. Kojima, P. Korneev, K. F. F. Law, J.-R. Marquès, A. Morace, C. Mossé, O. Peyrusse, S. Rose, M. Roth, S. Sakata, G. Schaumann, F. Suzuki-Vidal, V. T. Tikhonchuk, T. Toncian, N. Woolsey, and Z. Zhang, "Laser-driven strong magnetostatic fields with applications to charged beam transport and magnetized high energy-density physics," *Physics of Plasmas*, vol. 25, no. 5, p. 056705, 2018.

[31] P. Kaw and J. Dawson, "Relativistic nonlinear propagation of laser beams in cold overdense plasmas," *The Physics of Fluids*, vol. 13, no. 2, pp. 472–481, 1970.

[32] Z.-M. Sheng, K. Mima, Y. Sentoku, M. S. Jovanović, T. Taguchi, J. Zhang, and J. Meyer-ter Vehn, "Stochastic heating and acceleration of electrons in colliding laser fields in plasma," *Phys. Rev. Lett.*, vol. 88, p. 055004, Jan 2002.

[33] A. J. Kemp, Y. Sentoku, and M. Tabak, "Hot-electron energy coupling in ultraintense laser-matter interaction," *Phys. Rev. E*, vol. 79, p. 066406, Jun 2009.

[34] B. S. Paradkar, M. S. Wei, T. Yabuuchi, R. B. Stephens, M. G. Haines, S. I. Krasheninnikov, and F. N. Beg, "Numerical modeling of fast electron generation in the presence of preformed plasma in laser-matter interaction at relativistic intensities," *Phys. Rev. E*, vol. 83, p. 046401, Apr 2011.

[35] S. Kojima, M. Hata, N. Iwata, Y. Arikawa, A. Morace, S. Sakata, S. Lee, K. Matsuo, K. F. F. Law, H. Morita, *et al.*, "Electromagnetic field growth triggering super-ponderomotive electron acceleration during multi-picosecond laser-plasma interaction," *Communications Physics*, vol. 2, no. 1, pp. 1–12, 2019.

[36] A. Gurevich, L. Pariiskaya, and L. Pitaevskii, "Self-similar motion of rarefied plasma," *Sov. Phys. JETP*, vol. 22, no. 2, pp. 449–454, 1966.

[37] P. Mora, "Plasma expansion into a vacuum," *Phys. Rev. Lett.*, vol. 90, p. 185002, May 2003.

[38] E. L. Clark, K. Krushelnick, M. Zepf, F. N. Beg, M. Tatarakis, A. Machacek, M. I. K. Santala, I. Watts, P. A. Norreys, and A. E. Dangor, "Energetic heavy-ion and proton generation from ultraintense laser-plasma interactions with solids," *Phys. Rev. Lett.*, vol. 85, pp. 1654–1657, Aug 2000.

[39] A. Maksimchuk, S. Gu, K. Flippo, D. Umstadter, and V. Y. Bychenkov, "Forward ion acceleration in thin films driven by a high-intensity laser," *Phys. Rev. Lett.*, vol. 84, pp. 4108–4111, May 2000.

[40] R. A. Snavely, M. H. Key, S. P. Hatchett, T. E. Cowan, M. Roth, T. W. Phillips, M. A. Stoyer, E. A. Henry, T. C. Sangster, M. S. Singh, S. C. Wilks, A. MacKinnon, A. Offenberger, D. M. Pennington, K. Yasuike, A. B. Langdon, B. F. Lasinski, J. Johnson, M. D. Perry, and E. M. Campbell, "Intense high-energy proton beams from petawatt-laser irradiation of solids," *Phys. Rev. Lett.*, vol. 85, pp. 2945–2948, Oct 2000.

[41] P. K. Patel, A. J. Mackinnon, M. H. Key, T. E. Cowan, M. E. Foord, M. Allen, D. F. Price, H. Ruhl, P. T. Springer, and R. Stephens, "Isochoric heating of solid-density matter with an ultrafast proton beam," *Phys. Rev. Lett.*, vol. 91, p. 125004, Sep 2003.

[42] M. Roth, T. E. Cowan, M. H. Key, S. P. Hatchett, C. Brown, W. Fountain, J. Johnson, D. M. Pennington, R. A. Snavely, S. C. Wilks, K. Yasuike, H. Ruhl, F. Pegoraro, S. V. Bulanov, E. M. Campbell, M. D. Perry, and H. Powell, "Fast ignition by intense laser-accelerated proton beams," *Phys. Rev. Lett.*, vol. 86, pp. 436–439, Jan 2001.

[43] M. Borghesi, A. J. MacKinnon, A. R. Bell, R. Gaillard, and O. Willi, "Megagauss magnetic field generation and plasma jet formation on solid targets irradiated by an ultraintense picosecond laser pulse," *Phys. Rev. Lett.*, vol. 81, pp. 112–115, Jul 1998.

[44] G. Sarri, A. Macchi, C. A. Cecchetti, S. Kar, T. V. Liseykina, X. H. Yang, M. E. Dieckmann, J. Fuchs, M. Galimberti, L. A. Gizzi, R. Jung, I. Kourakis, J. Osterholz, F. Pegoraro, A. P. L. Robinson, L. Romagnani, O. Willi, and M. Borghesi, "Dynamics of self-generated, large amplitude magnetic fields following high-intensity laser matter interaction," *Phys. Rev. Lett.*, vol. 109, p. 205002, Nov 2012.

[45] S. Jiang, L. L. Ji, H. Audesirk, K. M. George, J. Snyder, A. Krygier, P. Poole, C. Willis, R. Daskalova, E. Chowdhury, N. S. Lewis, D. W. Schumacher, A. Pukhov, R. R. Freeman, and K. U. Akli, "Microengineering laser plasma interactions at relativistic intensities," *Phys. Rev. Lett.*, vol. 116, p. 085002, Feb 2016.

[46] O. Klimo, J. Psikal, J. Limpouch, J. Proska, F. Novotny, T. Ceccotti, V. Floquet, and S. Kawata, "Short pulse laser interaction with micro-structured targets: simulations of laser absorption and ion acceleration," *New Journal of Physics*, vol. 13, p. 053028, may 2011.

[47] D. Margarone, O. Klimo, I. J. Kim, J. Prokůpek, J. Limpouch, T. M. Jeong, T. Mocek, J. Pšikal, H. T. Kim, J. Proška, K. H. Nam, L. Štolcová, I. W. Choi, S. K. Lee, J. H. Sung, T. J. Yu, and G. Korn, "Laser-driven proton acceleration enhancement by nanostructured foils," *Phys. Rev. Lett.*, vol. 109, p. 234801, Dec 2012.

[48] T. Wang, X. Ribeyre, Z. Gong, O. Jansen, E. d'Humières, D. Stutman, T. Toncian, and A. Arefiev, "Power scaling for collimated γ-ray beams generated by structured laser-irradiated targets and its application to two-photon pair production," *Phys. Rev. Applied*, vol. 13, p. 054024, May 2020.

[49] J. Snyder, L. L. Ji, K. M. George, C. Willis, G. E. Cochran, R. L. Daskalova, A. Handler, T. Rubin, P. L. Poole, D. Nasir, A. Zingale, E. Chowdhury, B. F. Shen, and D. W. Schumacher, "Relativistic laser driven electron accelerator using micro-channel plasma targets," *Physics of Plasmas*, vol. 26, no. 3, p. 033110, 2019.

[50] M. Cerchez, A. L. Giesecke, C. Peth, M. Toncian, B. Albertazzi, J. Fuchs, O. Willi, and T. Toncian, "Generation of laser-driven higher harmonics from grating targets," *Phys. Rev. Lett.*, vol. 110, p. 065003, Feb 2013.

[51] D. J. Stark, T. Toncian, and A. V. Arefiev, "Enhanced multi-mev photon emission by a laser-driven electron beam in a self-generated magnetic field," *Phys. Rev. Lett.*, vol. 116, p. 185003, May 2016.

[52] P. Korneev, E. d'Humières, and V. Tikhonchuk, "Gigagauss-scale quasistatic magnetic field generation in a snail-shaped target," *Phys. Rev. E*, vol. 91, p. 043107, Apr 2015.

[53] P. Korneev, V. Tikhonchuk, and E. d'Humières, "Magnetization of laser-produced plasma in a chiral hollow target," *New Journal of Physics*, vol. 19, p. 033023, mar 2017.

[54] O. V. Gotchev, P. Y. Chang, J. P. Knauer, D. D. Meyerhofer, O. Polomarov, J. Frenje, C. K. Li, M. J.-E. Manuel, R. D. Petrasso, J. R. Rygg, F. H. Séguin, and R. Betti, "Laser-driven magnetic-flux compression in high-energy-density plasmas," *Phys. Rev. Lett.*, vol. 103, p. 215004, Nov 2009.

[55] M. Hohenberger, P.-Y. Chang, G. Fiksel, J. P. Knauer, R. Betti, F. J. Marshall, D. D. Meyerhofer, F. H. Séguin, and R. D. Petrasso, "Inertial confinement fusion implosions with imposed magnetic field compression using the omega laser," *Physics of Plasmas*, vol. 19, no. 5, p. 056306, 2012.

[56] C. N. Danson, P. A. Brummitt, R. J. Clarke, J. L. Collier, B. Fell, A. J. Frackiewicz, S. Hancock, S. Hawkes, C. Hernandez-Gomez, P. Holligan, M. H. R. Hutchinson, A. Kidd, W. J. Lester, I. O. Musgrave, D. Neely, D. R. Neville, P. A. Norreys, D. A. Pepler, C. J. Reason, W. Shaikh, T. B. Winstone, R. W. W. Wyatt, and B. E. Wyborn, "Vulcan Petawatt—an ultra-high-intensity interaction facility," *Nuclear Fusion*, vol. 44, pp. S239–S246, Nov. 2004.

[57] C. Hernandez-Gomez, S. P. Blake, O. Chekhlov, R. J. Clarke, A. M. Dunne, M. Galimberti, S. Hancock, R. Heathcote, P. Holligan, A. Lyachev, P. Matousek, I. O. Musgrave, D. Neely, P. A. Norreys, I. Ross, Y. Tang, T. B. Winstone, B. E. Wyborn, and J. Collier, "The Vulcan 10 PW project," *Journal of Physics: Conference Series*, vol. 244, p. 032006, Aug. 2010.

[58] Y. Tang, I. N. Ross, C. Hernandez-Gomez, G. H. C. New, I. Musgrave, O. V. Chekhlov, P. Matousek, and J. L. Collier, "Optical parametric chirped-pulse amplification source suitable for seeding high-energy systems," *Optics Letters*, vol. 33, pp. 2386–2388, Oct. 2008.

[59] C. Hooker, Y. Tang, O. Chekhlov, J. Collier, E. Divall, K. Ertel, S. Hawkes, B. Parry, and P. P. Rajeev, "Improving coherent contrast of petawatt laser pulses," *Optics Express*, vol. 19, pp. 2193–2203, Jan. 2011.

[60] S. P. D. Mangles, C. D. Murphy, Z. Najmudin, A. G. R. Thomas, J. L. Collier, A. E. Dangor, E. J. Divall, P. S. Foster, J. G. Gallacher, C. J. Hooker, D. A. Jaroszynski, A. J. Langley, W. B. Mori, P. A. Norreys, F. S. Tsung, R. Viskup, B. R. Walton, and K. Krushelnick, "Monoenergetic beams of relativistic electrons from intense laser–plasma interactions," *Nature*, vol. 431, p. 535, Sept. 2004.

[61] S. A. Gaillard, T. Kluge, K. A. Flippo, M. Bussmann, B. Gall, T. Lockard, M. Geissel, D. T. Offermann, M. Schollmeier, Y. Sentoku, and T. E. Cowan, "Increased laser-accelerated proton energies via direct laser-light-pressure acceleration of electrons in microcone targets," *Physics of Plasmas*, vol. 18, no. 5, p. 056710, 2011.

[62] S. Kneip, S. R. Nagel, C. Bellei, N. Bourgeois, A. E. Dangor, A. Gopal, R. Heathcote, S. P. D. Mangles, J. R. Marquès, A. Maksimchuk, P. M. Nilson, K. T. Phuoc, S. Reed, M. Tzoufras, F. S. Tsung, L. Willingale, W. B. Mori, A. Rousse, K. Krushelnick, and Z. Najmudin, "Observation of Synchrotron Radiation from Electrons Accelerated in a Petawatt-Laser-Generated Plasma Cavity," *Phys. Rev. Lett.*, vol. 100, p. 105006, Mar. 2008.

[63] M. Tabak, D.S. Clark, S.P. Hatchett, M.H. Key, B.F. Lasinski, R.A. Snavely, S.C. Wilks, R.P.J. Town, R. Stephens, E.M. Campbell, R. Kodama, K. Mima, K.A. Tanaka, S. Atzeni, and R. Freeman, "Review of progress in fast ignition," *Phys.Plasmas*, vol. 12, p. 057305, 2005.

[64] D. J. Hoarty, P. Allan, S. F. James, C. R. D. Brown, L. M. R. Hobbs, M. P. Hill, J. W. O. Harris, J. Morton, M. G. Brookes, R. Shepherd, J. Dunn, H. Chen, E. Von Marley, P. Beiersdorfer, H. K. Chung, R. W. Lee, G. Brown, and J. Emig, "Observations of the effect of ionization-potential depression in hot dense plasma," *Phys. Rev. Lett.*, vol. 110, p. 265003, Jun 2013.

[65] T. Heinzl, B. Liesfeld, K.-U. Amthor, H. Schwoerer, R. Sauerbrey, and A. Wipf, "On the observation of vacuum birefringence," *Optics Communications*, vol. 267, pp. 318–321, Nov. 2006.

[66] T. Heinzl and A. Ilderton, "Exploring high-intensity QED at ELI," *The European Physical Journal D*, vol. 55, pp. 359–364, Nov. 2009.

[67] C. K. Birdsall, A. B. Langdon, and A. B. Langdon, *Plasma Physics via Computer Simulation*. CRC Press, Oct. 2018.

[68] A. Pukhov, "Strong field interaction of laser radiation," *Reports on Progress in Physics*, vol. 66, pp. 47–101, dec 2002.

[69] A. Pukhov and J. Meyer-ter Vehn, "Laser wake field acceleration: the highly non-linear broken-wave regime," *Applied Physics B*, vol. 74, pp. 355–361, Apr. 2002.

[70] Kane Yee, "Numerical solution of initial boundary value problems involving maxwell's equations in isotropic media," *IEEE Transactions on Antennas and Propagation*, vol. 14, pp. 302–307, May 1966.

[71] T. D. Arber, K. Bennett, C. S. Brady, A. Lawrence-Douglas, M. G. Ramsay, N. J. Sircombe, P. Gillies, R. G. Evans, H. Schmitz, A. R. Bell, and C. P. Ridgers, "Contemporary particle-in-cell approach to laser-plasma modelling," *Plasma Physics and Controlled Fusion*, vol. 57, p. 113001, sep 2015.

[72] A. V. Higuera and J. R. Cary, "Structure-preserving second-order integration of relativistic charged particle trajectories in electromagnetic fields," *Physics of Plasmas*, vol. 24, no. 5, p. 052104, 2017.

[73] P. Londrillo, C. Benedetti, A. Sgattoni, and G. Turchetti, "Charge preserving high order pic schemes," *Nuclear Instruments and Methods in Physics Research Section A: Accelerators, Spectrometers, Detectors and Associated Equipment*, vol. 620, no. 1, pp. 28 – 35, 2010. COULOMB09.

[74] J.-L. Vay, "Simulation of beams or plasmas crossing at relativistic velocity," *Physics of Plasmas*, vol. 15, p. 056701, Feb. 2008.

[75] Z.-M. Sheng, K. Mima, J. Zhang, and J. Meyer-ter Vehn, "Efficient acceleration of electrons with counterpropagating intense laser pulses in vacuum and underdense plasma," *Phys. Rev. E*, vol. 69, p. 016407, Jan 2004.

[76] J. Meyer-ter Vehn and Z. M. Sheng, "On electron acceleration by intense laser pulses in the presence of a stochastic field," *Physics of Plasmas*, vol. 6, no. 3, p. 641, 1999.

[77] S. H. Strogatz, *Nonlinear Dynamics and Chaos with Student Solutions Manual: Nonlinear Dynamics and Chaos: With Applications to Physics, Biology, Chemistry, and Engineering, Second Edition*. Boulder, CO: Westview Press, 2 edition ed., Mar. 2015.

[78] E. Ott, T. Sauer, and J. A. Yorke, eds., *Coping with Chaos*. New York: Wiley-VCH, 1 edition ed., Sept. 1994.

[79] L. N. Hand and J. D. Finch, *Analytical Mechanics*. Cambridge University Press, 1998.

[80] F. V. Hartemann, E. C. Landahl, A. L. Troha, J. R. Van Meter, H. A. Baldis, R. R. Freeman, N. C. Luhmann, L. Song, A. K. Kerman, and D. U. L. Yu, "The chirped-pulse inverse free-electron laser: A high-gradient vacuum laser accelerator," *Physics of Plasmas*, vol. 6, pp. 4104–4110, Sept. 1999.

[81] M. Thévenet, A. Leblanc, S. Kahaly, H. Vincenti, A. Vernier, F. Quéré, and J. Faure, "Vacuum laser acceleration of relativistic electrons using plasma mirror injectors," *Nature Physics*, vol. 12, pp. 355–360, Apr. 2016.

[82] T. Plettner, R. L. Byer, E. Colby, B. Cowan, C. M. S. Sears, J. E. Spencer, and R. H. Siemann, "Proof-of-principle experiment for laser-driven acceleration of relativistic electrons in a semi-infinite vacuum," *Physical Review Special Topics - Accelerators and Beams*, vol. 8, p. 121301, Dec. 2005.

[83] A. L. Troha, J. R. Van Meter, E. C. Landahl, R. M. Alvis, Z. A. Unterberg, K. Li, N. C. Luhmann, A. K. Kerman, and F. V. Hartemann, "Vacuum electron acceleration by coherent dipole radiation," *Physical Review E*, vol. 60, pp. 926–934, July 1999.

[84] A. P. L. Robinson and A. V. Arefiev, "Interaction of an electron with coherent dipole radiation: Role of convergence and anti-dephasing," *Physics of Plasmas*, vol. 25, p. 053107, May 2018.

[85] A. Pukhov, Z.-M. Sheng, and J. Meyer-ter Vehn, "Particle acceleration in relativistic laser channels," *Physics of Plasmas*, vol. 6, no. 7, pp. 2847–2854, 1999.

[86] N. Naseri, D. Pesme, W. Rozmus, and K. Popov, "Channeling of Relativistic Laser Pulses, Surface Waves, and Electron Acceleration," *Phys. Rev. Lett.*, vol. 108, p. 105001, Mar. 2012.

[87] A. V. Arefiev, V. N. Khudik, A. P. L. Robinson, G. Shvets, L. Willingale, and M. Schollmeier, "Beyond the ponderomotive limit: Direct laser acceleration of relativistic electrons in sub-critical plasmas," *Physics of Plasmas*, vol. 23, no. 5, p. 056704, 2016.

[88] A. P. L. Robinson and A. V. Arefiev, "Breaking of dynamical adiabaticity in direct laser acceleration of electrons," *Physics of Plasmas*, vol. 24, p. 023101, Feb. 2017.

[89] A. V. Arefiev, V. N. Khudik, A. P. L. Robinson, G. Shvets, and L. Willingale, "Spontaneous emergence of non-planar electron orbits during direct laser acceleration by a linearly polarized laser pulse," *Physics of Plasmas*, vol. 23, p. 023111, Feb. 2016.

[90] T. W. Huang, A. P. L. Robinson, C. T. Zhou, B. Qiao, B. Liu, S. C. Ruan, X. T. He, and P. A. Norreys, "Characteristics of betatron radiation from direct-laser-accelerated electrons," *Physical Review E*, vol. 93, p. 063203, June 2016.

[91] X. Zhang, V. N. Khudik, and G. Shvets, "Synergistic Laser-Wakefield and Direct-Laser Acceleration in the Plasma-Bubble Regime," *Physical Review Letters*, vol. 114, p. 184801, May 2015.

[92] L. Willingale, A. G. R. Thomas, P. M. Nilson, H. Chen, J. Cobble, R. S. Craxton, A. Maksimchuk, P. A. Norreys, T. C. Sangster, R. H. H. Scott, C. Stoeckl, C. Zulick, and . K. Krushelnick, "Surface waves and electron acceleration from high-power, kilojoule-class laser interactions with underdense plasma," *New Journal of Physics*, vol. 15, p. 025023, 2013.

[93] A. P. L. Robinson, A. V. Arefiev, and D. Neely, "Generating "superponderomotive" electrons due to a non-wake-field interaction between a laser pulse and a longitudinal electric field," *Phys. Rev. Lett.*, vol. 111, p. 065002, Aug 2013.

[94] J. T. Mendonça, "Threshold for electron heating by two electromagnetic waves," *Phys. Rev. A*, vol. 28, pp. 3592–3598, Dec 1983.

[95] W. H. Press, B. P. Flannery, S. A. Teukolsky, and W. T. Vetterling, *Numerical Recipes: The Art of Scientific Computing (3rd ed.)*. Cambridge University Press, 2007.

[96] J. Lindl, "Development of the indirect-drive approach to inertial confinement fusion and the target physics basis for ignition and gain," *Physics of Plasmas*, vol. 2, no. 11, pp. 3933–4024, 1995.

[97] F. V. Hartemann, S. N. Fochs, G. P. Le Sage, N. C. Luhmann, J. G. Woodworth, M. D. Perry, Y. J. Chen, and A. K. Kerman, "Nonlinear ponderomotive scattering of relativistic electrons by an intense laser field at focus," *Phys. Rev. E*, vol. 51, pp. 4833–4843, May 1995.

[98] W. L. Kruer and K. Estabrook, "Jxb heating by very intense laser light," *The Physics of Fluids*, vol. 28, no. 1, pp. 430–432, 1985.

[99] E. Lefebvre and G. Bonnaud, "Nonlinear electron heating in ultrahigh-intensity-laser–plasma interaction," *Phys. Rev. E*, vol. 55, pp. 1011–1014, Jan 1997.

[100] J. May, J. Tonge, F. Fiuza, R. A. Fonseca, L. O. Silva, C. Ren, and W. B. Mori, "Mechanism of generating fast electrons by an intense laser at a steep overdense interface," *Phys. Rev. E*, vol. 84, p. 025401, Aug 2011.

[101] S. C. Wilks, W. L. Kruer, M. Tabak, and A. B. Langdon, "Absorption of ultra-intense laser pulses," *Phys. Rev. Lett.*, vol. 69, pp. 1383–1386, Aug 1992.

[102] A. V. Arefiev, B. N. Breizman, M. Schollmeier, and V. N. Khudik, "Parametric amplification of laser-driven electron acceleration in underdense plasma," *Phys. Rev. Lett.*, vol. 108, p. 145004, Apr 2012.

[103] J. M. Rax, "Compton harmonic resonances, stochastic instabilities, quasilinear diffusion, and collisionless damping with ultra-high-intensity laser waves," *Physics of Fluids B: Plasma Physics*, vol. 4, no. 12, pp. 3962–3972, 1992.

[104] A. Sorokovikova, A. V. Arefiev, C. McGuffey, B. Qiao, A. P. L. Robinson, M. S. Wei, H. S. McLean, and F. N. Beg, "Generation of superponderomotive electrons in multipicosecond interactions of kilojoule laser beams with solid-density plasmas," *Phys. Rev. Lett.*, vol. 116, p. 155001, Apr 2016.

[105] N. Iwata, S. Kojima, Y. Sentoku, M. Hata, and K. Mima, "Plasma density limits for hole boring by intense laser pulses," *Nature communications*, vol. 9, no. 1, p. 623, 2018.

[106] A. J. Kemp and L. Divol, "Interaction physics of multipicosecond petawatt laser pulses with overdense plasma," *Phys. Rev. Lett.*, vol. 109, p. 195005, Nov 2012.

[107] B. S. Paradkar, S. I. Krasheninnikov, and F. N. Beg, "Mechanism of heating of pre-formed plasma electrons in relativistic laser-matter interaction," *Physics of Plasmas*, vol. 19, no. 6, p. 060703, 2012.

[108] A. V. Arefiev, G. E. Cochran, D. W. Schumacher, A. P. L. Robinson, and G. Chen, "Temporal resolution criterion for correctly simulating relativistic electron motion in a high-intensity laser field," *Physics of Plasmas*, vol. 22, no. 1, p. 013103, 2015.

[109] S. C. Wilks, "Simulations of ultraintense laser–plasma interactions*," *Physics of Fluids B: Plasma Physics*, vol. 5, no. 7, pp. 2603–2608, 1993.

[110] S. V. Bulanov, N. M. Naumova, and F. Pegoraro, "Interaction of an ultrashort, relativistically strong laser pulse with an overdense plasma," *Physics of Plasmas*, vol. 1, no. 3, pp. 745–757, 1994.

[111] D. Wu, S. Krasheninnikov, S. Luan, and W. Yu, "Identifying the source of super-high energetic electrons in the presence of pre-plasma in laser–matter interaction at relativistic intensities," *Nuclear Fusion*, vol. 57, p. 016007, oct 2016.

[112] J. Kruger and M. Bovyn, "Relativistic motion of a charged particle in a plane electromagnetic wave with arbitrary amplitude," *Journal of Physics A: Mathematical and General*, vol. 9, pp. 1841–1846, nov 1976.

[113] A. P. L. Robinson, K. Tangtartharakul, K. Weichman, and A. V. Arefiev, "Extreme nonlinear dynamics in vacuum laser acceleration with a crossed beam configuration," *Physics of Plasmas*, vol. 26, no. 9, p. 093110, 2019.

[114] S. G. Bochkarev, E. d'Humières, V. T. Tikhonchuk, P. Korneev, and V. Y. Bychenkov, "Stochastic electron heating in an interference field of several laser pulses of a picosecond duration," *Plasma Physics and Controlled Fusion*, vol. 61, p. 025015, jan 2019.

[115] J. Peebles, M. S. Wei, A. V. Arefiev, C. McGuffey, R. B. Stephens, W. Theobald, D. Haberberger, L. C. Jarrott, A. Link, H. Chen, H. S. McLean, A. Sorokovikova, S. Krasheninnikov, and F. N. Beg, "Investigation of laser pulse length and pre-plasma scale length impact on hot electron generation on OMEGA-EP," *New Journal of Physics*, vol. 19, p. 023008, feb 2017.

[116] J. Peebles, A. V. Arefiev, S. Zhang, C. McGuffey, M. Spinks, J. Gordon, E. W. Gaul, G. Dyer, M. Martinez, M. E. Donovan, T. Ditmire, J. Park, H. Chen, H. S. McLean, M. S. Wei, S. I. Krasheninnikov, and F. N. Beg, "High-angle deflection of the energetic electrons by a voluminous magnetic structure in near-normal intense laser-plasma interactions," *Phys. Rev. E*, vol. 98, p. 053202, Nov 2018.

[117] A. Chourasia, D. Nadeau, and M. Norman, "Seedme: Data sharing building blocks," in *Proceedings of the Practice and Experience in Advanced Research Computing 2017 on Sustainability, Success and Impact*, PEARC17, (New York, NY, USA), pp. 69:1–69:1, ACM, 2017.

[118] L. Willingale, A. V. Arefiev, G. J. Williams, H. Chen, F. Dollar, A. U. Hazi, A. Maksimchuk, M. J.-E. Manuel, E. Marley, W. Nazarov, T. Z. Zhao, and C. Zulick, "The unexpected role of evolving longitudinal electric fields in generating energetic electrons in relativistically transparent plasmas," *New Journal of Physics*, vol. 20, p. 093024, sep 2018.

[119] A. V. Arefiev, A. P. L. Robinson, and V. N. Khudik, "Novel aspects of direct laser acceleration of relativistic electrons," *Journal of Plasma Physics*, vol. 81, no. 4, p. 475810404, 2015.

[120] A. Arefiev, Z. Gong, and A. P. L. Robinson, "Energy gain by laser-accelerated electrons in a strong magnetic field," *Phys. Rev. E*, vol. 101, p. 043201, Apr 2020.

[121] A. P. L. Robinson and A. V. Arefiev, "Net energy gain in direct laser acceleration due to enhanced dephasing induced by an applied magnetic field," *Physics of Plasmas*, vol. 27, no. 2, p. 023110, 2020.

[122] G. Zaslavskii, M. Y. Natenzon, B. Petrovichev, R. Sagdeev, and A. Chernikov, "Stochastic acceleration of relativistic particles in a magnetic field," *Sov. Phys. JETP*, vol. 66, pp. 496–503, 1987.

[123] Y. Zhang and S. I. Krasheninnikov, "Electron heating in the laser and static electric and magnetic fields," *Physics of Plasmas*, vol. 25, no. 1, p. 013120, 2018.

[124] Z. Gong, F. Mackenroth, T. Wang, X. Q. Yan, T. Toncian, and A. V. Arefiev, "Direct laser acceleration of electrons assisted by strong laser-driven azimuthal plasma magnetic fields," *Phys. Rev. E*, vol. 102, p. 013206, Jul 2020.

[125] E. Esarey, C. B. Schroeder, and W. P. Leemans, "Physics of laser-driven plasma-based electron accelerators," *Rev. Mod. Phys.*, vol. 81, pp. 1229–1285, Aug 2009.

[126] J. Towns, T. Cockerill, M. Dahan, I. Foster, K. Gaither, A. Grimshaw, V. Hazlewood, S. Lathrop, D. Lifka, G. D. Peterson, R. Roskies, J. R. Scott, and N. Wilkins-Diehr, "Xsede: Accelerating scientific discovery," *Computing in Science Engineering*, vol. 16, no. 5, pp. 62–74, 2014.

[127] D. P. Higginson, P. Korneev, C. Ruyer, R. Riquier, Q. Moreno, J. Béard, S. N. Chen, A. Grassi, M. Grech, L. Gremillet, H. Pépin, F. Perez, S. Pikuz, B. Pollock, C. Riconda, R. Shepherd, M. Starodubtsev, V. Tikhonchuk, T. Vinci, E. d'Humières, and J. Fuchs, "Laboratory investigation of particle acceleration and magnetic field compression in collisionless colliding fast plasma flows," *Communications Physics*, vol. 2, p. 60, Jun 2019.

[128] T. Johzaki, T. Taguchi, Y. Sentoku, A. Sunahara, H. Nagatomo, H. Sakagami, K. Mima, S. Fujioka, and H. Shiraga, "Control of an electron beam using strong magnetic field for efficient core heating in fast ignition," *Nuclear Fusion*, vol. 55, p. 053022, apr 2015.

[129] M. Bailly-Grandvaux, J. Santos, C. Bellei, P. Forestier-Colleoni, S. Fujioka, L. Giuffrida, J. Honrubia, D. Batani, R. Bouillaud, M. Chevrot, *et al.*, "Guiding of relativistic electron beams in dense matter by laser-driven magnetostatic fields," *Nature communications*, vol. 9, no. 1, p. 102, 2018.

[130] A. Arefiev, T. Toncian, and G. Fiksel, "Enhanced proton acceleration in an applied longitudinal magnetic field," *New Journal of Physics*, vol. 18, p. 105011, oct 2016.

[131] D. K. Kuri, N. Das, and K. Patel, "Collimated proton beams from magnetized near-critical plasmas," *Laser and Particle Beams*, vol. 36, no. 3, p. 276–285, 2018.

[132] H. Cheng, L. H. Cao, J. X. Gong, R. Xie, C. Y. Zheng, and Z. J. Liu, "Improvement of ion acceleration in radiation pressure acceleration regime by using an external strong magnetic field," *Laser and Particle Beams*, vol. 37, no. 2, p. 217–222, 2019.

[133] A. Macchi, M. Borghesi, and M. Passoni, "Ion acceleration by superintense laser-plasma interaction," *Rev. Mod. Phys.*, vol. 85, pp. 751–793, May 2013.

[134] H. Ruhl, S. V. Bulanov, T. E. Cowan, T. V. Liseĭkina, P. Nickles, F. Pegoraro, M. Roth, and W. Sandner, "Computer simulation of the three-dimensional regime of proton acceleration in the interaction of laser radiation with a thin spherical target," *Plasma Physics Reports*, vol. 27, pp. 363–371, May 2001.

[135] R. A. Snavely, B. Zhang, K. Akli, Z. Chen, R. R. Freeman, P. Gu, S. P. Hatchett, D. Hey, J. Hill, M. H. Key, Y. Izawa, J. King, Y. Kitagawa, R. Kodama, A. B. Langdon, B. F. Lasinski, A. Lei, A. J. MacKinnon, P. Patel, R. Stephens, M. Tampo, K. A. Tanaka, R. Town, Y. Toyama, T. Tsutsumi, S. C. Wilks, T. Yabuuchi, and J. Zheng, "Laser generated proton beam focusing and high temperature isochoric heating of solid matter," *Physics of Plasmas*, vol. 14, no. 9, p. 092703, 2007.

[136] T. Bartal, M. E. Foord, C. Bellei, M. H. Key, K. A. Flippo, S. A. Gaillard, D. T. Offermann, P. K. Patel, L. C. Jarrott, D. P. Higginson, M. Roth, A. Otten, D. Kraus, R. B. Stephens, H. S. McLean, E. M. Giraldez, M. S. Wei, D. C. Gautier, and F. N. Beg, "Focusing of short-pulse high-intensity laser-accelerated proton beams," *Nature Physics*, vol. 8, pp. 139–142, Feb 2012.

[137] P. L. Poole, L. Obst, G. E. Cochran, J. Metzkes, H.-P. Schlenvoigt, I. Prencipe, T. Kluge, T. Cowan, U. Schramm, D. W. Schumacher, and K. Zeil, "Laser-driven ion acceleration via target normal sheath acceleration in the relativistic transparency regime," *New Journal of Physics*, vol. 20, p. 013019, jan 2018.

[138] J. Ferri, E. Siminos, and T. Fülöp, "Enhanced target normal sheath acceleration using colliding laser pulses," *Communications Physics*, vol. 2, p. 40, Apr 2019.

[139] S. Kar, H. Ahmed, R. Prasad, M. Cerchez, S. Brauckmann, B. Aurand, G. Cantono, P. Hadjisolomou, C. L. S. Lewis, A. Macchi, G. Nersisyan, A. P. L. Robinson, A. M.

Schroer, M. Swantusch, M. Zepf, O. Willi, and M. Borghesi, "Guided post-acceleration of laser-driven ions by a miniature modular structure," *Nature Communications*, vol. 7, p. 10792, Apr 2016.

[140] S. C. Wilks, A. B. Langdon, T. E. Cowan, M. Roth, M. Singh, S. Hatchett, M. H. Key, D. Pennington, A. MacKinnon, and R. A. Snavely, "Energetic proton generation in ultra-intense laser–solid interactions," *Physics of Plasmas*, vol. 8, no. 2, pp. 542–549, 2001.

[141] A. Sgattoni, P. Londrillo, A. Macchi, and M. Passoni, "Laser ion acceleration using a solid target coupled with a low-density layer," *Phys. Rev. E*, vol. 85, p. 036405, Mar 2012.

[142] E. d'Humières, A. Brantov, V. Yu. Bychenkov, and V. T. Tikhonchuk, "Optimization of laser-target interaction for proton acceleration," *Physics of Plasmas*, vol. 20, no. 2, p. 023103, 2013.

[143] V. V. Ivanov, A. V. Maximov, R. Betti, L. S. Leal, R. C. Mancini, K. J. Swanson, I. E. Golovkin, C. J. Fontes, H. Sawada, A. B. Sefkow, and N. L. Wong, "Study of laser produced plasma in a longitudinal magnetic field," *Physics of Plasmas*, vol. 26, no. 6, p. 062707, 2019.

[144] L. S. Leal, A. V. Maximov, R. Betti, A. B. Sefkow, and V. V. Ivanov, "Modeling magnetic confinement of laser-generated plasma in cylindrical geometry leading to disk-shaped structures," *Physics of Plasmas*, vol. 27, no. 2, p. 022116, 2020.

[145] Z. M. Sheng and J. Meyer-ter Vehn, "Inverse faraday effect and propagation of circularly polarized intense laser beams in plasmas," *Phys. Rev. E*, vol. 54, pp. 1833–1842, Aug 1996.

[146] A. Robinson, D. Strozzi, J. Davies, L. Gremillet, J. Honrubia, T. Johzaki, R. Kingham, M. Sherlock, and A. Solodov, "Theory of fast electron transport for fast ignition," *Nuclear Fusion*, vol. 54, p. 054003, apr 2014.

[147] L. G. Huang, H. Takabe, and T. E. Cowan, "Maximizing magnetic field generation in high power laser–solid interactions," *High Power Laser Science and Engineering*, vol. 7, p. e22, 2019.

[148] J. Meinecke, H. W. Doyle, F. Miniati, A. R. Bell, R. Bingham, R. Crowston, R. P. Drake, M. Fatenejad, M. Koenig, Y. Kuramitsu, C. C. Kuranz, D. Q. Lamb, D. Lee, M. J. MacDonald, C. D. Murphy, H.-S. Park, A. Pelka, A. Ravasio, Y. Sakawa, A. A. Schekochihin, A. Scopatz, P. Tzeferacos, W. C. Wan, N. C. Woolsey, R. Yurchak, B. Reville, and G. Gregori, "Turbulent amplification of magnetic fields in laboratory laser-produced shock waves," *Nature Physics*, vol. 10, pp. 520–524, Jul 2014.

[149] S. Ali, J. R. Davies, and J. T. Mendonca, "Inverse faraday effect with linearly polarized laser pulses," *Phys. Rev. Lett.*, vol. 105, p. 035001, Jul 2010.

[150] Y. Shi, K. Weichman, R. J. Kingham, and A. V. Arefiev, "Magnetic field generation in a laser-irradiated thin collisionless plasma target by return current electrons carrying orbital angular momentum," *New Journal of Physics*, vol. 22, p. 073067, aug 2020.

[151] F. Brunel, "Not-so-resonant, resonant absorption," *Phys. Rev. Lett.*, vol. 59, pp. 52–55, Jul 1987.

[152] F. N. Beg, A. R. Bell, A. E. Dangor, C. N. Danson, A. P. Fews, M. E. Glinsky, B. A. Hammel, P. Lee, P. A. Norreys, and M. Tatarakis, "A study of picosecond laser–solid interactions up to 10^19 w·cm^{-}2," *Physics of Plasmas*, vol. 4, no. 2, pp. 447–457, 1997.

[153] J. Fuchs, P. Antici, E. d'Humières, E. Lefebvre, M. Borghesi, E. Brambrink, C. Cecchetti, M. Kaluza, V. Malka, M. Manclossi, *et al.*, "Laser-driven proton scaling laws and new paths towards energy increase," *Nature physics*, vol. 2, no. 1, p. 48, 2006.

[154] T. Ceccotti, A. Lévy, H. Popescu, F. Réau, P. D'Oliveira, P. Monot, J. P. Geindre, E. Lefebvre, and P. Martin, "Proton acceleration with high-intensity ultrahigh-contrast laser pulses," *Phys. Rev. Lett.*, vol. 99, p. 185002, Oct 2007.

[155] D. R. Welch, D. V. Rose, M. E. Cuneo, R. B. Campbell, and T. A. Mehlhorn, "Integrated simulation of the generation and transport of proton beams from laser-target interaction," *Physics of Plasmas*, vol. 13, no. 6, p. 063105, 2006.

[156] J. Kim, A. J. Kemp, S. C. Wilks, D. H. Kalantar, S. Kerr, D. Mariscal, F. N. Beg, C. McGuffey, and T. Ma, "Computational modeling of proton acceleration with multi-picosecond and high energy, kilojoule, lasers," *Physics of Plasmas*, vol. 25, no. 8, p. 083109, 2018.

[157] A. D. Sakharov, R. Z. Lyudaev, E. N. Smirnov, Y. I. Plyushchev, A. I. Pavlovskiĭ, V. K. Chernyshev, E. Feoktistova, E. I. Zharinov, and Y. A. Zysin, "Magnetic cumulation," in *Doklady Akademii Nauk*, vol. 165, pp. 65–68, Russian Academy of Sciences, 1965.

[158] C. M. Fowler, W. B. Garn, and R. S. Caird, "Production of very high magnetic fields by implosion," *Journal of Applied Physics*, vol. 31, no. 3, pp. 588–594, 1960.

[159] E. C. Cnare, "Magnetic flux compression by magnetically imploded metallic foils," *Journal of Applied Physics*, vol. 37, no. 10, pp. 3812–3816, 1966.

[160] H. Daido, F. Miki, K. Mima, M. Fujita, K. Sawai, H. Fujita, Y. Kitagawa, S. Nakai, and C. Yamanaka, "Generation of a strong magnetic field by an intense co$_2$ laser pulse," *Phys. Rev. Lett.*, vol. 56, pp. 846–849, Feb 1986.

[161] F. S. Felber, M. M. Malley, F. J. Wessel, M. K. Matzen, M. A. Palmer, R. B. Spielman, M. A. Liberman, and A. L. Velikovich, "Compression of ultrahigh magnetic fields in a gas-puff z pinch," *The Physics of Fluids*, vol. 31, no. 7, pp. 2053–2056, 1988.

[162] A. Velikovich, S. Gol'berg, M. Liberman, and F. Felber, "Hydrodynamics of compression of a plasma with a frozen-in magnetic field by a thin cylindrical wall," *Sov. Phys. JETP*, p. 261, 1985.

[163] N. Miura and H. Nojiri, "Recent advances in megagauss physics," *Physica B: Condensed Matter*, vol. 216, no. 3, pp. 153 – 157, 1996. Proceedings of the International Workshop on Advances in High Magnetic Fields.

[164] F. Pegoraro, S. V. Bulanov, F. Califano, T. Z. Esirkepov, M. Lontano, J. M. ter Vehn, N. M. Naumova, A. M. Pukhov, and V. A. Vshivkov, "Magnetic fields from high-intensity laser pulses in plasmas," *Plasma Physics and Controlled Fusion*, vol. 39, pp. B261–B272, dec 1997.

[165] C. Courtois, A. D. Ash, D. M. Chambers, R. A. D. Grundy, and N. C. Woolsey, "Creation of a uniform high magnetic-field strength environment for laser-driven experiments," *Journal of Applied Physics*, vol. 98, no. 5, p. 054913, 2005.

[166] J. P. Knauer, O. V. Gotchev, P. Y. Chang, D. D. Meyerhofer, O. Polomarov, R. Betti, J. A. Frenje, C. K. Li, M. J.-E. Manuel, R. D. Petrasso, J. R. Rygg, and F. H. Séguin, "Compressing magnetic fields with high-energy lasers," *Physics of Plasmas*, vol. 17, no. 5, p. 056318, 2010.

[167] V. T. Tikhonchuk, M. Bailly-Grandvaux, J. J. Santos, and A. Poyé, "Quasistationary magnetic field generation with a laser-driven capacitor-coil assembly," *Phys. Rev. E*, vol. 96, p. 023202, Aug 2017.

[168] D. Nakamura, A. Ikeda, H. Sawabe, Y. H. Matsuda, and S. Takeyama, "Record indoor magnetic field of 1200 t generated by electromagnetic flux-compression," *Review of Scientific Instruments*, vol. 89, no. 9, p. 095106, 2018.

[169] Z. Lécz and A. Andreev, "Laser-induced extreme magnetic field in nanorod targets," *New Journal of Physics*, vol. 20, p. 033010, mar 2018.

[170] T. Wang, T. Toncian, M. S. Wei, and A. V. Arefiev, "Structured targets for detection of megatesla-level magnetic fields through faraday rotation of xfel beams," *Physics of Plasmas*, vol. 26, no. 1, p. 013105, 2019.

[171] J. Park, S. S. Bulanov, J. Bin, Q. Ji, S. Steinke, J.-L. Vay, C. G. R. Geddes, C. B. Schroeder, W. P. Leemans, T. Schenkel, and E. Esarey, "Ion acceleration in laser generated megatesla magnetic vortex," *Physics of Plasmas*, vol. 26, no. 10, p. 103108, 2019.

[172] R. Sagdeev, "Cooperative phenomena and shock waves in collisionless plasmas," *Rev. Plasma Phys.*, vol. 4, p. 23, 1966.

[173] S. Weng, Q. Zhao, Z. Sheng, W. Yu, S. Luan, M. Chen, L. Yu, M. Murakami, W. B. Mori, and J. Zhang, "Extreme case of faraday effect: magnetic splitting of ultrashort laser pulses in plasmas," *Optica*, vol. 4, pp. 1086–1091, Sep 2017.

[174] A. Santangelo, A. Segreto, S. Giarrusso, D. D. Fiume, M. Orlandini, A. N. Parmar, T. Oosterbroek, T. Bulik, T. Mihara, S. Campana, G. L. Israel, and L. Stella, "A [CSC][ITAL]BeppoSAX[/ITAL][/CSC] study of the pulsating transient x0115+63: The first x-ray spectrum with four cyclotron harmonic features," *The Astrophysical Journal*, vol. 523, pp. L85–L88, sep 1999.

[175] K. N. Gourgouliatos and A. Cumming, "Hall effect in neutron star crusts: evolution, endpoint and dependence on initial conditions," *Monthly Notices of the Royal Astronomical Society*, vol. 438, pp. 1618–1629, 12 2013.

[176] R. A. Kopp and G. W. Pneuman, "Magnetic reconnection in the corona and the loop prominence phenomenon," *Solar Physics*, vol. 50, pp. 85–98, Sep 1976.

[177] S. Masuda, T. Kosugi, H. Hara, S. Tsuneta, and Y. Ogawara, "A loop-top hard x-ray source in a compact solar flare as evidence for magnetic reconnection," *Nature*, vol. 371, pp. 495–497, Oct 1994.

[178] P. Gilch, F. Pöllinger-Dammer, C. Musewald, M. E. Michel-Beyerle, and U. E. Steiner, "Magnetic field effect on picosecond electron transfer," *Science*, vol. 281, no. 5379, pp. 982–984, 1998.

[179] D. Lai, "Matter in strong magnetic fields," *Rev. Mod. Phys.*, vol. 73, pp. 629–662, Aug 2001.

[180] F. Herlach, *High magnetic fields: science and technology*, vol. 3. World Scientific Pub Co Inc, Singapore, 2003.

[181] X. Ribeyre, E. d'Humières, O. Jansen, S. Jequier, V. T. Tikhonchuk, and M. Lobet, "Pair creation in collision of γ-ray beams produced with high-intensity lasers," *Phys. Rev. E*, vol. 93, p. 013201, Jan 2016.

[182] O. Jansen, T. Wang, D. J. Stark, E. d'Humières, T. Toncian, and A. V. Arefiev, "Leveraging extreme laser-driven magnetic fields for gamma-ray generation and pair production," *Plasma Physics and Controlled Fusion*, vol. 60, p. 054006, mar 2018.

[183] J. K. Koga, M. Murakami, A. V. Arefiev, and Y. Nakamiya, "Probing and possible application of the qed vacuum with micro-bubble implosions induced by ultra-intense laser pulses," *Matter and Radiation at Extremes*, vol. 4, no. 3, p. 034401, 2019.

[184] S. A. Slutz and R. A. Vesey, "High-gain magnetized inertial fusion," *Phys. Rev. Lett.*, vol. 108, p. 025003, Jan 2012.

[185] W.-M. Wang, P. Gibbon, Z.-M. Sheng, and Y.-T. Li, "Magnetically assisted fast ignition," *Phys. Rev. Lett.*, vol. 114, p. 015001, Jan 2015.

[186] J. Honrubia, A. Morace, and M. Murakami, "On intense proton beam generation and transport in hollow cones," *Matter and Radiation at Extremes*, vol. 2, no. 1, pp. 28–36, 2017.

[187] P. A. Norreys, M. Santala, E. Clark, M. Zepf, I. Watts, F. N. Beg, K. Krushelnick, M. Tatarakis, A. E. Dangor, X. Fang, P. Graham, T. McCanny, R. P. Singhal, K. W. D. Ledingham, A. Creswell, D. C. W. Sanderson, J. Magill, A. Machacek, J. S. Wark, R. Allott, B. Kennedy, and D. Neely, "Observation of a highly directional γ-ray beam from ultrashort, ultraintense laser pulse interactions with solids," *Physics of Plasmas*, vol. 6, no. 5, pp. 2150–2156, 1999.

[188] M. Murakami and M. M. Basko, "Self-similar expansion of finite-size non-quasi-neutral plasmas into vacuum: Relation to the problem of ion acceleration," *Physics of Plasmas*, vol. 13, no. 1, p. 012105, 2006.

[189] F. Jüttner, "Das maxwellsche gesetz der geschwindigkeitsverteilung in der relativtheorie," *Annalen der Physik*, vol. 339, no. 5, pp. 856–882, 1911.

[190] B. Bezzerides, S. J. Gitomer, and D. W. Forslund, "Randomness, maxwellian distributions, and resonance absorption," *Phys. Rev. Lett.*, vol. 44, pp. 651–654, Mar 1980.

[191] T. Kluge, M. Bussmann, U. Schramm, and T. E. Cowan, "Simple scaling equations for electron spectra, currents, and bulk heating in ultra-intense short-pulse laser-solid interaction," *Physics of Plasmas*, vol. 25, no. 7, p. 073106, 2018.

[192] L. Landau and E. Lifshitz, *Course in Theoretical Physics, Vol. 6: Fluid Mechanics*. Pergamon Press Oxford, 1959.

[193] B. Shen, Z. Bu, J. Xu, T. Xu, L. Ji, R. Li, and Z. Xu, "Exploring vacuum birefringence based on a 100 pw laser and an x-ray free electron laser beam," *Plasma Physics and Controlled Fusion*, vol. 60, p. 044002, feb 2018.

[194] N. Kardjilov, A. Hilger, I. Manke, M. Strobl, and J. Banhart, "Imaging with polarized neutrons," *Journal of Imaging*, vol. 4, p. 23, Jan 2018.

[195] M. Murakami, "Analysis of radiation symmetrization in hohlraum targets," *Nuclear Fusion*, vol. 32, pp. 1715–1724, oct 1992.

[196] M. Murakami and D. Nishi, "Optimization of laser illumination configuration for directly driven inertial confinement fusion," *Matter and Radiation at Extremes*, vol. 2, no. 2, pp. 55–68, 2017.

[197] K. Weichman, J. J. Santos, S. Fujioka, T. Toncian, and A. V. Arefiev, "Generation of focusing ion beams by magnetized electron sheath acceleration," *Scientific Reports*, vol. 10, p. 18966, Nov 2020.

[198] K. Weichman, A. P. L. Robinson, M. Murakami, and A. V. Arefiev, "Strong surface magnetic field generation in relativistic short pulse laser–plasma interaction with an applied seed magnetic field," *New Journal of Physics*, vol. 22, p. 113009, nov 2020.

[199] M. Murakami, J. J. Honrubia, K. Weichman, A. V. Arefiev, and S. V. Bulanov, "Generation of megatesla magnetic fields by intense-laser-driven microtube implosions," *Scientific Reports*, vol. 10, p. 16653, Oct 2020.

[200] M. Murakami, A. Arefiev, and M. A. Zosa, "Generation of ultrahigh field by microbubble implosion," *Scientific Reports*, vol. 8, p. 7537, May 2018.

[201] M. Murakami, A. Arefiev, M. A. Zosa, J. K. Koga, and Y. Nakamiya, "Relativistic proton emission from ultrahigh-energy-density nanosphere generated by microbubble implosion," *Physics of Plasmas*, vol. 26, no. 4, p. 043112, 2019.

[202] P. Gibbon and A. R. Bell, "Collisionless absorption in sharp-edged plasmas," *Phys. Rev. Lett.*, vol. 68, pp. 1535–1538, Mar 1992.

[203] C. N. Danson, C. Haefner, J. Bromage, T. Butcher, J.-C. F. Chanteloup, E. A. Chowdhury, A. Galvanauskas, L. A. Gizzi, J. Hein, D. I. Hillier, and et al., "Petawatt and exawatt class lasers worldwide," *High Power Laser Science and Engineering*, vol. 7, p. e54, 2019.

[204] K. F. F. Law, M. Bailly-Grandvaux, A. Morace, S. Sakata, K. Matsuo, S. Kojima, S. Lee, X. Vaisseau, Y. Arikawa, A. Yogo, K. Kondo, Z. Zhang, C. Bellei, J. J. Santos, S. Fujioka, and H. Azechi, "Direct measurement of kilo-tesla level magnetic field generated with laser-driven capacitor-coil target by proton deflectometry," *Applied Physics Letters*, vol. 108, no. 9, p. 091104, 2016.

[205] P. Y. Chang, G. Fiksel, M. Hohenberger, J. P. Knauer, R. Betti, F. J. Marshall, D. D. Meyerhofer, F. H. Séguin, and R. D. Petrasso, "Fusion yield enhancement in magnetized laser-driven implosions," *Physical Review Letters*, vol. 107, p. 035006, Jul 2011.

[206] L. J. Perkins, B. G. Logan, G. B. Zimmerman, and C. J. Werner, "Two-dimensional simulations of thermonuclear burn in ignition-scale inertial confinement fusion targets under compressed axial magnetic fields," *Physics of Plasmas*, vol. 20, no. 7, p. 072708, 2013.

[207] D. Lai, "Matter in strong magnetic fields," *Reviews of Modern Physics*, vol. 73, pp. 629–662, Aug 2001.

[208] M. G. Haines, "Generation of an axial magnetic field from photon spin," *Physical Review Letters*, vol. 87, p. 135005, Sep 2001.

[209] Z. Najmudin, M. Tatarakis, A. Pukhov, E. L. Clark, R. J. Clarke, A. E. Dangor, J. Faure, V. Malka, D. Neely, M. I. K. Santala, and K. Krushelnick, "Measurements of the inverse faraday effect from relativistic laser interactions with an underdense plasma," *Physical Review Letters*, vol. 87, p. 215004, Nov 2001.

[210] Y. Shi, J. Vieira, R. M. G. M. Trines, R. Bingham, B. F. Shen, and R. J. Kingham, "Magnetic field generation in plasma waves driven by copropagating intense twisted lasers," *Physical Review Letters*, vol. 121, p. 145002, Oct 2018.

[211] J. Vieira, J. T. Mendonça, and F. Quéré, "Optical control of the topology of laser-plasma accelerators," *Physical Review Letters*, vol. 121, p. 054801, Jul 2018.

[212] R. Nuter, P. Korneev, I. Thiele, and V. Tikhonchuk, "Plasma solenoid driven by a laser beam carrying an orbital angular momentum," *Physical Review E*, vol. 98, p. 033211, Sep 2018.

[213] J. R. Davies, A. R. Bell, and M. Tatarakis, "Magnetic focusing and trapping of high-intensity laser-generated fast electrons at the rear of solid targets," *Physical Review E*, vol. 59, pp. 6032–6036, May 1999.

[214] L. Gorbunov, P. Mora, and T. M. Antonsen, Jr., "Magnetic field of a plasma wake driven by a laser pulse," *Physical Review Letters*, vol. 76, pp. 2495–2498, Apr 1996.

[215] Z. M. Sheng, J. Meyer-ter Vehn, and A. Pukhov, "Analytic and numerical study of magnetic fields in the plasma wake of an intense laser pulse," *Physics of Plasmas*, vol. 5, no. 10, pp. 3764–3773, 1998.

[216] L. M. Gorbunov, P. Mora, and T. M. Antonsen, "Quasistatic magnetic field generated by a short laser pulse in an underdense plasma," *Physics of Plasmas*, vol. 4, no. 12, pp. 4358–4368, 1997.

[217] V. Kaymak, A. Pukhov, V. N. Shlyaptsev, and J. J. Rocca, "Nanoscale ultradense z-pinch formation from laser-irradiated nanowire arrays," *Physical Review Letters*, vol. 117, p. 035004, Jul 2016.

[218] P. Tzeferacos, A. Rigby, A. Bott, A. Bell, R. Bingham, A. Casner, F. Cattaneo, E. Churazov, J. Emig, F. Fiuza, C. Forest, J. Foster, C. Graziani, J. Katz, M. Koenig, C. Li, J. Meinecke, R. Petrasso, H. Park, B. Remington, J. Ross, D. Ryu, D. Ryutov, T. White, B. Reville, F. Miniati, A. Schekochihin, D. Lamb, D. Froula, and G. Gregori, "Laboratory evidence of dynamo amplification of magnetic fields in a turbulent plasma," *Nature communications*, vol. 9, no. 1, p. 591, 2018.

[219] F. J. Wessel, F. S. Felber, N. C. Wild, H. U. Rahman, A. Fisher, and E. Ruden, "Generation of high magnetic fields using a gas-puff z pinch," *Applied Physics Letters*, vol. 48, no. 17, pp. 1119–1121, 1986.

[220] D. Wu and J. W. Wang, "Magetostatic amplifier with tunable maximum by twisted-light plasma interactions," *Plasma Physics and Controlled Fusion*, vol. 59, p. 095010, aug 2017.

[221] J. D. Jackson, *Electrodynamics*. Wiley Online Library, 1975.

[222] M. Gauthier, J. B. Kim, C. B. Curry, B. Aurand, E. J. Gamboa, S. Göde, C. Goyon, A. Hazi, S. Kerr, A. Pak, A. Propp, B. Ramakrishna, J. Ruby, O. Willi, G. J. Williams, C. Rödel, and S. H. Glenzer, "High-intensity laser-accelerated ion beam produced from cryogenic micro-jet target," *Review of Scientific Instruments*, vol. 87, no. 11, p. 11D827, 2016.